Atomic structure and electronic properties of Tb silicide nanowires

vorgelegt von
M. Sc. Phys.
Stephan Appelfeller
geb. in Neuhaus am Rennweg

von der Fakultät II - Mathematik und Naturwissenschaften
der Technischen Universität Berlin
zur Erlangung des akademischen Grades

Doktor der Naturwissenschaften
- Dr. rer. nat. -
genehmigte Dissertation

Promotionsausschuss:

Vorsitzender: Prof. Dr. rer. nat. Thomas Möller
Berichter: Prof. Dr. rer. nat. Mario Dähne
Berichter: Prof. Dr. rer. nat. Joachim Wollschläger

Tag der wissenschaftlichen Aussprache: 14.11.2018

Berlin 2018

Abstract

Metallic nanowires grown by self-organisation on Si surfaces may be interesting for future applications in Si based nanotechnology, but they will also show unique physical phenomena, e.g. Peierls transitions or Tomonaga-Luttinger liquid behaviour, if they are characterised by a one-dimensional electronic structure. This thesis concentrates on the physical properties of Tb silicide nanowires, which are interesting for both future applications and study of one-dimensional physics.

Terbium disilicides, which form after Tb deposition and annealing on Si substrates, are metals as bulk materials. Two different approaches are used to grow nanowires of these silicides. On one hand, presumably hexagonal $TbSi_2$ nanowires form due to an anisotropic lattice mismatch on Si(001) substrates. On the other hand, extended hexagonal $TbSi_2$ films form on planar Si(111) substrates and nanowire growth may be achieved by using substrates vicinal to Si(111), so-called Si(hhk) substrates, on which the film growth is disrupted by steps leading to structures confined in one direction.

The nanowires on Si(001) are analysed using a multitude of different experimental methods, which was only possible due to intensive collaborations with the workgroup of Prof. Dr. Michael Lehmann (TU Berlin) and within the Forschergruppe 1700 funded by the Deutsche Forschungsgemeinschaft.

Their growth is analysed in detail with scanning tunnelling microscopy and the parameter range, in which the nanowires predominantly form, is well defined by the Tb coverage and the annealing temperature. The nanowires may be overgrown by amorphous Si without structural change, but high-resolution transmission electron microscopy reveals structural changes for embedding in crystalline Si. Based on the cross-sectional data in combination with the surface science data, a new structural model is proposed for the nanowires. Not only the atomic, but also the electronic structure of the nanowires is analysed in detail. The nanowires are metallic, show a quasi-one-dimensional band structure and one-dimensional transport properties.

On Si(hhk) substrates, nanowires only form for $k > h$. For the other offcut direction only elongated stripes with rough edges are observed after optimisation of the preparation parameters. Both stripes and nanowires are characterised by the two-dimensional electronic structure of the extended $TbSi_2$, but with an anisotropic broadening presumably due to the confinement by their limited widths. An additional quasi-one-dimensional electronic structure is exclusively observed for preparations of samples showing the narrowest nanowires and possible corresponding surface structures, e.g. the nanowires or their edges, are discussed.

Zusammenfassung

Selbstorganisiert gewachsene metallische Nanodrähte auf Si-Oberflächen könnten für zukünftige Si-basierende Nanobauteile interessant sein, aber sie können auch einzigartige physikalische Phenomäne zeigen, z. B. Peierls Übergänge oder Charakteristiken von Tomonaga-Luttinger Flüssigkeiten, falls sie eine eindimensionale elektronische Struktur haben. Diese Dissertation konzentriert sich auf die physikalischen Eigenschaften von Terbiumsilizidnanodrähten, die für beides interessant sind: mögliche Anwendungen und die Untersuchung von eindimensionaler Physik.

Terbiumdisilizide, welche sich nach Tb-Abscheidung und Tempern auf Si-Substraten bilden, sind Metalle. Zwei Vorgehensweisen werden genutzt um Nanodrähte dieser Silizide zu wachsen. Einerseits bilden sich Nanodrähte mutmaßlich aus hexagonalem $TbSi_2$ aufgrund anisotroper Gitterfehlanpassung auf Si(001). Andererseits bilden sich großflächige $TbSi_2$-Filme auf Si(111) und das Verwenden von Si(hhk)-Substraten, die vizinal zu Si(111) sind, führt zu Nanodrähten, da das Filmwachstum durch Stufen unterbrochen wird.

Die Nanodrähte auf Si(001) werden mit einer Vielzahl an experimentellen Methoden untersucht. Dies war nur möglich durch intensive Zusammenarbeit mit der Arbeitsgruppe von Prof. Dr. Michael Lehmann und innerhalb der von der Deutschen Forschungsgemeinschaft finanzierten Forschergruppe 1700.

Das Nanodrahtwachstum wurde mittels Rastertunnelmikroskopie analysiert und der Temperatur- und Tb-Bedeckungsbereich, in dem sich die Nanodrähte bevorzugt bilden, gefunden. Beim Überwachsen der Nanodrähte mit amorphen Si treten keine strukturellen Änderungen auf aber beim Einbetten in kristallinem Si, wie mit hochaufgelöster Transmissionelektronmikroskopie festgestellt wurde. Mithilfe dieser Querschnittsdaten und Daten von oberflächensensitiven Messungen wird ein neues Strukturmodell entwickelt. Eine Untersuchung der elektronischen Eigenschaft zeigt, dass die Nanodrähte quasi-eindimensional metallisch sind und der Stromtransport durch sie eindimensional ist.

Auf Si(hhk)-Substraten bilden sich Nanodrähte nur für $k > h$. Für die andere Fehlschnittrichtung wurden lediglich längliche Streifen mit rauhen Kanten beobachtet, nachdem die Präparationsparameter optimisiert wurden. Sowohl Nanodrähte als auch Streifen zeigen die zweidimensional Bandstruktur von großflächigem $TbSi_2$, die allerdings anisotrop verbreitert ist, vermutlich durch die kleinen Nanostrukturbreiten. Eine zusätzliche quasi-eindimensionale elektronische Struktur wird für Proben mit dünnsten Nanodrähte gefunden und mögliche dazugehörige Oberflächenstrukturen, z.B. Nanodrähte oder deren Kanten, diskutiert.

Contents

1. Introduction **1**

I. Theoretical and experimental considerations 5

2. Scanning tunnelling microscopy **7**
2.1. The tunnelling process 7
2.2. Imaging 10
2.3. Spectroscopy 12

3. Photoemission spectroscopy **15**
3.1. The photoelectric effect 15
3.2. Core-level photoemission spectroscopy 17
3.3. Angle-resolved photoemission spectroscopy 19

4. Further experimental techniques **21**
4.1. Low energy electron diffraction 21
4.2. Electron microscopy 23
4.2.1. Scanning electron microscopy 24
4.2.2. Scanning transmission electron microscopy 26
4.2.3. High-resolution transmission electron microscopy 27
4.3. Reflection anisotropy spectroscopy 29
4.4. Electronic transport measurements 31

5. Silicon and rare earth metals **35**
5.1. Silicon 35
5.1.1. Planar and vicinal Si(001) surfaces 35
5.1.2. Planar and vicinal Si(111) surfaces 37
5.2. Rare earth metals and their silicides 42
5.3. Metals on Silicon 44
5.3.1. Thin film growth 44
5.3.2. Schottky barrier formation 46
5.4. Rare earth metals on Silicon 49
5.4.1. Growth and electronic properties on Si(001) 50
5.4.2. Growth and electronic properties on Si(111) 53

6. Experimental details **59**
6.1. Sample preparation 59

6.2. Experimental set-up at TU Berlin . . . 62
6.2.1. The ultrahigh vacuum system . . . 62
6.2.2. The scanning tunnelling microscope . . . 63
6.2.3. Tip preparation . . . 65
6.2.4. Data analysis . . . 66
6.3. Experimental set-up at BESSY II . . . 67
6.3.1. Synchrotron radiation by BESSY II . . . 67
6.3.2. The beamline . . . 70
6.3.3. The ultrahigh vacuum system . . . 71
6.3.4. The electron energy analyser . . . 73
6.3.5. Data analysis . . . 74

II. Results and discussion 77

7. Tb silicide nanostructures on Si(001) 81
7.1. Growth analysis . . . 81
7.1.1. Planar substrates . . . 82
7.1.2. Vicinal substrates . . . 97
7.1.3. Reflection anisotropy spectroscopy . . . 99
7.2. Overgrowth with Si . . . 103
7.2.1. Towards transmission electron microscopy samples . . . 104
7.2.2. Nanowire samples capped by amorphous Si . . . 106
7.2.3. Nanowire samples capped by crystalline Si . . . 110
7.2.4. Summary of Tb silicide nanowire overgrowth by Si . . . 116
7.3. Atomic structure analysis . . . 119
7.3.1. Scanning tunnelling microscopy and low energy electron diffraction 119
7.3.2. High resolution transmission electron microscopy . . . 122
7.3.3. Nanowire structure model . . . 128
7.3.4. Atomic structure of the wetting layer . . . 131
7.4. Electronic properties . . . 137
7.4.1. Core-level photoemission spectroscopy . . . 137
7.4.2. Scanning tunnelling spectroscopy . . . 147
7.4.3. Angle resolved photoemission spectroscopy . . . 151
7.4.4. Transport measurements . . . 162
7.5. Conclusion . . . 167

8. Tb silicide nanowires on vicinal Si(111) 169
8.1. Growth analysis . . . 169
8.1.1. Si(775) and Si(553) . . . 170
8.1.2. Si(557) and Si(335) . . . 172
8.1.3. Influence of Tb diffusion into the Si bulk . . . 175
8.2. Electronic properties . . . 177
8.2.1. Scanning tunnelling spectroscopy . . . 178
8.2.2. Core-level photoemission spectroscopy . . . 182

8.2.3. Angle resolved photoemission spectroscopy 186
8.3. Confinement effects 190
8.3.1. The broadening of the electronic structure 190
8.3.2. The quasi-one-dimensional structure 195
8.4. Conclusions 199

9. Summary and outlook **201**

Bibliography **205**

List of publications **229**

Instruction of students **231**

Acknowledgments **233**

1. Introduction

The world we know has three spatial dimensions and it is hard to imagine further ones. In contrast, it is simple to visualise lower dimensional objects, e.g. a line as a one-dimensional object. Ideally, such a line has neither width nor height and no kind of order is possible when the length of the line is sufficiently large. Figure 1.1 (a) elucidates this last aspect. In the left part, the perfect ferromagnetic ordering of a spin chain is shown. This is the energetically most favourable configuration given a negative coupling constant between the spins. In the spin chain with two domains depicted in the right part of figure 1.1 (a), the perfect order is destroyed. Such a two domain structure is energetically less favourable by a finite amount, but its entropy is larger. Assuming a chain length of $(N + 1)$ spins, there are N possible positions for the domain boundary leading to an entropy of $S = k_\mathrm{B} \ln N$ [1,2], which diverges to infinity for large N. Thus at $T > 0$, the free energy is lower for the two domain system than for the one domain system since the entropy gain by introducing a domain boundary is larger than the formation energy of the domain boundary for a sufficiently long chain. This reasoning holds also true for any other kind of order in a one-dimensional chain making the realisation of ideal, i.e. isolated, well-ordered, and infinitely long, one-dimensional structures infeasible at finite temperatures.

Such an argumentation, or even more complex ones also applicable for two-dimensional structures [5–8], did not deter theorists from being engaged with one-dimensional structures and from predicting various characteristics and phenomena depending on the initial assumptions. A very basic example is the dependence of the density of states (DOS) on the electron kinetic energy (E_kin) for a free electron gas [see figure 1.1 (b)]. In three dimensions, the DOS is proportional to the square root of the energy. For a two-dimensional free electron gas, the DOS is a constant, and confining a free electron gas to one dimension leads to a DOS inversely proportional to the square root of the energy. Another difference between the free electron gases confined to different dimensions is the morphology of their Fermi surfaces [see figure 1.1 (c)]. In three dimensions, the Fermi surface is a sphere with the radius of the Fermi wave vector (k_F), in two dimensions a circle, and in one dimension it only consists of two points.

Information on the Fermi surface of a metal can be deduced by the observation of a Kohn anomaly in the phonon dispersion [9, 10]. The Kohn anomaly describes a softening of phonons with certain wave vectors (K), e.g. $K = 2k_\mathrm{F}$. The magnitude of the softening strongly depends on the dimensionality of the metal and the energy of the phonons becomes zero in the one-dimensional case leading to a lattice distortion, the opening of a band gap, and formation of a charge density wave. This phenomenon is called the Peierls transition [see figure 1.1 (d)] and may be observed below a critical temperature (T_C), which, however, is zero for an ideal one-dimensional metal [11, 12].

Taking a closer look, the description of a one-dimensional metal as a free electron gas or as a Landau-Fermi liquid is inappropriate due to strong electron-electron interactions.

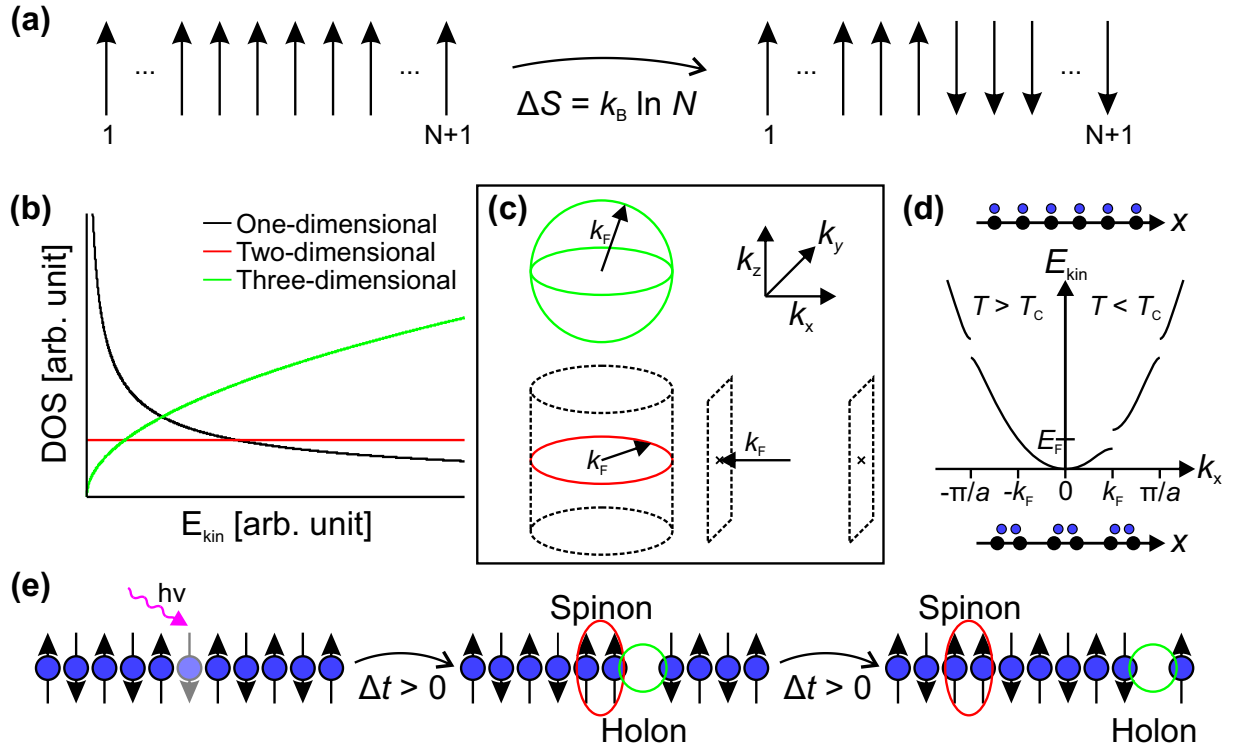

Figure 1.1.: Extraordinary one-dimensional world. (a) Spin chain characterised by complete ferromagnetic ordering on the left and a spin chain with a domain boundary on the right. (b) DOS of a free electron gas confined to one, two, and three dimensions. (c) The Fermi surface (green), the Fermi line (red), and the Fermi points (black) of a three-, two-, and one-dimensional free electron gas, respectively. The dashed areas illustrate the Fermi surfaces of the low-dimensional structures in a three-dimensional environment due to the indefiniteness of the respective $\boldsymbol{k}$ components perpendicular to the structures. (d) A one-dimensional metal at temperatures above (top and left central part) and below (right central and bottom part) the critical temperature for the Peierls transition. (e) Schematic illustration of the spin-charge-separation in a Tomonaga-Luttinger liquid [3, 4]. From left to right: An electron is excited out of the chain, a spinon and a holon form, and the spinon and the holon propagate with different velocities.

These become obvious when one imagines oneself in a narrow line of people. One cannot move forward or backward without the movement of the others, also already indicating that single particle excitations are not feasible in one dimension [13]. In contrast, one may easily move between other people without any interactions in a two-dimensional environment. A theory that takes strong interactions into account is the one of a Tomonaga-Luttinger liquid [14–18]. In this model, the basic excitations are bosons, the spinon as spin excitation and the holon as charge excitation, which propagate in general with different velocities leading to spin-charge separation [see figure 1.1 (e)].

In the 1970s, these theoretical models were required to describe observations made for conducting organic charge transfer salts, e.g. Bechgaard salts [12, 19–24]. The salts of interest grow as three-dimensional anisotropic crystals and form conduction channels along

their long axis. The hopping between individual channels is slow, so that the electrons are practically confined to a single channel and one-dimensional phenomena may be observed. This does not contradict the argumentation that ideal one-dimensional structures cannot exist since no single chain of organic molecules is probed, but the observation are made for a stable three-dimensional crystal. One may argue that the one-dimensional physics of a single channel is stabilised by the three-dimensional environment. Due to the interactions with the environment no pure one-dimensional physics, as described by the above discussed models, but some of their characteristics may be observed nevertheless, e.g. Peierls transitions at temperatures larger than zero [12, 24]. Thus, such structures are not called one-dimensional, but quasi-one-dimensional.

In addition to negligible hopping between conduction channels of the salts, the channels themselves have to be narrow for the observation of one-dimensional phenomena. As an estimation, an electron is confined to a lower dimension when its thermal de Broglie wave length (λ_{th}) is larger than the space it can occupy [25]. Thereby, the thermal de Broglie wave length for a free electron with three degrees of freedom is $\lambda_{\mathrm{th}} = h/p = h/\sqrt{2m_0E_{\mathrm{kin}}} = h/\sqrt{3m_0k_{\mathrm{B}}T}$ [26], which is about 6 nm at room temperature. This criterium gives an idea of the relevant scales, but should be taken carefully. The thermal de Broglie wave length increases with decreasing temperature, so that one may expect transitions from three-dimensional to one-dimensional behaviour upon cooling. In contrast, Bechgaard salts may show two-dimensional or even three-dimensional metallic characteristics at low temperatures and one-dimensional Tomonaga-Luttinger liquid behaviour at higher temperatures due to coherent hopping between the chains at low temperature [22, 23]. Thus, it is difficult to predict when a system may show one-dimensional behaviour, and experimental evidence is essential to claim it.

The most intensively studied quasi-one-dimensional systems are semiconductor nanowires [27–38], while this thesis concentrates on metallic structures. In addition to organic charge transfer salts, metallic systems with one-dimensional characteristics are, e.g., small-diameter single wall carbon nanotubes [39–43], purple bronze [44–46], or $SrCuO_2$ [3]. In contrast, no Tomonaga-Luttinger liquid behaviour was observed for atomic chains in break junctions, although the conductance through them is quantised [47, 48], due to their too small length [49]. Atomic chains can be stabilised on surfaces enabling larger chain lengths. Indeed, one-dimensional characteristics were reported for such systems in recent years, e.g. a Peierls-like transition for In chains on Si(111) [50–53], quasi-one-dimensional dispersions for Au chains on various vicinal Si(111) surfaces [54–56], or possibly a Tomonaga-Luttinger liquid behaviour for Au on Ge(001) [57–59]. Studies on such surface structures can nicely complement the ones on bulk crystals since other probing techniques are available, e.g. scanning tunneling microscopy (STM) and spectroscopy (STS). Furthermore, while the implementation of surface structures into applications is hard to imagine since they are unstable under ambient conditions, surface structures are easier tunable compared to bulk systems, e.g. the distance between chains at step edges and therewith their interaction may be varied by changing the vicinality of the substrate or the influence of doping can be easily monitored by deposition of few further atoms [55, 60].

The system of rare earth (RE) silicide nanowires on Si surfaces studied here represents a combination of bulk and surface systems. The nanowires are grown in ultra-high vacuum (UHV) on clean Si surfaces, but their structure is assumed to be derived from metallic bulk

rare earth silicides, compounds of rare earth metals and Si. It is tried to confine these bulk metals in their dimensions until one-dimensional characteristics are observed, possibly enabling the study of the crossovers from three to two dimensions and from two dimensions to one dimension. Two different approaches are used to confine the rare earth silicides.

On Si(111) surfaces, rare earth silicides grow as well-ordered two-dimensional thin films [61–69], which show the lowest known Schottky barrier heights to n-type Si [70, 71]. Moving from planar to vicinal Si(111) surfaces, the width of the films can be reduced, so that nanowires form, which are separated by steps [72–75]. The narrowest nanowires, which were observed on the Si(557) surface, have heights below 1 nm and widths of about 5 nm while still reaching lengths exceeding 1 μm [73]. Despite their small height and width, they clearly show a two-dimensional electronic structure [73–75].

In contrast to the film growth on Si(111), nanowires form by self-assembly even on planar Si(001) surfaces [76, 77]. Based on the assumption of nanowires formed by hexagonal rare earth disilicides, nanowire growth was predicted for the silicides of nine rare earth metals [78]. For seven of them, this prediction was verified [78–81], while no nanowire formation was observed for Sm [81] and no research on Tb structures was reported. The metallicity of these nanowires is well known [82, 83] and the reported band structures indicate a quasi-one-dimensional electronic structure, even though they seem to differ for various rare earth metals [84, 85].

The focus of this thesis lies on Tb silicide structures on various Si surfaces. Their growth as well as their atomic and electronic structure were analysed mainly using STM, STS, core-level (XPS), and angle-resolved photoemission spectroscopy (ARPES). These techniques are introduced in the chapters 2 and 3 of the first part on the theoretical and experimental background. The studies were complemented by low energy electron diffraction (LEED), various electron microscopy methods, reflection anisotropy spectroscopy (RAS), and transport measurements. These additional studies were mainly possible due to collaborations with the workgroup of Prof. Dr. Michael Lehmann and within the Forschergruppe 1700 (FOR1700) funded by the Deutsche Forschungsgemeinschaft (DFG). In chapter 4, the basics of these additional experimental methods are briefly presented. Subsequently, overviews on Si and its here used surfaces, of rare earth metals and their silicides, as well as on the growth of metals on Si in general and of rare earth induced structures in particular are given in chapter 5. The first part concludes with chapter 6 on the sample preparation and the experimental setups at the TU Berlin containing the STM and at BESSY II used for the photoemission experiments.

In the second part, the results of this thesis are presented and discussed. In chapter 7, the studies on Tb silicide nanostructures on Si(001) are elucidated. Thereby, results obtained within the collaborations are included to achieve a more extensive understanding of the system and to enable additional conclusions, e.g. STM and high-resolution transmission electron microscopy (HRTEM) studies are combined to determine the atomic structure of the observed nanowires. Then, the growth and electronic structure of Tb silicide structures on vicinal Si(111) surfaces are described in chapter 8 with emphasis on the observed quasi-one-dimensional characteristics on Si(335) as well as on general confinement effects. Chapter 9 completes this thesis with a summary and an outlook.

Part I.

Theoretical and experimental considerations

2. Scanning tunnelling microscopy

Scanning tunnelling microscopy is a surface science technique, which was developed by a team around G. Binnig and H. Rohrer in the beginning of the 1980s [86]. After demonstrating vacuum tunnelling [87] and mapping monoatomic steps [88], the atomic resolution image of the Si(111)7×7 reconstruction greatly helped to resolved the structure of this reconstruction, a problem discussed for over 20 years [89–92]. Due to this immediate large success, G. Binnig and H. Rohrer received the Nobel Prize in Physics together with E. Ruska, who was honored for the development of the electron microscope, already four years after their first publication of STM data [93].

The basic principle of an STM is rather simple: Bring a sharp metallic tip close to a conducting sample, apply a small voltage between tip and sample, so that a current flows, and scan the tip over the sample surface while measuring the current. This current depends on the tip-sample distance and therefore on the topography of the surface. Thus, the measured current can be used to get a real space image of the surface, potentially with atomic resolution depending on the tip structure. An advantage of STM is that the surface structure is only slightly disturbed by the measurement process since the tip does not have to touch the surface. Sample and tip do not have to be in contact to measure a current due to the tunnelling effect, which will be elucidated in section 2.1 before the imaging process is described in section 2.2. In addition to topographic data, an STM may be used to obtain information on the electronic structure of the surface. This will become already apparent in the next section, but will be further specified in section 2.3.

2.1. The tunnelling process

Electrons cannot overcome the potential barrier from a material to the vacuum with their thermal energy, about 25 meV at room temperature, since work functions (Φ) are typically about 4 eV. Thus, it should be impossible that electrons move from the tip into the sample if tip and sample are not in direct contact. However, taking into account the quantum nature of electrons, the electrons of the tip will have a non-zero probability density in the sample space if the potential barrier height and the distance between sample and tip are finite. Therefore, the tip electrons may cross over into the sample, which is called tunnelling through the potential barrier. Of course, the electrons of the sample also tunnel into the tip and both tunnelling rates are equal in equilibrium. When a voltage (V) is applied between tip and sample, one tunnelling direction is favoured over the other and a tunnelling current (I) develops.

The quantitative description of this STM tunnelling current is non-trivial and, up to now, not possible for realistic tunnelling geometries. Still, an approximation of the tunnelling current is possible, e.g., by an adaptation of Bardeen's theory developed for metal-oxide-

metal tunnelling junctions [94]. This was first done by Tersoff and Hamann in 1983 [95, 96]. The brief theoretical description of Bardeen's theory presented here follows the one of Chen [97–100], who expanded the theory of Tersoff and Hamann, and focuses on the main aspects necessary to understand the contrast mechanisms of STM. For readers interested in different approaches or more in-depth descriptions, the following papers and textbooks are recommended [101–106].

The tunnelling theory of Bardeen is a time-dependent perturbation theory in which the potential in one metal is perturbed by the constant one of the other metal starting at $t = 0$. Thus, the first step is to divide the complete space in one of the tip (R_T) and one of the sample (R_S) and analyse these subsystems (see figure 2.1). For a correct solution of the problem, one cannot assume that the potentials of the subsystems are that of the free sample ($U_{\mathrm{S}0}$) and free tip ($U_{\mathrm{S}0}$) since they overlap in the tunelling region. Instead, adjusted potentials have to be used to solve the stationary Schrödinger equations yielding ψ_μ and E_μ as the eigenfunctions and eigenvalues of the sample and χ_ν and E_ν as the ones for the tip.

When, e.g., the potential of the sample is perturbed by the potential of the tip at $t \geq 0$, electrons of the sample may populate states of the tip. Assuming that the eigenstates of the sample are orthogonal to the ones of the tip, e.g. appropriate subsets of the eigenstates of the complete tip-sample system, and elastic tunnelling, the transition rate ($w_{\mu\nu}$) from one eigenstate of the sample to one eigenstate of the tip is given by Fermi's golden rule:

$$w_{\mu\nu} = \frac{2\pi}{\hbar}\, \delta(E_\nu - E_\mu)\, |M_{\mu\nu}|^2 \tag{2.1}$$

with $M_{\mu\nu}$ the transition matrix element, here also called tunnelling matrix element since it describes the probability of the tunnelling:

$$M_{\mu\nu} = -\frac{\hbar^2}{2m_e} \int_\Sigma \left[\chi_\nu^* \nabla\psi_\mu - \psi_\mu^* \nabla\chi_\nu\right] d\underline{S} \tag{2.2}$$

with m_e the mass of the tunnelling electron. It should be noted that the tunnelling matrix element is determined by an integral over an arbitrary chosen separation surface (Σ) between the spaces of the sample and tip due to our choice of the potentials and the assumption of elastic tunnelling.

The tunnelling current is proportional to the tunnelling rate, but not only the two states ψ_μ and χ_ν contribute. Rather, all transitions from occupied states of the one metal into free states in the other metal have to be taken into account. Usually, this summation over discreet states is simplified into an integral of the densities of states of the sample (ρ_S) and tip (ρ_T) over the energy with the occupation of the states given by the Fermi-Dirac distribution (f). Accordingly, the tunnelling matrix element has to be averaged for all states of a certain energy, so that the tunnelling current is:

$$\begin{aligned} I = \frac{4\pi e}{\hbar} \int_{-\infty}^{+\infty} & \left[f\left(E_{\mathrm{FT}} - eV + \epsilon\right) - f\left(E_{\mathrm{FS}} - \epsilon\right)\right] \\ & \rho_\mathrm{S}\left(E_{\mathrm{FS}} - \epsilon\right) \rho_\mathrm{T}\left(E_{\mathrm{FT}} - eV + \epsilon\right) |M\left(\epsilon\right)|^2 d\epsilon \end{aligned} \tag{2.3}$$

with E_{FS} and E_{FT} the Fermi level of the sample and of the tip, respectively. When the features in the densities of states are wider than the thermal broadening of the Fermi-Dirac

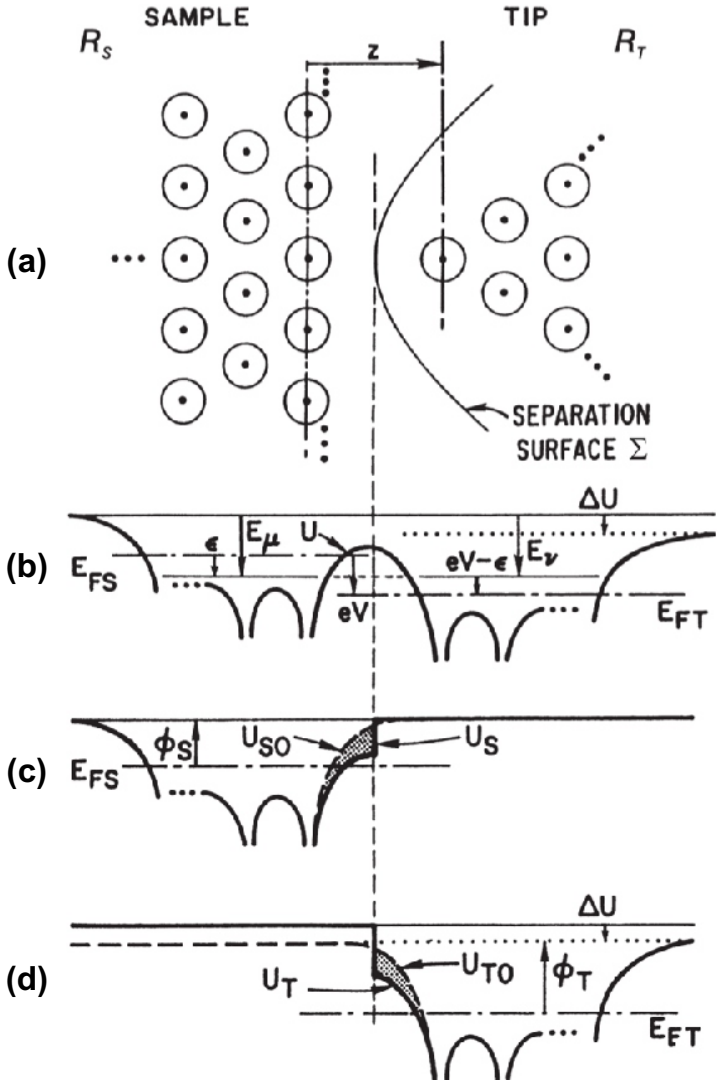

Figure 2.1.: (a) Overview on the tip-sample geometry. (b–d) The potential of the complete system (U) is divided in two parts, the potential in the sample (U_S) and the potential in the tip (U_T), so that $U = U_\mathrm{S} + U_\mathrm{T}$ and $U_\mathrm{S}U_\mathrm{T} = 0$. From [107].

distribution (about $4k_\mathrm{B}T$), e.g. at low temperatures, the Fermi-Dirac distributions may be approximated by step functions yielding:

$$I = \frac{4\pi e}{\hbar} \int_0^{eV} \rho_\mathrm{S}\left(E_\mathrm{FS} - \epsilon\right) \rho_\mathrm{T}\left(E_\mathrm{FT} - eV + \epsilon\right) |M\left(\epsilon\right)|^2 d\epsilon. \tag{2.4}$$

From the equations for the tunnelling matrix element and for the current (equations 2.2–2.4), it is apparent that one can calculate the tunnelling current for a given tunnelling voltage when all eigenstates of sample and tip and thereby also their densities are known. For the sample Bloch states of the volume and surface states, including states from single adatoms etc., have to be considered. In contrast to the sample, for which assumptions about the surface geometry may be possible, e.g. due to structure optimisation with density functional theory, the structure of the tip is usually completely unknown, so that rather

strong approximations are frequently made, e.g. the tip may be approximated by a spherical potential [95, 96]. After the eigenstates are determined for the free systems, they have to be adjusted subsequently to take the sample-tip interplay into account. Thus, calculating and predicting tunnelling currents is a complicated process. Fortunately, to understand the contrast mechanisms of STM, we do not have to know exact wave functions and only have to discuss the equations 2.2 and 2.4 in detail.

2.2. Imaging

With an STM, the local atomic structure of the sample is analysed by taking real space images of the sample under investigation. A tunnelling current has to be measured to get such an image. This current is determined by the applied voltage between tip and sample, by the DOS in tip and sample, and by the tunnelling matrix elements for the states of the tip and sample (see equation 2.4). Each tunnelling matrix element for a state of the tip and one of the sample depends on the overlap of the two states on a surface between tip and sample (see equation 2.2). Since the tip-sample gap is a classically forbidden region, the electron wavefunctions decay exponentially in this region. The decay constant (κ) of this decrease is given by:

$$\kappa(z) = \frac{\sqrt{2m_e\left(U(z) - E\right)}}{\hbar} \tag{2.5}$$

with z the position in the tip-sample gap. Assuming an average barrier height of 3 eV, being less than a typical work function due to the non-square barrier characteristics, and the free electron mass m_0 as electron mass, the average decay constant is about 9 nm^{-1}. Due to this strong dependence of the tunnelling matrix element on the tip-sample separation, the tunnelling current also varies strongly when the tip is moved away from or towards the sample. Experimentally, it was found that the tunnelling current changes by about one order of magnitude, when the tip-sample separation changes by 0.1 nm resulting in a very high resolution of the STM in the direction orthogonal to the sample surface [108].

Another interesting aspect, which can be extracted from equation 2.5, is that the tunnelling matrix element depends on the energy of the tunnelling electrons. Electrons with a high energy, i.e. those close to the Fermi level of the material at negative potential, contribute the most to the tunnelling current while electrons with a lower energy have to tunnel through a higher and wider barrier and do not contribute as much to the tunnelling current.

In addition to the tunnelling matrix element, the densities of states of sample and tip have a strong influence on the tunnelling current and therewith the images of the surface. The density of states of the sample changes laterally depending on the structure of the sample, e.g. some states are localised at certain atoms, so that even atoms situated at the same height may result in different tunnelling currents. This effect is especially apparent when different atomic species are found on a sample (see also section 2.3), e.g. only Ga atoms are seen in STM images of the GaAs(110) surface when the sample is at positive voltage, even though the As atoms lie structurally higher [109]. Of course the tip DOS has also an influence on the STM image, but it usually stayed constant during the recording of the images shown in this thesis.

Great care is needed when semiconductor surfaces are studied since they may have an energy region around their Fermi level without any states. Thus, the tunnelling current is zero for all tip-sample separations including negative ones, i.e. when the tip is within the sample. Fortunately, the Si surfaces studied in this thesis have comparatively many states in the bulk band gap, so that a tunnelling current is observed even at very low tunnelling voltages.

STM images can be generated in two different modes. The first one is the constant height modus, in which the tip scans over the sample at a constant height and the tunnelling current is measured resulting in an image of the current over lateral displacement. This mode is fast, but the tip may crash into the sample if the sample structure is too uneven, e.g. due to surface steps or adsorbates.

The second scan mode is the constant current mode. In this mode, the tip-sample separation is continuously adjusted during the scan by a feedback loop resulting in a constant tunnelling current. The STM image is then given by the tip height over the lateral displacement. Due to the time needed for the feedback loop, this scan mode is slower than the constant height mode, but it has the advantage that the tip evades protrusions on the sample. All images shown in this thesis were taken in the constant current mode.

Figure 2.2 (a) nicely illustrates the constant current mode. The tip is moved by a tripod of piezo elements (P_x, P_y, and P_z) over the surface (the experimental setup used for this thesis is discussed in section 6.2). The tunnelling current is held constant by the control unit (CU), which regulates the voltage at the z-piezo element (V_Z) adjusting the tip-sample separation (s). The movement of the tip is illustrated by the dashed line. From left to right, the tip-sample separation and therefore the tip height remains constant on the flat terrace of the sample. At a step on the sample (region A), the tip height has to change, so that the tip-sample separation on the upper terrace equals that on the lower terrace. The tip height adjustment (dashed line) is never as sharp as the surface structure (thick continuous line) since tunnelling does not only occur vertically, but also between the sides of the tip and surface structure. Thus, a convolution of the sample structure shape with the tip shape is always measured. Moving the tip further to the right, the tip scans over a sample area with a different electronic structure (region C). Since the tip-sample separation becomes larger (region B), e.g., the DOS of the sample is higher in this region.

When an STM image is recorded, the tip scans one line and is then moved one step orthogonal to that line before the next line is scanned. A part of an STM image recorded in this way is shown in figure 2.2 (b). The fast scan direction was from left to right and the slow one from top to bottom for this image. In the beginning the adatom structure of the Si(111)7×7 reconstruction is resolved (more about this structure in section 5.1). Then in the region marked by D, the tip changes repeatedly resulting in a different appearance of the surface even though the surface structure is the same as in the upper part of the image. This illustrates that STM images have to be carefully analysed and tip effects have to be taken into account, e.g. also tunnelling through multiple tips. The tip also plays a rather large role in STS. This technique is introduced in the following section, in which also the influence of the voltage on STM images is discussed.

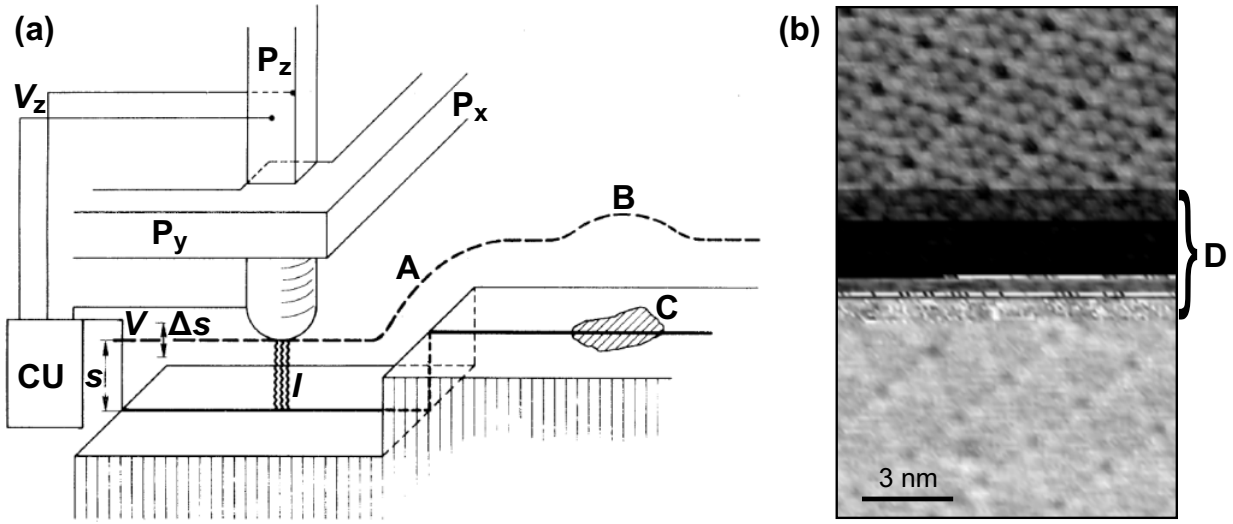

Figure 2.2.: (a) Schematic on the operation of an STM. Adapted from [88]. (b) Filled states STM image with multiple tip changes resulting in a change of the surface appearance (sample voltage $V = -1.5$ V, tunneling current $I = 120$ pA).

2.3. Spectroscopy

The aim of STS is to get information on the local electronic structure, specifically the DOS, of the sample at a specific position. Taking a closer look at equation 2.4, the tunnelling current depends on the integration of the densities of states of sample and tip over an energy range defined by the tunnelling voltage. Thus, the easiest way to get information on the sample DOS is to take STM images at different tunnelling voltages. Particularly, images of the empty states and filled states of the sample can be recorded by changing the polarity of the voltage. In this thesis, all given tunnelling voltages are the ones of the sample with the tip at the ground. Accordingly, empty states of the sample are imaged at positive voltages and filled states at negative voltages.

This selectivity to empty and filled states can be used to obtain chemical sensitivity in sample structures containing more than one atomic species, as already mentioned in the previous section for GaAs. The bonds of atoms of different elements are often accompanied by a charge transfer between the atoms due to an in general different electronegativity of the elements. There is a higher electron density at the atoms of the element with higher electronegativity and, consequently, the density of filled states is higher at these atoms, so that the tip has to retract from (approach to) the sample above these atoms when filled (empty) states are imaged.

With voltage dependent imaging, not only the differences between empty and filled states can be depicted, but also the addition of states at certain energies can become apparent. While the adatoms of the Si(111)7×7 reconstruction are nicely resolvable at low absolute tunnelling voltages independent of the voltage polarity, a change to a more triangular appearance, similar to the one after the tip change in figure 2.2 (b), is usually observed for tunnelling voltages below about -0.8 V. At the respective energy (-0.8 eV), states with their highest probability density in between the adatoms are located leading to the change

in the surface appearance.

The main drawback of voltage dependent imaging is that only information on the integrated DOS is gained. Thus, the detailed DOS cannot be obtained and small lines in the DOS may be overlooked since they are not apparent in the images. For such more detailed information on the energy scale, the recording of point spectra is suitable with the obvious drawback of the lost lateral information.

For the recording of a point spectrum, the scan is stopped above the structure of interest, the feedback loop is switched off, and an I-V curve is measured. The obtained spectrum is related to the electronic structure of the sample at the specific position. Simplifying equation 2.4 by assuming a constant tip DOS and a constant tunnelling matrix element leads to:

$$I = \frac{4\pi e}{\hbar}\rho_{\mathrm{T}}|M|^2 \int_0^{eV} \rho_{\mathrm{S}}\left(E_{\mathrm{FS}} - \epsilon\right) d\epsilon, \tag{2.6}$$

so that one obtains for the sample DOS at the energy given by the tip voltage:

$$\rho_{\mathrm{S}} \propto \frac{\mathrm{d}I}{\mathrm{d}V}. \tag{2.7}$$

This differential conductance ($\mathrm{d}I/\mathrm{d}V$) may be obtained by numerical differentiation of the I-V curve or directly during the measurement with a lock-in technique. The above made assumptions will only be suitable if narrow energy ranges are of interest. As already described in the previous section, the tunnelling matrix element depends on the energy of the tunnelling electrons and the tip DOS is certainly structured, particularly, if the tip apex is only a small cluster needed for high lateral resolution. Such small clusters have only few occupied and unoccupied states at distinct energies [110].

Theoretically and experimentally, it was found that the differential conductance normalised by the static conductance (I/V), conventionally called normalised differential conductance [$(\mathrm{d}I/\mathrm{d}V)/(I/V)$], gives a better agreement with the theoretically expected DOS [111, 112]. It should be noted that Stroscio *et al.* found a nice agreement of the normalized differential conductance with the sample DOS only [111], while the convolution of the densities of states of the tip and sample was considered by Lang *et al.* [112]. Sometimes, further processing steps are needed to obtain meaningful data, e.g. when there is a band gap without any DOS [113]. The use of additional processing steps is mentioned at the respective positions in this thesis. In addition to a better agreement with theory, the normalised differential conductance is also less dependent on the initial tip-sample separation than the differential conductance [108]. Nevertheless, similar to the differential conductance, also the normalised differential conductance will never completely reproduce the DOS, especially never only the one of the sample, and great care has to be taken when analysing the data [114].

Point spectra generate very local data, but the lateral distribution of a maximum in the DOS may be of interest too. To measure such a distribution, an STM image is recorded at the voltage corresponding to the peak energy while modulating the voltage by a high frequency and measuring the lock-in signal simultaneously. The obtained map of the differential conductance depends strongly on the DOS at the peak energy. The main drawback of this spectroscopic imaging is that multiple periods of the voltage modulation have to be measured during the recording for one point of the image. This large recording time per pixel has to be countered by a reduction of the image resolution since drift effects would lead to strongly distorted images.

3. Photoemission spectroscopy

Photoemission spectroscopy, also denoted photoelectron spectroscopy, is based on the photoelectric effect, which was first observed by H. Hertz in 1887 [115] and further investigated i.a. by W. Hallwachs and P. Lenard [116–118]. In the photoelectric effect, electrons are emitted from matter due to the irradiation with light. A. Einstein described the photoelectric effect theoretically in 1905 using the assumption that light consists of quanta [119]. Einstein's theory was tested throughout i.a. by R. A. Millikan in the following years [120]. P. Lenard, A. Einstein, and R. A. Millikan received their Nobel Prizes in Physics in 1905, 1921 and 1923, respectively, i.a. for their work on the photoelectric effect [121–123]. The photoelectric effect will be discussed in general in section 3.1.

While it was quickly realized that the spectrum of the emitted electrons depends on the light source, the elemental composition of the investigated sample and the emission angle, the acquisition and analysis of such spectra was highly complicated, e.g. due to sample contamination in the non-optimal vacua or by the use of non-monochromatised light [124–126]. A breakthrough regarding the energy resolution of photoelectron spectra was achieved by the work group of K. Siegbahn in the 1950s [127], for which he was awarded the Nobel Prize in 1981 [93]. The new precision in the measurement of the binding energies of core-level electrons, i.e. electrons that do not participate in chemical bonding, allowed an analysis of the elemental composition of samples including their stoichiometry and chemical environment [128, 129]. To achieve a high signal, electrons with the same kinetic energy that are emitted in different directions from the sample are focussed on the same spot in the analyser. In this thesis, all such angle-integrated measurements are termed XPS independent of the use of X-rays or ultraviolet light. More detailed information on XPS is given in the section 3.2.

Independent of the development of XPS using X-rays, progress was made in the analysis of valence electrons using ultraviolet light in a similar time frame [126, 130]. In condensed matter, valence electrons form dispersing bands. Thus, their energy depends strongly on their momentum resulting in a strong variation of the photoemission spectra with the emission angle. Such band mapping by ARPES was first done in the 1970s and is the main experimental technique for the analysis of valence band structures [126, 131]. Section 3.3 introduces the band mapping possibilities of ARPES in more detail. It should be noted that band mapping is only the basic application of ARPES [132], and that the progress to more sophisticated instruments is still on-going [133, 134].

3.1. The photoelectric effect

The following brief introduction to photoemission should be sufficient to understand the experimental results presented in this thesis. An quantitative description is not included and

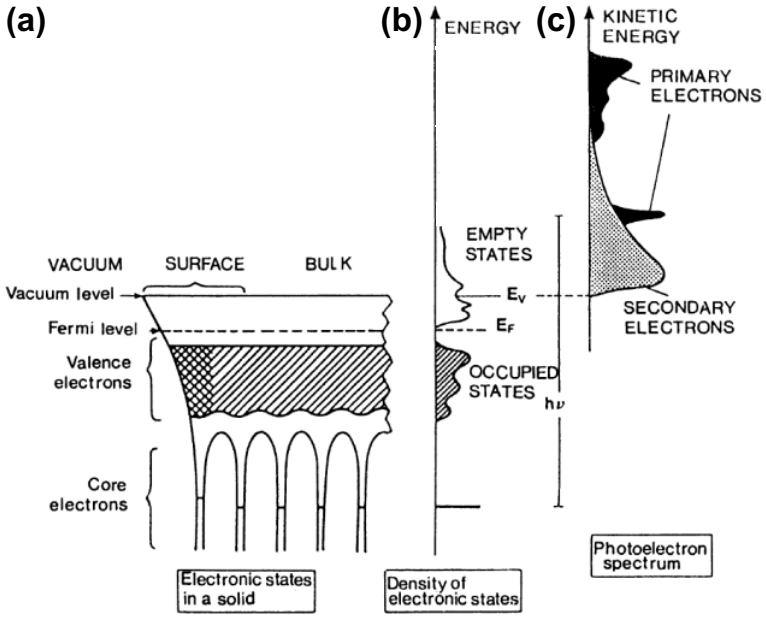

Figure 3.1.: (a) Diagram of the potential and the energy levels in a solid and (b) its corresponding DOS. (c) Energy distribution of the photoelectrons generated by the illumination of the solid with photons with the energy $h\nu$. Adapted from [138].

most arguments are made in the more intuitive three-step model, in which the photoemission process is divided in the electron excitation, the travel of the electron through the solid, and the transmission of the electron through the surface, instead of using the correct one-step model [135–137]. For more in-depth information, the reader is referred to textbooks, e.g. reference [135], on which this introduction is based.

A photon with the energy $h\nu$ may be absorbed by matter to excite an electron from its occupied, i.e. filled, state to an unoccupied, i.e. empty, state. If the energy of the excited electron is larger than the vacuum level (E_V), it may escape from its bound state into the vacuum with the kinetic energy:

$$E_\mathrm{kin} = h\nu - E_\mathrm{Bin} - \Phi \tag{3.1}$$

with E_Bin the binding energy of the initial state with respect to the Fermi level ($E_\mathrm{Bin} > 0$) and with Φ the work function, as in chapter 2. From equation 3.1, it is apparent that the spectrum of the photoelectrons depends on the DOS of the sample since electrons only have certain binding energies. This is illustrated in figure 3.1, in which the black coloured part of the photoelectron spectrum in (c) represents the occupied DOS in (b). Thereby, the photoelectron spectrum is slightly broadened due to the natural line width and, in the experiment, also due to the resolution of the experimental setup.

In addition to these so called primary electrons, the photoelectron spectrum also includes a background of secondary electrons [grey in figure 3.1 (c)], i.e. electrons that escape out of the sample after one or more inelastic scattering events. Not shown in figure 3.1 (c) are secondary electrons with distinct kinetic energies, e.g. Auger electrons, or with distinct energy differences with respect to the primary electrons, e.g. due to losses by the excitation of bulk or surface plasmons. For secondary electrons, equation 3.1 is not valid any more

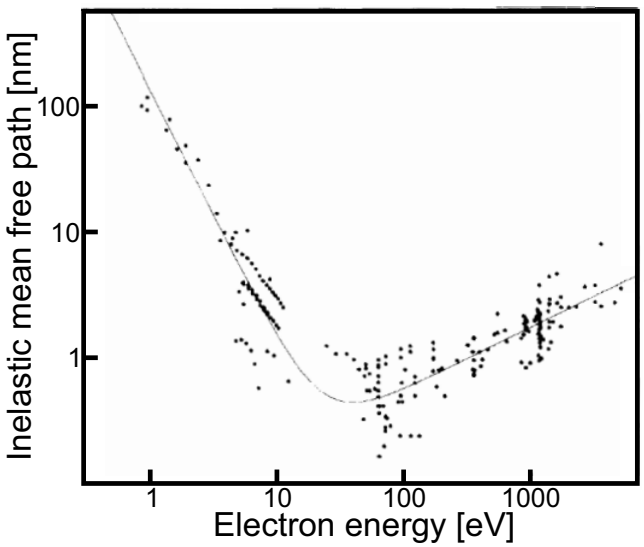

Figure 3.2.: The dependence of the electron inelastic mean free path (Λ) on its energy above the Fermi level (E). The points represent measurements, while the line is a least square fit to the equation $\Lambda = aE^{-2} + bE^{1/2}$ with a and b the fit parameters. Adapted from [139].

and their quasi continuous part declines sharply at the vacuum level, the minimum energy of photoelectrons.

The length that an electron may travel in a solid without losing energy is described by the inelastic mean free path, which is defined as the distance, after which the number of electrons of an energy is reduced to $1/e$ of its initial value. The general dependence of the inelastic mean free path of an electron on its energy above the Fermi level has a rather similar course for all materials and is shown in figure 3.2 [139–144]. The main differences between materials are the exact position of the minima, e.g. for Si between 20 eV and 40 eV [145], and in the low energy region, which depends strongly on the electronic band structure of the material [146]. The inelastic mean free path is typically below 1 nm in the energy region between about 30 eV and 100 eV above the Fermi level. Consequently, a considerable fraction of the primary electrons with such a kinetic energy stem from the surface of the solid and not from the bulk. Thus, very surface sensitive measurements are possible by choosing the photon energy in a way that the photoelectrons of the states that one is interested in have a kinetic energy between 30 eV and 100 eV. Another possibility to tune the surface sensitivity is the variation of the angle, under which the photoelectrons are detected. In doing so, measuring normal to the surface results in the lowest surface sensitivity.

3.2. Core-level photoemission spectroscopy

After the photoemission process, one electron is missing in the solid. When the initial state (ψ_i) is a state of the solid with N electrons, the final state (ψ_f) is a properly antisymmetrised

combination of a state of the solid with $(N-1)$ electrons and the state of the photoelectron (sudden approximation). XPS measures the binding energy in the final state, which does not correspond to the binding energy in the initial state since the $(N-1)$ electron system relaxes, thereby changing the energy levels in a non-trivial manner. These relaxation effects are particularly strong for core holes with high binding energies and can only be neglected for valence band holes that are screened perfectly.

In general, there are multiple final states possible resulting in the splitting of lines into components. As an example, assume a photoelectron is emitted from a closed shell. The remaining electrons in this shell then have the total angular momentum L and the total spin $S = 1/2$, which may couple parallel or antiparallel to each other. Thus, there are two final states distinguished by the total momentum $J = |L \pm S|$ of the shell with the photohole. These states are energetically separated by the spin-orbit coupling, except for s levels ($L = 0$). The intensity ratio between the two components is given by their degeneracy $2J + 1$, e.g. for $p_{3/2}$ and $p_{1/2}$ levels the intensity ratio is $2 : 1$. Deviations from such theoretical ratios may be observed due to the different kinetic energies of the photoelectrons resulting in different inelastic mean free paths, especially for low kinetic energies [see figure 3.2]. It should be noted that spectra of s levels may also be split, e.g. by exchange splitting due to coupling of the photohole shell with an open valence shell.

Another reason for a shift in energy of a core level is the chemical environment. Even though only the valence electrons participate in the bonding to neighbouring atoms, the resulting charge distribution influences also core levels. This chemical shift is rather unique for a specific environment. Thus, an analysis of chemical shifts can be used for structural analysis, when chemical shifts of known structural arrangements are available for comparison, especially in combination with the determination of the general chemical composition of a sample by XPS due to the element specific binding energies.

A special chemical environment is a surface, where bonding partners are missing leading to so-called surface core-level shifts. While contributions of the surface may be negligible when high photon energies are used, which result in high kinetic energies and large inelastic mean free paths, it is possible to estimate the depths of atoms having specific surface core-level shifts by a variation of the surface sensitivity resulting in changes of the relative intensities of the components from the various atoms. In addition to these specific chemical shifts, at semiconductor surfaces due to band bending also the complete line may be shifted in energy, i.e. a change of the Fermi level position in the band gap. Band bending will be further discussed in section 5.3.2.

As the abbreviation XPS chosen here indicates, usually X-rays are used for core-level photoemission experiments. Due to their high photon energy, many core levels are accessible allowing a rather precise chemical analyses. Furthermore, the X-ray photons have a momentum, which is not negligible compared to the one of the electrons in the solid, so that multiple excitation paths are available and the spectra resemble the DOS well. In contrast, when UV light is used for photoemission, the photon momentum is small and only direct transitions are possible in the solid. This leads to a strong dependence of the energy of the escaping electrons on their emission direction especially for the dispersing valence electrons, which can be used to map their band structure, as is illustrated in the next section.

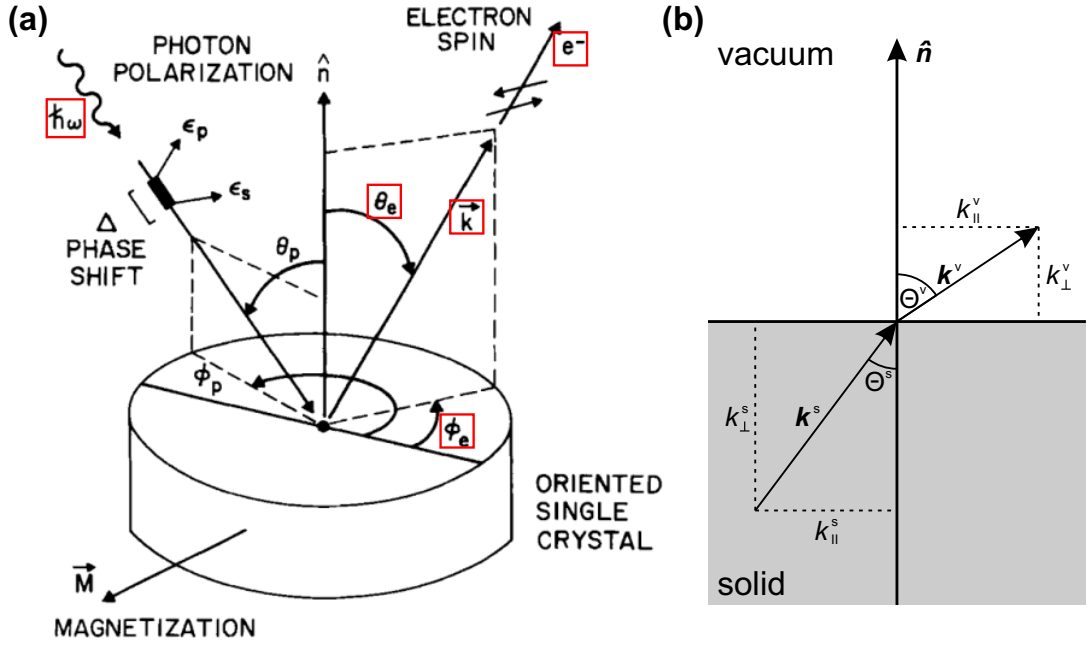

Figure 3.3.: (a) Overview on the photoemission process. A photon with the energy $\hbar\omega = h\nu$ and with a polarisation, given by the component in the plane of incidence ϵ_p, the component perpendicular to the plane of incidence and thus parallel to the surface ϵ_s, and a possible phase shift Δ, impinges on the solid under an azimuthal angle θ_p and a polar angle ϕ_p. The photoelectron is emitted in a direction given by its azimuthal angle θ_e and its polar angle ϕ_e with the momentum $\boldsymbol{p} = \hbar\boldsymbol{k}$. There may be a distinguished magnetisation direction $\boldsymbol{M}$, so that the electron can by analysed regarding the respective spin component. From [126]. (b) Refraction of a photoelectron at the surface. The component of $\boldsymbol{k}$ parallel to the surface is conserved $\boldsymbol{k}_{||}^\mathrm{v} = \boldsymbol{k}_{||}^\mathrm{s}$. In contrast, the component of $\boldsymbol{k}$ perpendicular to surface is reduced after the emission $k_\perp^\mathrm{v} < k_\perp^\mathrm{s}$ since the electron has to overcome the work function of the solid, also leading to a larger polar angle $\theta^\mathrm{v} > \theta^\mathrm{s}$. In both (a and b) $\hat{\boldsymbol{n}}$ is the surface normal.

3.3. Angle-resolved photoemission spectroscopy

After the more phenomenological description of the photoelectric effect and XPS, a more detailed view is necessary in the following. Figure 3.3 (a) gives an overview on the various experimental parameters, which influence the number of observable photoelectrons, i.e. the photocurrent J. The ARPES measurements presented in this thesis concentrate on the influence of the entities marked by red boxes in figure 3.3 (a), but effects due to the other dependencies may be observed.

The aim of ARPES is the measurement of the valence band structure $E_\mathrm{B}(\boldsymbol{k})$. The binding energy can be determined by equation 3.1, but further considerations have to be made regarding the momentum ($\boldsymbol{k}$). To escape from the solid into the vacuum, the photoelectrons have to overcome the potential barrier in the direction normal to the surface, which depends on the work function of the solid. Thus, the electrons excited in the solid need a minimum momentum in this direction to be emitted from the solid, and their momentum is reduced after the emission, as is illustrated in figure 3.3 (b). The parallel momentum component of

the photoelectron, in contrast, is the same as that of the excited electron in the solid. In addition, the momentum of the photons used in this work is small, so that the photoelectron also has the same momentum parallel to the surface as the initial electron:

$$\boldsymbol{k}_{||}^{\mathrm{i}} \approx \boldsymbol{k}_{||}^{\mathrm{s}} = \boldsymbol{k}_{||}^{\mathrm{v}} = \frac{\sqrt{2m_0 E_{\mathrm{kin}}}}{\hbar} \sin\theta_{\mathrm{e}} \begin{pmatrix} \cos\phi_{\mathrm{e}} \\ \sin\phi_{\mathrm{e}} \end{pmatrix}. \tag{3.2}$$

A direct determination of the momentum component perpendicular to the surface is not possible, but it may by estimated, e.g. by the assumption that the state of the excited electron in the solid is free-electron like. Since the systems studied in this thesis are low dimensional surface structures, their electronic structure depends only on the momentum parallel to the surface, so that a complete determination of their band structures is possible without further assumptions.

Similar to the tunneling current, the photocurrent is proportional to the transition rate between the N bound electrons initial state and the $(N-1)$ remaining electrons plus photoelectron final state (w_{if}), which is given by Fermi's golden rule:

$$\omega_{\mathrm{ij}} = \frac{2\pi}{\hbar} \left| \left\langle \Psi_{\mathrm{f}} \middle| H^{\mathrm{int}} \middle| \Psi_{\mathrm{i}} \right\rangle \right|^2 \delta\left(E_{\mathrm{f}} - E_{\mathrm{i}} - h\nu\right) \tag{3.3}$$

with the perturbation operator H^{int} being the light-matter interaction Hamiltonian, which can be approximated by the dipole operator for large wavelengths of the light compared to the excitation volume, as is the case for the photons used here in the ARPES experiments. Similar as the final state, also the initial state may be written as a properly antisymmetrised combination of the state of the $(N-1)$ bound electrons and the Bloch state of the one electron that gets excited. The integral in equation 3.3 may then be separated into two parts. The first part is the transition probability from the one electron Bloch state to the photoelectron state due to the perturbation by the light given by the matrix element $M_{\mathrm{fi}}(\boldsymbol{k})$. The second part is the overlap of the states of the $(N-1)$ remaining electrons before and after the photoemission process. Together with the energy conservation, the second part can be identified with the spectral function $[A(\boldsymbol{k},\nu)]$, so that for the total photocurrent follows:

$$J \propto \sum_{\mathrm{f,i},\boldsymbol{k}} |M_{\mathrm{fi}}(\boldsymbol{k})|^2 A(\boldsymbol{k},\nu). \tag{3.4}$$

So-called matrix element effects are often observed in ARPES experiments, e.g. transitions may be forbidden for certain light polarisations, and can be used to gain additional knowledge [147].

The spectral function describes the probability to find an excitation for the momentum $\boldsymbol{k}$ and a specific energy, which is given by the photon energy $h\nu$ for photoemission. For non interacting systems, the spectral function gives delta peaks for direct transitions in the one-electron picture, i.e. the one-electron band structure. For interacting systems, the spectral function is renormalised by the self energy, which gives the response of a particle on the change it produces in a system. This leads to a change of the line width due to the introduction of a life time, a shift in energy due to the mass renormalisation, and the movement of spectral weight in an incoherent part. Further information on the spectral function is found in textbooks on many-body physics and in review articles [148–151].

4. Further experimental techniques

In addition to the main methods STM, STS, ARPES and XPS discussed in the previous chapters 2 and 3, further experimental techniques were used to gain information on the studied systems. These additional techniques complement the main ones nicely, e.g. while STM allows the determination of the local surface structure and analyses of the local growth, LEED, discussed in section 4.1, gives global structural information of the surface, scanning electron microscopy (SEM), introduced in section 4.2.1, enables large scale growth characterisation, and HRTEM, presented in section 4.2.3, allows a view beneath the surface and the structural analysis of deeper lying layers. Furthermore, it is possible to study the overgrowth of structures by thicker layers with HRTEM, which is not possible by surface science methods. Such measurements will be accompanied by chemical characterisation with energy dispersive X-ray analysis (EDX) using scanning transmission electron microscopy (STEM), described in section 4.2.2. At the end of this chapter, RAS, a method that gives unique fingerprints of surface structures, is discussed, and transport measurements, with which the long range conductivity of nanostructures will be probed, are introduced. All these introductions will be rather brief, but references for further reading are given.

4.1. Low energy electron diffraction

The diffraction of low energy electrons is one of the most used methods to characterise surfaces with periodic structures [152]. It was first observed by C. J. Davisson and L. H. Germer in the 1920s [153, 154], which was the first evidence for the wave behaviour of electrons. Due to this, C. J. Davission received the Nobel Prize in Physics in 1937 together with G. P. Thomson, who also observed electron diffraction, but used high energy electrons [123, 155–157].

The basic principle of LEED is rather simple, an electron beam impinges on a sample and the elastically backscattered electrons are detected. A schematic of a conventional set-up, similar to the one used in this thesis, is shown in figure 4.1 (a). The inelastically scattered electrons are suppressed by grids, before the elastically scattered ones are accelerated by a high voltage on a fluorescent screen, which may be photographed by a CCD detector. The use of low energy electrons of 20 eV to 500 eV, which have small inelastic mean free paths (see figure 3.2), makes this method surface sensitive. In addition, the corresponding de Broglie wavelengths of 0.27 nm to 0.05 nm are in the region of typical inter-atomic distances [26]. Thus, not just scattered, but in particular diffracted electrons can be observed.

The incoming electrons have the momentum $\boldsymbol{k}_0$ and the momentum of the diffracted electrons is changed by the scattering vector $\Delta\boldsymbol{k}$. For constructive interference the Laue equations have to be fulfilled [161]. They can be summarised to:

$$\Delta\boldsymbol{k} = \boldsymbol{G} \tag{4.1}$$

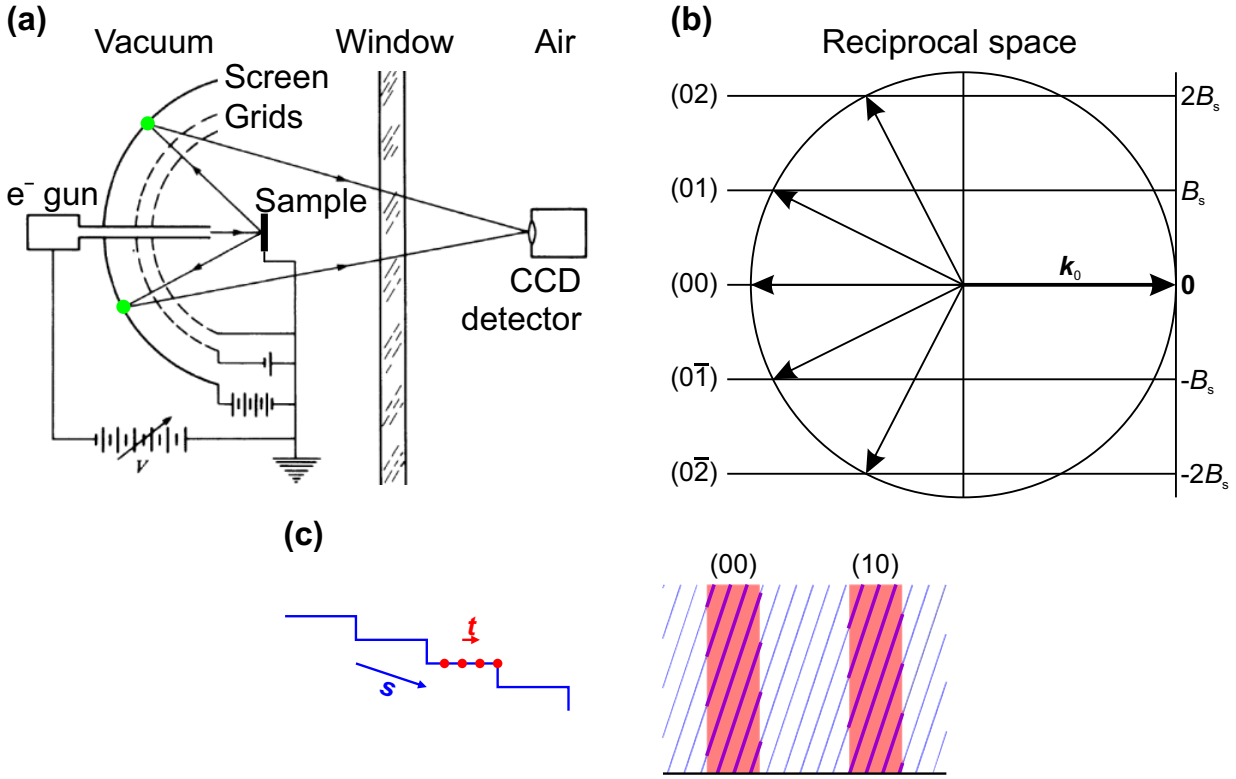

Figure 4.1.: (a) Schematic LEED set-up. Adapted from [158]. (b) Ewald reconstruction for normal incidence. After [159]. (c) Reciprocal lattice rods of a vicinal surface. In the left part, the real space lattices of the regular step array with lattice constant s (blue) and on a terrace with lattice constant t (red) are depicted, while the corresponding reciprocal lattice rods are schematically shown in the right part. The overlap of both reciprocal lattices (purple) corresponds to the measured reciprocal lattice rods of the complete vicinal surface. After [160].

with $\boldsymbol{G}$ a reciprocal lattice vector. For LEED, the reciprocal lattice of interest is the one of the surface.

A periodic surface structure can be described by two vectors $\boldsymbol{a}_\mathrm{s}$ and $\boldsymbol{b}_\mathrm{s}$. Similar as in solid, its reciprocal lattice can be defined by:

$$\boldsymbol{A}_\mathrm{s} = 2\pi \frac{\boldsymbol{b}_\mathrm{s} \times \boldsymbol{c}_\mathrm{s}}{\boldsymbol{a}_\mathrm{s}(\boldsymbol{b}_\mathrm{s} \times \boldsymbol{c}_\mathrm{s})} \tag{4.2}$$

and so forth with $\boldsymbol{c}_\mathrm{s}$ a vector perpendicular to the surface. The length of $\boldsymbol{c}_\mathrm{s}$ approaches infinity because of the broken translation symmetry. This assumption still leads to finite lengths of $\boldsymbol{A}_\mathrm{s}$ and $\boldsymbol{B}_\mathrm{s}$, but the length of $\boldsymbol{C}_\mathrm{s}$ is vanishing. Thus, the reciprocal lattice is not described by points as for a three-dimensional crystal, but by rods that are separated by multiples of $\boldsymbol{A}_\mathrm{s}$ and $\boldsymbol{B}_\mathrm{s}$.

The fulfilment of the condition given by equation 4.1 can be illustrated by an Ewald construction [162]. A two-dimensional cut through such a construction is shown in figure 4.1 (b) for normal incidence of the electrons as is the conventional geometry in LEED. Diffraction spots are seen on the fluorescent screen in the directions of the intersections of the Ewald

sphere with the reciprocal lattice rods. The two-dimensional projection of the spot pattern normal to the surface directly resembles the reciprocal lattice, so that the periodicities of the surface structure in real space can be easily determined.

Not only planar, but also so-called vicinal surfaces were investigated in this thesis. Vicinal surfaces are characterised by an offcut angle with respect to a main crystal plane and often form regular step structures. For such surfaces, the LEED image may not consist of single spots any more. Due to the reduced width of the terraces, the rods of the periodic structure on the terraces broaden. In addition, the step structure leads to a reciprocal lattice that is tilted with respect to the normal of the terraces. Constructive interference is now only possible, if the Laue equations are fulfilled for both reciprocal lattices. Thus, the overlap of both reciprocal lattices gives the reciprocal lattice structure of the vicinal surface as depicted in figure 4.1 (c). An Ewald sphere may now intersect multiple segments belonging to one reciprocal lattice rod of the terrace structure resulting in multiple spots observed on the screen.

In this thesis, LEED was used to analyse the surface periodicity which is then given in the Wood notation [163]. In addition, it is possible to gain knowledge on the inner structure of one unit cell of the periodic surface structure by analysing the spot intensity, which may even vanish, with varying electron energy (IV-LEED) or on the distribution of such unit cells, e.g. average domain sizes, by the analyses of spot profiles (SPA-LEED) [160]. Further information on LEED can be found in the references cited throughout this section or in reference [164].

4.2. Electron microscopy

The resolution of optical microscopes is restricted to about half of the wavelength of the used wave [165, 166]. Thus, the smallest length scales that can be resolved by a visible-light microscope are about 200 nm. Such a length scale is three orders of magnitude larger than typical atomic distances in crystals. To enable the resolution of crystal structures, electrons may be used since they have de Broglie wavelengths in the range of atomic distances, as mentioned in the previous section, or even much smaller.

The first electron microscope was built by M. Knoll and E. Ruska in the beginning of the 1930s [167], and soon electron microscopes surpassed visible-light microscopes [168]. For his work on electron microscopy, E. Ruska received the Nobel Prize in physics in 1986 together with G. Binnig and H. Rohrer, who were honoured for the development of STM [93]. In these first electron microscopes, the electrons that transmitted through a sample were imaged on a fluorescent screen leading to the name transmission electron microscope (TEM).

In addition to the directly transmitted beam other signals, which may be monitored to gain further information on the sample, are generated when the electron beam interacts with the sample (see figure 4.2). Furthermore, a parallel electron beam may probe an area of the sample to record images or an electron beam may be focussed and scanned over the sample. Consequently, there are many variants of electron microscopes. Here, only the variations used in this thesis are introduced. The influence of the various electron sources, e.g. cold or heated field emission guns, and electron optics are not discussed in detail. Information on these aspects can be found in standard textbooks, e.g. reference [169], which focusses on

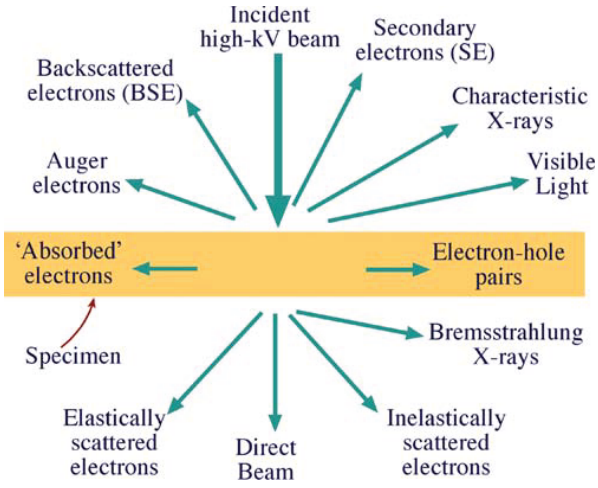

Figure 4.2.: Signals generated when a high-energy electron beam interacts with a sample. From [169].

transmission electron microscopy, but also describes general aspects of electron microscopy.

4.2.1. Scanning electron microscopy

As indicated by its name, a focussed electron beam is scanned over a sample in an SEM. While the amount of absorbed electrons was used as imaging signal in the first SEM build in the middle 1930s, the secondary electron yield is the most used signal today and is also used in this thesis [170]. In contrast to the definition of secondary electrons in PES (see section 3.1), only electrons leaving the sample with kinetic energies below 50 eV are called secondary electrons in electron microscopy [171]. Due to their low kinetic energy, the majority of these secondary electrons have small inelastic mean free paths, so that they originate from the surface of the sample (see figure 3.2).

The small inelastic mean free paths lead to a higher secondary electron yield when the local normal of the sample surface is tilted with respect to the direction of electron incidence, e.g. due to the larger interaction volume of the incident beam from which secondary electrons may escape the sample [see figure 4.3 (a)]. Furthermore, lower lying areas on the sample lead to a reduced secondary electron yield since the possible escape angle is reduced, while the most secondary electrons are emitted from edges of the sample morphology since the secondary electrons may escape from two different surfaces. Thus, SEM is a topography sensitive method, but, similar to STM, other surface characteristics, e.g. the local work function, also influence the appearance in SEM. Another similarity to STM is that conductive samples are easier analysed by SEM since the electron bombardment of the sample may lead to charging of sample areas resulting in distorted images or anomalous contrasts [171]. Still, insulating samples can be imaged with SEM when very low electron beam currents are used or the sample is coated by a metal, e.g. Au.

The schematic set-up of an SEM is shown in figure 4.3 (b). An electron beam is ejected from the electron gun and reaches its smallest diameter at the so-called crossover, which acts as a virtual electron source. To achieve a high electron current, a condenser lens

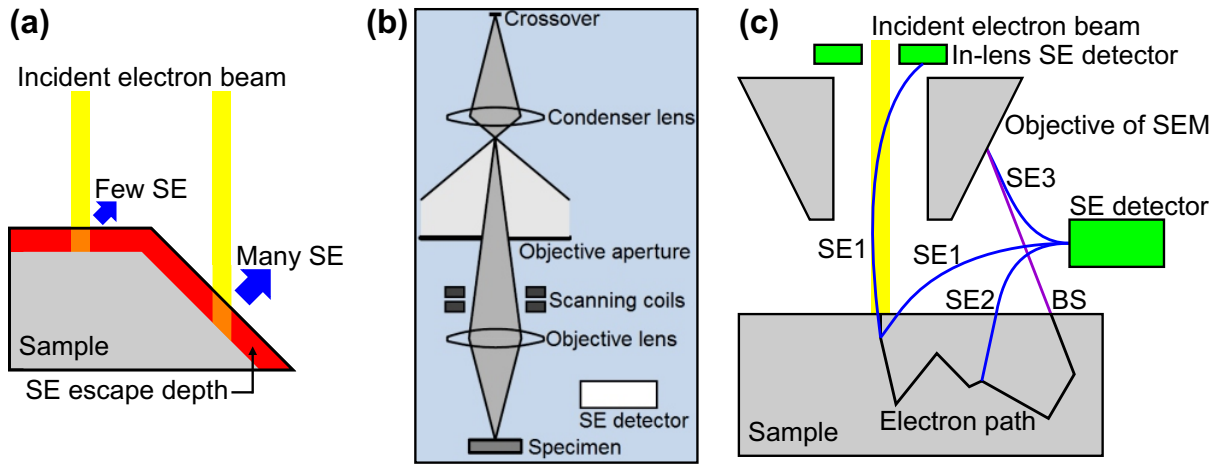

Figure 4.3.: (a) Schematic illustrating the increased secondary electron (SE) yield from tilted sample areas. (b) Principle set-up of an SEM. Adapted from [171]. (c) Schematic showing the sources of the different secondary electrons (SE1 to SE3), an electron path through the sample of a backscattered electron (BS), and possible placements of secondary electron detectors.

collects the electrons from the crossover. The beam passes an aperture before the objective lens focusses the beam on the sample. The focussed electron beam can be scanned over the sample by magnetic deflection using scanning coils and the secondary electron yield is measured by a collector during the scan. A strong condenser lens results in a strongly focussed electron beam with small diameter and a small aperture is necessary for a large depth of focus, the length in which the blur of the focus is small, but a strong condenser lens and a small aperture also lead to a low electron current and, consequently, a low signal.

For an SEM, the main resolution restriction is usually not the Abbe diffraction limit due the small wavelength of the electrons, e.g. the acceleration voltage of 15 keV used here results in a wavelength of about 10 pm. Already the spread of secondary electrons used as measurement signal results in a resolution limit much larger than the Abbe diffraction limit.

Due to the low kinetic energy of the secondary electrons, they can be easily attracted by a positive potential of a few hundred V, which does only negligibly influence the backscattered electrons with a much higher kinetic energy. Thus a detector, e.g. an Everhart-Thornley detector [172], situated next to the sample detects all secondary electrons, while being less sensitive to higher energy electrons [see figure 4.3 (c)]. Unfortunately, secondary electrons are not only generated in the region, where the incident beam hits the sample, but also by electrons that are scattered through the sample resulting in a large part of the signal originating from a region with a radius of several hundred nm [see figure 4.3 (c)] [173]. The measurement of secondary electrons produced by scattered electrons can be reduced when the secondary electron detector is situated within the lens enabling a higher resolution [see figure 4.3 (c)] [174].

Other resolution limiting effects are astigmatism, and spherical and chromatic aberration of the lenses. While astigmatism, i.e. the distortion of images by inhomogeneities of the lenses, can be countered rather easily by so-called stigmator lenses, the compensation of

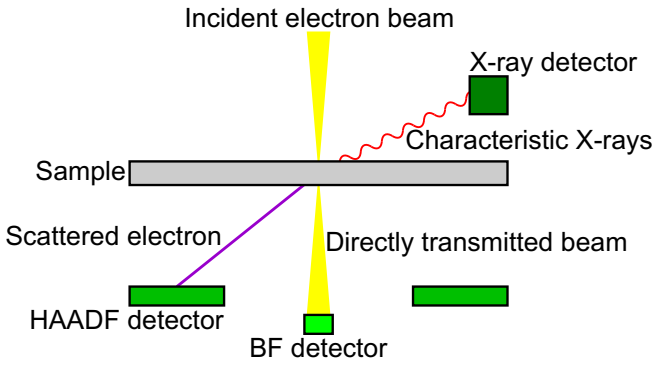

Figure 4.4.: Overview on the in the STEM studies gathered signals. The bright field (BF) detector measures the directly transmitted beam, the high-angle annular dark field (HAADF) detector quantifies the strongly scattered transmitted electrons, and the X-ray detector detects the X-rays generated due to the electron beam sample interaction.

spherical aberration, i.e. the reduced focal length for electrons with increasing distance from the optical axis, is more complicated and typically the dominant lens error [169].

The effect of spherical aberration is especially large for the SEM used here since its working distance is large with 15 mm. To reduce its influence, the electrons are accelerated after their extraction from the electron gun and only decelerated to the measurement energy close to the sample, so that a maximum resolution of 4 nm is possible [175].

4.2.2. Scanning transmission electron microscopy

An STEM is a combination of an SEM and a TEM, and the first one was developed in the end of the 1930s [170, 176]. Similar as in an SEM and in contrast to a TEM, a focussed electron beam is scanned over the sample in STEM. Now as in a TEM a thin sample is used resulting in the partly transmittance of the incident electron beam through the sample, so that the intensity of the transmitted beam can be used as signal. Thus in contrast to SEM, the samples will not have to be conductive if electron absorption is low, but have to be thinned down to typical thicknesses smaller than 100 nm [169].

As the electron beam passes through the sample, electrons are scattered leading to an intensity reduction of the directly transmitted beam. This intensity is mapped depending on the position of the focus spot in so called bright field images (see figure 4.4). While atomic resolution due to phase contrast, which will be discussed further below, is possible in STEM [177], bright field images are usually dominated by amplitude contrast. One form of amplitude contrast is the so-called mass-thickness contrast. The thicker the sample, and the higher the atomic number and thus the mass of the atoms, the more electrons are scattered by Rutherford scattering [178]. Thus, thick areas and areas with heavy atoms appear darker in bright field STEM images.

In addition, Bragg diffraction also reduces the intensity of the directly transmitted beam [179]. This so-called diffraction contrast is typically rather low in STEM bright field images, but is an additional and one of the main information sources in conventional TEM [169].

For high scattering angles ($> 5°$), the influence of Bragg scattering becomes negligible [169], but still, some electrons are scattered this far of the optical axis due to Rutherford scattering. Measuring the intensity of these electrons in dependence of the focussed electron beam position leads to so-called HAADF images. In these HAADF images, areas containing atoms with large atomic numbers appear bright. Images with such a high contrast with respect to the atomic number are not possible in conventional TEM [169].

Another advantage of STEM is that one can easily combine it with other techniques to gain additional data with high lateral resolution since any signal generated by the electron beam sample interaction, presented in figure 4.2, may be measured during the STEM image acquisition. In this thesis, STEM is combined with EDX for a chemical analysis of the sample. The high energy electron beam ionises atoms in the sample leading to the emission of X-rays from these atoms. The energies of the emitted X-rays are characteristic for each element, so that an EDX spectrum contains information about the elements ionised by the electron beam. When now the EDX signal is measured during the scanning of the electron beam, maps of the chemical composition of the sample are generated. Such EDX measurements are also possible in conventional SEM, but there the lateral resolution is reduced due to the ionisation of atoms by scattered electrons. The influence of such scattered electrons is not as strong in STEM due to the thin samples.

4.2.3. High-resolution transmission electron microscopy

High-resolution TEM is a special TEM mode with a higher effort on the correction of the various lens errors, so that images with higher resolution are obtainable [see figure 4.5 (a)]. In contrast to STEM, the condenser lens system generates an approximately parallel beam, which may be monochromatised to reduce the influence of chromatic aberration before the sample is illuminated. The complete illumination of the investigated area enables faster image acquisition than in STEM reducing the influence of the drift of the sample during the measurement, so that high-resolution images are easier achievable.

The imaging system can be reduced to two main lenses, the objective lens and the intermediate lens. The interplay of these lenses leads to the magnified image of a sample area on the screen, as is illustrated for bright field imaging by the coloured ray diagram in figure 4.5 (a). Even though no such data is presented in this thesis, dark field imaging and the measurement of diffraction patterns are also possible. For dark field imaging, the direct beam is blanked by the objective aperture, and diffraction patterns can be viewed by a change of the strength of the intermediate lens [grey rays in figure 4.5 (a)]. In the TEM used here, the spherical aberration of the objective lens is corrected by a lens system between objective and intermediate lens. At the end of the beam path, the image is projected by the projection lens on the screen.

In conventional TEM, the main contrast mechanism is the diffraction contrast, i.e. a bright field image with intensity variations will be observed if some of the Bragg scattered electrons do not pass the objective aperture. If very thin samples are investigated, which are needed to achieve high resolution since inelastic scattering in the sample leads to a strong influence of chromatic aberration, the diffraction contrast will be reduced and the main contrast mechanism will be phase contrast. This contrast arises due to the interference of the elastically scattered electrons with the electrons that did not scatter.

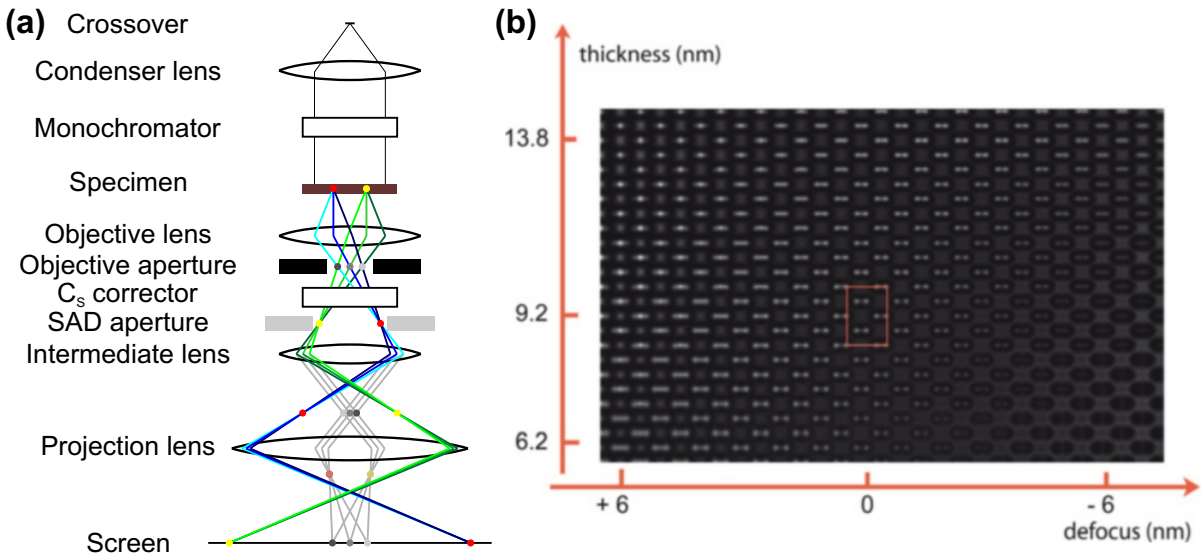

Figure 4.5.: (a) Schematic (HR)TEM set-up including ray diagrams. The black rays indicate the width of the electron beam, the coloured rays describe selected electron paths from the yellow and red point in the imaging mode of the TEM and the grey rays, which lie beneath the coloured ones up to the intermediate lens, correspond to selected electron paths when diffraction patterns are measured. The objective aperture may be used to select specific diffraction spots and to blank the direct beam. The selected area diffraction (SAD) aperture may be brought into the beam path to select an area of the intermediate image. (b) Simulated stitched HRTEM image of Si viewed along the [110] direction for various sample thicknesses and varying defocus [small spherical aberration (C_S) of only 1 μm]. From [180].

Any thickness variation, tilting, composition variation, etc. of the sample changes the electron exit wave that leaves the sample. This wave is then modulated by the imaging system, i.e. the exit wave is convoluted by the contrast-transfer function [169]. Thus, the interference pattern observed on the screen is not only changed by the sample, but also strongly dependent on the exact imaging conditions, e.g. structures with large spatial frequency cannot be observed when the objective aperture blanks focal points too close to the optical axis. Consequently, the detailed interpretation of HRTEM images is very complex, so that image simulations have to be used, but these strong dependencies also lead to a large information depth in the images, i.e. much may be learned from image series, in which everything is aligned optimally.

A simulated HRTEM image is shown in figure 4.5 (b). Even though only the sample thickness and the defocus, i.e. the distance of the sample with respect to the focal plane of the objective lens, was changed, the image changes drastically, e.g. the contrast between neighboring areas may inverse or small single spots may broaden or become double spots. The simulated HRTEM image also reveals that the symmetry of the sample is generally reproduced by HRTEM images. Thus, even when no detailed structural information may be obtained since the simulations cannot be matched one-to-one onto the measured images, the sample symmetry may be derived.

For the structural analysis of nanostructures, the general parameters of the sample, e.g. thickness and tilt angle, can be determined by the simulation of the known substrate structure. Since the phase information is lost when images are taken, which only record the intensity of the electrons, a single image is not sufficient to reconstruct the exit wave needed to identify the sample parameters. Thus, a series of images with a defocus variation is measured quickly, so that all other parameters remain approximately constant. The defocus variation changes the contrast-transfer function in a determined way, so that different information on the sample exit wave is extracted from each image resulting in a complete characterisation of the exit wave. With the obtained general sample parameters, the HRTEM images of the nanostructures can be simulated and the validity of structure models can be determined.

4.3. Reflection anisotropy spectroscopy

The development of RAS started in the 1980s under the name reflectance difference spectroscopy (RDS) [181, 182]. While the term RDS is still used in some publications [183], the term RAS is used in this thesis since it distinguishes this method from other techniques in which also differences in reflectance are measured, e.g. of clean and oxidised samples [184].

In contrast to most surface science techniques, e.g. LEED or XPS, RAS is a purely optical method, so that it can also be used under non-UHV conditions, e.g. to characterise samples during their growth by metal-organic vapour phase epitaxy [185]. Despite the large penetration depth of photons, RAS can be surface sensitive due to the physical quantity measured being the difference of reflectance in two orthogonal polarisation directions. The bulk of cubic materials, e.g. Si, is optically isotropic due to their isotropic dielectric function, so that a RAS signal can only originate from the surface of a cubic material. An anisotropic reflectance from a surface may arise, e.g., by the formation of anisotropic reconstructions or the growth of an anisotropic film. Both exemplary situations may also lead to anisotropic strain in the topmost bulk layers.

When RAS is used to monitor epitaxial growth, the reflectance anisotropy is monitored for one or few specific photon energies, so that lasers may be used. In contrast, when spectra over a wide photon energy range, e.g. 1.5 eV to 5.0 eV, are obtained, a Xe lamp is typically used as light source. Initially, the difference in reflectance was measured by using linearly polarised light and mechanically turning the sample or the polariser [181, 182]. Additional information is gained and faster measurements needed for growth monitoring are possible when the reflected light is analysed using a photoelastic modulator (PEM). A schematic RAS set-up using a PEM and a Xe lamp is shown in figure 4.6.

The non-polarised light of the Xe lamp is polarised in such a way that the polarisation direction lies between the main axes of the surface, e.g. between the [110] and [1$\bar{1}$0] directions for (001) surfaces. The light is partially reflected at the surface and the difference of the reflectivity (Δr) for the two orthogonal directions x and y is normalised to the total reflectivity (r):

$$\frac{\Delta r}{r} = 2\frac{r_\mathrm{x} - r_\mathrm{y}}{r_\mathrm{x} + r_\mathrm{y}} \tag{4.3}$$

with all reflectivities as the complex Fresnel reflection coefficients for the electric field

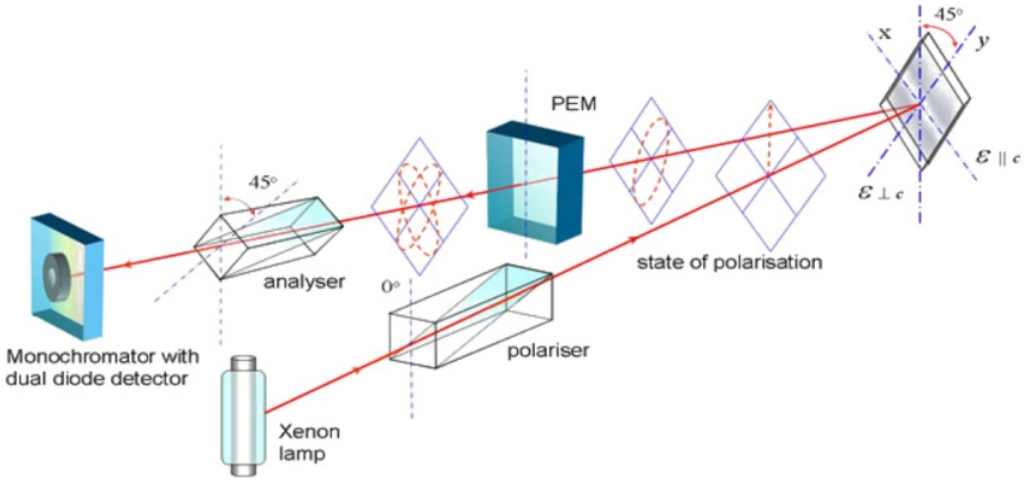

Figure 4.6.: Schematic RAS set-up. From [186].

[187, 188]. In general, the light is elliptically polarised with a rotated main polarisation axis after the reflection. A difference in the real parts of the reflectivities r_x and r_y results in a change of the amplitude ratio of the electric field in the two directions and therewith in a turning of the polarisation direction. Different imaginary parts of the reflectivities r_x and r_y lead to a phase shift between the two electric field components resulting in elliptical polarisation.

In the PEM, a photoelastic material is mechanically stressed by a piezo ceramic driven by a voltage, which oscillates close to the resonance frequency of the material (in the order of 10^5 Hz). Thus, the PEM periodically retards the part of the reflected light that has its polarisation axis parallel to the modulation axis of the PEM. The polarisation state is then analysed by a second polariser, which is rotated by 45° with respect to the first polariser and the modulation axis of the PEM, before the intensity of the reflected light is measured in dependence on the photon energy.

Due to the manipulation of the light by the PEM, the measured intensity is not constant for a specific photon energy. Analysing the set-up by the Jones matrix formalism yields that intensity oscillations that vary with an odd or even multiple of the PEM frequency are proportional to the imaginary or real part of the reflectivity difference, respectively [188,189]. These intensity variations, which are about three orders of magnitude smaller than the time independent background intensity, are detected using a lock-in technique.

In a typical RAS spectrum, the normalised difference of the reflected intensity ($\Delta R/R$) is plotted with respect to the photon energy. This so-called RAS signal is related to the reflectivity difference by:

$$\frac{\Delta R}{R} = 2\,\mathrm{Re}\,(\Delta r/r) \tag{4.4}$$

for small anisotropies [188]. The RAS spectrum is related to the electronic structure of the surface, but a detailed interpretation is non-trivial. In recent years, more in-depth information was extracted from RAS spectra by comparisons of experimental and calculated RAS spectra [190, 191]. For further information on RAS, the references [188, 192] are a good starting point.

4.4. Electronic transport measurements

The aim of electronic transport measurements is the determination of the sample resistivity (ρ) [or conductivity ($\sigma = 1/\rho$)]. The resistivity of materials ranges from 10^{-8} Ωcm to 10^{16} Ωcm and is used to categorise metals, semiconductors, and insulators either by its value or by its temperature dependence [193]. The categorisation may not be unambiguous, e.g. strongly doped semiconductors may show an increasing resistivity with temperature, which is typical for metals [194]. In this thesis, a material is denoted a metal, when there is a finite DOS at the Fermi level, even though its resistivity may be high due to localisation effects.

Applying an electric field (E) to a sample results in an electric current (I) in the sample with the current density $J = I/A$. Here, A is the area the current flows through. The electron transport may be ballistic or diffuse. We concentrate on the diffuse regime in which the resistivity is given by Ohm's law:

$$\rho = \frac{E}{J}. \tag{4.5}$$

Information on ballistic transport, i.e. transport without inelastic scattering, is found in references [175, 195].

The resistivity is not directly accessible in transport experiments, but may be determined from the resistance (R), which is given by the ratio of applied voltage (V) and current. In a two-point measurement, two probes are used to apply a voltage at the sample and to measure the resulting current [see figure 4.7 (a)]. Unfortunately, such an arrangement does not measure the resistance of the sample alone, but also includes the resistances of the probes and the contact resistances between probe and sample. Especially, the contact resistance may be large, e.g. on semiconductors where Schottky barriers form (see section 5.3.2).

Better suited to measure the resistance of a sample are arrangements with four probes, as is known for over 100 years [196, 197]. Various arrangements of the probes are possible, but here we concentrate on a linear one with equidistant spacing of the probes [see figure 4.7 (b)]. Typically, a current is driven through the outer two probe, while the voltage drop between the inner two probes is measured. Since no current flows from the inner two probes to the voltmeter, the ratio of current and voltage only depends on the sample resistance.

From experience with macroscopic resistance measurements on cables or similar, we may expect a linear growth of the resistance with the distance between the probes. This does not hold true for probe distances that are in the range or smaller than the dimensions of the sample. If the sample has a considerable length and width, the current does not flow only in a straight line between the probes, but in a two-dimensional manner as depicted in figure 4.7 (b). This compensates the expected resistance growth and the resistance becomes independent of the probe distance in four-probe measurements. When also the depth is sufficiently large, the resistance even decreases with increasing probe distance in four-probe measurements due to the three-dimensional current flow [see figure 4.7 (c)].

A quantitative description is possible when taking into account Ohm's law (equation 4.5) and that the voltage is given by:

$$V = -\int E \,\mathrm{d}\, r. \tag{4.6}$$

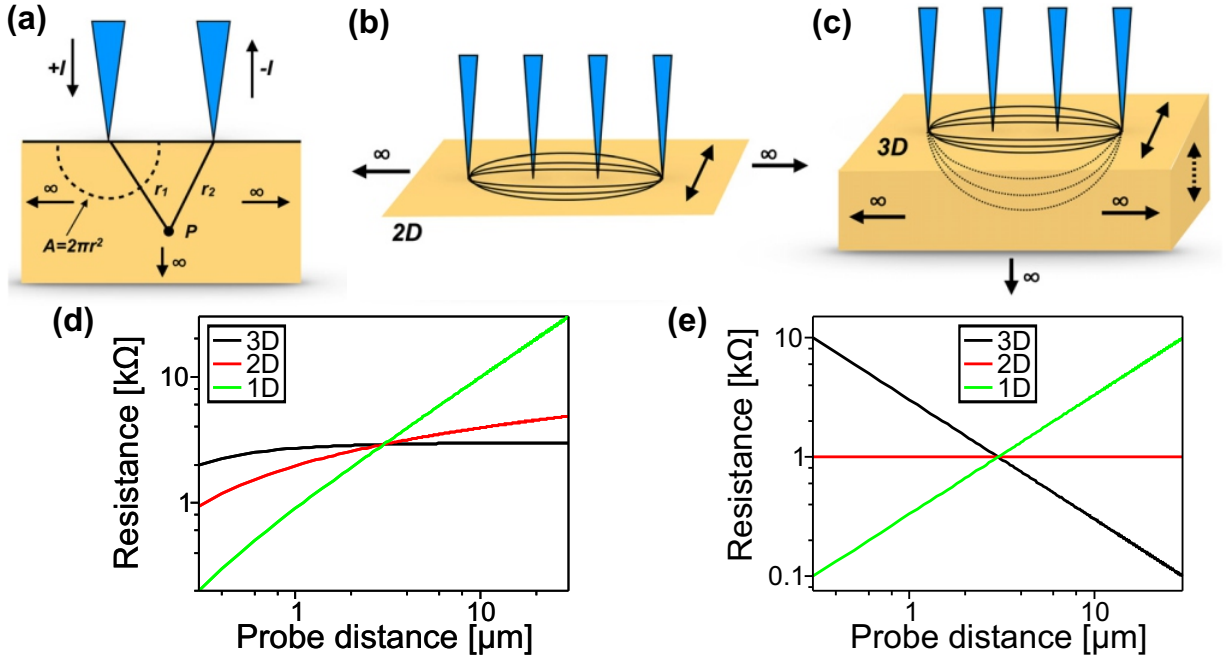

Figure 4.7.: (a) A two-point probe arrangement for resistivity measurements. From [196]. (b and c) Linear four-point probe set-ups for resistivity measurements with lines indicating the current flow in two-, and three-dimensional systems, respectively. From [196]. (d and e) Arbitrary sample resistance-probe spacing diagrams illustrating the differences due to the dimensionality of the sample for (d) a two-point probe and (e) a linear four-point probe arrangement, in which all four probes are equidistantly separated. The radius of the probes is 100 nm.

In three dimensions, the current from or to a probe is constant through the half sphere around the centre of the probe leading to $J_{3d} = I/(2\pi r^2)$ with r the distance from the centre of the probe [see figure 4.7 (a)]. Similarly, the two-dimensional current density is constant through a ring with the small average height h, i.e. a cylinder, surrounding the probe, and the one-dimensional one is constant along the sample with the small average area A. Thus, we can define $J_{2d} = I/(2\pi r \cdot h)$ and $J_{1d} = I/A$. Now, we also introduce the bulk, sheet, and wire resistivity as ρ_{3d} measured in Ωcm, $\rho_{2d} := \rho_{3d}/h$ measured in Ω, and $\rho_{1d} := \rho_{3d}/A$ measured in Ω/cm, respectively.

Since we measure with small spacings (s) between the probes, we have to take into account the finite dimensions of our probes. We assume that they have the same symmetry as the areas of constant current, e.g. a half sphere in three dimensions, with a fixed radius r_p. By using the equations 4.5 and 4.6, the potential at a position given by the vector $\boldsymbol{r}$ from the centre of the probe is for the various dimensions:

$$V_{3d}(\boldsymbol{r}) = -\frac{I\rho_{3d}}{2\pi}\int_{r_p}^{r}\frac{1}{r'^2}\,\mathrm{d}\,r' = \frac{I\rho_{3d}}{2\pi}\left(\frac{1}{r}-\frac{1}{r_p}\right), \tag{4.7}$$

$$V_{2d}(\boldsymbol{r}) = -\frac{I\rho_{2d}}{2\pi}\int_{r_p}^{r}\frac{1}{r'}\,\mathrm{d}\,r' = \frac{I\rho_{2d}}{2\pi}\ln\frac{r_p}{r}, \tag{4.8}$$

$$V_{1\mathrm{d}}(r) = -\frac{I\rho_{1\mathrm{d}}}{2}\int_{r_\mathrm{p}}^{r} 1\,\mathrm{d}\,r' = \frac{I\rho_{1\mathrm{d}}}{2}(r_\mathrm{p} - r)\,. \tag{4.9}$$

With these equations, we can calculate the potential generated by the source and drain probe at any position by superposition and consequently also the potential difference between two points. One has to take into account that the centre of one current driving probe is shifted by the vector $(s\ 0\ 0)^\mathrm{T}$ or $(3s\ 0\ 0)^\mathrm{T}$ for a two-probe or a four-probe configuration, respectively, that the current at the drain is negative, and that the surfaces of the probes are equipotential areas. Thus, the probes basically short-circuit a sample area. Nevertheless, we assume that the potential that one probe generates on the surface of another probe is the potential that is produced at the position of the centre of the other probe with the other probe missing. This approximation holds true for small probe dimensions. Furthermore, the equations 4.7 to 4.9 are not defined for $r < r_\mathrm{p}$. Thus, we set the potential inside a probe to that of its surface [$V(r < r_\mathrm{p}) = V(r_\mathrm{p}) = 0$]. Applying these considerations, the sample resistance between the two probes in a two-probe transport measurement is related to the resistivity for the various dimensions by:

$$R_{3\mathrm{d}}^{2\mathrm{p}}(s) = \frac{\rho_{3\mathrm{d}}}{\pi}\left(\frac{1}{r_\mathrm{p}} - \frac{1}{s}\right) \overset{s\gg r_\mathrm{p}}{\approx} \text{const.}, \tag{4.10}$$

$$R_{2\mathrm{d}}^{2\mathrm{p}}(s) = \frac{\rho_{2\mathrm{d}}}{\pi}\ln\frac{s}{r_\mathrm{p}} \overset{s\gg r_\mathrm{p}}{\propto} \ln s, \tag{4.11}$$

$$R_{1\mathrm{d}}^{2\mathrm{p}}(s) = \rho_{1\mathrm{d}}(s - r_\mathrm{p}) \overset{s\gg r_\mathrm{p}}{\propto} s. \tag{4.12}$$

For the sample resistance between the inner two probes in a linear four-probe configuration, we obtain:

$$R_{3\mathrm{d}}^{4\mathrm{p}}(s) = \frac{\rho_{3\mathrm{d}}}{2\pi s} \propto \frac{1}{s}, \tag{4.13}$$

$$R_{2\mathrm{d}}^{4\mathrm{p}}(s) = \frac{\rho_{2\mathrm{d}}}{\pi}\ln 2 = \text{const.}, \tag{4.14}$$

$$R_{1\mathrm{d}}^{4\mathrm{p}}(s) = \rho_{1\mathrm{d}} s \propto s. \tag{4.15}$$

The complete independence of the sample resistances on the probe dimensions for four-probe measurements is due to the above assumptions. In more detailed analyses the probe dimension has an influence [194, 198, 199]. The derived dependencies between sample resistance and probe separation can be used to determine the dimensionality of the electron transport. Exemplary plots of the equations 4.10 to 4.15 are shown in the figures 4.7 (d and e). The linear proportionality for one-dimensional systems most relevant for this thesis is well established and experimentally confirmed [196, 200, 201]. Interestingly, the proportionalities change for the different measurement geometries in two and three dimensions showing that one always has to take the measurement geometry into account even for qualitative statements.

The above relations are derived for ideal samples. In real samples, the determined resistivity may deviate from the ideal ones, e.g. scattering of bulk electrons at surfaces

and interfaces may change the bulk resistivity, especially for thin samples [202–204]. In general, the finite size of a sample has a strong influence on the observed resistivity [196]. Often, there are multiple current channels complicating the analysis, e.g. when one wants to quantify the transport of a surface, it is often superposed by a large current through the bulk of the sample [194].

5. Silicon and rare earth metals

Silicon was used as a substrate for all samples studied in this thesis. On these substrates, rare earth metals were deposited, which react with the Si of the substrate to form silicide nanostructures during a brief annealing period. Before the state of knowledge regarding these nanostructures is presented in section 5.4, basic information on Si and the used surfaces (section 5.1), rare earth metals and bulk rare earth silicides (section 5.2), as well as metal growth on Si (section 5.3) is given.

5.1. Silicon

While Si is only necessary in trace amounts for human life [205], today's life style would be impossible without Si. Silicon is the basis of information technology as the most important substrate material [206]. It is used in its crystalline form having a diamond structure with a lattice constant of $a_{\mathrm{Si}} = 0.543$ nm and an indirect band gap of 1.12 eV at room temperature [207–209]. In semiconductor industry, the most used Si surface is Si(001). This surface is introduced in the following since it is used as a substrate in this work, too. Subsequently, the Si(111) surface and its vicinal surfaces, which were also used for nanowire growth, will be described.

5.1.1. Planar and vicinal Si(001) surfaces

Cutting a Si crystal perpendicular to its [001] direction results in the formation of a Si(001) surface. Considering the diamond lattice structure of Si [see figure 5.1 (a)], we determine the Si(001) surface lattice constant to $a_{\mathrm{Si(001)}} = a_{\mathrm{Si}}/\sqrt{2} = 0.384$ nm, the single layer step height to $s_{\mathrm{Si(001)}} = a_{\mathrm{Si}}/4 = 0.136$ nm, and the surface atomic density to $n_{\mathrm{Si(001)}} = 6.78 \times 10^{14}$ cm^{-2}. In the following, the atom density of unreconstructed surfaces will also be referred to as one monolayer (ML).

On the unreconstructed surface, every surface atom on a terrace has two dangling bonds [see figure 5.1 (b)]. Since such dangling bonds are energetically unfavourable, the atoms form dimers via σ- and π-bonds reducing the dangling bond density by one half [see figure 5.1 (b)] [210]. Symmetric dimers would be semi-metallic, but additional energy is gained by a buckling of the dimers leading to an energy gap opening [see figure 5.1 (b)] [211, 212]. This buckling is accompanied by a charge transfer from the lower to the higher lying Si atom [212–214]. This electronic surface structure leads to a Fermi level of about $(0.48 \pm 0.02$ eV) above the valence band maximum (VBM) for n-type Si [215–217].

An STM image of a clean Si(001) surface is shown in figure 5.2 (a). Mainly symmetrically appearing dimers are observed since the measurements are performed at room temperature, at which the buckled dimers switch theirs buckling directions much faster than resolvable

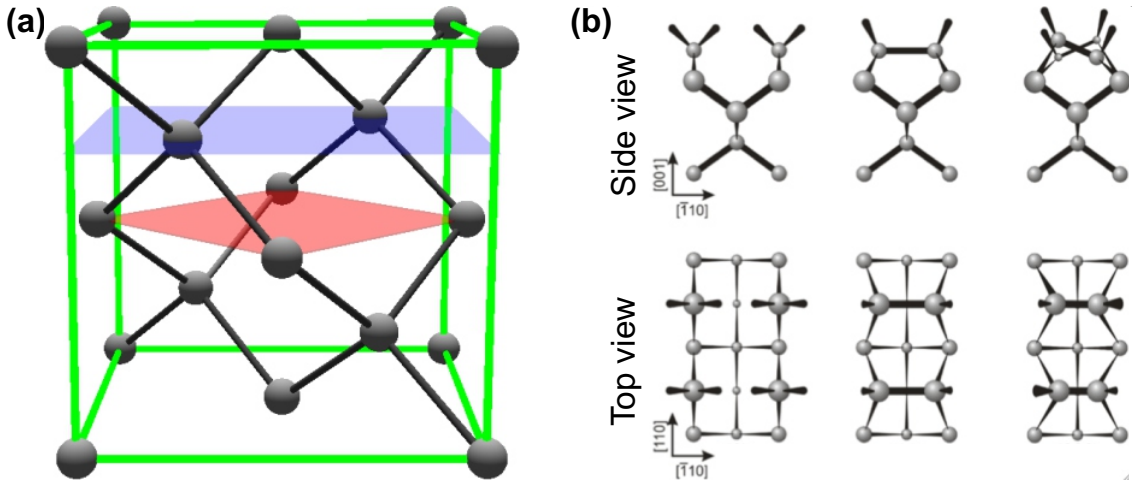

Figure 5.1.: (a) Model of the Si lattice with two neighbouring Si(001) planes highlighted in red and blue. The red area represents a Si(001) surface unit cell of the unreconstructed surface. (b) Side and top view on the structure models of the unreconstructed Si(001) surface (left) and of Si(001) surfaces with symmetric dimers (centre) and buckled dimers (right). From [211, 218].

by STM leading to a symmetric appearance [219, 220]. At defects or steps, the dimers may be pinned in one buckling direction, which may also influence neighbouring dimers. During structural analysis with respect to the Si dimers, one has to take into account that, in contrast to filled state STM images, empty state STM images may show high appearing areas not above Si dimers, but in between them [219–221].

The dimers form rows leading to a 2×1 reconstruction. On neighbouring terraces separated by a single layer step, the dimer rows are perpendicular to each other due to the rotation of the bond directions in the Si lattice by 90° [see figures 5.1 (a) and 5.2 (a)]. The two domain structure of such a planar Si(001) surface with single layer steps is also seen in LEED images, in which ×2 spots are seen in both directions [red and green arrows in figure 5.2 (a)]. The observation of a 2×1 reconstruction in LEED clearly reveals the missing of any long range ordering between dimer rows at room temperature, while such ordering into a 2×2 or $c(2\times4)$ reconstruction is observed at low temperatures [222, 223].

On planar surfaces with only single layer steps, one differentiates between two step types. S_A steps are steps with the dimer rows on the upper terrace parallel to the step edge and S_B steps have the dimer rows on the upper terrace perpendicular to the step edge [224]. On vicinal Si(001) substrates with an offcut angle $> 2°$ towards [110], double layer steps form leading to parallel dimer rows on neighbouring terraces. In accordance with theory [224], mainly dimer rows that are perpendicular to the step edges are seen in STM [see figure 5.2 (b)]. The LEED image of such a vicinal surface also indicates the single domain structure [red arrows in figure 5.2 (b)]. Moreover, the LEED spots split due to the regular step structure as discussed in section 4.1 [yellow arrows in figure 5.2 (b)]. From the distance between the spots of a reflex, the step-to-step distance can be determined. An analysis of the spot splitting in the LEED image in figure 5.2 (b) results in an average step-to-step distance of (2.6 ± 0.2) nm, which is in excellent agreement with the expected

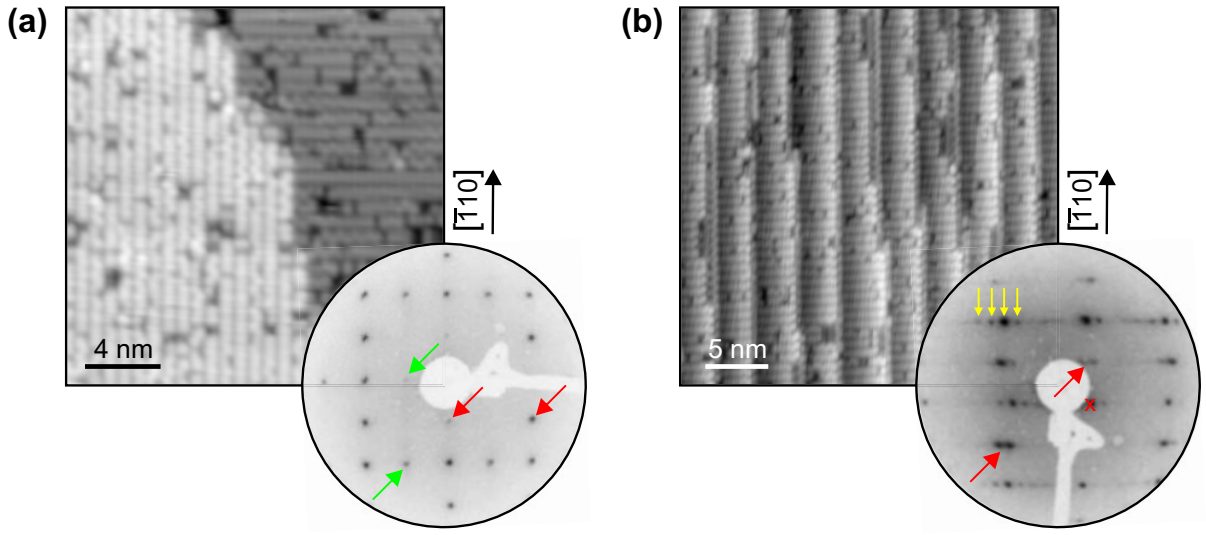

Figure 5.2.: (a) STM image of a planar Si(001)2×1 surface (sample voltage $V = -1.5$ V, tunneling current $I = 100$ pA), and a LEED image taken at a kinetic energy of $E_{\mathrm{kin}} = 50$ eV. (b) STM image of a vicinal Si(001) sample with 4° offcut towards [110] ($V = -1.5$ V, $I = 100$ pA) and LEED image of a vicinal Si(001) sample with 6° offcut towards [110] ($E_{\mathrm{kin}} = 50$ eV). The red cross marks the main (0 0) reflex.

value of 2.6 nm for a Si(001) sample with 6° offcut.

When one analyses the electronic structure of Si(001) samples with ARPES, using vicinal instead of planar samples has the advantage that the direction parallel and perpendicular to the Si dimer rows can be distinguished due to the single domain nature of the surface. Figures 5.3 (a and c) show the dispersion perpendicular and parallel to the dimer rows, respectively, while the nomenclature is defined in figure 5.3 (b). Most interesting is the band A that is assigned to the dimers. As predicted by theory (lines D_{up}), the band disperses only in the direction of the dimer rows, so that it is quasi-one-dimensional. In addition, various surface resonances and the band B are observed [the grey areas in figures 5.3 (a and c) represent the projected bulk dispersion]. The weakly dispersing band B may stem from extended areas with buckled dimers, e.g. due to a rather high defect density [225].

Even though there are only two different types of surface atoms, the upper and the lower dimer atoms, high resolution XPS clearly resolves seven components contributing to the Si-2p spectrum shown in figure 5.3 (d). There are the three components associated with the Si bulk (B), the upper dimer (S_{u}), and the lower dimer (S_{d}), but in addition also components (S' and C) from subsurface atoms with a different environment than bulk atoms due to strain from the surface reconstruction [228, 229]. Furthermore, there are two components (D and L) whose origins are still under debate [228, 230].

5.1.2. Planar and vicinal Si(111) surfaces

Si(111) surfaces are formed by the planes highlighted in figure 5.4 (a). The Si(111) surface has the same surface lattice constant ($a_{\mathrm{Si(111)}} = a_{\mathrm{Si}}/\sqrt{2} = 0.384$ nm) and a similar atom density ($n_{\mathrm{Si(111)}} = 7.83 \times 10^{14}$ cm^{-2}) as the Si(001) surface, but a much larger single step

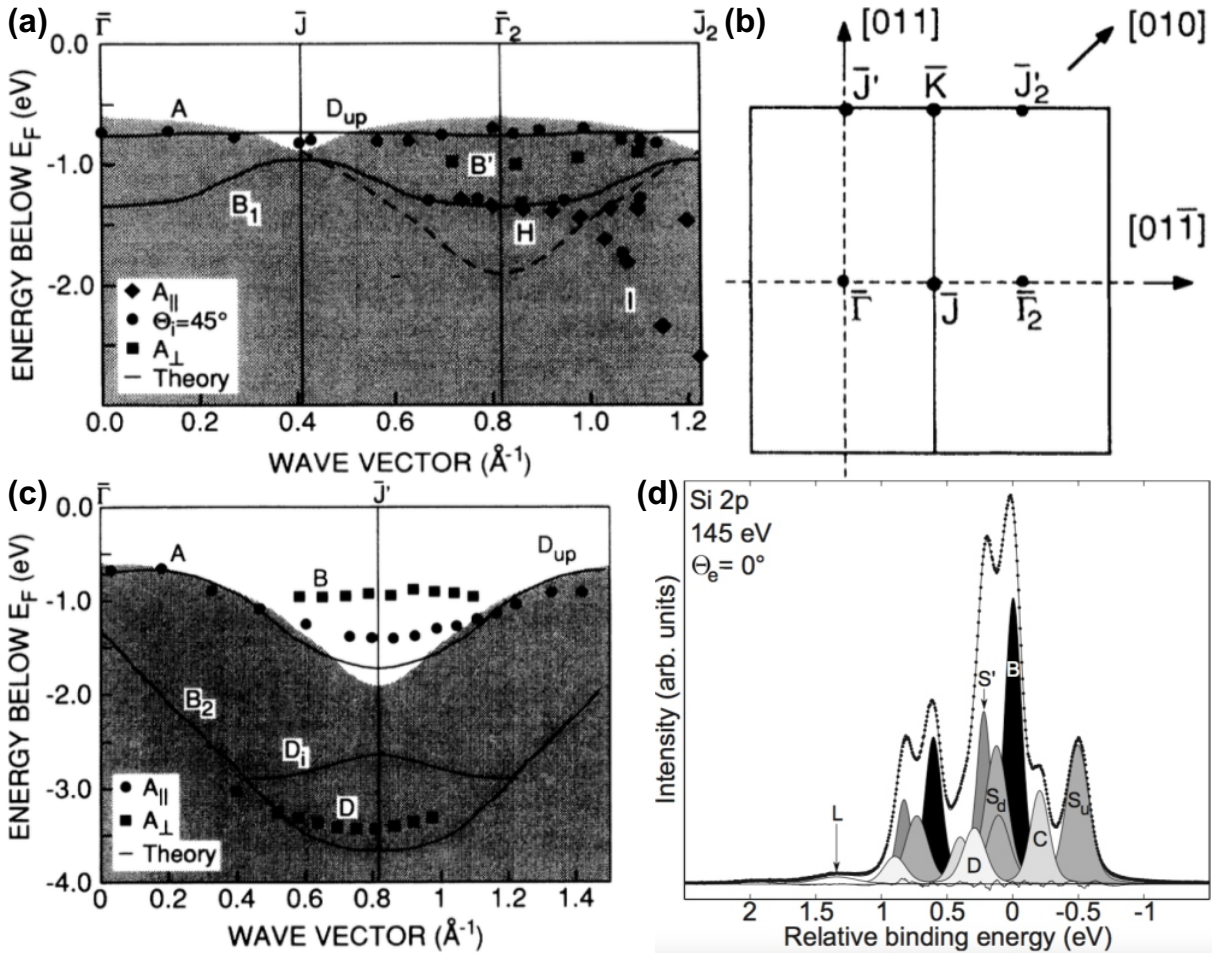

Figure 5.3.: (a and c) ARPES results of vicinal Si(001) (a) parallel and (c) perpendicular to the step edges (obtained with various photon energies). From [225]. Theory data from [226,227]. (b) Schematic of the surface Brillouin zone of the 2×1 domain of a Si(100) surface with the ×2 periodicity parallel to $[01\bar{1}]$. From [225]. (d) High-resolution Si-2p spectrum of a planar Si(001) surface ($h\nu = 145$ eV). From [228].

height of $s_{\mathrm{Si}(111)} = a_{\mathrm{Si}}/\sqrt{3} = 0.314$ nm since bilayers are formed. Due the back bonding of the topmost surface atoms to three atoms in the lower layer, every surface atom only has one dangling bond. Thus, the Si(111) surface is the Si surface with the lowest dangling bond density and consequently the lowest surface energy making it the preferred cleavage plane of Si crystals.

After cleaving in UHV, the Si(111) surface directly reconstructs into a 2×1 periodicity without reducing the dangling bond density [231–233]. Annealing at 650 °C leads to the irreversible conversion into the energetically most favourable surface structure, the 7×7 reconstruction [234–239]. Larger patches of other reconstructions are only observed when the initial annealing was at lower temperatures or when the sample is quenched from temperatures above 830 °C, at which the long range order of the surface vanishes leading to an apparent 1×1 phase [234, 240–244].

The 7×7 reconstruction is described by the dimer-adatom-stacking fault model, which is

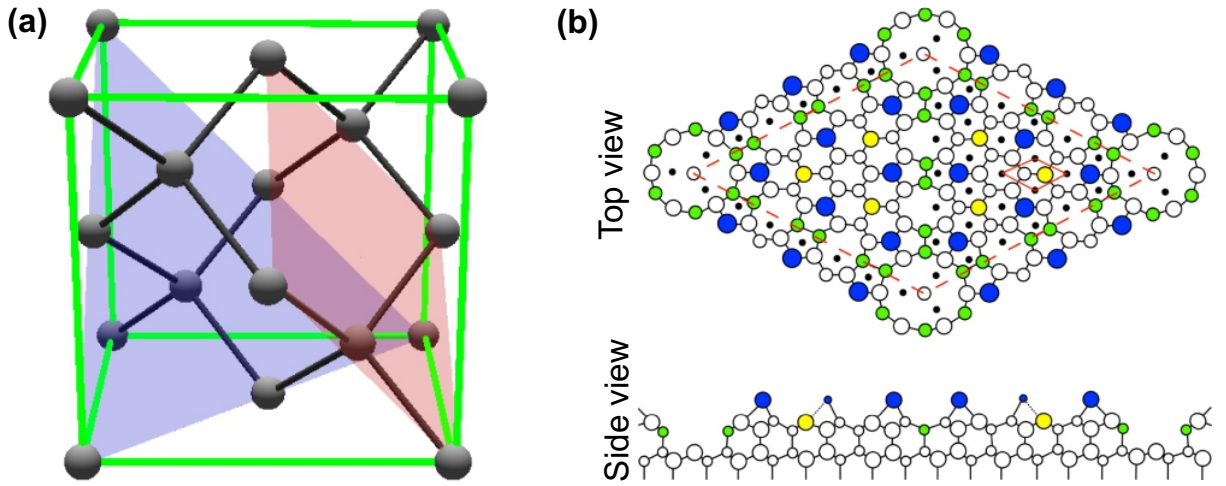

Figure 5.4.: (a) The Si diamond lattice structure with two neighbouring Si(111) planes indicated in blue and red. The red area represents a Si(111) surface unit cell of the unreconstructed surface. (b) Top and side view of the Si(111)7×7 reconstruction with adatoms, rest atoms, and dimer atoms coloured blue, yellow, and green, respectively. The stacking fault is in the left half unit cell. The hatched rhombus marks the 7×7 unit cell and the continuous rhombus a 1×1 unit cell. Adapted from [91].

shown in figure 5.4 (b) [91]. Dimers are formed since they saturate dangling bonds, but their formation leads to energetically unfavourable stacking fault areas. Parallel dimer rows directly next to each other do not fit structurally on the hexagonal Si(111) planes, so that triangular areas with holes at their corners form [237]. A further reduction of dangling bonds is achieved by the addition of adatoms on the triangular areas. Only 19 dangling bonds remain in a 7×7 unit cell that initially had 49 dangling bonds. They are situated at the adatoms (12 per unit cell), the rest atoms (6 per unit cell), and at the corner-hole (1 per unit cell). A charge transfer from the adatoms saturates the dangling bonds at the rest and corner-hole atoms, so that 5 electrons are filling the adatom dangling bond states [245]. Due to the odd number of remaining electrons in a unit cell, one expects a metallic behaviour of the surface. Indeed, many indications for a state at the Fermi level were found [245–255], but the Si(111) surface is very close to a Mott transition and has a too low sheet conductivity to be termed metallic based on transport behaviour [194, 254, 255].

Initially, no band crossing the Fermi level was found in ARPES even though there was intensity at the Fermi level in PES [251, 256]. In figure 5.5 (a), the bands S_1 and S_1' are attributed to the adatoms, but show a weak dispersion in general. The S_2 band stems from the rest atoms in agreement with STM data [250]. Then, experiments with higher resolution allowed the observation of an electron pocket at the centre of the 7×7 Brillouin zone [see figure 5.5 (b)] [251, 252].

The Si(001) surface with two distinct surface atoms already led to seven components in the Si-2p spectra. On the Si(111), there are many more distinct surface atoms, e.g. dimer atoms, adatoms, rest atoms, or atoms that have a different environment due to the stacking fault. Thus, we expect a multitude of spectral components. Unfortunately, even high-resolution PES cannot resolve all different spectral components [256], but the Si-2p

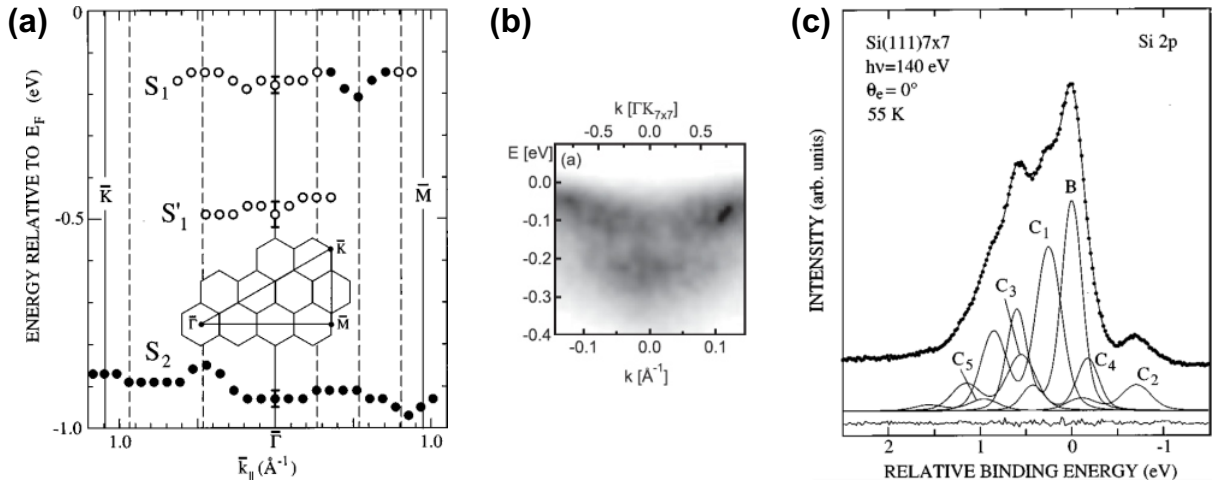

Figure 5.5.: (a) ARPES data of a planar Si(111)7×7 surface (photon energy $h\nu = 21.2$ eV). In the inset, small hexagons represent Brillouin zones of the 7×7 reconstruction while the included $\overline{\mathrm{M}}$ and $\overline{\mathrm{K}}$ points are from the 1×1 Brillouin zone. From [256]. (b) High-resolution ARPES results of a planar Si(111)7×7 surface close to the Fermi level ($h\nu = 34$ eV). From [252]. (c) High-resolution Si-2p spectrum of a planar Si(111)7×7 surface ($h\nu = 140$ eV). From [256].

spectrum can be well described by one bulk component (B) and five surface components (C_1 to C_5) [see figure 5.5 (c)]. The limited resolution makes an assignment of the components to specific structures of the surface difficult, but the C_2 component may stem from the rest atoms and C_3 from the adatoms [256–259]. The Fermi level lies higher on the Si(111) surface than on the Si(001) surface at about (0.69 ± 0.04 eV) above the VBM for n-type substrates [216, 260].

Generally, STM images of the Si(111) 7×7 reconstruction are dominated by the high appearing adatoms and the low appearing corner holes. In the filled states STM image shown in figure 5.6 (a), the triangular half unit cells appear rather flat since in addition to the adatom states also states of the rest atoms contribute to the image at the chosen tunneling voltage [compare with figure 5.5 (a)].

Interesting for the growth of nanowires are vicinal Si(111) surfaces. Here, we concentrate on four so-called Si(hhk) surfaces, which are vicinal Si(111) surfaces with an offcut towards $[11\overline{2}]$ that is usually chosen, so that h and k are rather small natural numbers [see figure 5.6 (b)]. Two substrates, Si(335) and Si(553), have large absolute values of their offcut angles, while the Si(557) and Si(775) surfaces have smaller absolute values of their offcut angles. Furthermore, the Si(335) and Si(557) surfaces have positive offcut angles ($h < k$) and the other substrates, Si(553) and Si(775), have negative ones ($h > k$). The two offcut directions are not equivalent. This is already obvious from the structure of the unreconstructed surfaces, e.g. along the blue hatched line in figure 5.6 (b) for the Si(335) surface. For $h < k$, each edge atom has two dangling bonds. In contrast, the edge atoms each have only one dangling bond each for $h > k$.

The difference between the offcut directions is also seen with STM of the reconstructed surfaces. The clean Si(hhk) substrates with $h < k$ shown in figures 5.6 (c and d) have a

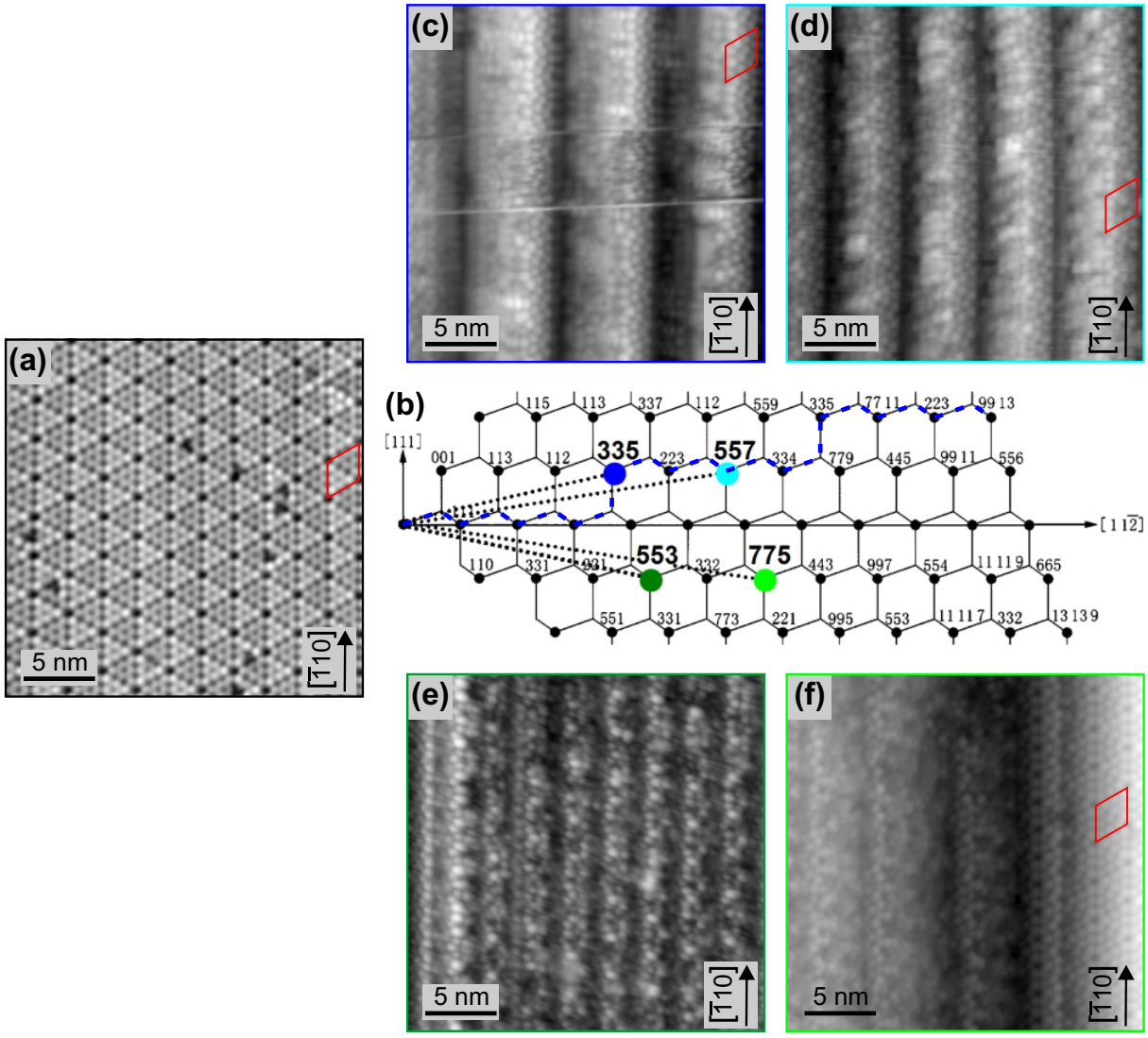

Figure 5.6.: (a) STM image of a planar Si(111)7×7 surface ($V = -1.0$ V). (b) View of the Si lattice along $[\bar{1}10]$. A cut parallel to $[\bar{1}10]$ through the leftmost atom and any other atom highlighted as a black dot leads to a surface with the given Miller indices. Adapted from [55]. (c and d) STM images of Si(hhk) surfaces with $h < k$. Si(335) with an offcut angle of +14.4° with respect to the Si(111) surface is shown in (c) ($V = +1.5$ V) and Si(557) in (d) (offcut angle of +9.5° and $V = -1.5$ V). (e and f) STM images of Si(hhk) surfaces with $h > k$. Shown are Si(553) in (e) (offcut angle of −12.3° and $V = +1.0$ V) and Si(775) in (f) (offcut angle of −8.5° and $V = -1.5$ V). The red rhombi mark 7×7 unit cells. The tunneling currents were 100 pA for all images.

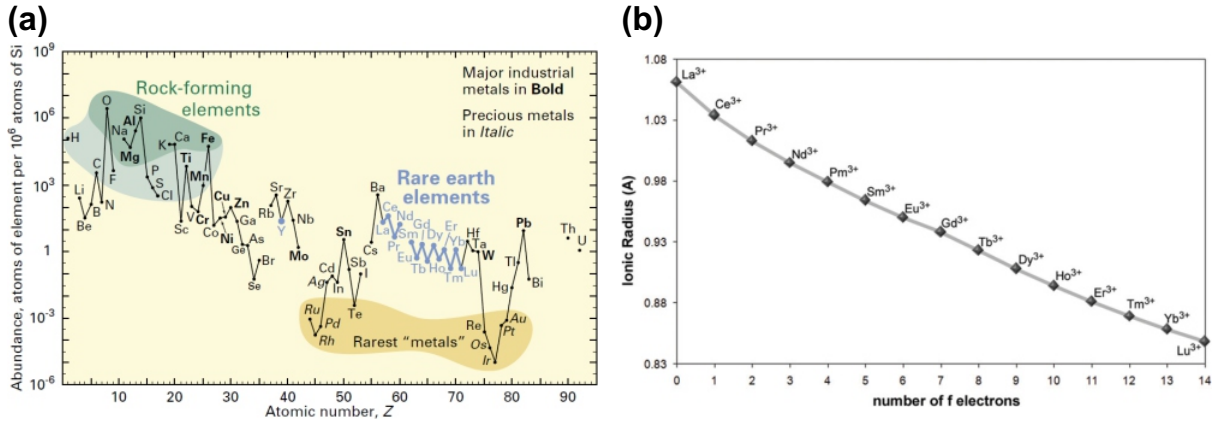

Figure 5.7.: (a) Diagram on the relative abundance of the elements in the Earth's upper crust. The identification of Sc as rare earth element is missing. From [268]. (b) The lanthanide contraction. From [269].

regular arrangement of steps alternating with (111) facets that each contain a single 7×7 unit cell [261–263]. However, the distance between neighbouring Si(111) terraces is larger on the Si(335) surface than on the Si(557) surface showing that a wider step structure is needed to compensate the difference to Si(111) for the larger offcut angle. For the other offcut direction, the situation is different and less uniform. On the Si(775) surface, seen in figure 5.6 (f), wide (111) terraces with multiple 7×7 unit cells alternate with large areas of a fairly regular step structure [264]. Usually, no (111) facets that are sufficiently wide to host a 7×7 unit cell are found on Si(553) substrates as shown in figure 5.6 (e) [265], but it may be possible to achieve a surface morphology similar to the one of the Si(hhk) surfaces with $h < k$, if a Si(553) substrate is quenched from high temperature [266].

5.2. Rare earth metals and their silicides

The rare earth elements are Sc, Y, and the lanthanides [267]. They are not rare in the Earth's crust, e.g. much more abundant than Au [see figure 5.7 (a)], but there are only few places where their concentration is sufficiently high for profitable mining. Furthermore, they always occur together in minerals and their separation is complicated due to their chemical similarity, leading to their rareness.

Rare earth metals are used for a long time for catalysts in cars and in petroleum refinement, as phosphors, or in alloys of Al and Fe [270]. A rising importance has their use in Ni-metal-hydride batteries, Sm-Co magnets, and Nd-Fe-B magnets, which are found, e.g., in generators of wind turbines or in hard disk drives [270, 271]. Furthermore, rare earth metals are found in many parts of smart devices [271]. Another important application with rare earth metals are Nd:YAG lasers (Y stands for the rare earth metal), which are widely used in medicine and manufacturing. Such infrared lasers are also used in today's research, but rare earth elements proved their importance for physics already a long time ago. In the 1920's, data of rare earth elements contributed significantly during the development of quantum theory [272]. The Tb mainly employed in this work is up to now rarely used as an

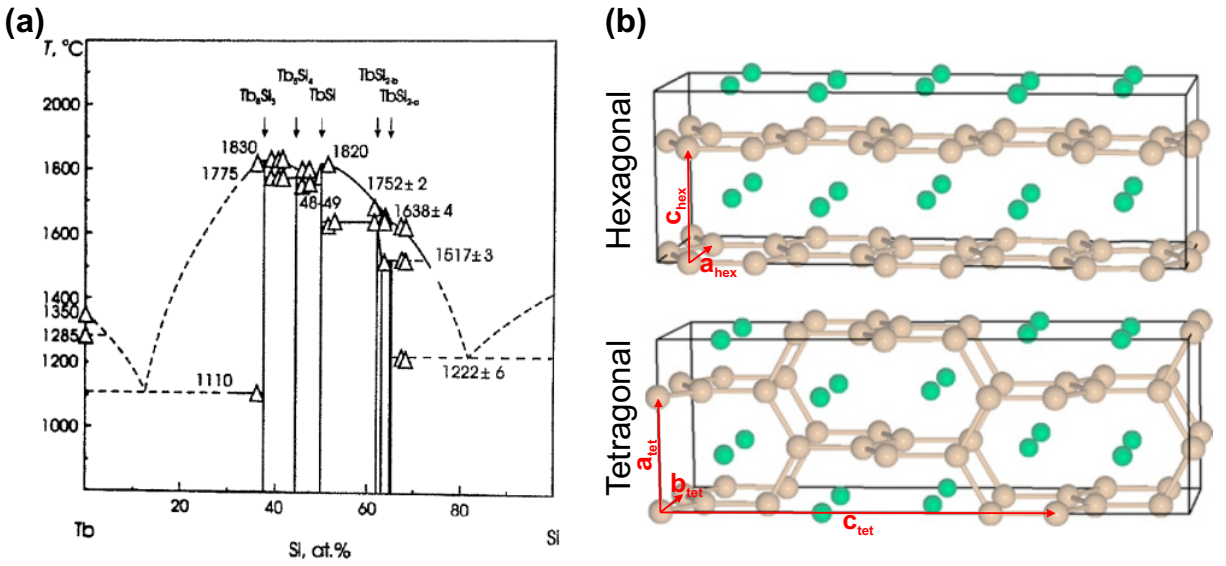

Figure 5.8.: (a) Binary phase diagram of Tb and Si. From [273] (b) Structure of the idealised (i.e. without Si vacancies) Si-richest rare earth silicides, hexagonal and tetragonal $RESi_2$. Rare earth atoms are shown in green and Si atoms depicted in beige. Adapted from [274].

essential rare earth metal, but may be utilised as luminescent material or in magnets as an additive.

In compounds, most rare earth elements are found in a trivalent oxidation state, which explains their chemical similarity. The $4f$ electrons of the lanthanides do not participate in the chemical bonding, so that their high magnetic moments are not quenched, which makes the lanthanides interesting for the application in magnetic structures, e.g.for permanent magnets. Since the electrons in the $4f$ orbitals shield the charge of the nucleus ineffectively, the ionic radius of the lanthanide 3+ ions reduces with increasing number of $4f$ electrons [see figure 5.7 (b)]. This contraction is responsible for changing lattice constants of compounds that have the same structure with the exception of a different involved rare earth element. Di- and rarely tetravalent oxidation states may also occur, with the divalent state rather common for Eu and Yb and less common for Sm and Tm.

The rare earth elements react easily with Si, and many rare earth silicides with different stoichiometries may form, as illustrated for Tb in figure 5.8 (a). In this work, rare earth layers with heights well below 1 nm react with extended Si crystals during annealing, so that the formation of silicides with high Si concentration is most likely. These are the hexagonal $RESi_{2-x}$ and the orthorhombic $RESi_{2-x}$.

Ideally, these structures would have the stoichiometry of $RESi_2$ and the structures shown in figure 5.8 (b), but the bulk silicides grow with Si vacancies ($TbSi_{2-x}$), which may be responsible for the observation of an orthorhombic (lattice constants $a \neq b$) instead of tetragonal structure (lattice constants $a = b$). The vacancy density of the hexagonal structure is generally assumed to be 1/6 of the Si lattice sites leading to a Tb_3Si_5 stoichiometry while the orthorhombic structure has a lower vacancy density [273].

The c/a ratio of the real hexagonal bulk silicides is larger than one, e.g. for Tb_3Si_5

$a_{hex} = 0.385$ nm and $c_{hex} = 0.415$ nm [273]. In contrast, the idealised hexagonal structure without vacancies has a c/a ratio smaller than one, e.g. calculations yield $a_{hex} = 0.410$ nm and $c_{hex} = 0.397$ nm for $TbSi_2$ [275]. Similarly, calculations typically overestimate the length of the tetragonal c_{tet} lattice constant in comparison to the c_{ort} lattice constant of the orthorhombic phase. For completeness, the experimental lattice constants of the orthorhombic phase are $a_{ort} = 0.405$ nm, $b_{ort} = 0.397$ nm and $c_{ort} = 1.338$ nm [273].

The Si rich silicides are metallic having a finite DOS at the Fermi level, a resistivity typical for metallic compounds, e.g. $\rho = 9 \times 10^{-5}$ Ωcm at room temperature for a 12 nm thick Tb_3Si_5 film, and an increasing resistivity with increasing temperature [275, 276]. Another interesting property of rare earth silicides is the existence of magnetic ordering at low temperatures, e.g. $TbSi_{2-x}$ shows antiferromagnetic ordering at low temperatures for both structural phases, but with different Néel temperatures for the different atomic structures [276, 277].

5.3. Metals on Silicon

In this work, rare earth silicides and Si overlayers are grown on silicon surfaces using molecular beam epitaxy, i.e. by the in-UHV evaporation of elements, usually combined with solid phase epitaxy, i.e. the reaction of a solid overlayer with the solid substrate. In the first part of this section, the processes occurring during epitaxy are discussed, while details of the preparation procedures are presented in chapter 6. The influence of the metallic overlayers on the electronic structure of the Si substrate are introduced in the second part of this section.

5.3.1. Thin film growth

During any epitaxial process, a material is deposited on a surface. This material may be in atomic form or in compounds, e.g. molecules or clusters. The processes discussed in the following for atoms may also occur for compound materials in a similar form, but usually the compounds have to decompose to enable epitaxial growth.

An overview on the atomic processes of epitaxy is given in figure 5.9. Atoms are deposited on a surface with a rate given by the offered atom amount and the sticking coefficient, which decreases with increasing temperature. Initially, the atoms are physisorbed, i.e. weakly bound by van der Waals interaction, and they may have excess thermal energy to diffuse over the surface. During the diffusion they may collide inelastically with other atoms, which may lead to the nucleation of islands. There the atoms are chemisorbed, i.e. chemically bonded to the substrate. Other sites, where the chemisorption probability is increased, are surface steps, island edges or surface defects. Depending on the thermal energy of the atoms also the reverse processes, i.e. detachment from islands or steps and desorption, may occur.

If the thermal energy of the deposited atoms is too low, the atoms cannot diffuse to the energetically most favourable positions leading to the growth of amorphous films, which lack long range order. Such films usually have a rather homogeneous height determined by the deposition rate, but rough surfaces as illustrated in figure 5.10 (a).

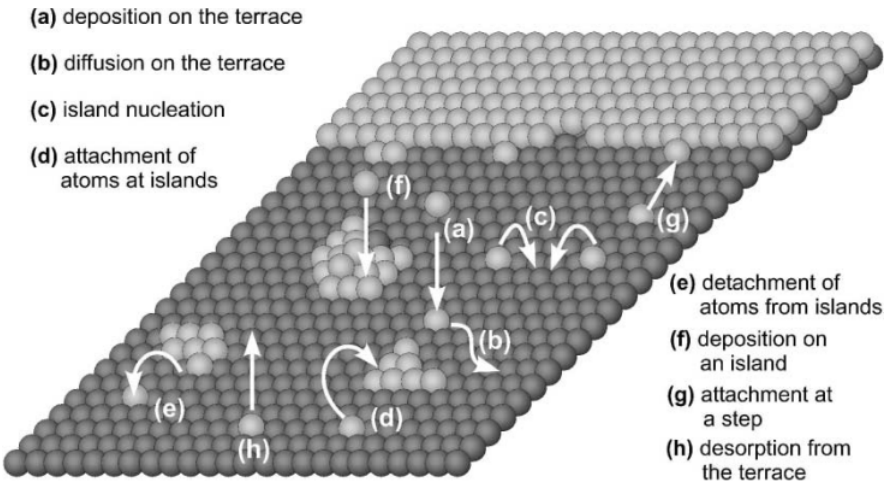

Figure 5.9.: Illustration showing the atomic processes during epitaxy. Not shown is the diffusion across step edges, which is hindered by the Ehrlich-Schwoebel barrier [278, 279]. From [280].

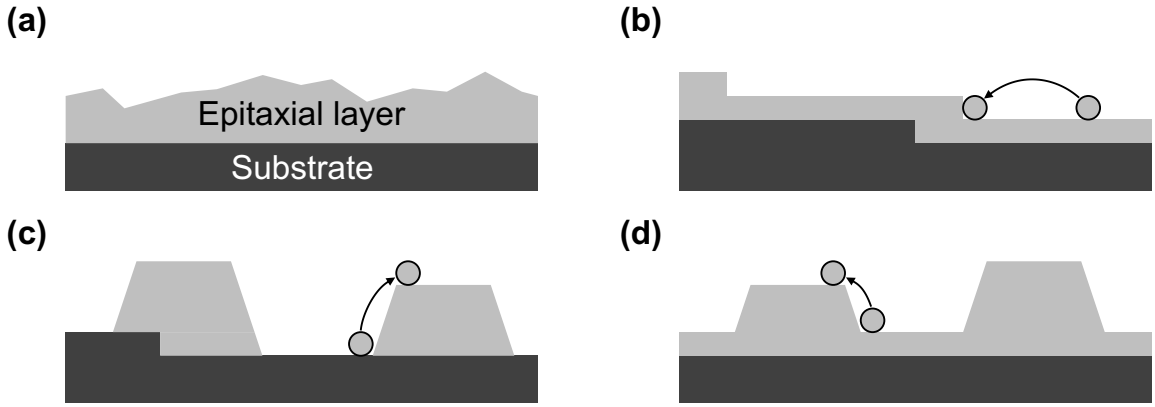

Figure 5.10.: Schematic illustrating the different growth modes. (a) Amorphous growth typical for low growth temperatures, at which diffusion is suppressed. (b) Layer or step-flow growth, also known as Frank-van-der-Merwe growth, observed for $\sigma_S > \sigma_I + \sigma_F$. (c) Island or Volmer-Weber growth occurring for $\sigma_S < \sigma_I + \sigma_F$. (d) Stranski-Krastanow growth, in which layer growth is observed up to a critical thickness, where island growth begins. The initial flat layer is called wetting layer and material of this wetting may also diffuse to the islands.

Amorphous films of rare earth metals and Si were grown in this work by molecular beam epitaxy at room temperature. Annealing these films may lead to their restructuring or to reactions with the substrate. Such rearrangement processes are solid phase epitaxy processes. Alternatively, the substrate may be annealed during the molecular beam epitaxy to directly form a crystalline overlayer. When a reaction between deposited overlayer and substrate takes place, so that the final film also includes atoms from the substrate, the term reactive deposition epitaxy is frequently used.

In thermodynamic equilibrium, various growth modes may occur depending on the

energies per area, i.e. the surface tensions, of the clean substrate σ_S, of the film σ_F, and of the interface between film and substrate σ_I. In analogy to the wetting of surfaces by liquids, the ideal contact angle θ_C, i.e. the angle between film surface and film-substrate interface, is given with these energies by the Young's relation [281–283]:

$$\sigma_S = \sigma_I + \sigma_F \cos\theta_C. \tag{5.1}$$

The contact angle can be between 0 and 180°. Thus, the maximum of the right side of equation 5.1 is $\sigma_I + \sigma_F$, and if σ_S is larger than this sum, islands are unstable. The resulting growth mode is the layer growth, during which each layer is grown after the former by attachment of atoms to the surface steps [see figure 5.10 (b)]. Due to these processes, this growth mode is also called step-flow growth. Frank and van der Merwe studied such a growth leading to the additional denotion of this growth mode as Frank-van-der-Merwe growth [284–286]. If equation 5.1 has an solution, islands are grown on the terraces or at steps [see figure 5.10 (c)]. This island growth mode is also denoted Volmer-Weber growth due to their studies [287].

The relation between the various surface tensions may change with the thickness of the overlayer, e.g. strain may increase the film energy leading to the formation of dislocations or a change from layer to island growth, which is denoted Stranski-Krastanow growth [288]. Such a change of growth mode is often observed in heteroepitaxy, in which the film is a different material than the substrate, e.g. in the epitaxial growth of semiconductor quantum dots [289, 290].

The resulting structures rarely depend only on thermodynamics, but kineticts often play a major role during the epitaxy. Not only may amorphous films grow, but, e.g., atoms may not reach steps due to a too low diffusion length, leading to their chemisorption on terraces even when layer growth should take place based on the surface tensions.

5.3.2. Schottky barrier formation

A metal-semiconductor contact may have a current rectifying characteristics [291]. The reason for this behaviour is the formation of an energy barrier for the charge carriers that decreases or increases depending on the polarity of the applied voltage. In the following, the formation of this so-called Schottky barrier Φ_B will be discussed based on virtual gap states. In addition, band bending at surfaces will be discussed in general.

The Schrödinger equation has to be solved for the electrons to correctly describe the electronic structure of a solid. The eigenstates of electrons in a solid, in which the electrons are in the periodic potential of the crystal lattice, are Bloch waves:

$$\Psi(\boldsymbol{r}) = \mathrm{e}^{i\boldsymbol{k}\cdot\boldsymbol{r}} u(\boldsymbol{r}) \tag{5.2}$$

with $u(\boldsymbol{r})$ a function with the same periodicity as the crystal lattice [292]. Due to the high density of atoms in solids, the eigenvalues of the Bloch waves, i.e. their energy levels, are not well separated, but form quasi-continuous bands. In general, a certain crystal momentum ($\boldsymbol{k}$) corresponds to a certain eigenvalue, but due to the periodicity of the lattice in solids, the crystal momentum is not well defined with respect to changes by a reciprocal lattice

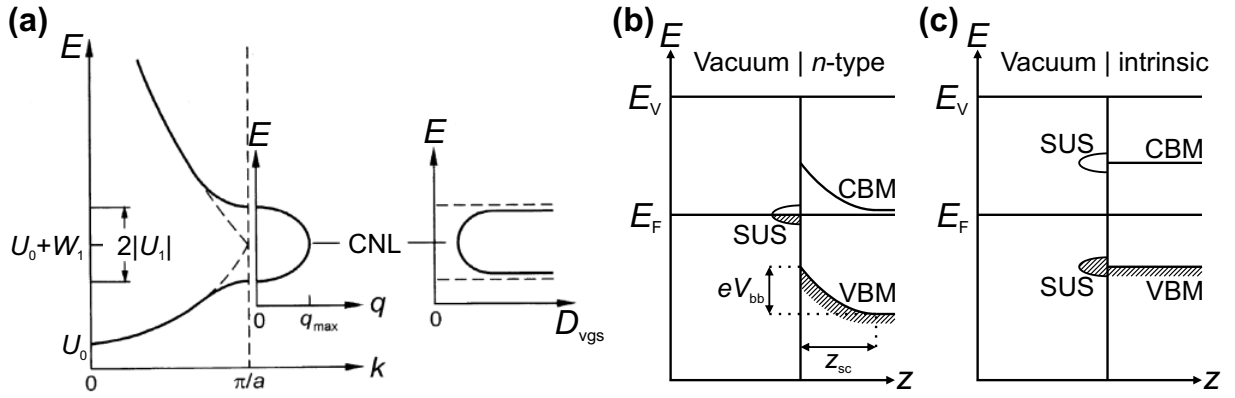

Figure 5.11.: (a) Band structure of a one-dimensional solid for real and complex wave vectors (left) and density of states of the virtual gap states (right). CNL is the charge-neutrality level. The potential of the lattice is assumed to be of the form $U = U_0 - U_1 \cos(2\pi z/a)$ with a the lattice constant, U_0 the potential offset, and U_1 the amplitude of the potential modulation. It is $W_1 = \hbar^2\pi^2/(2m_0a^2)$ with m_0 the free electron mass. From [293]. (b and c) Surface state formation for a (b) covalent n-type and (c) ionic intrinsic semiconductor and their respective influences on the band bending at the surface. CBM is the conduction band minimum, V_{bb} the band bending voltage, z_{sc} the width of the space-charge region, and SUS stands for surface state. After [294].

vector, so that a description with multiple eigenvalues for a certain crystal momentum is possible [209].

An electron dispersion $E(\boldsymbol{k})$ is shown in figure 5.11 (a) for a one-dimensional system ($\boldsymbol{r} = z$). The dispersion is not continuous, but a band gap opens due to the periodic potential of the lattice. The crystal momentum of the electrons is real for all energy bands, but the Schrödinger equation can also be solved in the band gap using complex wave vectors of the form $k = \pi/a + iq$. Such eigenstates with complex wave vectors do not exist in the bulk of the solid, since they grow exponentially and consequently cannot be normalised, so that they are denoted virtual gap states.

The situation is different at a surface. There the perfect periodicity of the solid is broken and surface states with complex wave vectors that decay not only into the vacuum, but also into the bulk may exist. For covalently bonded semiconductors these surface states typically lie close to the middle of the band gap [see figure 5.11 (b)]. Thus, it is energetically favourable to fill these states by the majority charge carriers (electrons for a n-type and holes for a p-type semiconductor). This charge transfer to the surface leads to a space-charge region close to the surface and a band bending by eV_{bb}. As depicted in figure 5.11 (b), the space-charge region and consequently the band bending region has the width:

$$z_{\mathrm{dep}} = \sqrt{2\epsilon\epsilon_0 \left|V_{\mathrm{bb}}\right| / (en_{\mathrm{d}})} \tag{5.3}$$

with and n_{d} the density of the dopant [293]. For moderately doped Si substrates, as used in this work, the width of the space charge region is in the order of several 100 nm. Thus, surface sensitive photoemission spectroscopy may measure strongly shifted band positions compared to the expected positions for the bulk. The exact band positions depend on the

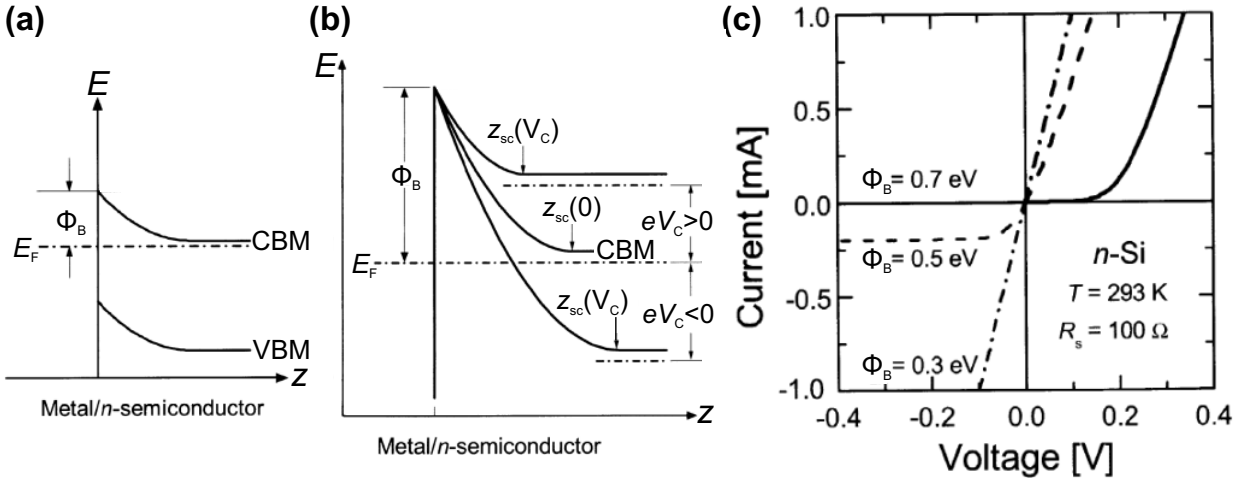

Figure 5.12.: (a) Band diagram illustrating the Schottky barrier formation for an n-type semiconductor. (b) Diagram showing the influence of an applied voltage (V_C) on the energy barrier at an interface of metal and n-type semiconductor. (c) Simulated transport characteristics for varying Schottky barrier height. R_S is the series resistance of the Schottky diode. All images from [293].

doping type and the surface orientation since the forming surface states differ for varying orientations. The band bending at the surface is typically much lower for non-polar surfaces of ionic semiconductors, where surface states close to the VBM and CBM form. The surface states may not only be well separated in energy, but also spatially, e.g. for surfaces of III-V semiconductors the filled surface states are primarily located at the group-V atoms and the empty surface states are mostly located at the group-III atoms [109].

Similar as on surfaces, states with complex wave vectors exist at interfaces between metals and semiconductors. Matching the Fermi levels of metal and semiconductor at the interface, the band gap of the semiconductor overlaps at least partially with the conduction band of the metal. Here, states of the metal conduction band decay into the semiconductor leading to the formation of metal-induced gap states in the semiconductor [296]. In a first approximation, the density of the metal-induced gap states is that of the virtual gap states [see figure 5.11 (a)], since their wave functions have to match those in the semiconductor. These metal-induced gap states are filled up to the charge-neutrality level, leading to a space-charge region and band bending at the interface [see figure 5.12 (a and b)]. The charge-neutrality level is the energy, up to which the additional density of virtual states in the gap is compensated by a reduced density of states in the valence band, so that the semiconductor is not charged [294]. The gap states are a mixture of the valence and conduction band states and their character changes from dominantly valence band-like to mainly conduction band-like at the charge-neutrality level.

Up to now, the same Schottky barrier would be expected for all metals on the same semiconductor. An additional filling or depletion of the metal-induced gap states arises from the formation of an interface dipole due to different electronegativities of the semiconductor and metal. If the density of metal-induced gap states is high, the change of the Schottky barrier is small and $\Phi_B \approx E_{CBM} - E_{CNL}$ for electrons and n-type semiconductors [297].

Indeed, very similar Schottky barriers, corresponding to a Fermi-level position close to the middle of the band gap, are observed for many semiconductors rather independently of the metal [293, 298, 299]. This phenomenon is called Fermi-level pinning. In contrast, if the density of metal-induced gap states goes to zero, the Schottky barrier for electrons is rather given by $\Phi_B \approx \Phi_M - \chi$ with Φ_M the work function of the metal [300, 301]. In addition, the Schottky barrier is influenced by defect states at the interface and by image forces [293].

If a positive voltage is applied to the n-type semiconductor with respect to the potential of the metal, the height of the energy barrier that the electrons have to overcome will be given by the Schottky barrier height [see figure 5.12 (b) with $eV_C < 0$], and a very low current due to thermally excited electrons in the metal is measured. In contrast, if a negative voltage is applied at the n-type semiconductor, the energy barrier reduces with respect to the Schottky-barrier height with increasing voltage [see figure 5.12 (b) with $eV_C > 0$], so that much larger currents are observed. Such a diode characteristics is seen in figure 5.12 (c), in which I-V curves are plotted for varying Schottky barrier heights. There is an unambiguous rectifying behaviour for high barrier heights. In contrast, a nearly linear I-V curve, i.e. ohmic behaviour, may be observed for low barrier heights. Such ohmic contacts are needed for contacting semiconductor devices in electronics, e.g. at one end of the semiconductor in a Schottky diode, and may be achieved by choosing contact metals with the right electronegativity or by heavily doping the surface layers [302].

All statements made above for n-type semiconductors apply in an analogous manner for p-type semiconductors. Furthermore, the concepts introduced here are also applicable for other interfaces, e.g., in semiconductor heterostructures. A discussion of these and additional informations in general can be found in references [293, 299].

5.4. Rare earth metals on Silicon

Initially, rare earth silicides were produced by reduction of rare earth oxides with Si [303]. In this process, rare earth silicides with many different stoichometries were formed. With the advance of UHV systems, direct growth of rare earth silicides on clean Si substrates by deposition of the pure rare earth metals and annealing was studied [304–306]. Interestingly, silicides with high Si content form directly, and no initial formation of silicides with low Si content is observed [304, 306]. Furthermore, the reaction of the rare earth layers with the Si occurs in a very small temperature range, especially on Si(001) surfaces [304]. This indicates that the silicides form at temperatures, for which the diffusion of Si, the dominantly diffusing species [305], is already high and nucleation is the growth-limiting process. Such a growth behaviour is mainly known for silicides [307, 308]. Another interesting aspect of rare earth silicides are their very low Schottky-barrier heights on n-type Si of about 0.4 eV [309, 310].

The up-to-now discussed initial studies used rare earth films with thicknesses of several nm. In the following, the rare earth silicide structures forming on Si(001) and Si(111) for rare earth coverages below 1 nm are introduced in more detail. It should be mentioned that no structures will be discussed, in which the rare earth metal is divalent.

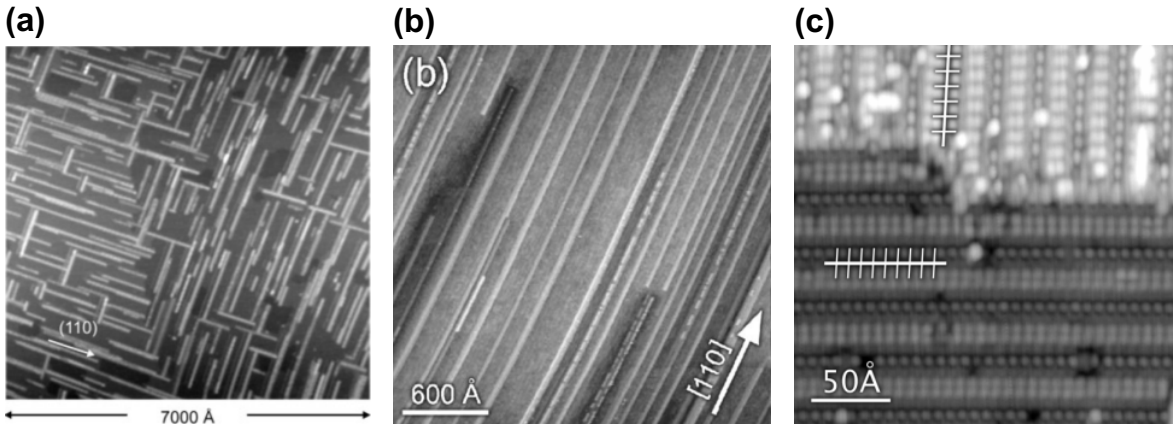

Figure 5.13.: (a) First reported STM image of $RESi_2$ nanowires, in this case $DySi_2$ nanowires on Si(001) prepard by deposition of about 0.5 ML Dy and annealing at 600 °C. From [76]. (b) STM image of parallel $DySi_2$ nanowires on vicinal Si(001). From [319]. (c) Detailed STM image of the Dy-induced 2×7 reconstructed wetting layer. From [331].

5.4.1. Growth and electronic properties on Si(001)

The investigation of rare earth silicide nanostructures on Si(001) started about 20 years ago [76, 311]. In addition to island growth and to the formation of a wire-like wetting layer, nanowires were observed, which attracted the most attention [66, 75–85, 274, 312–330]. The very first reported STM image of such nanowires is shown in figure 5.13 (a). The formed Dy silicide nanowires had lengths up to over 200 nm and widths below 3 nm.

Due to the two-domain structure of planar Si(001) substrates, also the nanowires grow in two domains. This two-domain growth limits the length of the nanowires, because individual nanowires do not cross each other. Single-domain growth and consequently also longer nanowires are observed on vicinal Si(001) surfaces, as seen in figure 5.13 (b) [84, 317–319].

While nanowires may grow in bundles, these bundles form well separated [see figures 5.13 (a and b)]. The area in between is typically covered by a mixture of a 2×7 reconstructed structure, sub units of this structure and Si dimer rows [76, 79, 82, 329–333]. This 2×7 reconstruction is observed for most rare earth elements when the metal coverage is too low to form nanowires. It may even cover the complete surface, as shown in figure 5.13 (c). Thus, this 2×7 reconstruction forms a wetting layer that may be partially consumed upon nanowire formation. This wetting layer is non-metallic as observed by ARPES [85], so that the nanowires should not be electrically connected. The atomic structure of the wetting layer is still under debate. There is a structure model proposed by Preinesberger *et al.*, but this model does not fit observations made by another group [331, 332]. Another model proposed in theoretical studies is solely based on the adsorption of rare earth metal adatoms between the Si dimer rows [334]. The observation of such a structure after annealing at rather high temperatures of up to 600 °C seems unlikely, since the Si diffusion is high at these temperatures [305] and should enable energetically more favourable atomic configurations, e.g. the formation of Si cages around rare earth atoms.

In contrast, the structure of the nanowires appears to be well understood. The large height of the nanowires above the surrounding surface and their compact appearance in

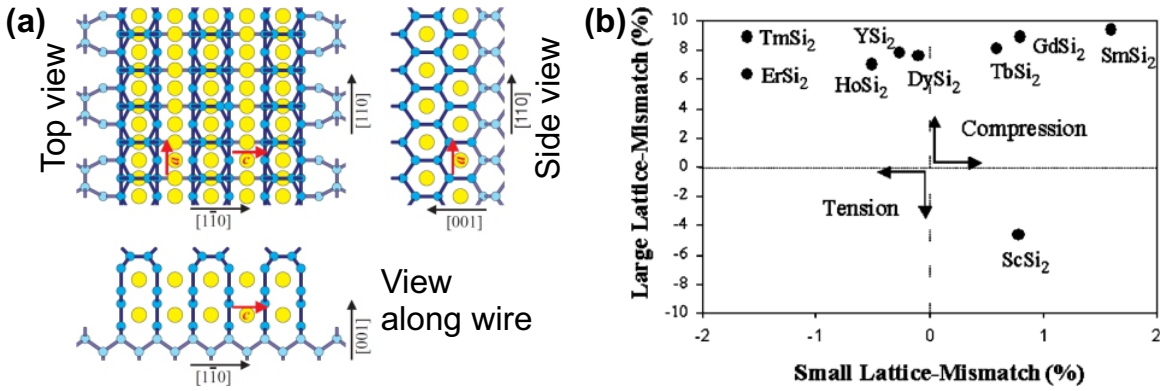

Figure 5.14.: (a) Structure model of $RESi_2$ nanowires on Si(001). Si atoms are blue and RE atoms yellow. From [85]. (b) Prediction for nanowire forming silicides based on the anisotropic lattice mismatch of the hexagonal RE_3Si_5. From [78].

STM indicate that the nanowires are not just a surface reconstruction, but are built of silicides [76]. Since the direct formation of silicides with high Si content is observed even for rather thick rare earth layers [304, 306], the nanowires should also have a high Si content. The growth of highly anisotropic islands, i.e. nanowires, can be nicely explained by assuming a hexagonal instead of tetragonal $TbSi_2$ atomic structure. Both structures show locally a similar bonding configuration of the Si atoms possibly leading to epitaxial growth, but the tetragonal structure should grow isotropically on the surface. In contrast, the hexagonal structure shows an anisotropic lattice mismatch to the substrate. For many rare earth silicides, the experimental a_{hex} lattice parameter agrees nicely with the Si(001) surface lattice constant while the experimental c_{hex} lattice parameter strongly differs. Thus, the growth of the silicide is nearly limitless along a_{hex} and hindered in c_{hex} direction leading to the structure model shown in figure 5.14 (a).

Based on this structure model, Chen *et al.* proposed nanowire growth for various rare earth silicides [see figure 5.14 (b)]. These predictions were confirmed for all but two cases [78–81]. Sm silicide nanowires were not observed [81], and no studies on Tb were reported. Thus, this thesis about Tb silicide structures closes this knowledge gap. It should be noted that other rare earth silicides form distinctly different wire-like structures [335], but no silicide that is not present in figure 5.14 (b) is known for the formation of the here discussed nanowires [81].

Despite the success of the growth model in predicting nanowire formation, there is one problem with the growth model and consequently with the atomic structure model. It is based on the experimental lattice parameters obtained for the defective bulk silicide structure. While vacancies of rare earth atoms were proposed [330], no evidence for Si vacancies in the nanowires were reported up to now. The vacancy formation in the bulk silicides is presumably driven by the reduction of compressive strain present in the planar graphene-like Si layers. Such strain may be strongly reduced in the nanowires due to vertical relaxation. Thus, a 1 : 2 stoichiometry of rare earth metal to Si is generally assumed for the nanowires [77, 81, 312]. Such a stoichiometry leads to different lattice parameters, as discussed in section 5.2 [275]. The anisotropy of the silicide lattice constants reduces and

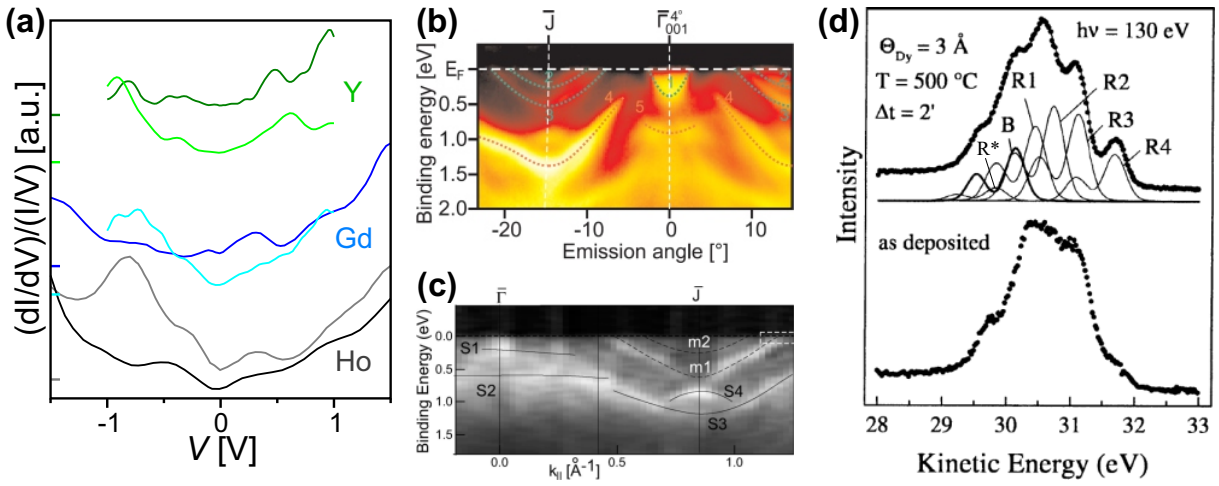

Figure 5.15.: (a) Overview on the reported STS data for various $RESi_2$ nanowires on Si(001). Adapted from the following references: black [82], grey [81], light blue [315], dark blue [83], light and dark green [330]. The inner ticks mark the zero lines of the respective spectra. (b) Band dispersion parallel to $DySi_2$ nanowires on vicinal Si(001) ($h\nu = 41$ eV). From [75, 85]. (c) Band dispersion parallel to $GdSi_2$ nanowires on vicinal Si(001) ($h\nu = 21.2$ eV). From [84]. (d) Si-2p spectra for amorphous Dy (bottom) and $DySi_2$ nanowires (top) on Si(001). From [215].

the c_{hex} lattice constant is closer to the lattice constant of the Si(001) substrate. Thus, the growth model may be incorrect and the atomic structure of the rare earth silicide nanowires has to be analysed further, as performed within this thesis.

Due to the chemical similarities of the rare earth elements, they only differ in the amount of $4f$ electrons, which do not participate in the bonds, so that the same atomic structure of the rare earth silicide nanowires is expected, even if the structure model discussed above is not correct. Similarly, the electronic structure of the rare earth silicide nanowires is assumed to be rather independent of the rare earth metal. Indeed, all reported STS spectra indicate a finite density of states at the Fermi level indicating the metallicity of all rare earth silicide nanowires [80–83, 315, 325, 330]. Some changes of the electronic structure, e.g., with the width of the wires are expected, but cannot explain the large differences in the reported STS data shown in figure 5.15 (a). Even the spectra of Y silicide nanowires, which were taken on nanowires with the same width, differ considerably, e.g. in the position of observed maxima. As a reason for this variation, rare earth vacancies are discussed [330].

The situation regarding reported ARPES data is similarly heterogeneous. All measurements show a strong dispersion parallel to the nanowires and bands crossing the Fermi level [84, 85, 319]. Nevertheless, the exact dispersions differ. Initially, Preinesberger *et al.* reported two bands crossing the Fermi level, one centred around the $\overline{\mathrm{J}}$ point and one around the $\overline{\Gamma}$ point for Dy silicide nanowires. Later, Wanke *et al.* were able to resolve two bands crossing the Fermi level around the $\overline{\mathrm{J}}$ point for Dy and Er silicide nanowires [see figure 5.15 (b)]. This observation of two bands around $\overline{\mathrm{J}}$ agrees with the data obtained by Yeom *et al.* for Gd silicide nanowires, but no band crossing the Fermi level at the $\overline{\Gamma}$ point was reported in their study [see figure 5.15 (c)]. Band dispersion plots in the direction

perpendicular to the nanowires do not show dispersing bands in the region close to the Fermi level [84, 85, 319], so that the nanowires may have a quasi-one-dimensional electronic structure, but additional data covering a larger part of the $\boldsymbol{k}$ space are needed to determine this conclusively.

Core-level photoemission spectra are only available for Dy silicide nanowire samples [215]. As expected, the Si-2p spectrum changes strongly when an amorphous rare earth metal overlayer is annealed and nanowires form [see figure 5.15 (d)]. Five spectral components related to silicide structures (R1 to R4 and R*) are found in addition to the component of the bulk (B). Due to the higher electronegativity of the rare earth metals compared to Si [336, 337], the charge transfer from rare earth atoms to Si results in a shift of the Si core levels to lower binding energy. Consequently, a higher kinetic energy is expected for electrons emitted from Si-2p core levels of atoms bonding to rare earth atoms. This is the case for the components R1 to R4. Based on the shift to ever higher kinetic energies and on the dependence of their relative intensities on the photon energy, the positions of the Si atoms corresponding to the Si-2p components get less bulk-like and more surface-like with increasing index of the component [215]. The R* component does not fit the expectation of a higher kinetic energy possibly due to strain and may be related to the wetting layer [215]. Up to now not discussed in the literature is the change in band bending upon nanowire formation, which can be measured by the shift of the Si bulk component B.

5.4.2. Growth and electronic properties on Si(111)

The growth of thin rare earth silicide layers on planar Si(111) is already investigated for about 30 years and rather well understood. Historically, after studying mainly thin films of multiple layers [61–66, 69, 71, 215, 276, 311, 338–363], the monolayer structure was investigated intensively [61–71, 215, 355–378], before submonolayer structures also moved in the focus of research [68, 71, 357, 361, 362, 376–383]. Here, the structures relevant for this work will be introduced the other way around.

For submonolayer rare earth metal coverages and annealing at about 500 °C, a variety of surface reconstructions are observed. In figure 5.16 (a), an STM image of the most frequently observed structures is shown exemplarily for Tb. The most dominant structure is typically the $2\sqrt{3}\times2\sqrt{3}$R30° superstructure if no special preparation parameters are chosen to trigger the preferential growth of a different structure [381, 382]. A more detailed STM image of this superstructure is shown as inset in figure 5.16 (a). No homogeneous layer, but triangular domains of $2\sqrt{3}\times2\sqrt{3}$R30° ordered protrusions are observed, which rotate by 60° when a domain boundary is crossed.

The atomic structure model of the $2\sqrt{3}\times2\sqrt{3}$R30° superstructure is shown in figure 5.16 (b). Distorted hexagons of rare earth atoms are bound to the unreconstructed Si(111) surface, i.e. the stacking fault regions of the Si(111)7×7 reconstruction are destroyed. The six rare earth atoms are all positioned approximately above Si atoms of the lower layer of the Si bilayer (T_4 site) and bound to twelve Si atoms of the upper layer of the Si bilayer. In addition, this structure is stabilised by the formation of delocalised states at the ring of rare earth atoms similar as, e.g., in benzene. One of these states is highlighted in figure 5.16 (b). This atomic structure model was first developed based on experimental data and was later nicely confirmed by theory [362, 377–379].

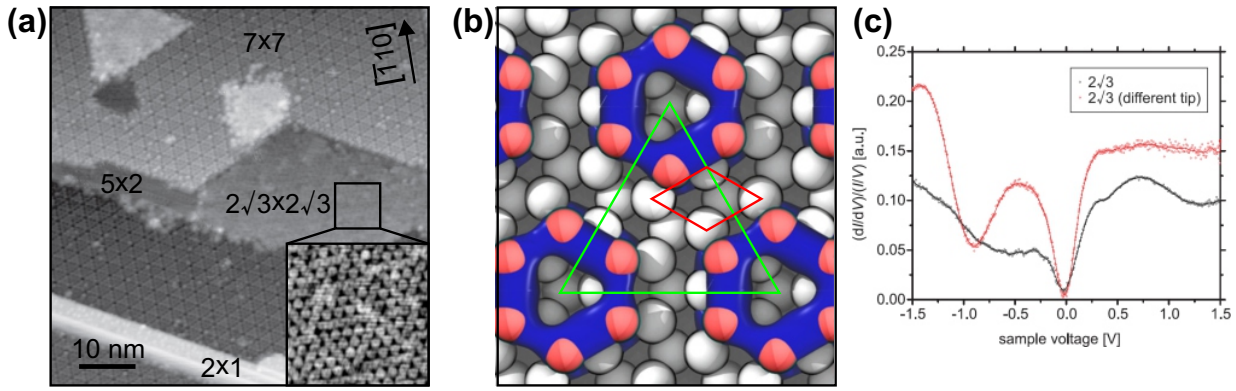

Figure 5.16.: (a) Overview STM image showing the diversity of Tb induced submonolayer structures (0.4 ML Tb annealed at 550 °C, $V = -2.0$ V, $I = 100$ pA). The inset is a 8 nm wide close-up of the $2\sqrt{3}\times2\sqrt{3}$R30° superstructure ($V = +1.5$ V, $I = 100$ pA). From [361]. (b) Atomic structure model of the $2\sqrt{3}\times2\sqrt{3}$R30° superstructure with rare earth atoms in red an Si atoms in white. An isosurface of the uppermost occupied state is shown in blue. The red rhombus marks one 1×1 unit cell and the green triangle a half of a $2\sqrt{3}\times2\sqrt{3}$R30° unit cell. From [362]. (c) STS spectra of the Tb induced $2\sqrt{3}\times2\sqrt{3}$R30° submonolayer. From [384].

Regarding the electronic structure of the $2\sqrt{3}\times2\sqrt{3}$R30° superstructure, the agreement between experiment and theory is not as good. Theory computes a band gap of over 0.2 eV, but no such gap is observed in the STS data of this reconstruction induced by Er and Tb [379,384]. Two STS spectra are exemplarily shown in figure 5.16 (c). There is no extended region where the normalised differential conductance is zero. Thus, this reconstruction is at least semimetallic [379, 384]. It should be noted that once a semiconducting behaviour of the Er induced $2\sqrt{3}\times2\sqrt{3}$R30° reconstruction was observed [382].

An even better agreement of theory and experiment is achieved for the rare earth silicide mono- and multilayer, i.e. not only the atomic, but also the electronic structure are in accord [347, 349, 356, 358, 362, 364, 365]. Figure 5.17 (a) shows an overview STM image of a preparation, in which the Tb coverage is about three times that of the preparation shown in figure 5.16 (a). The most prominent structures are two types of flat-appearing islands. The lower appearing islands have straight edges and show a 1×1 reconstructed surface in detailed STM images [see figure 5.17 (a)]. The higher appearing islands have round edges and, in general, a surface rather similar to the lower islands, but small relaxations of the surface atoms lead to a $\sqrt{3}\times\sqrt{3}$R30° structure. It should be noted that rather extreme tunnelling conditions of low voltage and high current have to be applied to obtain atomic resolution on the islands. In between the islands, a mixture of the submonolayer structures or even patches of clean Si are typically observed.

Analysing the height of the islands, the lower appearing islands can be assigned to one monolayer of hexagonal rare earth disilicide and the higher appearing islands correspond to two silicide layers, which agrees well with the used Tb coverage. The atomic structure model of the monolayer is shown in figure 5.17 (b). Its stoichiometry is that of the ideal hexagonal $TbSi_2$, when all atoms above the uppermost substrate bilayer are considered, i.e. layer Si_1, Si_2, and RE in figure 5.17 (b). No Si vacancies form, but the surface bilayer

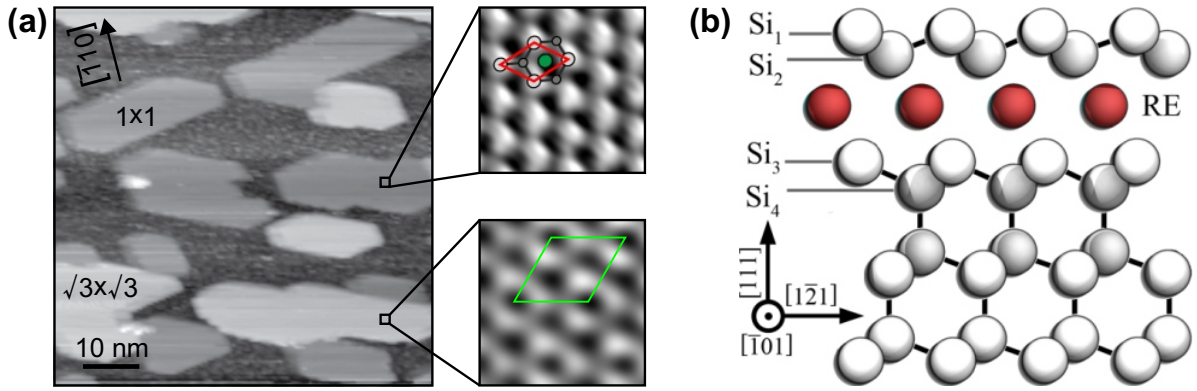

Figure 5.17.: (a) Overview STM image (left) of mono- and multilayer Tb silicide islands (1.1 ML Tb annealed at 550 °C, $V = -2.5$ V, $I = 100$ pA) and detailed STM images of the monolayer (top) showing a 1×1 structure and of the multilayer (bottom) showing a $\sqrt{3}\times\sqrt{3}$R30° structure (both 1.6 nm wide, both $I = 4.0$ nA, top $V = -0.4$ V, and bottom $V = -0.3$ V) From [69,361]. (b) Atomic structure model of the rare earth disilicide monolayer. Changing the rare earth metal leads to small variations of the distances between the layers Si_1 to Si_4 and RE. From [362].

is buckled to reduce the strain expected for flat, vacancy free layers. Interestingly, the buckling direction rotates by 180° between substrate and surface. The rare earth atoms lie in the Si rings with respect to the surface bilayer, but, similar as the rare earth atoms of the $2\sqrt{3}\times2\sqrt{3}$R30° superstructure, at T_4 sites with respect to the substrate.

The growth of additional silicide layers leads to the formation of flat Si layers with vacancies between the rare earth layers. The rare earth atoms lie always in the Si rings of the silicide, also with respect to the surface bilayer, which is still buckled. In contrast to the monolayer, a buckling of the surface in the same direction as the substrate is energetically more favourable for the multilayer. The vacancies of the first flat Si layer beneath the surface may lie beneath the upper or lower atom of the buckled surface bilayer. The different vacancy positions lead to different relaxations in the surface bilayer and therewith a different appearances in STM [353,354,362]. Thus, for the rare earth silicide multilayer also depth information is obtained with the surface sensitive technique STM. In the following, only the monolayer structure will be discussed in detail since most of the time rare earth coverages too low to observe multilayer formation were used in this work.

There are few reports that include STS data for the rare earth silicide monolayer [370, 373,374,384]. In general, different tips produce vastly different spectra [373,384], as is seen in figure 5.18 (a). The black graph was determined to represent the DOS more reliably by comparison with the DOS derived in calculations [67,384], but the red graph is in better agreement with further experimental data [370,373,374]. All experimental spectra show a maximum slightly above the Fermi level [position D in figure 5.18 (a)]. This is related to an only weakly dispersing band found in calculations in the centre of the Brillouin zone [67,362,370]. Another always observed characteristics is a finite density of states at the Fermi level. Thus, the rare earth silicide monolayers are clearly metallic.

This is also seen in ARPES measurements, in which intensity is observed up to the Fermi

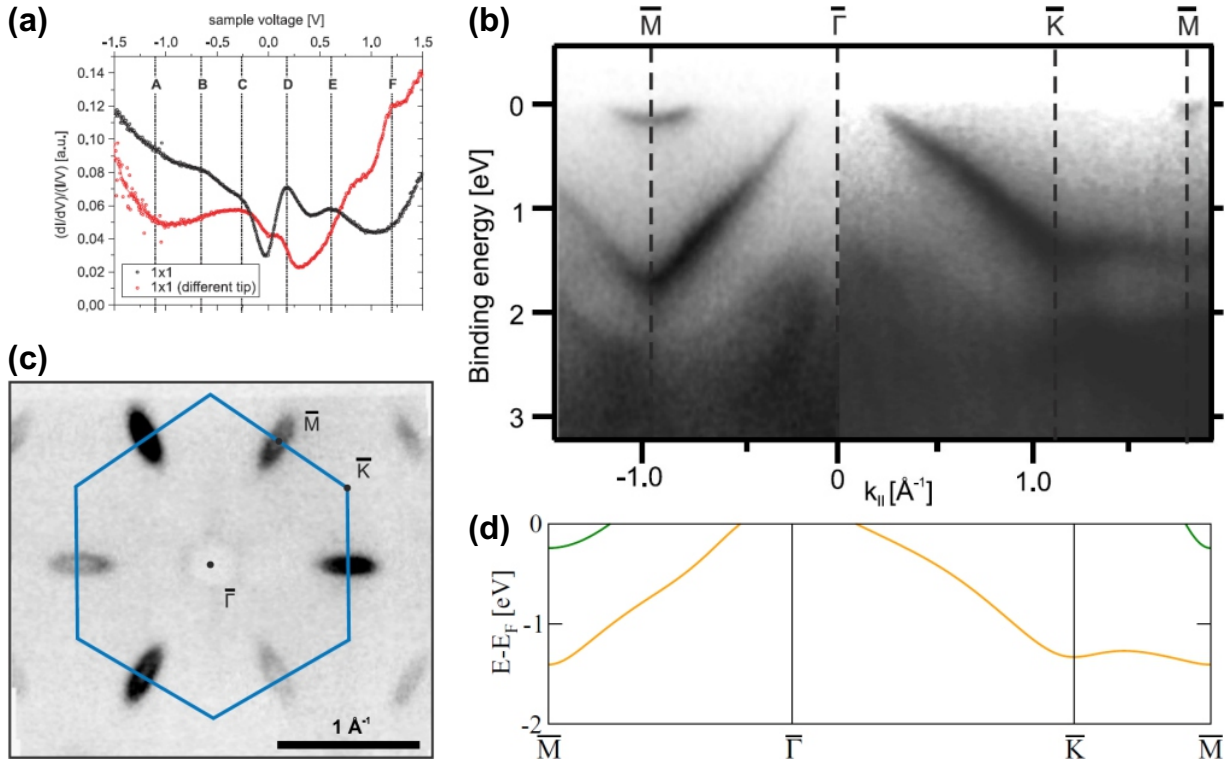

Figure 5.18.: (a) STS spectra of the Tb induced 1×1 monolayer. From [384]. (b and c) Band dispersion and Fermi surface, respectively, of the $TbSi_2$ monolayer as measured by ARPES ($h\nu = 100$ eV). From [69]. (d) Band dispersion of the $DySi_2$ monolayer obtained by calculations. The dispersion is representative also for other rare earth metals. From [362].

level [see figures 5.18 (b and c)]. At the $\overline{\mathrm{M}}$ points, there are highly anisotropic electron pockets. The electron-like character of these states is determined by the curvature of their dispersion, which is positive. If a negative curvature is observed, the state is hole-like. This is the case for the state around $\overline{\Gamma}$, which is only faintly visible on the Fermi surface due to matrix element effects, but clearly distinguishable in the dispersion plot. For comparison, a calculated band structure is shown in figure 5.18 (d). As already mentioned above, the agreement between theory and experiment is extremely good. From the theoretical data, it is apparent that also the hole pocket is sightly anisotropic, which is not as easily seen in the experimental data. It should be noted that, in contrast to the strong variations in the ARPES data available for rare earth silicide nanowires on Si(001) (see section 5.4.1), rather similar data are observed for the rare earth silicide monolayer on Si(111) not only by theory [67, 362], but also in experiment [67, 69, 360, 364].

A difference between the rare earth metals is that the diffusion of rare earth atoms into the bulk and the partial reagglomeration at the surface during annealing was reported for Gd and Tb [69, 381, 384, 385], but not for the other rare earth metals. This has to be taken into account when discussing dependences on the deposited rare earth amount, especially when substrates are reused for multiple preparations.

One very interesting aspect of the monolayer silicide is its influence on the Fermi level

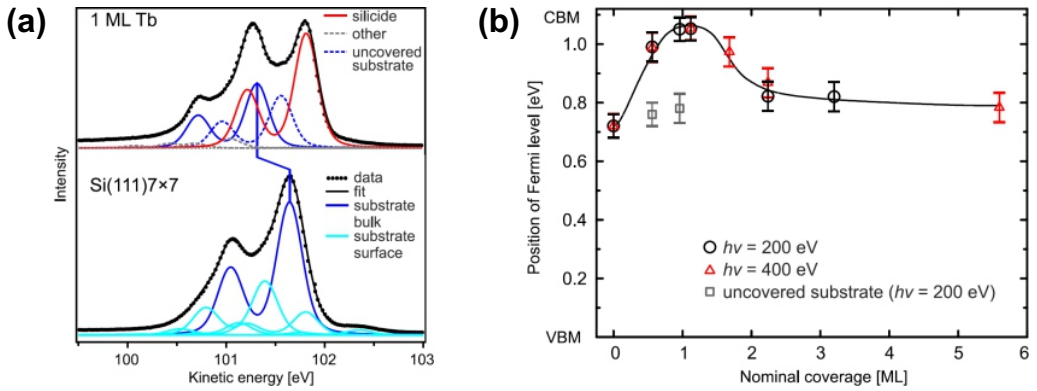

Figure 5.19.: (a) Si-2p photoemission spectra of the clean Si(111) 7×7 reconstruction and of the same substrate covered by a $TbSi_2$ monolayer ($h\nu = 200$ eV). From [69]. (b) Variation of the Fermi-level position in the band gap with the thickness of the hexagonal Tb silicide layer. From [69].

at the interface. The shifts of the bulk Si-2p component measured by XPS indicate a strong movement of the Fermi level towards the conduction band minimum corresponding to Schottky barrier heights below 0.1 eV on n-type Si [69–71, 367]. This extreme Fermi-level position is exclusive for the monolayer structure. For multiple layers, i.e. when the silicide forms with Si vacancies, the Schottky barrier heights known from contacts between bulk materials are recovered. Figure 5.19 shows these aspects exemplarily for Tb.

The reason for this band bending behaviour is the change of the silicide structure and the accompanying change of the density of states of the metallic silicide at the Fermi level [70, 71]. The monolayer silicide has only small electron and hole pockets at the Fermi level leading to a low density of states at the Fermi level [see figures 5.18 (a, b, and c)]. This low density of states results in a low density of metal induced gap states. Thus, the band bending is strongly influenced by the difference between the small work function of the rare earth silicide and the larger electron affinity of Si leading to Fermi-level positions close to the conduction band minimum. The multilayer silicide, in contrast, is characterised by a higher density of states at the Fermi level leading to a higher density of metal induced gap states [71, 362] and consequently a Fermi level closer to the centre of the Si band gap. A strong influence of defect states on the band bending can be excluded due to the good epitaxial growth.

Due to the low and uniform lattice mismatch between the hexagonal rare earth silicide and the Si(111) surface, the silicides always form as well ordered and two-dimensional layers on planar substrates. To reduce the dimension of the layers in one direction, vicinal surfaces may be used [386]. On such stepped surfaces, nanowire growth may occur due to the reduced width of the Si(111) terraces resulting in the growth of the two-dimensional structure preferentially along the step edges. Indeed, the formation of rare earth silicide nanowires was observed for Gd and Dy on stepped Si(111) surfaces [72, 385], but the only in depth studies are available for thin Er and Dy layers on Si(557) [73–75].

There, well defined nanowires with a uniform appearance, typical widths of 3 nm to 5 nm, and lengths sometimes exceeding 1 μm are observed [74], as shown in figure 5.20 (a). Despite

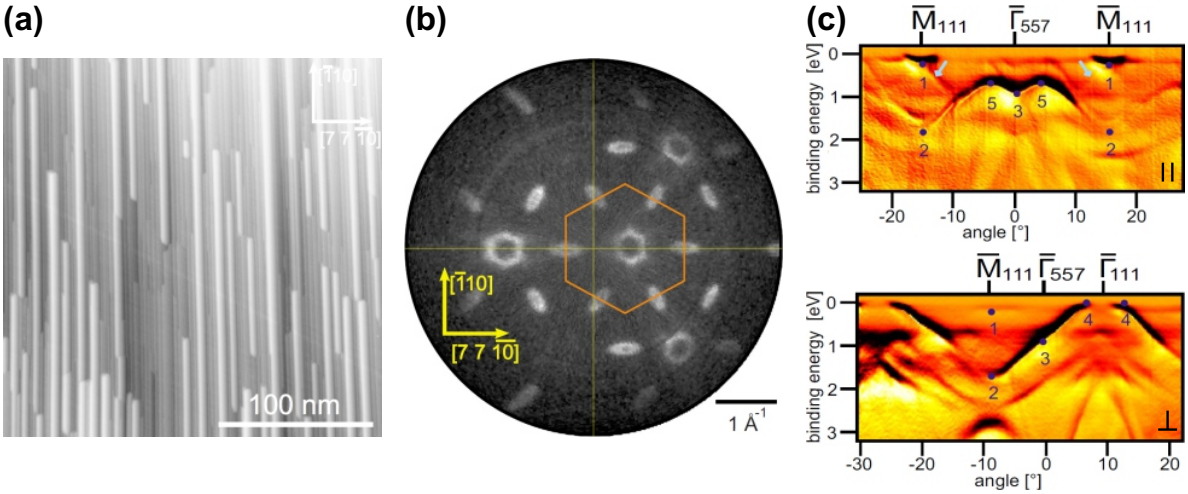

Figure 5.20.: (a) STM image of $DySi_2$ nanowires on Si(557). From [73]. (b) Fermi surface of $DySi_2$ nanowires on Si(557) ($h\nu = 41$ eV). From [74]. (c) Band dispersions of the $DySi_2$ nanowires on Si(557) ($h\nu = 41$ eV). From [73].

their strongly reduced width, the nanowires clearly show the two-dimensional electronic structure known from the two-dimensional monolayer on planar surfaces [see figures 5.20 (b and c) and 5.18 (b and c)]. Apparently, the hexagonal silicide monolayer also forms on the Si(111) terraces of the vicinal surface. This is consistent with observations made by STM, e.g. the nanowires show straight edges at their ends, which are typical for the monolayer on planar surfaces [see figure 5.17 (a)], and their inclination with respect to the surface normal agrees with the offcut angle of the Si(557) surface [73].

The nanowire formation leads to wider Si(111) terraces than observed on the clean surface [see section 5.1.2]. This effect should be reduced on vicinal surfaces with larger offcut angle and possibly also on vicinal surfaces with a different offcut direction. Narrower nanowires may than show stronger confinement effects, e.g. a one-dimensional electronic structure.

6. Experimental details

In this work, nanostructures on surfaces are analysed. This is not possible under ambient conditions and even at a pressure of only 10^{-6} mbar a surface is covered by one layer of adsorbates in about 1 s assuming a sticking coefficient of 1 [387]. Thus, UHV conditions with pressures below 10^{-9} mbar are needed as base pressure for the sample preparation and especially during time-intensive measurements to guarantee a stable sample.

The main part of this thesis is about STM, STS, XPS, and ARPES measurements. These were performed at two different UHV chamber systems. The STM set-up is situated at the TU Berlin and introduced in section 6.2. The photoemission experiments were performed with synchrotron radiation at BESSY II (Helmholtz-Zentrum Berlin), and the set-up is presented in section 6.3. At both systems, samples were prepared in the same way. This general preparation procedure is elucidated in section 6.1.

LEED measurements were performed at the same chamber systems as the STM experiments with an ErLEED 3000-D by Vacuum Science Instruments. This also applies for the RAS measurements, which used a transportable RAS set-up of the Leibniz-Institut für analytische Wissenschaften – ISAS – e.V. The image-aberration corrected FEI Titan 80-300 Berlin Holography Special TEM of the work group of Prof. Dr. Michael Lehmann (TU Berlin) was used for HRTEM imaging [388], and HAADF and EDX measurements were performed with a FEI Tecnai Osiris operating in its STEM mode at the Leibniz-Institut für innovative Mikroelektronik – IHP – in Frankfurt (Oder). Transport measurements took place in a UHV chamber system of the workgroup of Prof. Dr. Herbert Pfnür (Leibniz Universität Hannover) and Prof. Dr. Christoph Tegenkamp (then Leibniz Universität Hannover, now TU Chemnitz) [175]. They were performed with an Omicron LT Nanoprobe 4-tip STM. This instrument is equipped with a ZEISS UHV GeminiSEM column used for overview SEM imaging and for monitoring the positioning of the tips in transport experiments.

6.1. Sample preparation

The first part of the sample preparation is the preparation of clean substrates, which are the starting point of the second part, the nanostructure growth.

In the beginning, a Si sample is produced from a Si wafer by scratching the desired sample shape in the Si wafer with a diamond scriber and breaking this piece from the wafer. In this work, a large variety of different substrates were used. Most of them were n-type doped with P, but some of the planar Si(001), some of the Si(001) with 4° offcut towards [110], and the Si(557) substrates were p-type doped with B. The usual resistivity of the substrates was between 1 Ωcm and 100 Ωcm.

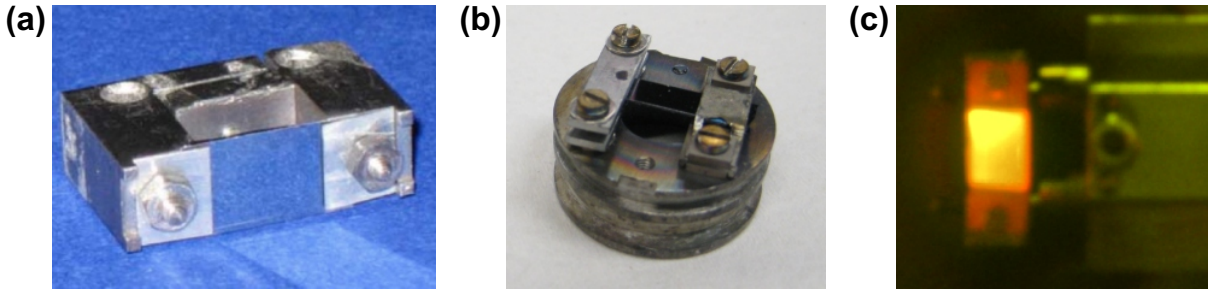

Figure 6.1.: (a) Sample holder used at the TU Berlin. The left and the right part are electrically isolated by ceramics. (b) Sample holder used for photoemission experiments at BESSY II. The right sample fixation stage is isolated from the rest of the sample holder by ceramics. (c) Photograph of a glowing Si sample, which was edited to show an orange glow as observed with the eye.

The Si samples are rinsed with ethanol and deionised water to remove coarse contaminations, e.g. dust, and possible oily residues before they are mounted in the sample holder. Different kinds of sample holders are used at the TU Berlin and at BESSY II, but both consist of two electrically isolated parts that are connected by the Si sample [see figures 6.1 (a and b)]. This enables the heating of the substrates by passing a current through them. During the initial assembly of the sample, great care is taken to avoid any contact between steel tools, which often contain Ni as an additive, and the Si substrates since such contacts may lead to Ni contamination of the surfaces which cannot be removed by our cleaning procedure. All parts of the sample holder with contact to the Si sample are thus made of Ta or Mo.

The samples are then transferred into the vacuum chamber system. There, they are heated up to 600 °C to 800 °C for about 12 h to desorb water and other volatile contaminations. Typically, a rather low temperature was used for vicinal surfaces to avoid the bunching of steps, which may occur at high temperatures, if the oxide layer desorbs already completely during the 12 h [389–392]. At any time during the heating, the pressure was kept below 10^{-8} mbar, so that good UHV conditions could be recovered rapidly.

The temperature of the substrate is controlled by a pyrometer (accuracy ±20 °C) during any heating. Every temperature was measured with an emissivity setting of about 0.7 at the pyrometer, even though the emissivity of Si varies strongly with temperature in the relevant infrared spectral range. This results in an underestimation and overestimation of low and high temperatures, respectively. It should be noted that the emissivity is depending on the doping of the Si substrate and also on possible overlayers, e.g. an oxide film [393]. Since the determination of the exact emissivity for every sample and temperature is not feasible, a constant emissivity setting was chosen.

After the initial degassing, the substrates are flash annealed up to 1150 °C to 1200 °C to remove the remaining oxide layers and possible carbide contaminations from the surface [394]. During the flash annealing, the sample is heated from the base temperature, at which the sample was held for 12 h, to a certain temperature for a short time. If the pressure remains at this temperature for 10 s below a chosen critical pressure, typically 2×10^{-9} mbar or lower, this temperature is increased in the next step by 50 °C. This procedure is repeated

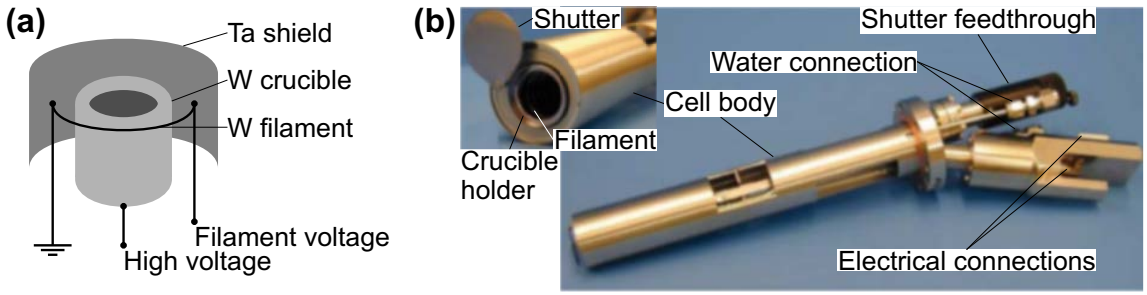

Figure 6.2.: (a) Schematic set-up of a homebuilt electron beam evaporator used for the evaporation of rare earth metals. (b) Commercial effusion cell from DCA Instruments Oy used for the evaporation of Si. From [397].

up to the above-mentioned end temperatures. Since a substrate may heat inhomogeneously [see figure 6.1 (c)], the measuring point of the pyrometer is adjusted to the hottest area of the sample during the flash annealing.

To achieve a well ordered surface with a low defect density, the sample is cooled down slowly with a rate of about 1 °C/s from a temperature above 800 °C. Other cooling recipes were also tried to achieve a higher surface homogeneity [317, 395, 396], but resulted typically in very similar surface morphologies as observed for the slow cooling from above 800 °C. The success of the preparation of a clean substrate was checked by STM at the TU Berlin and by XPS at BESSY II.

For the growth of nanostructures, rare earth metals are deposited on the clean substrates. The metals are evaporated from home-built electron beam evaporators [see figure 6.2 (a)]. There, electrons are released by thermal emission from a filament and then accelerated by a high voltage of about 500 V on a W crucible that holds pieces of the rare earth metal. The rare earth metal within the heated crucible then evaporates.

The thickness of the deposited rare earth metal film is determined by the deposition time and the deposition rate. This rate is measured prior to the nanostructure growth by a quartz crystal microbalance (accuracy 20 %) and may be adjusted by changing the acceleration voltage or the current between filament and crucible. Rates above 0.05 nm/min are usually chosen for nanowire growth. For the metal deposition, the sample is moved to the measurement position of the microbalance, and the pressure is typically below 10^{-8} mbar. This is achieved by prior careful degassing of the evaporators.

In this work, the rare earth metal coverages are given in monolayers (ML), with one monolayer defined by the surface atom density of the bare substrates [see section 5.1]. Such 1 ML Tb corresponds to a film thickness of 0.217 nm and 0.251 nm on Si(001) and Si(111), respectively. For vicinal substrates, the atom densities of the respective planar substrates are used.

During or after the metal deposition the sample is annealed at elevated temperatures to enable the nanostructure formation. Most of the time, the sample was annealed for 2 min after the metal deposition at room temperature since then there are only two preparation parameters left, the metal thickness and the annealing temperature, leading to a manageable parameter space. The annealing temperature is measured in the centre of the sample, where also the measurements are usually performed.

In addition to the bare nanowires, also the overgrowth of nanowires by Si was studied on Si(001) substrates. Si was evaporated with a commercial effusion cell, in which the crucible is heated directly by the radiation of a filament [see figure 6.2 (b)]. Due to the strong heat emission from this cell, even a water cooled quartz crystal microbalance does not allow the measurement of a reasonable deposition rate. Instead the rate was calibrated by Si homoepitaxy on Si(111). Samples of nanowires capped by amorphous or crystalline Si films are the basis for the *ex-situ* TEM experiments. Crystalline Si films may be grown by annealing during the Si deposition or by annealing the initially amorphous Si film.

Most substrates are reused multiple times, i.e. the substrates are cleaned by flash annealing after a measurement. Typically, a clean surface is recovered, but the defect density increases with time, so that this procedure cannot be used endlessly. In addition, the possible dissolving of rare earth metal atoms in the Si bulk during the flash annealing and their resegregation to the surface during the annealing have to be taken into account fo the thickness determination.

6.2. Experimental set-up at TU Berlin

In the following, the experimental set-up is discussed. Afterwards, the analyses of data obtained at this set-up is elucidated.

6.2.1. The ultrahigh vacuum system

A photograph of the set-up at the TU Berlin is shown in figure 6.3. The UHV chamber system consists of two main chambers, the preparation chamber (A) and the STM chamber (B). Connected to the preparation chamber is the load-lock, which is a small chamber that can be pumped rapidly and which is used for the transfer of samples into and out of the vacuum. The movement of the samples in the chambers is achieved by transfer rods (2) and a manipulator (3). Inside the preparation chamber is a sample garage (4), which can hold up to 5 samples.

The samples can be heated on the manipulator. For heating, the sample is usually moved to the left part of the preparation chamber, where a large window is situated (see inset in figure 6.3). Through this window the temperature of the Si substrate can be easily monitored with the pyrometer (5). The evaporators (6) are connected to the preparation chamber from below, and above them the quartz crystal microbalance (7) is mounted on a linear feedthrough to move it into and out of the beams of the evaporators. In the centre of the evaporator cluster flange a rotary feedthrough connected to a shutter is mounted. This shutter is used to interrupt the beam of the running evaporator before and after the deposition on the sample.

The UHV in the preparation chamber is maintained by an ion getter pump (9) and a Ti sublimation pump (10), which is used occasionally to reduce pressure maxima, e.g. after the transfer of new samples into the UHV. Those pumps cannot be started at ambient conditions. The initial pump-down after a venting of the chamber is done either via the load-lock with a turbomolecular pumping station (8), which has a membrane pump as roughing pump, or via the transfer chamber (C), where another turbomolecular pump (15)

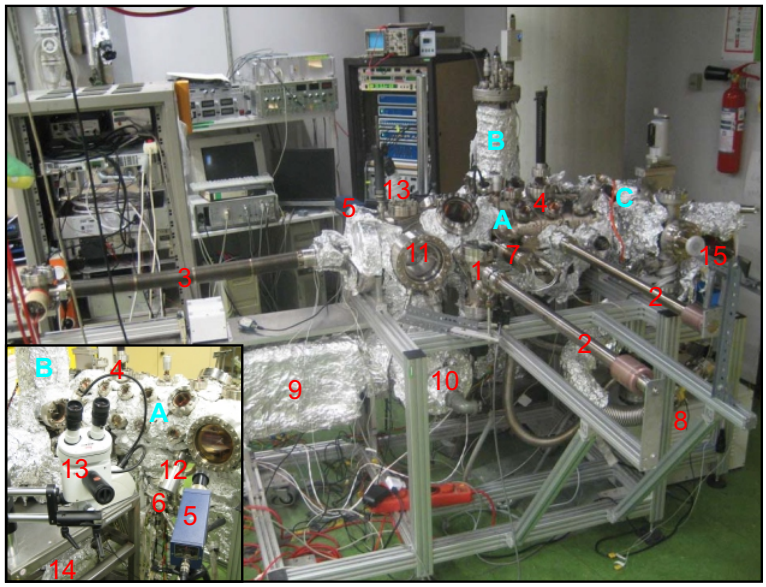

A Preparation chamber
1 Load-lock
2 Transfer rods
3 Manipulator
4 Sample garage
5 Pyrometer
6 Evaporators
7 Microbalance
8 Turbomolecular pump
9 Ion getter pump
10 Ti sublimation pump
11 LEED system
12 RAS window

B STM chamber
13 Visible-light microscope
14 Ion getter pump

C Transfer chamber
15 Turbomolecular pump

Figure 6.3.: Photograph of the chamber system at the TU Berlin. The most crucial parts are numbered and described on the right. The inset shows the chamber system from the other side, so that the evaporators and the RAS window are visible.

is connected. No turbomolecular pump should run during STM experiments since their vibrations disturb the measurement.

Also attached to the preparation chamber are the LEED system (11) and the RAS window (12). A special window with low strain is needed for RAS since an additional polarisation signal may be introduced by strained windows. The base pressure of the preparation chamber is typically below 5×10^{-10} mbar.

In the STM chamber, there is an even better base pressure below 10^{-10} mbar, so that measurements over several hours are possible. This chamber contains the STM, a tip garage for up to 12 tips and a tip heating stage (see sections 6.2.2 and 6.2.3). The STM chamber is also equipped with an ion getter pump (14) and a Ti sublimation pump (not shown), which is rarely used. If only the STM chamber is vented, it can be directly pumped with the turbomolecular pumping station. Helpful for the measurements is the visible-light microscope (13), which is used to monitor the approach of the tip to the sample.

6.2.2. The scanning tunnelling microscope

In the STM chamber, the stiff STM unit is suspended by soft springs to reduce the transfer of vibrations from the surroundings [see figure 6.4 (a)]. In addition, any vibrations of the system are damped with eddy-current retarders. This combination of damping systems makes STM measurements, which are extremely sensitive to vibrations due to the small tip-sample separation, possible on the fourth floor of the building. For the transfer of the sample or of tips, the STM has to be locked, which is achieved by a linear feedthrough that lifts the entire STM unit with a plate.

A close-up photograph of the STM unit is shown in figure 6.4 (b). The tip on the

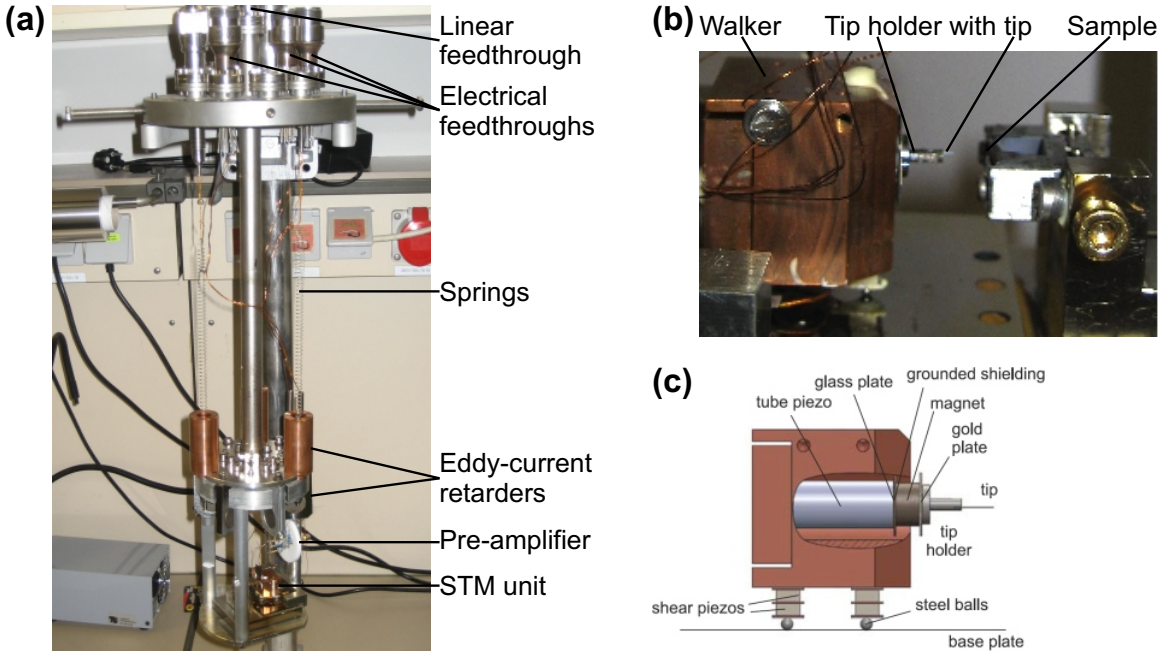

Figure 6.4.: (a) Photograph of the complete STM set-up with the STM unit locked. (b) Close-up of the STM unit. (c) Schematic drawing of the walker with the scanning piezo element visible. From [384].

magnetisable tip holder is held by a magnet on a tube piezo element that is mounted in a Cu block [see figure 6.4 (c)]. This Cu block is the so-called walker, because it can move over a steel base plate. The movement is achieved by stacks of shear piezo elements with steel balls under them. When a saw tooth voltage is applied to the shear piezo elements, the steel balls and consequently the walker stick to the base plate on the flank with low slope, but slip over the base plate on the high slope flank. Due to a different orientation of the shear piezo elements in a stack a two-dimensional movement is possible. In addition, the walker can be rotated, when not all shear piezo stacks are operated in the same way.

With the walker, the tip is coarsely approached to the sample until the tip and its mirror image in the sample nearly touch when viewed through the visible-light microscope. During the software regulated fine approach, the tip is moved towards the sample using the tube piezo element until a tunnelling current is measured or the tube piezo element is fully elongated. If no tunnelling current occurred, the tip is retracted and the walker approaches the sample by a distance smaller than the maximum elongation of the tube piezo element. This procedure is repeated until there is a tunnelling contact between tip and sample. The tunnelling current is taken at a gold plate between magnet and tip holder and already pre-amplified in the vacuum.

The scanning motion of the tip needed for imaging is also realised by the tube piezo element. Since high voltages are necessary for the deformation of piezo elements, a glass plate isolation and a grounded shield are situated between the tube piezo element and the magnet, so that no stray electric fields of the piezo elements disturb the measurement.

For the control of the STM, e.g. application of voltages and current measurement, and

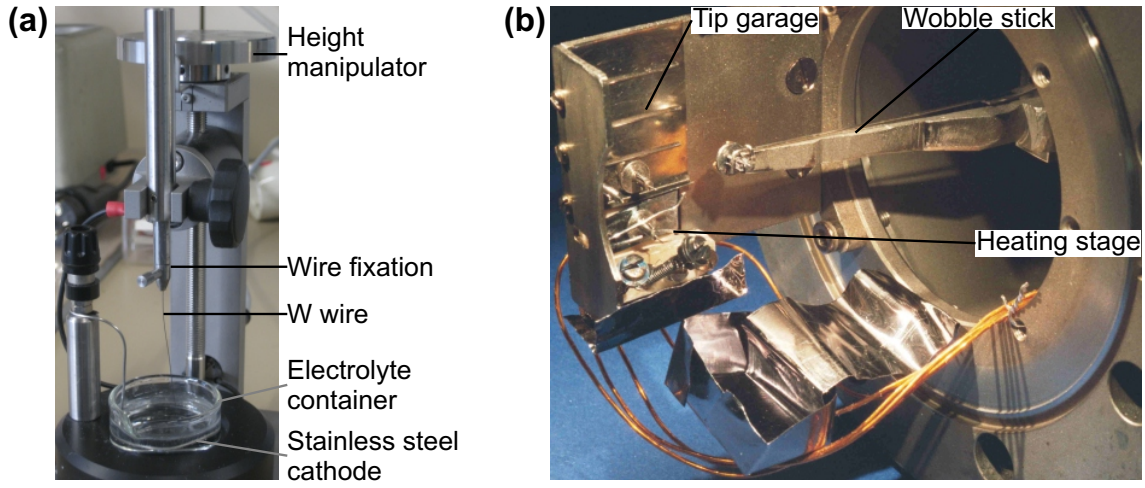

Figure 6.5.: (a) Photograph of the commercial W-tek tip etching tool made by Omicron NanoTechnology. (b) The tip garage with electron-beam heating stage for the storage and cleaning of the tips in UHV.

for data acquisition a commercial Nanonis SPM controller by SPECS was used. This system has a built-in software lock-in amplifier. This amplifier was used to measure the differential conductance simultaneously with the current during STS. For the calibration of the lock-in amplifier, the tip is retracted a bit, so that the modulation voltage only generates a capacitive current with 90° phase shift. Adjusting the phase to the highest signal in this configuration and subsequently shifting the phase setting by 90° allows to measure the pure differential conductance since the tunnelling current is in phase with the voltage modulation.

6.2.3. Tip preparation

Crucial for atomic resolution is a probe in the same dimension, i.e. an atomically sharp tip is needed. In this work, home made electrochemically etched W tips were used [398, 399]. For the etching, a commercial tip etching tool was mainly used [see figure 6.5 (a)].

Before the etching, a W wire with a diameter of 0.25 mm is annealed in a N_2 atmosphere to improve the material quality. Then, a piece of the W wire is fastened in the etching tool and immersed into 10% NaOH solution. To etch the W wire, a voltage of 5 V is applied between the wire and a ringlike cathode, which surrounds the wire. The etching occurs along the entire immersed wire segment, but is fastest at the liquid surface since the rest of the wire is partially shielded by sinking reaction products, e.g. $(WO_4)^{-2}$ [399]. This results in a strong necking-in of the wire at the liquid surface and ultimately in the breaking off of the lower part of the immersed wire segment. It is important to switch off the etching voltage rapidly after the break off since the upper part, which is used as a tip in STM, is blunted by further etching [398].

The apex is checked with a visible-light microscope, before the tip is rinsed in ethanol and deionised water to remove coarse contaminations, e.g. salts. Then the tip is spot-welded to a tip holder and once again checked under the visible-light microscope to exclude any

bending of the tip by accidental contact. The tips are transferred into the UHV on tip shuttles, which can carry up to three tip holders. Via the load-lock and the preparation chamber, the tip shuttles are moved into the STM chamber. There the tips are transferred with a wobble stick in the tip garage, in which up to twelve tip holders can be placed [see figure 6.5 (b)]. Below the tip garage, there is an electron beam heating stage, where the surface oxide of the tips is removed by electron bombardment before the tips are used in the STM.

A tip giving good resolution right from the start is very rare. Furthermore, most tips are unstable and may change during the measurement, especially in the beginning. Often, tips stabilise with time, so that patience is needed. The resulting tip may be good, but can also be blunt or have multiple micro tips, which are in tunnelling contact with the sample leading to multiple imaging of the structures on the sample. If the tip is not optimal, one can try to force changes of the tip. Typical methods used to force tip changes are from gentle to extreme: manual variation of the tunnelling voltage, applying voltage pulses of the same polarity, changing the polarity during a voltage pulse, and even crashing the tip into the sample. In general, everything is allowed that may result in a better tip, but it has to be kept in mind that the tip influences the obtained images and spectra. Especially, a tip may not be metallic any more after Si of the substrate was attached to the tip. A tip has to be changed when no tunnelling contact can be realised with it.

6.2.4. Data analysis

Recorded STM images can be viewed with the Nanonis Scan Viewer, which is part of the Nanonis Simulator package by SPECS. From this program, the STM images are usually exported into the WSXM software [400], which was used for data analysis, e.g. measuring of tip height profiles or calculation of two-dimensional Fourier transformations, and for data processing, e.g. subtraction of tilted backgrounds or application of filters. Great care was taken during filtering to avoid the production of artefacts.

STS spectra can be viewed by the Nanonis Data Viewer of the Nanonis Simulator package, and the positions, where the spectra were taken, can be derived with the Scan Viewer, which can display spectroscopy locations. Unfortunately, the STS data have to be transposed before they can be easily used in standard data analysing and visualisation software, and the spectra taken during an image have to be individually selected to show their location. This rather time intensive routine was accelerated by the self-written STSC program using LabView by National Instruments and the Nanonis Programming interface by SPECS.

In the STSC program, STM images can be opened and the locations of all spectra that were taken during the acquisition of an image are shown automatically. In addition, the spectra can be displayed and averaged. Such an averaging is needed, since every individual spectrum is usually noisy due to the limited time available for a measurement before the drift of the tip becomes too large, e.g. the tip may drift from a position above a wire onto the substrate. The simultaneous averaging of conductance and differential conductance is possible, so that data consistency is easily secured. Every spectrum has to be included in the average spectrum individually. It was refrained from an implementation of mass averaging since the user should evaluate every spectrum. Strongly deviating spectra, e.g. spectra that show large jumps in the conductance graph due to tip changes, should be

excluded from the average. The files generated by the STSC program are easily imported in other data analysing and visualisation programs.[1]

For the further processing of STS data, the QtiPlot software by IONDEV SRL and the Origin software by OriginLab Corporation were used. Mainly two steps were taken, at first current offsets were subtracted, and then the normalised differential conductance was calculated. If only few spectra were averaged and the conductance graph was still rather noisy, the conductance graph had to be smoothed to circumvent strong oscillations of the normalised differential conductance around the Fermi level.

LEED images were imported into the SPIP software by Image Metrology. This software was used to extract intensity profiles and for image processing, e.g. converting into grey scale images and smoothing images, so that the grid structure of the fluorescence screen is washed out.

6.3. Experimental set-up at BESSY II

This section begins with an introduction to synchrotron radiation. Then the photons are followed from their generation in the undulator through the beamline into the measurement chamber, where they interact with the sample. This chamber is part of the UHV set-up used for this thesis, which was provided by the workgroup of Prof. Dr. Karsten Horn (Fritz-Haber-Institut of the Max-Planck-Gesellschaft) and the workgroup of Dr. Christian Papp (Friedrich-Alexander-Universität Erlangen-Nürnberg). After decribing this UHV chamber system, the photoelectron analyser is discussed and the processing of the measured ARPES and XPS data is presented.

6.3.1. Synchrotron radiation by BESSY II

In this work, nanostructures on surfaces are studied. The nanostructures only cover a part of the surface and they degrade with time even in UHV. Thus, a high intensity light source is needed for photoemission experiments to enable measurements in a reasonable time. Here, synchrotron radiation provided at BESSY II was used. Synchrotron radiation is the electromagnetic radiation that is emitted by charged particles when they are accelerated radially, e.g. in a magnetic field by a Lorentz force. Such particles emit electromagnetic radiation in a broad spectrum, so that synchrotron radiation offers the additional benefit of a tunable photon energy when using a monochromator. Thus, core-level photoemission and surface sensitive ARPES measurements are possible with the same set-up. The main drawback of synchrotron radiation is that it is only available at dedicated facilities making data production only possible during granted measurement periods, so-called beamtimes.

Synchrotron radiation is calculable leading to its use in metrology [401,402]. The maximum photon flux of the radiation along a tangential axis is observed close to the critical photon

[1] Other self written software include a grid spectroscopy module and a tip height surveillance program that can track the drift over a long time period, e.g. a weekend, and automatically moves the walker away from the sample, if a crash of the tip into the sample is imminent (if the tube piezo element is fully retracted and a high tunnelling current is measured).

energy

$$E_{\mathrm{C}} = \frac{3e\gamma^3\hbar c^2 B}{2E} \tag{6.1}$$

with the Lorentz factor $\gamma = (1 - v^2/c^2)^{-1/2}$ (v velocity of the charged particle in the laboratory reference frame), B the magnetic field, which accelerates the charged particle, and $E = mc^2$ the total energy of the charged particle (m is the relativistic mass of the charged particle) [403, 404]. The critical energy increases with increasing velocity, with decreasing rest mass of the charged particle, and with increasing magnetic field. Half of the radiated power, which scales with m^{-4}, comes from photons with an energy smaller than the critical energy [403]. To have an widely usable radiation source with high photon output, electrons are used due to their low rest mass, and the critical photon energy is often in the range of keV. For such critical photon energies, the electron must have energies in the range of GeV corresponding to velocities very close to the speed of light.

At BESSY II, the electrons are generated in an electron gun and accelerated by a linear particle accelerator, a radio frequency cavity, to 50 MeV, before they are guided into the synchrotron. In the synchrotron, the electrons are further accelerated in a radio frequency cavity, but they are directed back to the entrance of the cavity by dipole magnets. The strength of the dipole magnets is increased synchronously with the energy of the electrons, so that the electron path stays constant. At an energy of 1.7 GeV, the electrons are injected from the synchrotron into the storage ring, where they move on an approximately circular path by bending dipole magnets. At these bending magnets and at various insertion devices situated at the straight segments between bending magnets, synchrotron radiation is generated for experimental use. The energy lost to the radiation is restored to the electrons by a radio frequency cavity. Thus, the electrons have a constant energy in the storage ring, and the field of the bending magnets can remain constant. With time, electrons are lost in the storage ring, e.g. by collisions with residual gas atoms in the UHV. BESSY II is operated in the top-up mode, i.e. electrons are injected every few minutes to replace lost ones leading to an approximately constant beam current in the storage ring and, consequently, a constant photon flux at the experiment. The above and further information on BESSY II, e.g. its dimensions or the bunched structure of the electron current, is available on the website of the Helmholtz-Zentrum Berlin [405].

The synchrotron radiation is generated by relativistic electrons. In the electron reference frame, which moves with the electrons, the radiation is emitted in the pattern known from dipole antennas [see figure 6.6 (a)]. In the laboratory reference frame, this radiation pattern changes drastically. The radiation is now mainly emitted into a cone with a low angular width scaling with the inverse Lorentz factor [see figure 6.6 (a)]. Not only the radiation pattern is different in the laboratory reference frame, but also the spectral composition of the radiation changes drastically. Due to the large velocity of the electrons in the laboratory reference frame, the radiation emitted by the electrons is strongly Doppler shifted [403].

In this work, the radiation of an insertion device, an undulator, was used. An undulator is a periodic magnetic structure, which leads to an oscillating movement of the passing electrons [see figure 6.6 (b)]. In an undulator the amplitude of this oscillation is small, so that the radiation cones overlap and interference effects are observed. To characterise an

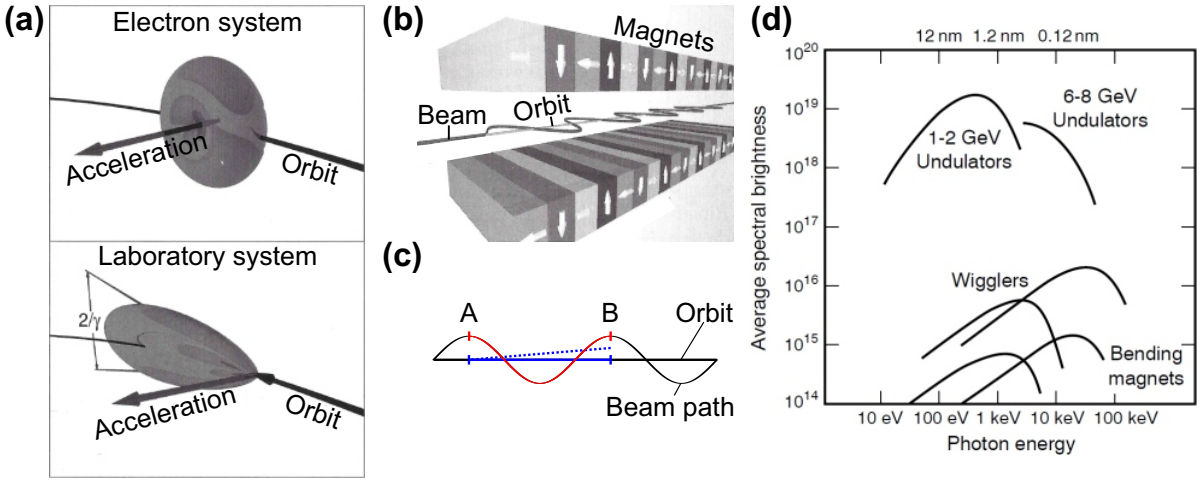

Figure 6.6.: (a) Radiation pattern of a relativistic electron that is accelerated in a magnetic field in the reference frame of the electron (top) and in the laboratory reference frame (bottom). Adapted from [404]. (b) Schematic of the electron beam path in an undulator. Adapted from [404]. (c) Illustration on the constructive interference in an undulator, which will be observed if the phases of the photons emitted at the points A and B match. The optical path difference is approximately given by the difference of the path length of one oscillation of the electron beam (red) and the photon path length (blue), which depends on the emission angle (compare dotted and continuous blue lines). (d) General trends of the spectral brightness, i.e. the total average photon flux in an energy interval of 0.1% per area and divergence of the electron beam, for synchrotron radiation generated by different magnetic structures. From [403].

undulator, the dimensionless periodic magnet parameter K is defined as

$$K = \frac{eB_0\lambda_\mathrm{U}}{2\pi m_0 c} \tag{6.2}$$

with B_0 the amplitude and λ_U the period of the oscillating magnetic field, and m_0 the free electron rest mass [403]. Typical values of K are lower or in the order of 1 for an undulator.

For constructive interference in the undulator, the phases of the radiation emitted after every full oscillation of the electron have to match. Since the electrons move approximately with c, this implies that the difference between the path lengths of one oscillation of an electron and the photon, which depends on the emission angle, has to be a multiple of the photon wavelength [see figure 6.6 (c)]. In general, the fundamental wavelength of the photons emitted by an undulator is given by:

$$\lambda_\mathrm{Ph} = \frac{\lambda_\mathrm{U}}{2\gamma^2}\left(1 + \frac{K^2}{2} + \gamma^2\theta\right), \tag{6.3}$$

when the radiation is observed under the angle θ with respect to the orbit. This fundamental wavelength of an undulator can be varied. Changing the vertical distance between the magnets modifies the magnetic field, therewith K, and consequently the fundamental wavelength. Similar as for other optical interference objects, the number of periods N

influences the emitted radiation. The bandwidth of the emitted radiation scales with N^{-1} and the on-axis photon flux with N^2, while the integrated photon flux scales only with N, i.a., since the angular width of the emittance cone scales with $N^{-1/2}$ [403]. Typical numbers of periods are in the order of tens in storage rings, so that the electric field of the radiation is rather weak and does not influence the electrons. The polarisation of the synchrotron radiation will be linearly horizontal if the undulator is build as depicted in figure 6.6 (b).

Not only photons with the fundamental wavelength are observed, but also higher harmonics. These higher harmonics are used to expand the spectral range of an undulator to higher photon energies. Interestingly, even order harmonics are not observed parallel to the orbit in contrast to the uneven order harmonics [403]. In general, an increasing K parameter leads to stronger higher harmonics, but if the K parameter of a magnetic structure is too large (> 1), the periodic magnetic structure will not be an undulator any more, but a wiggler. In a wiggler, the radiation cones do not overlap completely and interference effects are negligible, so that the emitted radiation spectrum is similar to that of bending magnets, e.g. the angular width of the emittance cone is the same, but has a higher photon flux due to the multiple sources.

In figure 6.6 (d) a comparison of the emitted synchrotron radiation of the different magnetic structures is shown. The broad spectrum of a bending magnet is constant for constant electron beam parameters. While the spectrum of a wiggler is also always broad, it may be tuned by varying the magnetic field. The shown undulator spectrum is the envelope of the maxima of undulator spectra with varying undulator gap for one specific harmonic. A single undulator spectrum is characterised by a narrow peak when one specific harmonic is considered. Further information on synchrotron radiation, e.g. on the influence of the electron beam parameters on the undulator spectrum, is found in references [403, 404].

6.3.2. The beamline

The photoemission experiments were mainly performed at the UE56/2 PGM-1 beamline of BESSY II and once at the UE56/2 PGM-2 beamline. Both beamlines use the same insertion device, the undulator UE56/2, and have a similar set-up, so that only the PGM-1 beamline is discussed.

The photons are generated by an APPLE II type double undulator. Here, APPLE stands for advanced planar polarised light emitter. By dividing the magnetic structure of an undulator in four parts, which can be individually shifted with respect to each other, various polarisation states of the produced light can be realised [406]. In this work, only linear horizontally polarised light was used, i.e. the electric field always had a parallel and a perpendicular component with respect to the sample surface due to the orientation of the sample. Unfortunately, only one half of the undulator was allowed to be used, and its gap must not be too small, otherwise the injection efficiency would drop too low and the top-up mode of BESSY II would not be maintained. This reduced the possible intensity and restricted the minimum photon energy to 62 eV.

The set-up of the beamline is shown in figure 6.7. Since all materials have strong absorption and a refractive index only slightly smaller than 1 in the X-ray regime, no lenses or similar optical elements used for visible light can be used. Instead mirrors are utilised since they reflect the X-rays totally under grazing incidence because the vacuum is the

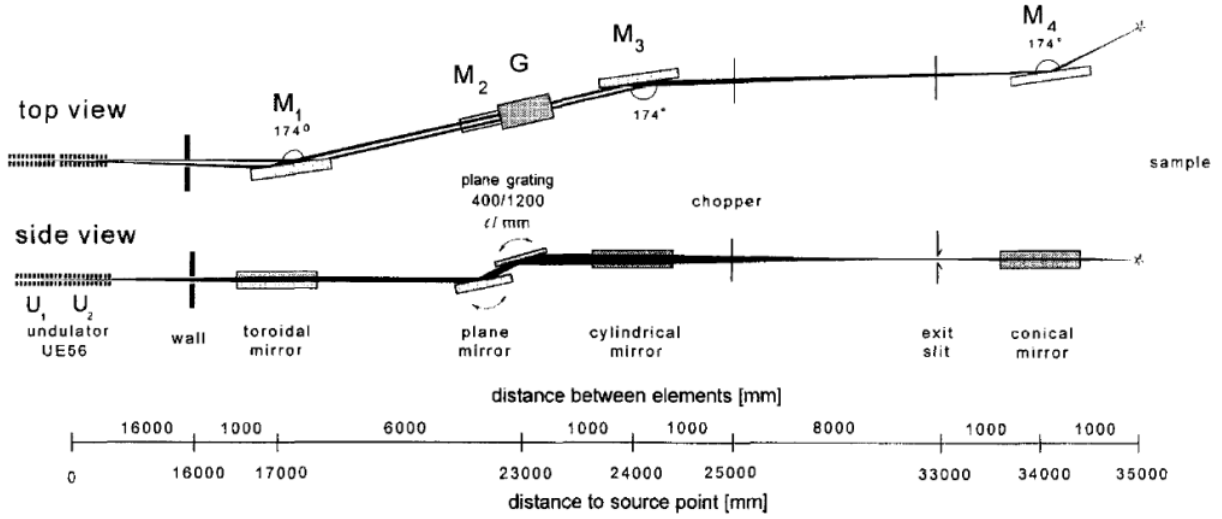

Figure 6.7.: Optical layout of the UE56-PGM beamline at BESSY II. The UE 56/2 PGM-1 beamline has presumably the same set-up, but the chopper is not used. From [407].

optically thicker medium.

The synchrotron radiation generated by the undulator is horizontally focussed on the sample and vertically collimated by the toroidal mirror M_1. The mirror M_2 deflects the beam vertically on the plane reflection grating, at which the collimated beam is diffracted leading to a vertical colour dispersion. In this work, the grating with 400 lines/mm was used for a higher photon flux.

The use of a collimated beam in the monochromator enables the relatively free choice of a fix-focus ratio (c_{ff}) without changing the optical elements behind the grating [407]. This fix-focus ratio is given by the division of the cosine of the incidence angle by the cosine of the diffraction angle. A high value enables a higher energy resolution while at low values the intensities of higher order beams are suppressed. Typically, a fix-focus ratio of 2.25 is used at the UE56/2 PGM-1 beamline, but a high background by higher order radiation was observed in this work for this value, so that the fix-focus ratio was reduced to 1.30.

The collimated beam is then vertically focussed on the exit slit by the cylindrical mirror M_3. Due to the diffraction by the grating, the vertical position of the focus spot depends on the photon energy, and only light within a narrow energy range transmits through the exit slit. The dispersive beam is then vertically refocussed by a conical mirror M_4. In the focus, the spot size is about 90 μm horizontally and vertically given by the exit slit size. Ideally, the sample is exactly positioned in this focus during a measurement.

6.3.3. The ultrahigh vacuum system

The general set-up of the UHV system used at BESSY II is similar to the one at the TU Berlin [see figures 6.8 (a and b)]. There is a UHV chamber for the photoemission experiments and a separate one for the sample preparation. The base pressures in these chambers is typically about 2×10^{-10} mbar. An additional chamber is used for sample storage, but there the pressure is at best in the upper 10^{-8} mbar range, so that no clean

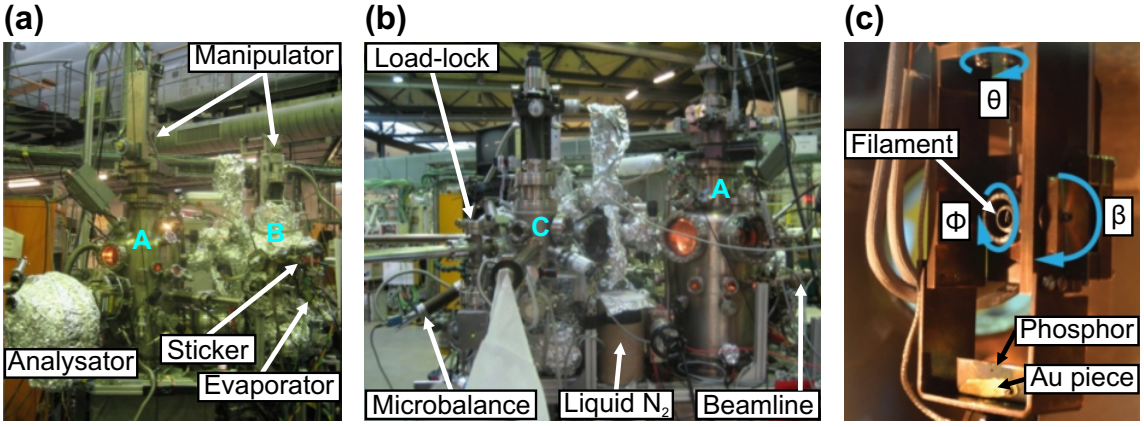

Figure 6.8.: (a and b) Photographs of the UHV set-up at BESSY II taken from different perspectives. The letters A, B, and C mark the measurement chamber, the preparation chamber, and the sample garage chamber, respectively. (c) Photograph of the measurement manipulator head. The rotations along β and θ are possible during a measurement, while the rotation along ϕ is only possible in between measurements by taking the sample from the manipulator and remounting it under a different angle. A filament can be used to heat the sample with an electron beam, but was not used in this work. From [408].

samples should be stored there. Attached to the sample garage is the load-lock for the transfer of samples into and out of the vacuum.

The sample is heated on the manipulator in the preparation chamber. In contrast to the set-up at the TU Berlin, the contacting of the sample is not included in the manipulator. Instead, two electrical Cu contacts of the so-called sticker can be moved onto the sample holder by a linear feedthrough. Soft Cu is used as contact material since it can be deformed by the wobble stick in the preparation chamber, so that the contacts can be fitted to the always slightly changing geometries. The temperature is monitored by the same pyrometer as used at the TU Berlin. Small differences in the measured temperatures may occur between the two set-ups since the sample is monitored through different windows and the measurement point of the pyrometer could not always be moved to the sample centre at BESSY II due to the Cu contacts interrupting the line of sight.

The same evaporators as at the TU Berlin are used at BESSY II. Again, the deposited metal amount is known by the deposition time and the prior determination of the deposition rate with a quartz crystal microbalance. No shutter is situated between the manipulator with the sample and the evaporator, but the manipulator can be rotated, so that the sample faces the evaporator only during deposition time. The necessity of this rotation for a well-defined metal coverage makes a annealing of the sample during the deposition unfeasible. Instead, all samples were annealed after the metal deposition.

The measurement chamber is equipped with a manipulator that enables the translation of the sample in all three spacial dimensions and a rotation of the sample around three orthogonal axes [see figure 6.8 (c)]. For a measurement, the sample is moved, so that it approximately faces the analysator (normal emission geometry), i.e. the sample normal is rotated by about 53° with respect to the incoming photons. In this position, XPS

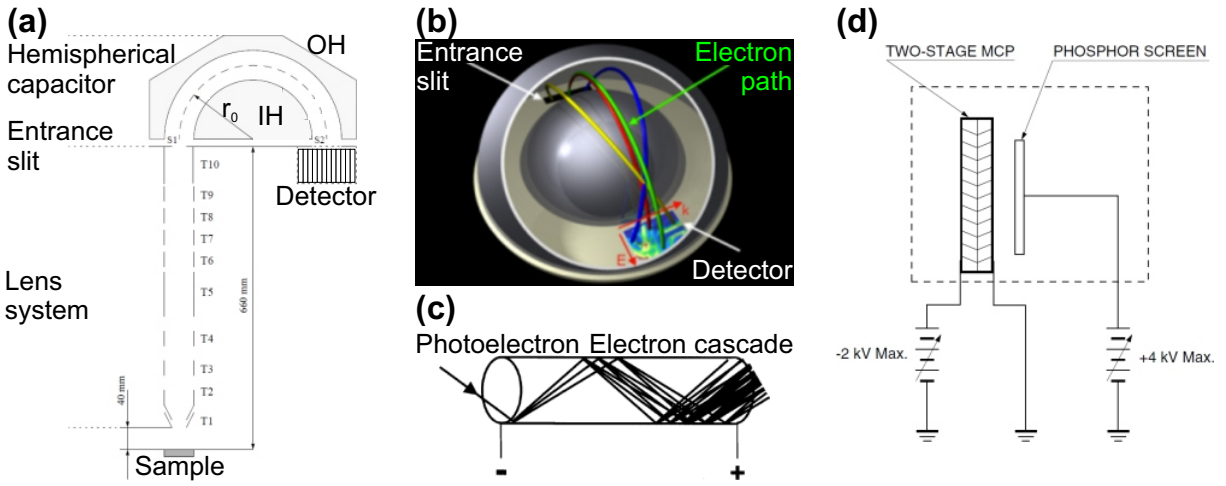

Figure 6.9.: (a) Schematic view of the PHOIBOS 100 hemispherical analyser by SPECS as seen from the side. IH is the inner hemisphere, OH the outer one, and $r_0 = 100$ mm the nominal capacitor radius. Adapted from [409]. (b) Illustration of various electron paths through the hemispherical analyser. From [410]. (c) Electron multiplication in a channel. From [404]. (d) Schematic set-up of the microchannel plate (MCP) detector. The phosphor screen is photographed by a CCD detector. From [411].

measurements are performed. For ARPES measurements, the sample is usually rotated around β and θ, so that the $\overline{\Gamma}$-point is in the centre of the measurement region. A dispersion plot along one direction is taken at once because of the two-dimensional detector (see section 6.3.4). For the measurement of three-dimensional data sets, the sample is rotated in β.

In addition to the sample holder stage, a Au piece and a phosphor are mounted on the manipulator head. The Au piece can be used to calibrate the Fermi level and the phosphor is needed for the alignment of the entire chamber system. In the measurement chamber, a cooling trap operating with liquid N_2 was routinely used to reduce the pressure and enable longer measurements. A reduction of the thermal broadening in the photoemission data can be achieved by cooling the sample, but this cooling may lead to photovoltage effects due to the reduced conductivity of the Si substrate.

6.3.4. The electron energy analyser

The central part of the photoemission measurement system is the PHOIBOS 100 hemispherical energy analyser by SPECS. This analyser consists out of three main parts: the lens system, the hemispherical capacitor, and the electron detector [see figure 6.9 (a)]. Between lens system and hemispherical capacitor, the entrance slit to the hemisphere is situated centred at the nominal capacitor radius. This slit is horizontally in the measurement geometry, i.e. aligned along the viewing direction of figure 6.9 (a).

The electrons emitted from the sample are collected and focussed on the entrance slit by the lens system. This entrance slit is imaged on the electron detector by the hemispherical capacitor. In the hemisphere, slower electrons with lower kinetic energy are more strongly

deflected, so that they arrive closer to the inner hemisphere on the electron detector [see figure 6.9 (b)]. The electrons with the pass energy (E_{pass}) arrive at the nominal capacitor radius at the detector,. The pass energy can be varied and determines together with the exit slit width of the monochromator, the possible energy resolution. Decreasing pass energies lead to better resolution. The photoelectrons are decelerated or accelerated by the lens system, so that different initial kinetic energies may correspond to the pass energy.

There are two different focusing modes of the lens system. In the so-called XPS mode, all photoelectrons emitted from the same point of the sample are focussed on the same point on the entrance slit. Here, the width of the intensity observed on the detector in the direction perpendicular to the energy axis depends on the width of the focus spot and, especially, on how well the system is aligned. In the ARPES mode, the electrons are manipulated in such a way that those with same initial parallel momentum are imaged at the same spot on the detector. Since a two-dimensional detector is used, an energy range is measured simultaneously in XPS mode and a large range of the dispersion along one direction is obtained at once in ARPES mode leading too better data quality, e.g. due to better statistics, when compared to data taken by using a point detector.

The first part of the detector is a microchannel plate stack, which multiplies the photoelectrons arriving at the end of the hemisphere. In the simplest case a microchannel plate is a semiconductor plate with holes, which have diameters in the μm region. Between both sides of the plate a high voltage is applied, so that electrons gain much energy when passing through a hole and can create multiple secondary electrons when they hit the side wall of a hole [see figure 6.9 (c)]. To guarantee several multiplication processes, the holes are not perpendicular to the plate surface, but slightly tilted. To enable larger multiplications, microchannel plates can be stacked, but with each additional plate lateral resolution is lost, since the electrons coming from one hole of a plate may enter multiple holes in the next one. After multiplication, the electrons are accelerated onto a phosphor screen, which is monitored by a CCD detector [see figure 6.9 (d)].

The data acquisition software, which includes the control of both the analyser and the manipulator, is based on a LabView software package written by Eli Rotenberg and Aaron Bostwick at the Advanced Light Source at Lawrence Berkeley National Lab [408].

6.3.5. Data analysis

IgorPro by WaveMetrics Inc. with the FITS7 extension, i.a. by Eli Rotenberg (Lawrence Berkley National Laboratory), Jonathan Denlinger (Lawrence Berkley National Laboratory), and Larry Hutchinson (WaveMetrics Inc.), was used to view and analyse all photoemission data.

Overview and valence band XPS spectra are only used for qualitative purposes, e.g. for a determination if the sample is oxidised. In contrast, Si2p core-level spectra were least squares fitted. Spin-orbit split Voigt profiles were used to include lifetime broadening, which gives a Lorentzian shape, and instrumental broadening, which is assumed to be Gaussian. A constant Lorentzian width of 0.07 eV to 0.10 eV (full width at half maximum) was used for all peaks in a spectrum. The Gaussian widths varied for the different components of a spectrum and laid between 0.30 eV and 0.40 eV unless specified otherwise. To reduce the number of fit parameters, a fixed spin-orbit splitting of 0.60 eV and a fixed intensity

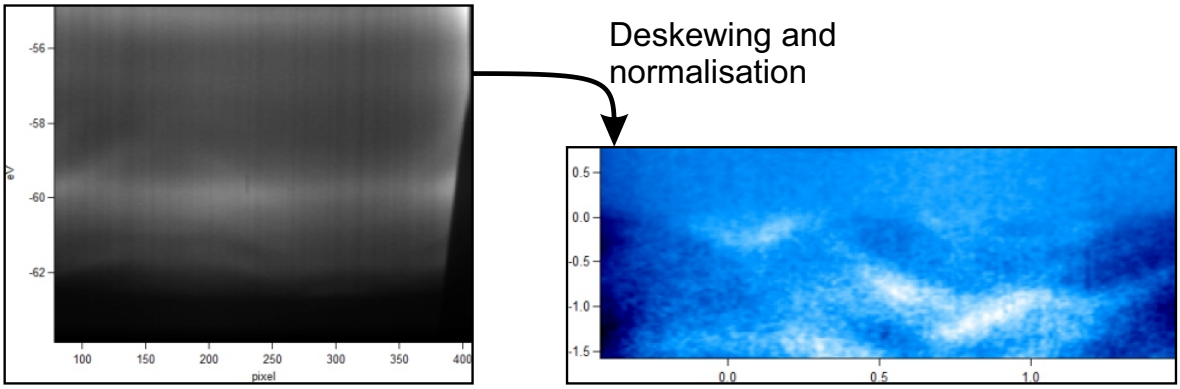

Figure 6.10.: Screenshots of dispersion plots viewed in IgorPro before (left) and after (right) the data processing. The vertical axes represent the kinetic energy axes. Both axes were inverted during the data processing.

ratio of 2 : 1 were used. Constant and Shirley-type backgrounds were considered [412]. The more sophisticated Tougaard-type backgrounds were not used since they are qualitatively similar to Shirley type backgrounds when the detailed energy electron loss function is unknown, as is the case for the rare earth silicide nanostructures [135, 413]. No asymmetric Doniach-Šunjić line shapes had to be considered for quantitatively good fits [414], which is consistent with previous findings [215, 228].

For the fitting, the IgorPro FitXPS procedure by Han-Jin Noh (Chonnam National University) was used, but had to be expanded to accommodate seven spectral components, which is needed for the clean Si(001) surface [228]. While this procedure in principle allows for the software assisted optimisation of fit parameters, most parameters were mainly optimised by hand. For most samples, Si2*p* spectra were taken with different photon energies. There, the single spectra were fitted individually, but the same spectral composition was used for all spectra of the same sample, i.e. great care was taken that the spectral components have the same energy shifts ($\Delta E = \pm 0.01$ eV) independent of the photon energy.

The analysis of ARPES data is a rather delicate process. While the hemispherical analyser allows for the measurement of two-dimensional data, the mapping of the momentum and energy is not straight forward because of distortion effects. In general, a rectangular dispersion section is imaged as a trapezium with bent energy contours. The initially measured and the dispersion extracted in the end are shown together in figure 6.10.

Starting with the measured data, the kinetic energy axis is inverted as the first step. Then the energy bending is corrected. Ideally, this is done by fitting the Fermi edge for every energy distribution curve, which is possible for metal samples since the incoherent contribution of photoelectrons enables the observation of the Fermi edge in the complete $\boldsymbol{k}_{||}$-space. Here, this was done by eye and checked by the appearance of the dispersion plot, which should be symmetric with respect to $\overline{\Gamma}$. The correction of the trapezium-like distortion can be done more reliably. The dispersion plots show straight lines of reduced intensity [see figure 6.10]. These lines have to be perfectly vertical after the correction.

No dispersion plots rotated with respect to the edges of the measured data cuboid can be displayed with IgorPro, but the complete data set can first be rotated, so that the high

symmetry directions are parallel to the edges of the new data cuboid. During this step the measured angle is converted in $\boldsymbol{k}_{||}$ by specifying the photon energy. This conversion is checked and often corrected using the known dimensions of the first Brillouin zone.

The most interesting data region is the one close to the Fermi level. Unfortunately, the bands in this region are often rather weak compared to the intensity of energetically lower lying bands, e.g. of the Tb-4f electrons. To highlight this region close to the Fermi level, a background is subtracted using a self written IgorPro procedure. For this purpose, the data cuboid is cut, so that regions without intensity or with uncharacteristically large intensity are not included any more, e.g. the rightmost part of the original data shown in figure 6.10 would be excluded. Then the average energy distribution curve of this data cuboid is calculated. The average energy distribution curve is subtracted from each individual energy distribution curve at a specific $\boldsymbol{k}_{||}$, after it was weighted by the mean value of this individual energy distribution curve. Due to this weighting step during the background subtraction, no low intensity lines are observed any more [see figure 6.10]. While dispersion plots processed by the above described procedure are shown most of the time, the background can also be reduced by using a division instead of a subtraction or by using this procedure for momentum distribution curves instead of energy distribution curves. In general, those methods result in qualitatively similar dispersion plots with negligible variations of the derived dispersion curves.

From the dispersion plots, the effective masses of some bands are extracted. When it was possible, this was done using the data without background subtraction by fitting the intensity maxima of the band observed in energy distribution curves for specific $\boldsymbol{k}_{||}$. Otherwise the background was subtracted or the contour of the band was used to approximate the dispersion of the band. The course of the obtained points is then fitted by a parabola and the effective mass is calculated with respect to the mass of the free electron m_0.

All shown energy surfaces, e.g. Fermi surfaces, use background subtracted dispersion data since the low intensity lines greatly disturb the appearance of these surfaces often leading to artefacts that appear as one-dimensional structures.

Part II.

Results and discussion

In the following, the results of this thesis are presented and discussed, but first the main objectives of this thesis are briefly summarised.

There was no data on Tb induced structures on Si(001). Thus the initial question was: Do nanowires similar to the ones observed for other rare earth metals form as was predicted [78]? Answering this question positively leads to multiple other questions. Which dimensions do the nanowires have and how does one prepare these nanowires, e.g. is there a minimum annealing temperature needed or is there a maximum Tb coverage up to which nanowires form?

The prediction of Tb nanowires on Si(001) is based on a structure model that fits only when using lattice parameters of hexagonal rare earth disilicides with Si vacancies [78], which may not be present in the nanowires. In this work, this problem is not only elucidated by having a look from above on the nanowires with STM, but also by having a look at the inner structure of the nanowires with HRTEM. Moreover, it was up to now unknown if the nanowires are stable with respect to the overgrowth with Si.

Not only the atomic structure of the nanowires is not definitively known, but also their electronic structure is under debate. There are indications for a one-dimensional electronic structure [80, 84, 85], but those are partially contradicting and there were no ARPES data covering the complete first Brillouin zone.

Only one material combination was used to study the rare earth silicide growth on vicinal Si(111) surfaces up to now, Dy silicides on Si(557) [73, 74]. Nanowires with widths of only about 5 nm and lengths up to 1 μm formed, but still showed a two-dimensional electronic structure. One of the aims of this thesis is to expand these initial studies using Tb as rare earth metal and various vicinal Si(111) surfaces. Changes of the nanowire widths are expected for different substrates. These varying widths correspond to different confinement situations for the electrons in the nanowires, which influence the electronic structure observed in ARPES. Even a one-dimensional electronic structure may be possible if the confinement is sufficiently strong, i.e. if the nanowires are sufficiently narrow.

7. Tb silicide nanostructures on Si(001)

Terbium silicide nanowires may form on Si(001) surfaces, but there is a multitude of other Tb induced nanostructures observed depending on the preparation parameters, e.g. a wire-like 2×7 reconstructed wetting layer. The first section of this chapter illustrates and discusses the growth of the various nanostructures on planar and vicinal substrates using mainly STM data. In addition, this section 7.1 includes RAS results, which show that RAS is able to differentiate between nanowire and wetting-layer growth.

Subsequently, the overgrowth of Tb silicide nanowires by Si is analysed in section 7.2 using STM for low Si coverages and multiple TEM techniques for several nm thick Si films. With the acquired HRTEM data and information obtained by STM, the atomic structure of the nanowires is discussed in detail in section 7.3, while considerations on the atomic structure of the wetting layer are also elucidated.

Then, results on the electronic properties of the Tb silicide nanostructures are presented in section 7.4. While the wetting layer and the nanowires were both studied by STS and XPS, ARPES and transport measurements were only taken on nanowires. Finally, the main results of this chapter are summarised in section 7.5.

7.1. Growth analysis

The main focus of this work is on Tb silicide nanowires, which may form as single wires or in bundles closely packed with grooves between individual nanowires. Often the wetting layer is observed together with the nanowires and, as an intermediate structure between wetting layer and nanowires, so-called dark wires may be present. These four wire-like structures are the most discussed in the following growth analysis, and exemplary STM images of them are shown in figure 7.1.

All structures appear as continuous lines in lower resolution STM images [see figure 7.1 (a)], but they can still be differentiated by their dimensions. The apparent height and width of the structures increases from wetting layer to dark wire to nanowire. STM images with higher resolution reveal the 2×7 structure of the wetting layer while the dark wires and nanowires still appear continuous [see figure 7.1 (b)]. Thus, the grid-like appearing wetting layer may be described as wetting layer rows. On every terrace, these wire-like structures form parallel to each other and their growth direction changes by 90° with every single layer step. This is expected since the bond direction of the surface changes by 90° with every layer (see section 5.1.1).

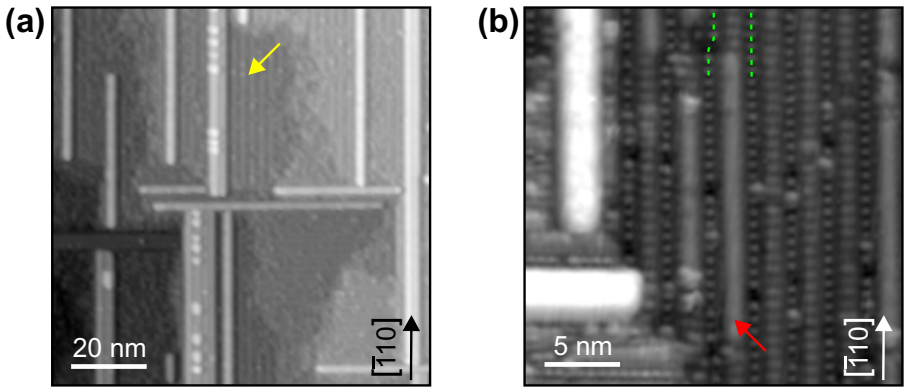

Figure 7.1.: (a) STM image of a planar sample with single and bundled nanowires (0.50 ML Tb annealed at 600 °C, sample voltage $V = -1.5$ V, and tunneling current $I = 250$ pA). In addition to the nanowires also patches of the wetting layer are observed, e.g. in the area marked by the yellow arrow. (b) STM image of a planar sample prepared by depositing 0.70 ML Tb on the clean surface and annealing for 2 min at 450 °C ($V = -1.5$ V, $I = 250$ pA). Most of the area is covered by the wetting layer, but there are also two nanowires and some dark wires. The dark wires appear continuous and often slightly higher than the wetting layer. One of them is marked by the red arrow. The green hatched lines indicate a shift of the wetting layer alignment.

7.1.1. Planar substrates

Most samples were prepared by deposition at room temperature and subsequent annealing for 2 min. Thus, there are only two parameters, which influence the growth of Tb induced structures, the Tb coverage and the annealing temperature. In the following, the various temperature regimes are discussed from a temperature too low for nanowire formation to a temperature too high for nanowire formation. For each temperature regime, a broad range of Tb coverages is covered.

Different annealing schemes are briefly discussed afterwards, before the growth analysis on planar Si(001) substrates is concluded.

Low-temperature regime

The lowest sample temperature that can be realised at the STM chamber system is room temperature, defining the lower limit of possible annealing temperatures. When Tb is deposited on a clean Si(001) substrate and the sample is not heated afterwards, an amorphous Tb layer forms. In STM, such a layer appears as small clusters that are randomly distributed on the surface as is seen in figure 7.2 (a). The monoatomic steps that lie beneath the amorphous Tb layer are clearly visible with the left one appearing rather straight like an S_A-step and the right one rough like an S_B-step. In contrast, no corrugations resembling the Si dimer rows of the 2×1 reconstruction are observed with STM. Nevertheless, LEED shows a two-domain 2×1 reconstruction even for larger coverages than used in the preparation shown in figure 7.2 (a) [see figure 7.2 (b)]. Thus, also the dimer reconstructions may still be present after the deposition of Tb.

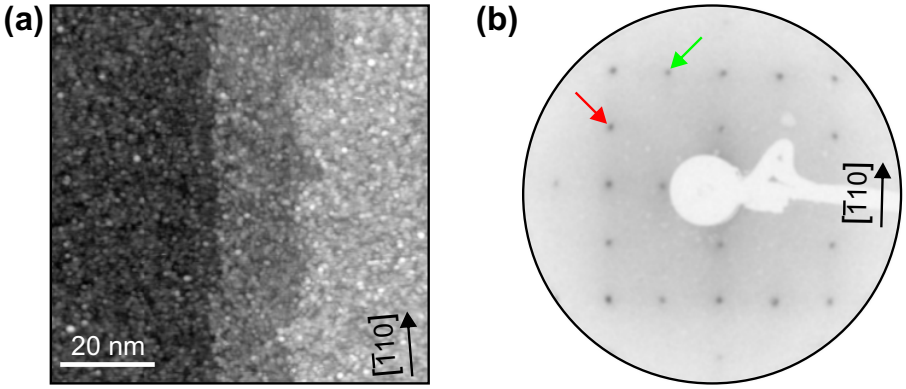

Figure 7.2.: (a) STM image of 0.40 ML Tb deposited on a clean Si(001) surface at room temperature ($V = -1.5$ V, $I = 100$ pA). (b) LEED image of a Si(001) surface covered by 0.75 ML Tb that were deposited at room temperature ($E_{\mathrm{kin}} = 50$ eV). The arrows indicate the two-domain 2×1 periodicity.

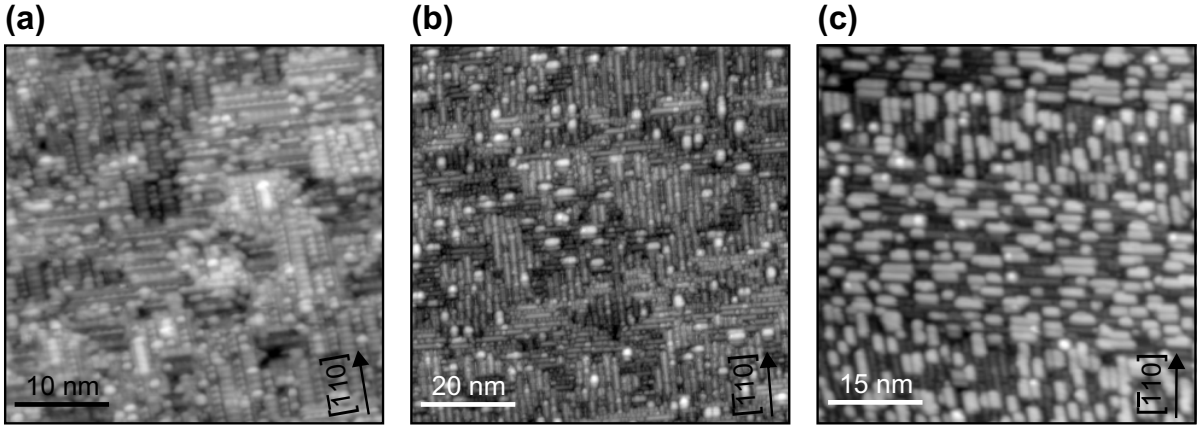

Figure 7.3.: STM images of (a) 0.40 ML Tb, (b) 0.85 ML Tb, and (c) 1.45 ML Tb annealed at 400 °C [(a and b) $V = -1.0$ V, (c) $V = -1.5$ V, $I = 100$ pA for all images].

Figure 7.2 (a) shows the appearance of 0.40 ML amorphous Tb on Si(001) in STM. Annealing such a layer at 400 °C leads to the surface morphology shown in figure 7.3 (a). Most structures resemble subparts of the wetting layer, although areas with complete 2×7 unit cells are rare, as well as dark wires, but the surface is extremely uneven. No homogeneous terraces are observed. Instead, every terrace is disturbed by holes. The holes have a depth of one atomic layer as is seen by the rotation of the structures by 90° in the holes.

The formation of silicide structures and these holes during the annealing suggest three conclusions. Firstly, Si is able to diffuse even for such low annealing temperatures since silicide structures form. Secondly, the Si density in the wetting layer is different from the one of the clean Si surface because otherwise no lateral diffusion of Si would be needed, so that no or at least not so many holes would form. Thirdly, although Si can diffuse, its diffusion length, the diffusion length of Tb and the one of the silicide structures are not sufficiently large to form large homogeneous terraces during the annealing.

While the general surface morphology remains very uneven, higher Tb coverages and an annealing temperature of 400 °C lead to the evolution of the wetting layer structures to dark wires and of the dark wires to very short nanowires with lengths below 5 nm [see figures 7.3 (b and c)]. Thus, it is not possible to grow well-defined Tb silicide nanowires, e.g. characterised by high aspect ratios, with such a low annealing temperature and higher annealing temperatures have to be used.

Interestingly, homogeneous terraces are formed for high Tb coverages [see figure 7.3 (c)], so that the diffusion lengths may also depend on the Tb amount on the surface.

Optimum-temperature regime

For the preparations shown in figure 7.4, a similar amount of Tb as for the preparations presented in figures 7.2 (a) and 7.3 (a) was used. For annealing at 500 °C, randomly distributed rows of the wetting layer form [see figure 7.4 (a)]. In between these wetting layer rows, the surface is disordered. These disordered areas consist of fractions of the wetting layer, short Si dimer rows, and a wide variation of cluster-like aggregates of Tb and Si. Such disordered areas are also observed for higher annealing temperatures, but the wetting layer structures agglomerate in larger patches with increasing annealing temperature [see figures 7.4 (b and c)]. Due to the presence of both wetting layer patches and Si dimer rows [see, e.g., the yellow arrow in figure 7.4 (b)], it is seen that the wetting layer rows run perpendicular to the Si dimer rows, which is consistent with observations made for Dy and Y [330, 332, 333]. This will be further discussed in section 7.3.

In figure 7.4 (d), a nanowire, whose growth altered the surface morphology by displacing step edges, is observed surrounded by a disordered surface while figure 7.4 (c) shows large patches of the wetting layer. Both images were taken of the same preparation with the tip moved by a few μm between the acquisitions of the images. While the temperature and possibly also the Tb coverage may vary over larger scales [see e.g. figure 6.1 (c) for an inhomogeneously heated sample], such variations should be minimal over a μm scale. Thus, the used preparation parameters are at the threshold for nanowire formation. Especially for such threshold conditions, the obtained surface morphology does not only depend on the global preparation parameters, but also on local properties. For instance small fluctuations of the Tb density, e.g. by a locally higher defect density or surface step accumulation, may enable the nucleation of nanowires in certain sample areas, but not in others.

For all preparations shown in figure 7.4, the annealing temperatures were sufficiently high to always allow the formation of homogeneous terraces after the silicide formation. Thus, there are no holes observed any more, but there is a different phenomenon that certainly depends on the diffusion properties of the atoms on the surface. The wetting layer only forms on every second terrace for annealing at 600 °C [see figure 7.4 (c)]. Such a behaviour was also observed for the 2×7 reconstruction with Y as rare earth metal [330], but no satisfying explanation is possible at the moment due to the interplay of too many parameters, e.g. anisotropic diffusion lengths depending on the substrate orientation, which changes by 90° with every step, or varying Schwoebel barriers for different step types.

Increasing the coverage to about 0.5 ML a closed film of the wetting layer forms for an annealing temperature of 500 °C, as shown in figure 7.5 (a). There, some brighter appearing lines corresponding to dark wires and one nanowire are seen in addition to the stripes of the

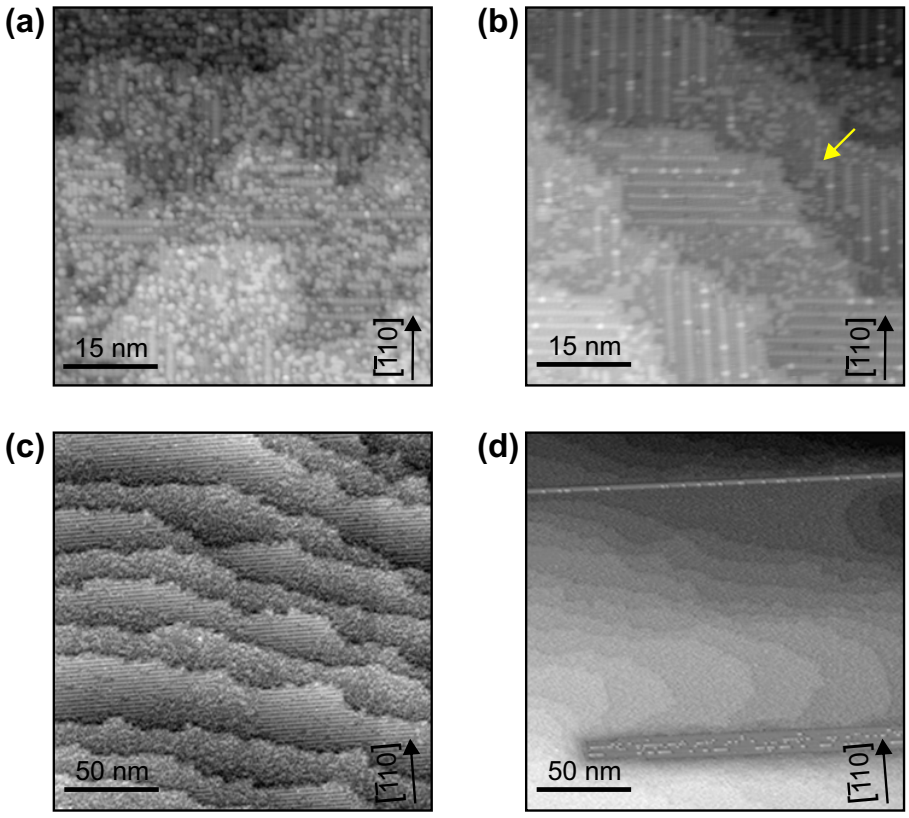

Figure 7.4.: STM images taken with $V = -1.5$ V and $I = 100$ pA of preparations with 0.35 ML Tb annealed at (a) 500 °C, (b) 550 °C, and (c and d) 600 °C. The yellow arrow in (b) marks some horizontal Si dimer rows.

wetting layer rows. The formation of a global film before the formation of local structures resembles the Stranski-Krastanov growth mode, allowing the designation of the film as wetting layer in this work.

Taking the preparation for a closed wetting layer film as reference, a small increase of the Tb coverage leads to the formation of nanowires while the wetting layer stays intact in between them [see figure 7.5 (c)]. A different surface morphology arises when the annealing temperature instead of the Tb coverage is increased [see figure 7.5 (b)]. Nanowires are also observed, but the surface area in between them is not exclusively filled with the wetting layer. These different forms of the coexistence of nanowires and wetting layer are shown in detail in figure 7.6. In the STM image of the preparation that used a lower annealing temperature, the wetting layer is basically undisturbed by the formation of the nanowire. At a higher annealing temperature, only patches of the wetting layer are observed while most of the surface between the nanowires is disordered. A modest increase in Tb coverage neither leads to the destruction of the wetting layer in between the nanowires for low annealing temperatures nor to an extended growth of the wetting layer for high annealing temperatures [see figures 7.5 (d – f)].

In this Tb coverage regime, the density of the nanowires increases with increasing Tb coverage for all annealing temperatures [see figure 7.5]. Since the nanowires do not cross

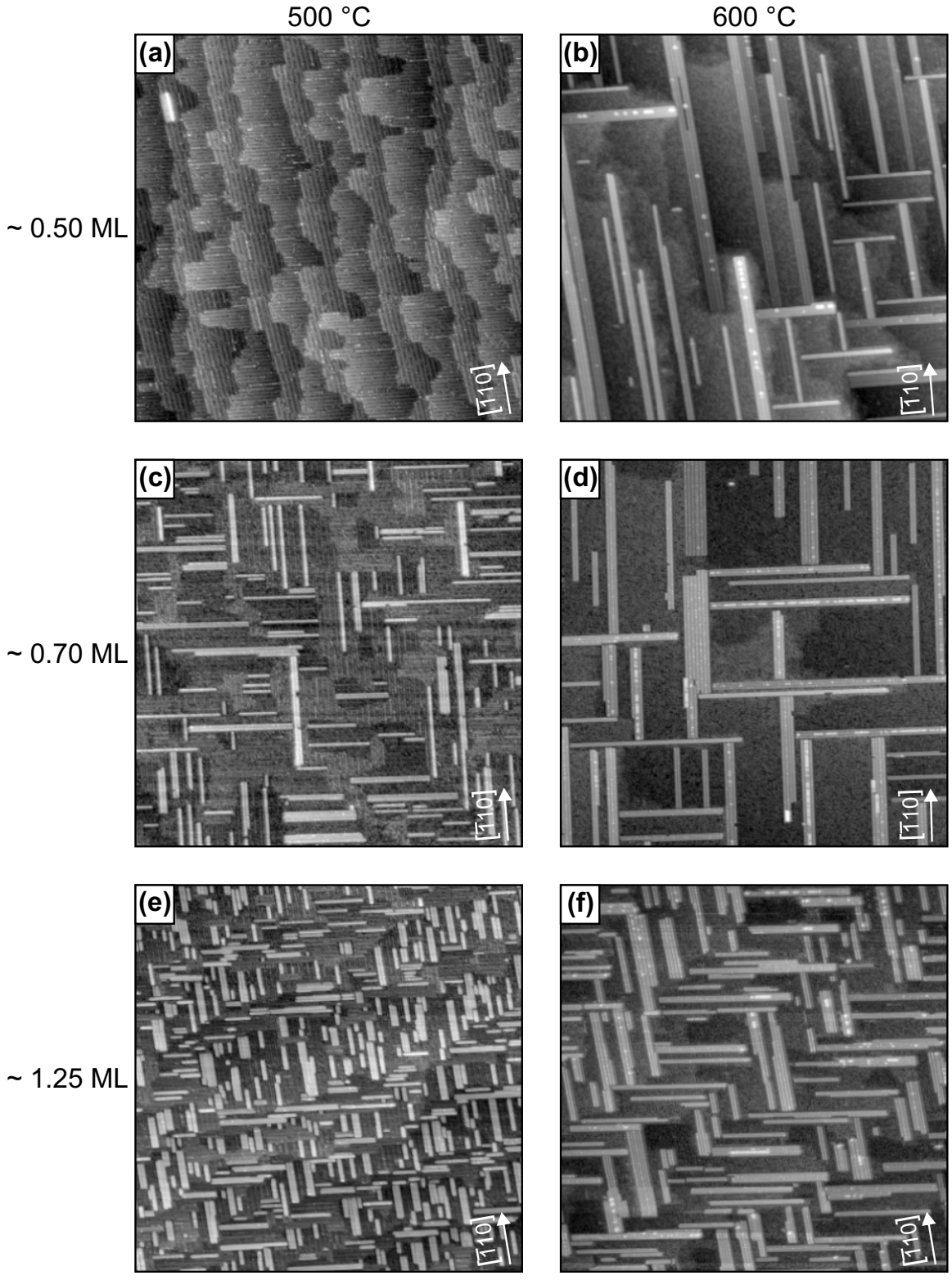

Figure 7.5.: Overview STM images (200 nm wide) for various preparation conditions [for all images $V = -1.5$ V and $I = 100$ pA, except (b) $I = 250$ pA, (c) $V = -1.7$ V, and (f) $V = -2.0$ V].

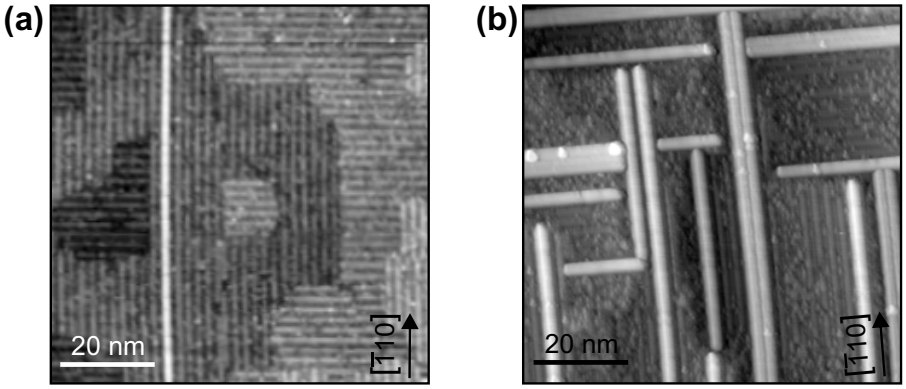

Figure 7.6.: Comparison of the coexistence of wetting layer and nanowires for different annealing temperatures. (a) STM image of a sample with 0.60 ML Tb annealed at 500 °C ($V = +1.5$ V, $I = 100$ pA). (b) STM image of a preparation using a Tb coverage of 0.50 ML and an annealing temperature of 600 °C ($V = -1.5$ V, $I = 250$ pA).

each other, this increasing density results in a reduction of the length of the nanowires due to an earlier interruption of the nanowire growth. Thus, the longest nanowires form for low nanowire densities, as observed for the preparations shown in the figures 7.4 (d) and 7.5 (b). There the length of a nanowire can exceed 300 nm and is only limited by step bunching or insufficient Tb supply for further growth. Since the possible Tb supply depends on its diffusion length, the longest nanowires are found for higher annealing temperatures.

The nanowires do not only become denser, but also form broader bundles, i.e. bundles incorporating more nanowires, with increasing Tb coverage. While this general trend is observed independently of the annealing temperature, the detailed bundle formation is annealing temperature dependent. This is illustrated by the histogram shown in figure 7.7. Mainly single nanowires and small bundles are observed for the preparations using a lower annealing temperature while broader bundles are formed for higher annealing temperatures, almost leading to the extinction of single nanowires for higher Tb coverages. The different bundling behaviour can be understood by taking into account the reduced diffusion lengths at lower temperatures leading to a more separated growth. In addition, the nanowires grow parallel to the wetting layer rows, so that diffusion barriers perpendicular to these rows may slow down the agglomeration of wider nanowire bundles at lower temperatures, at which the wetting remains intact between the nanowires.

Also dependent on the annealing temperature is the formation frequency of an additional layer on top of the nanowires, which appears as rectangular protrusion with round edges. Those are often observed for higher annealing temperatures [see figures 7.5 (b, d, and f)], but are rather uncommon for lower annealing temperatures [see figures 7.5 (c and e)]. This formation of an additional layer is not more frequent with increasing Tb coverage, but instead additional nanowires grow.

The continued increase of the number of nanowires leads to the nearly complete filling of the Si(001) surface with nanowires for Tb coverages of about 2 ML [see figure 7.8]. Such a high surface density of nanowires was never reported for nanowires of other rare earth metals [79, 82, 313, 316, 330]. Nevertheless, this is most likely no particularity of Tb silicide

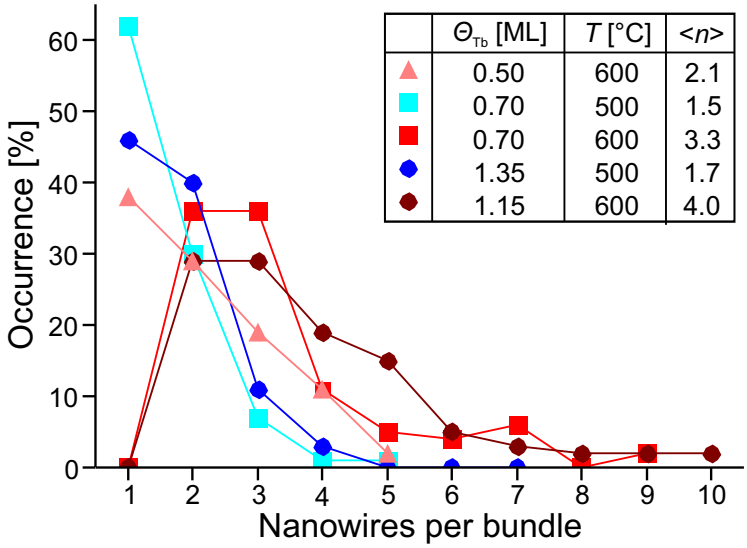

Figure 7.7.: Histogram of the occurrences of nanowires as a function of the number of nanowires in a bundle for the preparations shown in figure 7.5. Θ_{Tb} is the Tb coverage, T is the annealing temperature, and $< n >$ the average bundle width. The nanowire bundles are weighted by the number of nanowires they consist of, i.e. a bundle of four nanowires counts as four nanowires. Data points are only inserted, when bundles of the respective size were observed. The lines connecting data points are guides to the eyes.

nanowires, but rather owned to the fact that such high rare earth metal coverages were never investigated using post-deposition annealing. When the sample is annealed during the rare earth metal deposition, different surface morphologies are observed for high rare earth metal coverages [see below].

For such high Tb coverage, the appearance of the surface in between the nanowires is always disordered even for annealing at 500 °C, but the density of islands, i.e. structures with a smooth surface that appear higher and wider than nanowires [see yellow arrow in figure 7.8 (a)], is decreased for annealing at 600 °C. At higher temperatures, fewer Tb is available for island formation since more Tb is incorporated in additional layers on the nanowires. A complex interplay of thermodynamics and kinetics may be the reason for the direct growth of islands at lower temperatures.

The close-packed nanowires represent a grating with varying lattice constant. Thus the average lattice constant of the grating, which corresponds to the sum of average nanowire width and average width of the grooves between nanowires, should be discernible by diffraction techniques. Indeed, not only streaks, indicative for the growth of one-dimensional structures, but also additional spots on the main axes are seen in LEED for a sample densely covered with nanowires [see figures 7.9 (a and b)]. The LEED image can be analysed more in depth by taking intensity profiles along the main axes, as shown exemplarily in figure 7.9 (c). There are rather faint maxima at the $\times 2$ positions, which will be further discussed in section 7.3. The more intense maxima close to the main ($\times 1$) maxima do not coincide with an integer periodicity of $a_{\mathrm{Si(001)}}$, but lie between the expected positions for

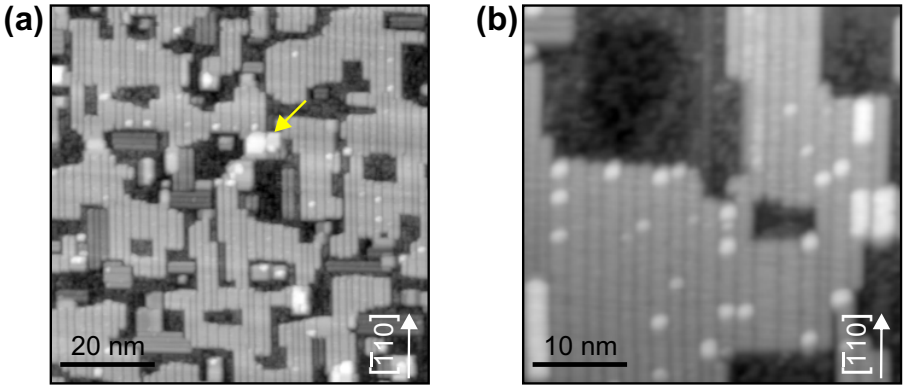

Figure 7.8.: STM images taken with $V = -1.5$ V and $I = 100$ pA of samples prepared by depositing 2.20 ML Tb and annealing at (a) 500 °C and (b) 600 °C. The yellow arrow in (a) marks a small island.

$\times 5$ and $\times 6$ periodicities for all main axes. The average peak position corresponds to a $(5.4 \pm 0.2)\, a_{\mathrm{Si}(001)}$ periodicity.

Before comparing the LEED results with STM results, a few comments on the LEED data are necessary. By a variation of the electron energy, additional spots on the main axes are also observed close to the other main spots, e.g. close to the one at $k_{[110]} = 0$ in figure 7.9 (c), but distinct intensity maxima are never observed at multiples of the distances of the additional spots from the main spots. Such additional spots are expected for well ordered system, but, here, the variance of the structural periodicity is too large, so that further spots are not discernible [415]. Such a rather large variance may also lead to an underestimation of the underlying average periodicity [415]. For LEED data of Gd silicide nanowires with a smaller variance, the integer periodicity observed in LEED could be related to the average groove-to-groove distance [84]. If this is also possible here, will be shown in the following.

The average groove-to-groove distances are determined with STM to find out if the additional LEED spots close to the main spots are due to the close packed nanowires. The histogram of the observed groove-to-groove distances for this preparation is shown in black in figure 7.9 (d). There are four clearly distinguishable peaks that are separated by (0.4 ± 0.1) nm agreeing with the lattice constants of the Si(001) substrate and of the $TbSi_2$ structures presented in section 5.2. The average groove-to-groove distance is (2.2 ± 0.2) nm corresponding to $(5.7 \pm 0.6)\, a_{\mathrm{Si}(001)}$. This value obtained from local measurements in real space agrees very well with the periodicity of $(5.4 \pm 0.2)\, a_{\mathrm{Si}(001)}$ observed globally in momentum space by LEED.

For the preparations with 2.20 ML Tb (see figure 7.8), the groove-to-groove distance histograms are shown in red and blue in figure 7.9 (d). The course of the histograms is very similar to the already discussed one with 4 clearly distinguishable peaks. Furthermore, the same average groove-to-groove distance as for the preparation with 1.85 ML Tb is found for both preparations with 2.20 ML Tb. Thus, the optimal nanowire width of densely packed nanowires is independent of the annealing temperature.

The width of inner nanowires in nanowire bundles appears also rather independent of

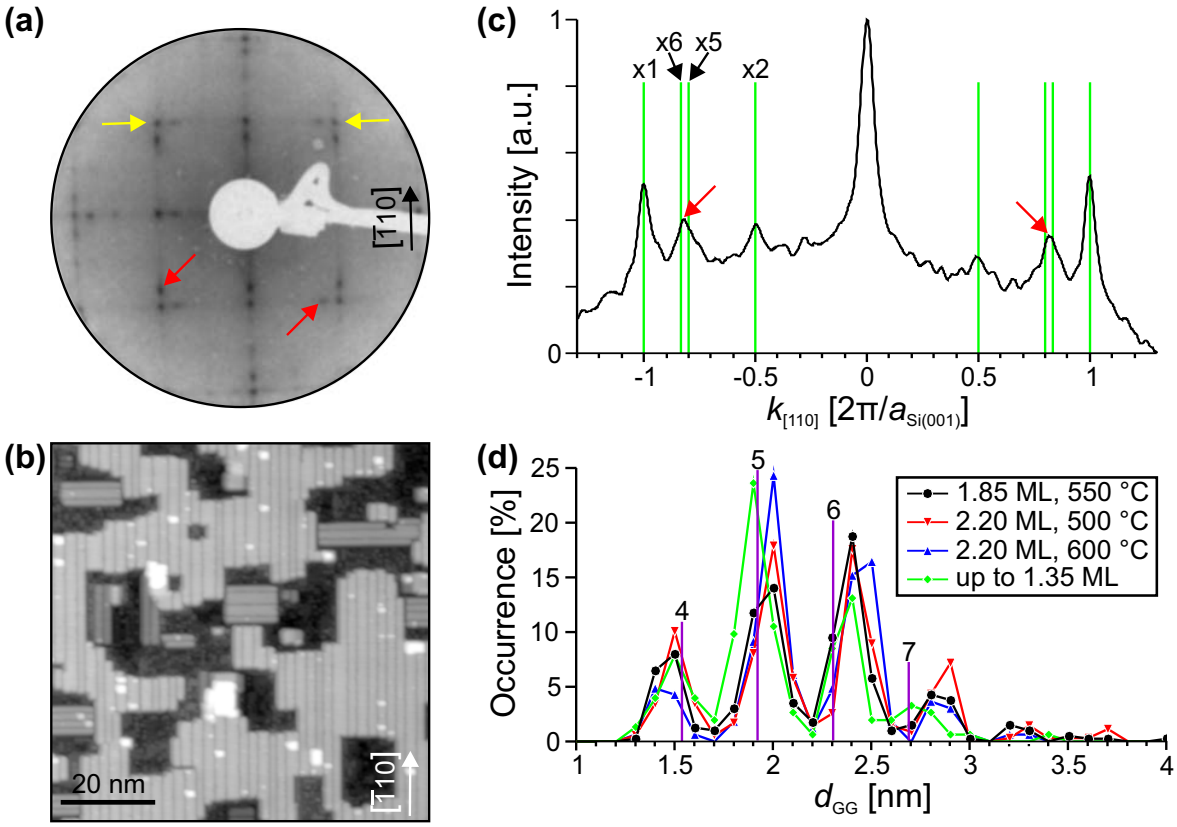

Figure 7.9.: (a) LEED and (b) STM image of the same preparation with 1.85 ML Tb annealed at 550 °C (E_{kin} = 89 eV, $V = -1.5$ V, and I = 100 pA). The red arrows in (a) mark additional spots due to the bundling. (c) Intensity profile between the yellow arrows in (a). The red arrows and the green lines mark the additional spots and expected maxima positions for certain periodicities of $a_{Si(001)}$, respectively. (d) Histogram of groove-to-groove distances (d_{GG}) for the preparation treated in this figure in black, for those shown in figures 7.8 (a and b) in red and blue, respectively, and for small bundles of at most 5 nanowires in green. The numbers at the vertical lines indicate the theoretical groove-to-groove distances in units of $a_{Si(001)}$. The lines connecting data points are guides to the eyes.

the deposited Tb amount. The green graph in figure 7.9 (d) is the distribution of the measured groove-to-groove distances for bundles with less than 6 nanowires. It was obtained by including the data of over 10 different preparations with varying Tb coverages below 1.35 ML. This histogram is very similar to the already above discussed histograms of preparations with higher Tb coverages and no definite tendency to smaller groove-to-groove distances can be discerned, e.g. every peak height of the low Tb coverage data is in the range of the respective ones of the other preparations.

The peak positions of the low coverage data nicely coincide with multiples of the substrate lattice constant [see figure 7.9 (d)]. This is expected since the epitaxial layer should adopt the lateral lattice constants of the substrate when the lattice mismatch is not too high. In contrast, the peak positions for the other preparations are slightly shifted to higher

values. Systematic measurement errors cannot be excluded since the absence of suitable large surface areas with structures of known dimensions prevented the calibration of the STM during those measurements. As an estimations, errors of up to 10% may occur due to different tunnelling geometries, e.g. varying tip lengths or non-perpendicular approaches of the tip to the sample. Such systematic errors are reduced for the histogram of the smaller bundles since the data of many measurements were averaged. Further uncertainties arise due to the unknown structure of the grooves, which have an inhomogeneous width in detailed STM images [see figure 7.8 (b)], and an often slightly higher appearance of wider nanowires compared to narrower nanowires.

The deviations do not have to be caused by measurement errors. Dislocations at the interface between silicide and substrate may occur for bundle widths larger than a critical value. Then the strain in the bundle can be reduced by relaxation of the silicide layer possibly leading to the observation of groove-to-groove distances as multiples of the silicide lattice constants, which are slightly larger than that of the substrate (see sections 5.1.1 and 5.2).

For Y silicide nanowires, a dominance of nanowires widths that are odd multiples of the Si(001) lattice constant was reported [80]. In the present data, there is no indication for such a dominance in the histograms of groove-to-groove distances [see figure 7.9 (d)]. It should be noted that single nanowires were analysed in the study about Y silicide nanowires [80]. Single nanowires are not analysed here since their apparent width strongly depends on the tip shape and on the exact tunneling conditions, complications that are not present when analysing groove-to-groove distances in nanowire bundles.

High-temperature regime

Most STM images of Si(001) samples that are covered with Tb amounts typically used for nanowire formation but annealed at 700 °C resemble the one shown in figure 7.10 (a). Silicon dimer rows are clearly resolved although they are often interrupted, i.e. the surface appears like a clean Si(001) surface with rather high defect density.

By scanning very large areas of the surface (μm^2), islands can be found on such samples [see figure 7.10 (b)]. Most of them have a rectangular shape and, in addition to lateral dimensions of at least several tens of nanometers, are characterised by large heights. The exact height of an island cannot be measured with top view STM since the islands grow into the surface, as revealed by the formation of trenches surrounding the islands. The formation of such trenches, which requires intense Si diffusion, indicates that the islands are made of Tb silicide and not agglomerations of elemental Tb.

Using rather low tunneling voltages and high tunneling currents, the surface of such islands can be resolved with STM [see the inset in figure 7.10 (b)]. The observed surface structure is consistent with a $c(2\times2)$ reconstruction with respect to the Si substrate. Such a reconstruction is, e.g, in agreement with islands formed by tetragonal $TbSi_2$, which are terminated by Si dimers. The formation of such islands is not exclusive for Tb, but also reported for other rare earth elements [76, 313, 330]. They are presumably the energetically most favourable Tb silicide nanostructure and all the deposited Tb is assembled in these islands leading to basically clean surface in between.

With increasing Tb coverage the density of the islands increases, but even for a Tb

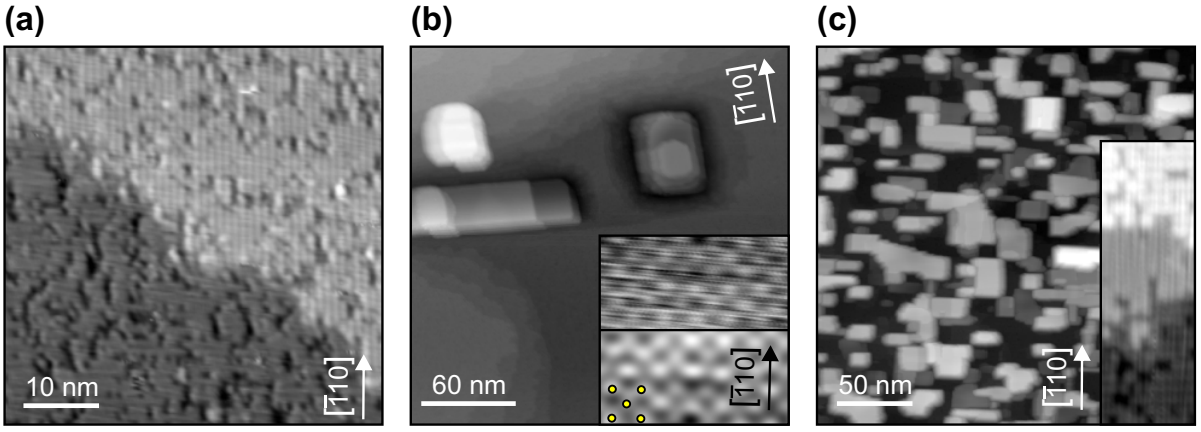

Figure 7.10.: (a) STM image showing Si dimer rows, although 0.70 ML Tb were deposited and annealed at 700 °C ($V = -2.5$ V and $I = 100$ pA). (b) STM image of a surface area, where islands formed by depositing 0.95 ML Tb and annealing at 700 °C ($V = -1.5$ V and $I = 100$ pA). The islands are imaged multiple times due to the tip shape The inset shows a 5 nm wide STM image taken on an island ($V = +0.5$ V, $I = 1$ nA). The lower half of the inset is heavily filtered to highlight the surface reconstruction and the yellow dots illustrate a $c(2\times2)$ surface structure based on the Si(001) surface lattice constant. (c) STM image of a Si(001) sample that is covered by many islands (4.60 ML Tb annealed at 700 °C, $V = -1.5$ V, and $I = 100$ pA). The 20 nm high inset shows the surface between islands ($V = -1.5$ V and $I = 100$ pA). The vertical Si dimer rows are not well resolved since the fast scanning direction was approximately from top to bottom.

coverage of about 4.5 ML, the largest Tb coverage used in this thesis, no completely connected film of islands forms [see figure 7.10 (c)]. Instead the surface between islands still appears as a clean Si(001) surface [see the inset in figure 7.10 (c)], which is rather remarkable after the deposition of multiple layers of a different material.

Different annealing schemes

In order to reduce the number of preparation parameters, the samples were always annealed for 2 min after the deposition of Tb in the preparations discussed above. In the UHV setup at the TU Berlin, it is also possible to anneal the sample during the Tb deposition. Since the samples were only annealed during the Tb deposition and not additionally afterwards, the only additional preparation parameter is the deposition rate. The experiments described in the following were performed with deposition rates of about 0.3 ML/min to 0.5 ML/min.

The formation of small surface clusters was reported for Dy, when the sample was heated at a low temperature of about 300 °C during the deposition of submonolayer amounts of the rare earth metal [384]. While such surface clusters are not the focus of this theses, the knowledge about their existence helps during the discussion of atomic structure models (see section 7.3). Thus, their formation with Tb as rare earth metal was tested.

Similar to the surface clusters induced by Dy, the Tb induced surface clusters are hardly visible in filled states STM images, but readily observable in empty states STM images [see figures 7.11 (a and b)]. The filled states STM image appears quite blurred and defective,

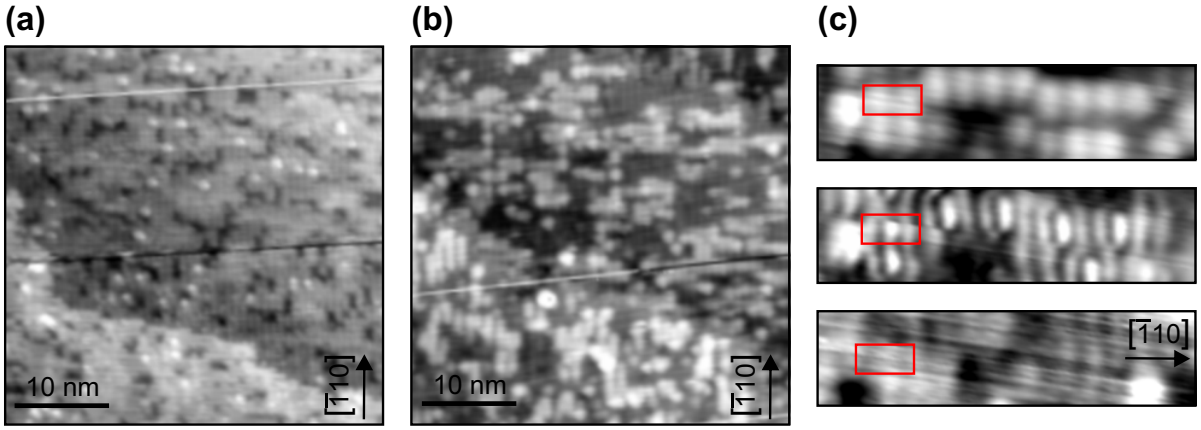

Figure 7.11.: (a) Filled and (b) empty states STM images of a Si(001) sample that was covered by 0.30 ML Tb while being held at 300 °C ($V = \pm 1.5$ V, $I = 100$ pA). The dark and bright lines are scan lines, in which the tip changed. (c) Detailed STM images showing the voltage dependent appearance of the Tb induced surface cluster [all 10 nm wide and taken at the same position with $I = 100$ pA, $V = +3.0$ V (top), $V = +1.0$ V (centre), and $V = -3.0$ V (bottom)].

but there are still Si dimer rows observed. In contrast, the empty states image is dominated by rows of protrusions that run perpendicular to the underlying Si dimer rows. The smallest structural unit is made of two protrusions and covers an area of $4 \times 2\, a^2_{\mathrm{Si(001)}}$ [see figure 7.11 (c)]. The appearance of this structure does not only change with the voltage polarity, but also when voltages with lower absolute values are used, e.g. for small positive sample voltages [central part of figure 7.11 (c)], the clusters appear as three instead of two protrusions with the central one much brighter than the outer ones.

When moderate Tb coverages and annealing temperatures known for the formation of nanowires are used while annealing during the deposition, the resulting surface morphologies are rather similar to the ones known for post deposition annealing [see figure 7.12 (a)]. However, the critical temperatures needed for the formation of nanostructures may all be slightly decreased since the Tb atoms impinging on the surface have not lost their energy to the surrounding before the annealing step. For higher Tb coverages the differences between annealing during or after the metal deposition are larger, e.g. no nearly complete filling with nanowires is observed when 2 ML Tb are deposited at high temperatures [see figure 7.12 (b)]. The observed surface morphology agrees with the assumption that, after the first nanowires formed, additional Tb attaches to the nanowires to form silicide structures, resulting in a nearly clean surface in between the silicide structures. While wide nanowire bundles form, no complete filling of the surface with nanowires is observed since the formation of islands takes place when perpendicular nanowires approach each other. The complete filling of the surface by nanowires by post-deposition annealing may be due to the simultaneous silicide formation everywhere on the surface and not dominantly at specific sites. The formation of silicide islands as the most stable nanostructures at high temperatures appears to be independent of the annealing scheme [see figure 7.12 (c)].

The last annealing scheme that will be discussed is the flash annealing, which may be used to recover locally clean Si(001) surfaces after preparations. For Si(111) substrates, it

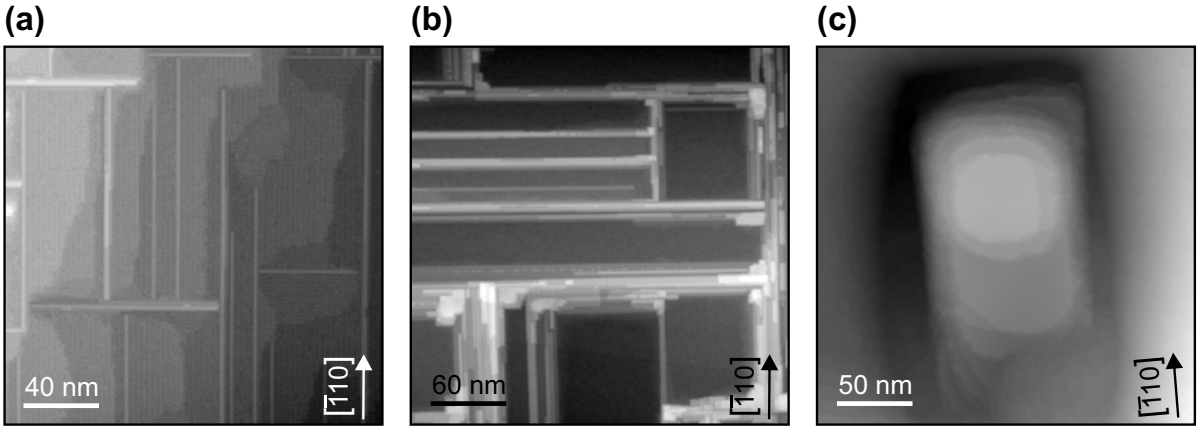

Figure 7.12.: STM images of preparations during which the sample was annealed during the Tb deposition [all images $V = -1.5$ V and $I = 100$ pA, except $V = -2.5$ V in (a)]. (a) 0.70 ML Tb deposited at 550 °C, (b) 2.05 ML at 550 °C, and (c) 0.40 ML at 700 °C.

was reported that Tb diffuses into the bulk during a preparation [384]. Furthermore, this Tb may also segregate back to the surface even after flash annealing in subsequent preparations, so that submonolayer surface reconstructions may be observed without Tb deposition simply by annealing a reused sample. However, such a behaviour was not observed for Si(001) substrates, although it should be mentioned that it was not extensively tested, but huge islands form during the flash annealing. This was first observed during SEM measurements within the framework of transport measurements on the nanowires in collaboration with the workgroup of Prof. Dr. Herbert Pfnür and Prof. Dr. Christoph Tegenkamp at the Leibniz Universität Hannover [see figure 7.13 (a)], but a similar huge island was also found in this work by STM [see figure 7.13 (b)]. Surrounding these huge islands are surface areas that show a reduced Tb nanostructure density. This is directly seen in the STM image, in which only few nanowires are imaged although about 2 ML Tb were deposited, but also in the SEM image, in which the huge islands have bright halos. Accidentally measuring with STM in such an area may give the wrong impression of a preparation, and further parts of the surface should be analysed when the Tb coverage appears too low. It should also be noted that these islands cause background signals in all globally averaging measurement techniques.

While such huge islands were not reported for other rare earth metals, they were also observed in Hannover during attempted transport measurements on Dy silicide nanowires on Si(001) [417]. Thus, they may form for all rare earth elements during flash annealing.

Summary of Tb silicide nanostructure growth on planar substrates

Terbium may induce a manifold of different nanostructures on planar Si(001) substrates. A schematic phase diagram mainly based on the data for 2 min post-deposition annealing is given in figure 7.14. In addition to a region, in which cluster growth may be observed, the phase diagram may be divided in three main parts, which are with increasing annealing temperature: the low-temperature regime, the optimum-temperature regime for nanowire

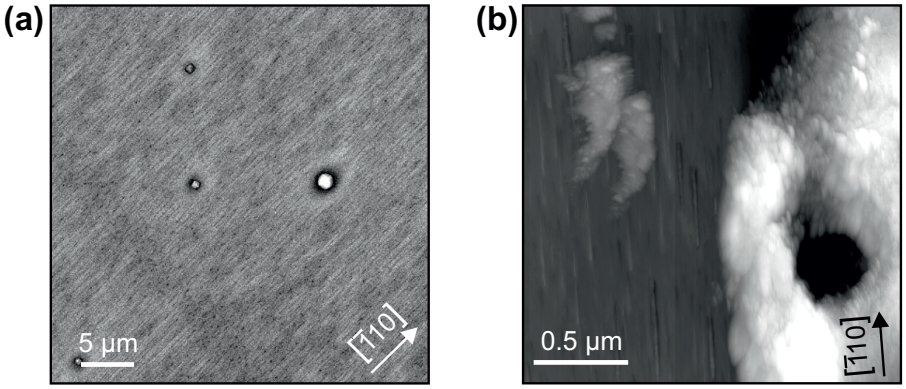

Figure 7.13.: (a) SEM image of a preparation with about 0.8 ML Tb deposited at 700 °C taken with a primary electron beam acceleration voltage of $V_{\mathrm{SEM}} = 15$ kV and an emission current of $I_{\mathrm{SEM}} = 1$ nA. From [416]. (b) STM image of 2.10 ML Tb deposited at 550 °C ($V = -5.0$ V and $I = 50$ pA). For both preparations vicinal substrates were used (growth discussed in subsection 7.1.2).

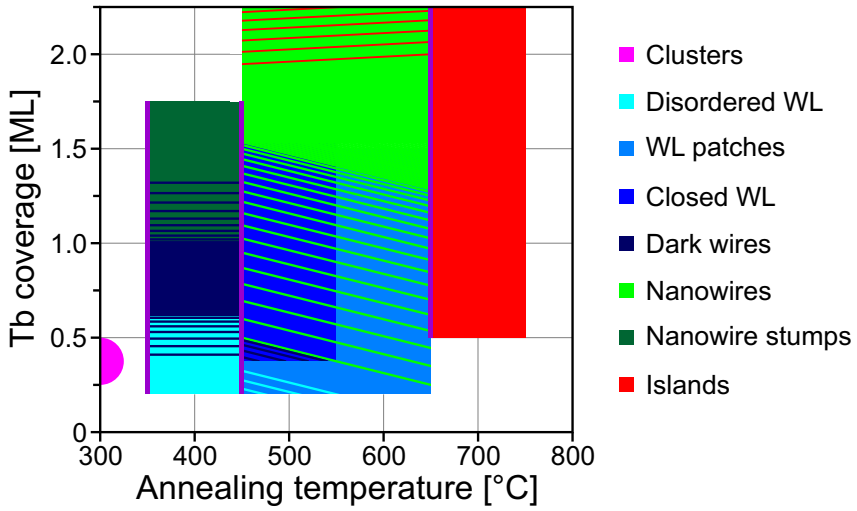

Figure 7.14.: Schematic phase diagram of Tb silicide nanostructures growth on Si(001).

growth, and the high-temperature regime.

At low annealing temperatures, there is an evolution from disordered wetting layer structures over dark wires to nanowire stumps. The parameter regions, in which one of those structure dominates, are coloured differently in figure 7.14. To illustrate that the transitions are not abrupt, the parameter regions are hatched at their boundaries.

In the optimum-temperature regime for nanowire growth, the growth is more diverse. For most parameters patches of the well ordered wetting layer reconstruction or even a complete filling of the surface with the wetting layer may be observed, but for low annealing temperatures, disordered wetting layer areas and dark wires may also be observed. With increasing Tb coverage, the density of Tb silicide nanowires increases until they become the dominant nanostructure and the wetting layer is not observed between them any more.

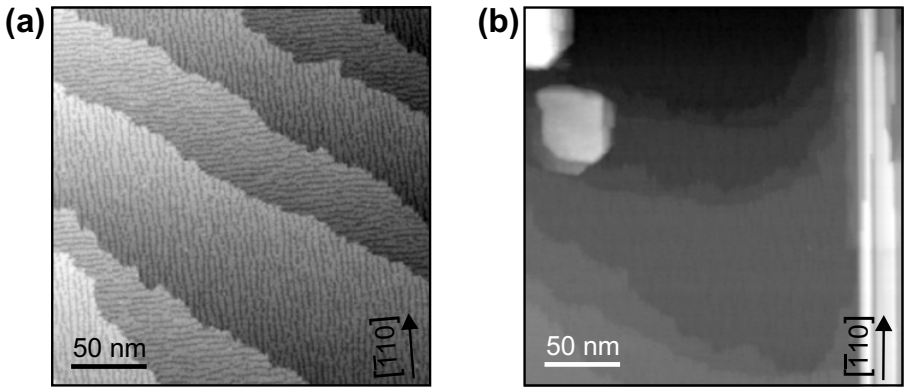

Figure 7.15.: (a) STM image of a nominally clean, but contaminated Si sample ($V = -2.5$ V and $I = 100$ pA). (b) STM image of the same substrate as in (a) with 0.45 ML Tb annealed at 600 °C ($V = -1.5$ V and $I = 500$ pA). The preparation parameters are very similar to the one used in the preparation shown in figure 7.5 (b).

The hatched are is tilted since the nanowire growth is initiated at lower Tb coverages for higher temperatures. For very large Tb coverages, island growth is observed.

In the high-temperature regime, Tb silicide islands are the only Tb-induced nanostructures. In between them, the surface appears like a bare Si(001) surface and with increasing coverage, the density of the islands increases.

The phase diagram is based on the Tb deposition rates and temperatures measured at the TU Berlin setup. Especially, the measured temperatures may be different at other setups. Nevertheless, it is possible to look up how preparation parameters have to be changed to achieve a certain surface morphology with this phase diagram.

It was mentioned above that often lower temperatures are sufficient to form a specific nanostructure when the sample is already annealed during the deposition. As for the temperature differences between different UHV setups, the phase diagram should still be applicable for estimating the influence of relative changes of the preparation parameters at least for the lower Tb coverages.

A different growth than predicted by the phase diagram also occurs for substrates that are not completely clean. In figure 7.15 (a), the Si dimer rows of a nominally clean substrate are strongly disrupted by lower appearing lines, which run perpendicular to the dimer rows. Such lines are characteristic for Ni contamination [418]. On this substrate, the growth of islands and unusually wide nanowires was observed for an annealing temperature of only 600 °C and submonolayer Tb coverages [see figure 7.15 (b)]. Thus, the presented phase diagram is only correct for clean substrates.

Up to now only planar substrates were discussed. Vicinal substrates exhibit double steps, which may allow the easier formation of certain structural motifs leading to a different growth behaviour. Thus, the validity of the phase diagram shown in figure 7.14 for vicinal substrates is discussed in the following subsection.

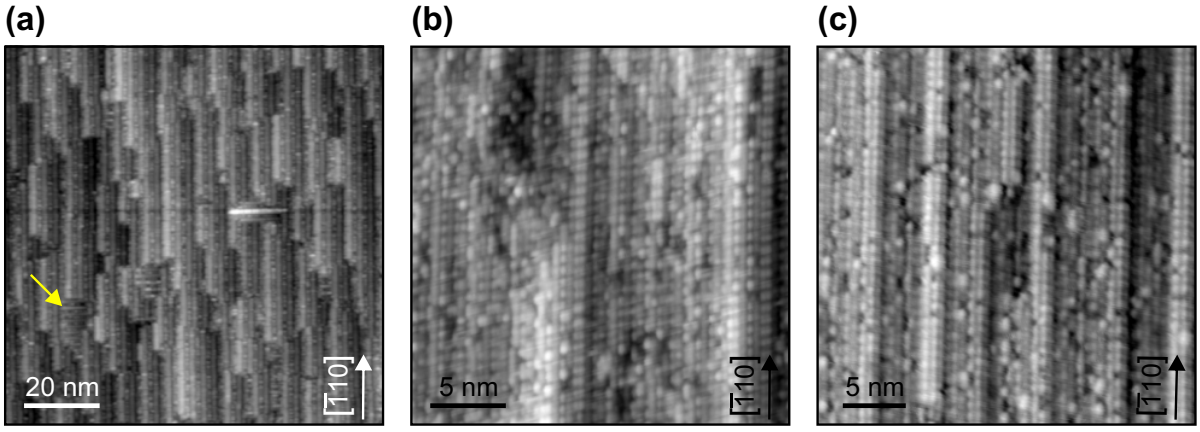

Figure 7.16.: STM images of (a) 0.45 ML Tb annealed during deposition at 450 °C on a Si(001) substrate with 2° offcut ($V = -2.5$ V and $I = 100$ pA), (b) 0.35 ML Tb annealed after deposition at 450 °C on a Si(001) substrate with 4° offcut ($V = -1.5$ V and $I = 100$ pA), and (c) 0.35 ML Tb annealed after deposition at 500 °C on a Si(001) substrate with 6° offcut ($V = -0.8$ V and $I = 100$ pA). The yellow arrow in (a) marks wetting layer rows of the minority domain.

7.1.2. Vicinal substrates

Substrates with offcut angle between 2° and 6° were used as vicinal Si(001) substrates. All angles are nominally towards [110], but offcuts towards [$\bar{1}\bar{1}0$], [$\bar{1}10$], and [$1\bar{1}0$] are equivalent due to the symmetry of the Si crystal. While the values of the observed offcut angles always nicely agree with the nominal ones, they are never purely towards [110]. This leads to a small misalignment of step edges in the order of few nm in [110] direction for a step length of 100 nm. Thus, no endless growth of nanowires is possible even if they align parallel to the nominal step direction as is expected. The wetting layer rows grow perpendicular to the Si dimer rows, which are perpendicular to the step edges on vicinal Si(001) [see section 5.1.1]. Since the nanowires form parallel to the wetting layer rows, they should also be parallel to the nominal step direction.

The growth of the wetting layer on vicinal substrates is illustrated in figure 7.16. On every surface, rows of the wetting layer are observed. As expected, they form dominantly parallel to the step edges, and only a very small part of the surface is covered by the minority domain even for the rather small offcut angle of only 2° [see yellow arrow in figure 7.16 (a)].

In general, the growth is very similar to the one observed on planar surfaces, e.g. a lower annealing temperature is needed for the formation of ordered patches when the sample is annealed during the Tb deposition instead of afterwards [see figures 7.16 (a and b)]. With increasing offcut angle, the average number of wetting layer rows on every terrace reduces, which is in agreement with the decreasing terrace width. For the substrate with 2° offcut, about 3 rows are observed on every terrace, while usually only one is seen on substrates with 6° offcut [see figures 7.16 (a and c)].

The main differences between planar and vicinal substrates are that the wetting layer often does not appear as well-ordered on vicinal substrates as on planar substrates and that nanowires form for lower Tb coverages than on planar surfaces, especially when the

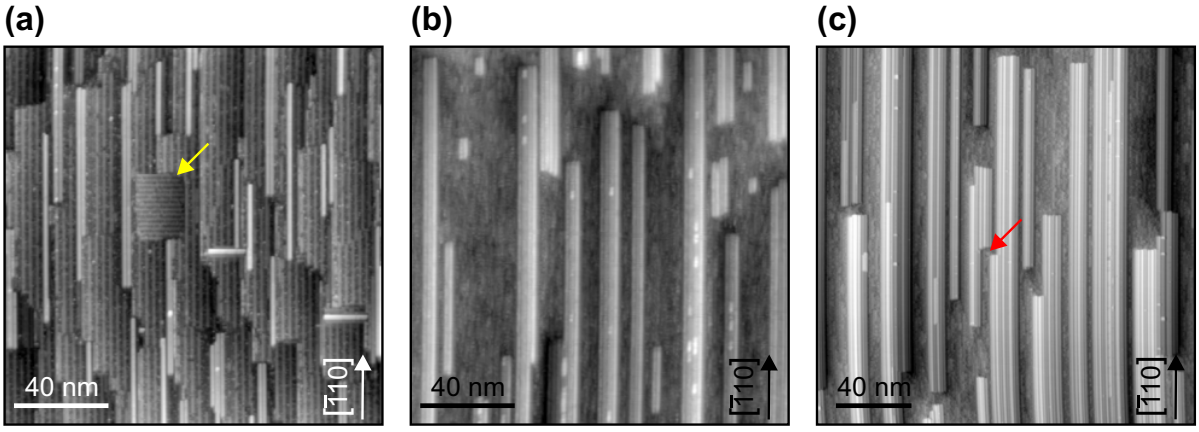

Figure 7.17.: STM images of (a) 0.35 ML Tb annealed during deposition at 500 °C on a Si(001) substrate with 2° offcut ($V = +1.5$ V and $I = 100$ pA), (b) 1.00 ML Tb annealed after deposition at 600 °C on a Si(001) substrate with 4° offcut ($V = -1.5$ V and $I = 100$ pA), and (c) 1.50 ML Tb annealed after deposition at 600 °C on a Si(001) substrate with 6° offcut ($V = -1.5$ V and $I = 100$ pA). The yellow arrow in (a) marks wetting layer rows of the minority domain and the red one in (c) indicates an area, where nanowires on different terraces hinder their growth.

substrate has a higher offcut angle. Both differences can be explained by the reduced terrace widths of the substrates. Typically, a terrace has a width that is different from an integer multiple of the width of the complete wetting layer reconstruction ($7\,a_{\mathrm{Si}(001)}$). Thus, other structures also form on the terraces, so that no completely ordered surface results. Any order is further disrupted by the misalignment of the steps, which results in the intersections of wetting layer rows by steps. Since the steps are not perfectly parallel, the step misalignment also results in varying terrace widths further preventing ordering. Without perfect order of the wetting layer, it is impossible to form a complete coverage of the surface with the wetting layer. Thus, the critical Tb coverage, at which additional Tb cannot be included into the wetting layer any more, is reduced for vicinal surfaces compared to planar surfaces. The deposition of such additional Tb may then lead to locally higher Tb concentration initiating the nanowire formation for Tb coverages that are lower than typical for nanowire formation on planar surfaces.

Similar to the wetting layer rows, also the nanowires form mainly parallel to the step edges on vicinal surfaces (see figure 7.17). This is consistent with the observation made on planar surfaces that the wetting layer rows are parallel to the nanowires on the same terrace. As on planar surfaces, the nanowires appear as rather structureless elongated protrusions, which may form bundles, in which individual nanowires are separated by grooves. Furthermore, the formation of an additional layer is observed on some wires, which is also known for nanowires on planar substrates. Thus, the nanowires on planar and vicinal surfaces are assumed to have the same structure based on these STM observations. This non-trivial assumption will be further tested by HRTEM and XPS in chapters 7.3 and 7.4, respectively.

Not only the nanowire appearance, but also their general growth on vicinal surfaces is similar to the one on planar surfaces. The nanowire growth may displace step edges, resulting in nanowire lengths exceeding 500 nm and bundle widths surpassing 10 nm, which

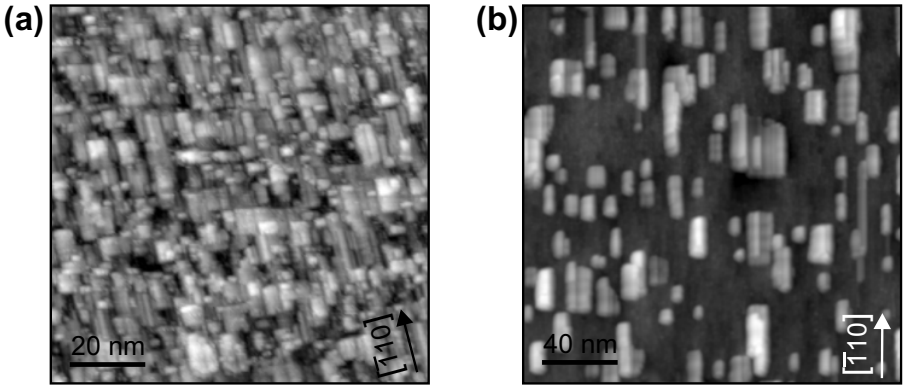

Figure 7.18.: STM images of island growth on a Si(001) substrate with 6° offcut. (a) 2.20 ML Tb annealed after deposition at 500 °C ($V = -1.5$ V and $I = 100$ pA) and (b) 2.00 ML Tb annealed after deposition at 600 °C ($V = -1.5$ V and $I = 100$ pA). The multiple imaging of structures due to the tip shape cannot be excluded for the STM image shown in (a).

is much wider than the average terrace width on clean vicinal surfaces, e.g. being about 4 nm for 4° offcut. The length of a nanowire is only limited by the Tb supply, by step bunches due to the step misalignment, or by other nanowires. Although most nanowires are parallel to each other, they may still hinder the growth of each other when they form on different terraces and approach each other with their widths larger than the average terrace width [see red arrow in figure 7.17 (c)].

Interestingly, a nearly complete filling of a vicinal surface with nanowires was never observed. Instead, islands form when preparation parameters were used that led to a nearly complete nanowire filling on planar surfaces (see figure 7.18). Thus, the dominant nanowire formation as well as the dominant island formation begin at lower Tb coverages on vicinal surfaces. Otherwise, the nanowire growth characteristics on planar and vicinal substrates are remarkably similar, and no structure exclusive to vicinal substrates was observed.

7.1.3. Reflection anisotropy spectroscopy

The RAS measurements were mainly conducted by Dr. Sandhya Chandola (ISAS Berlin), with me being responsible for the growth of the Tb silicide nanostructures and their characterisation by STM. In the interpretation and discussion of the data participated all authors of reference [419].

Vicinal substrates have to be used for RAS measurements since it is a globally averaging methode and the signals of the two equal domains present on planar surfaces would cancel out each other. The RAS spectra of various preparations are presented in figure 7.19 while STM images of the same preparations are shown in figure 7.20.

As reference for the RAS data of the Tb silicide nanostructures, the RAS signal of the bare Si(001) surface was recorded [black spectrum in figure 7.19 and figure 7.20 (e)]. The spectrum measured here nicely reproduces the literature data [420–422]. It is characterised by a small minimum at 1.6 eV, a broad minimum between 2.0 eV and 3.5 eV, which

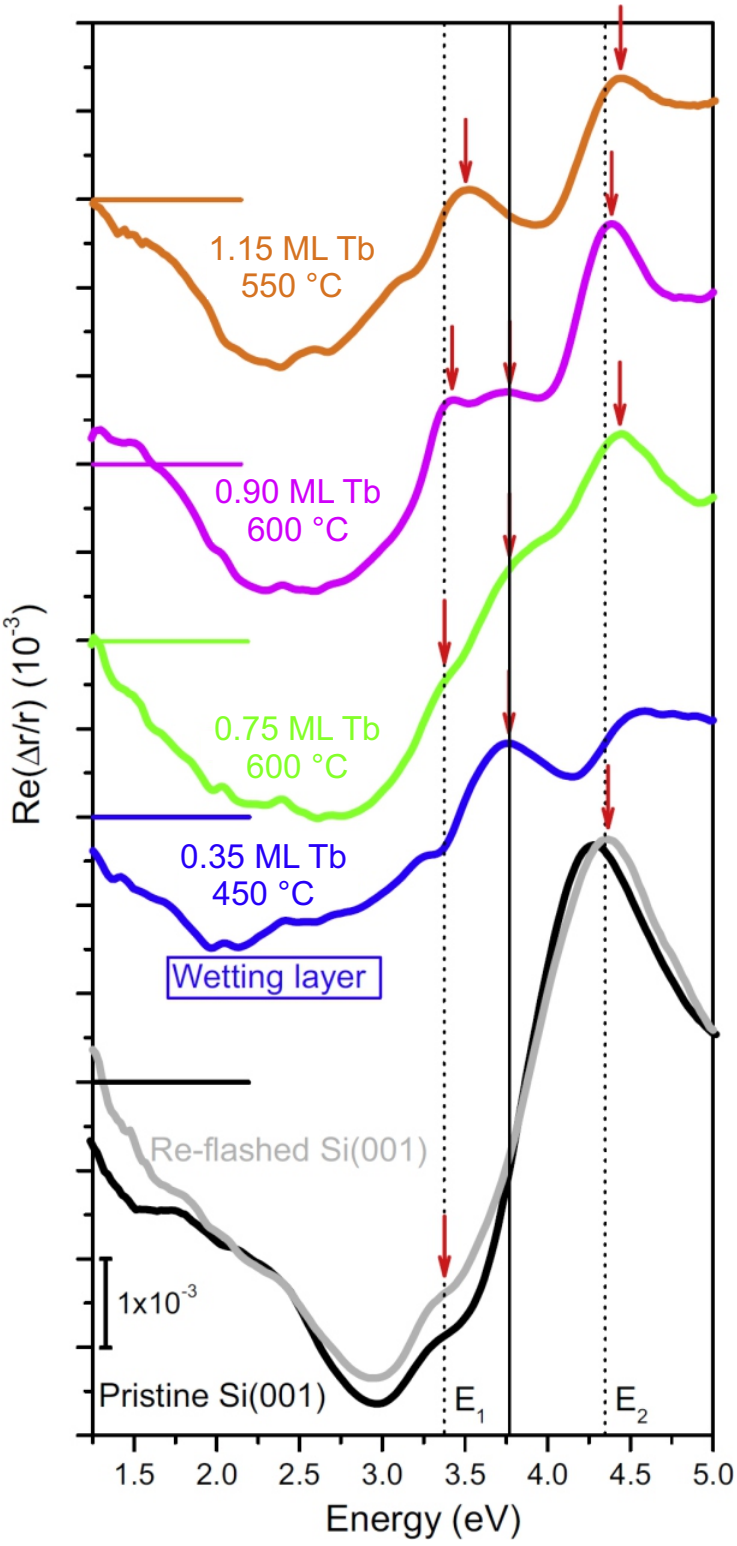

Figure 7.19.: RAS spectra of various samples that used Si(001) substrates with 4° offcut towards [110] and were prepared by Tb deposition at room temperature and annealing afterwards. The exact preparation parameters are given at the graphs. Adapted from [419].

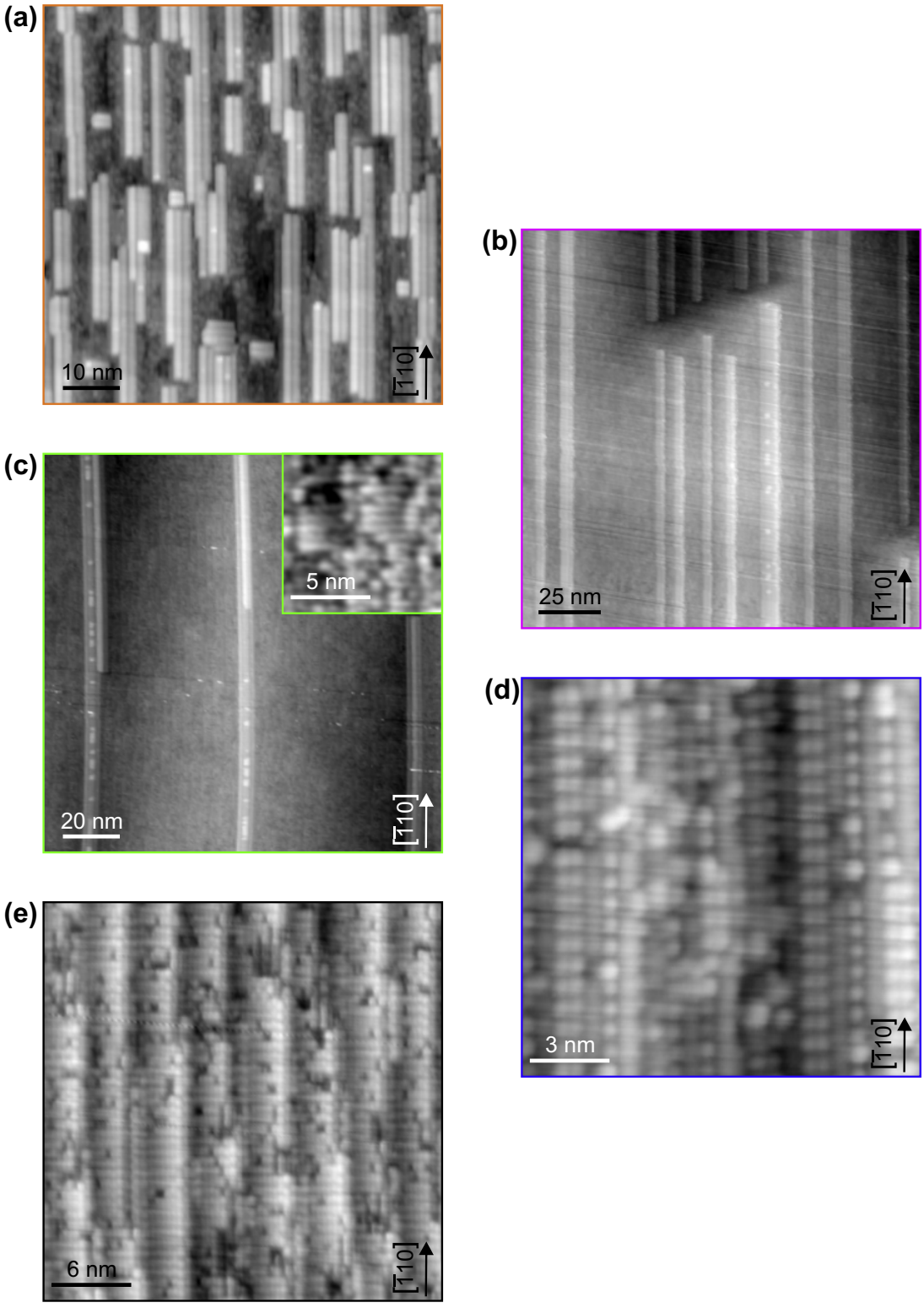

Figure 7.20.: STM images of the preparations, whose RAS spectra are shown in figure 7.19 (all $V = -1.5$ V and $I = 100$ pA). The order from top to bottom and colours of the frames correspond to the order and the colours of the graphs in figure 7.19. Adapted from [419].

incorperates a shoulder at 3.4 eV, and by a rather strong maximum around 4.2 eV. All these extrema can be assigned to certain surface structures.

The dip at 1.6 eV stems from delocalised states of the Si dimer rows [423]. To observe this minimum, the vicinal samples must not have a too large offcut and must be rather defect free since the delocalised state does not form for too short dimer rows which are disrupted by steps or defects. The depth of the broad minimum starting at 2.0 eV depends on the density of the double steps [424, 425]. The decline of the graph gets steeper at about 2.5 eV. Especially this sharper minimum around 3.0 eV is sensitive to adsorbates. Thus, it may be related directly to the dangling bonds at the step edges [424].

Up to now, all structures in the spectra could be directly related to surface structures. Beginning at 3.4 eV, extrema may also stem from bulk transitions, e.g. the shoulder at 3.4 eV and the maximum at 4.2 eV are located at the E_1 and E_2 critical points of Si, respectively. These surface-modified optical bulk transitions give a RAS signal since the anisotropic strain by the single domain surface reconstruction induces an anisotropic reflectance. Thus, they are also related to surface structures like steps and Si dimers [425–427].

During the RAS measurements, the samples were reused multiple times, i.e. a clean surface was re-prepared after a nanowire preparation by flash annealing and subsequent slow cooling. As in STM, no large changes are observed with RAS for these re-flashed samples (see grey graph in figure 7.19). The total anisotropy is slightly decreased, but the general course of the graph remains. The main difference is the vanishing of the small minimum at 1.6 eV, presumably due to an increased defect density. There is a steeper rise towards low energies, which may be caused by the missing of the minimum, but is also a signature for anisotropic metallic systems in general [428]. Here, such a metallic system may be the huge islands observed by SEM (see section 7.1), although their density on the surface may be too low to introduce a measurable signal.

The RAS spectrum drastically changes when 0.35 ML Tb are deposited on the vicinal substrate and annealed at 450 °C (see figure 7.19). STM shows that the surface is mainly covered by a rather disordered wetting layer and Si dimer rows are sparse [see figure 7.20 (d)]. Consequently, the minimum at 1.6 eV signaling well ordered dimer rows is missing. Furthermore, there is no pronounced broad minimum starting at 2.0 eV any more, indicating that the structure of the steps must have changed, e.g. by Tb covering the step edges. There is a new large maximum at 3.8 eV while the maxima at the Si critical points are strongly decreased.

In addition to the data of the clean substrate and the wetting layer, there are RAS spectra of three different nanowire samples shown in figure 7.19. While all samples showed nanowire formation, the density of them varied. The sample, for which the spectrum shown in green in figure 7.19 was taken, showed the lowest density and the sample corresponding to the orange spectrum had the highest nanowire density [see figures 7.20 (a to c)]. In between the nanowires, a step structure similar to the one of the clean substrate is observed. There are even some Si dimer rows [see inset in figure 7.20 (c)], but most terraces appear disordered. Thus, the broad minimum starting at 2.0 eV is observed in the RAS spectra of the nanowires due to the presence of the double steps, but the minimum at 1.6 eV is not visible since Si dimer rows are sparse. Interestingly, the sharper minimum at 3.0 eV is also missing indicating that the dangling bonds at the double steps may be saturated.

Not only the broad minimum, but also the maxima at the Si critical points are observed

in the RAS spectra of the samples with low and middle nanowire density, green and magenta spectra in figure 7.19, respectively. They appear slightly shifted to higher energies, which may lead to the merging of the silicide related maximum at 3.8 eV with the maximum at the E_1 critical point for the highest nanowire surface density (see orange graph in figure 7.19). The maxima at 3.8 eV are easily distinguishable for the preparations with lower Tb coverages and its observation for the wetting layer and the nanowires indicates that similar structural motives are likely to be found for both nanowires and wetting layer. It may be related to the formation of hybrid states of Si-3s3p and Tb-6s5d orbitals, i.e. to the silicide formation by bonds between Si and Tb. Such bonding states were found for Ho silicide nanostructures by metastable de-excitation spectroscopy and have an energy difference of about 4 eV to Si-3p states, which agrees well with the energy of the silicide maximum at 3.8 eV in RAS [429].

The Tb silicide nanowires may not only be responsible for the observation of the silicide maximum, but may also contribute to the maxima at the Si critical points. The silicide formation certainly introduces strain in the topmost Si layers of the substrate. While this argument may also be made for the wetting layer, the strain on the substrate increases with the thickness of the strained epitaxial layer. Thus, the influence of the nanowires may be much stronger than the one of the wetting layer. Furthermore, the strain due to the nanowires is different from the one due to the Si dimer reconstruction of the clean surface, which may be the reason for the slight shift in the energy positions of the maxima.

Concluding the above made observations, it is unambiguous that RAS is sensitive to the rare earth silicide formation and may even distinguish between nanowire and wetting layer growth. All silicide structures show a maximum at 3.8 eV, which is not observed for clean substrates, but most of the extrema characteristic for the clean substrate, e.g. the broad minimum starting at 2.0 eV or maxima at the Si critical points, are exclusively observed for nanowire samples. One may also expect that the observation of a rise towards small energies may be used to distinguish between the growth of metallic nanowires or of the non-metallic wetting layer. Indeed, such a rise was observed for all nanowire preparations, but it is also found for the wetting layer sample, possibly because the sample was not used for the first time and re-flashed clean substrates already show a similar rise.

Further information on the RAS results can be found in reference [419]. In this reference, results for Dy silicide nanostructures are presented in addition to the data for Tb silicide structures discussed here. The findings with Dy and Tb as rare earth metals agree well with each other. Thus, RAS is expected to be a suitable fingerprint technique for rare earth silicide nanostructure growth on Si(001) independent of the used rare earth metal, which also justifies the above discussion of Ho silicide studies.

7.2. Overgrowth with Si

Studying the growth and the properties of Tb silicide nanowires is very interesting, but the ultimate goal is to use them in future devices. Unfortunately, the nanowires are unstable under ambient conditions. Thus, they have to be protected by a passivation layer. Ideally, this layer would be crystalline Si to enable the most easiest integration in today's technology. A crystalline Si layer does not form for Si deposition at room temperature, meaning that the sample has to be annealed at elevated temperatures during or after the Si deposition. It

is unknown if the rare earth silicide nanowires on Si(001) remain stable upon Si deposition and annealing, but studies on the overgrowth of two-dimensional rare earth silicide layers on Si(111) by Si indicate their stability [369, 430]. Thus, the nanowires on Si(001), which may be formed of the same silicide, may also be stable.

7.2.1. Towards transmission electron microscopy samples

Initial studies on the overgrowth of rare earth silicide nanowires on Si(001) were performed by the student Milan Kubicki for Dy silicide nanowires [431]. These studies will be summarised briefly and build the basis for the following experiments.

Dysprosium silicide nanostructures were grown by deposition of submonolayer amounts of Dy and post-deposition annealing. A typical STM image of such a preparation is shown in figure 7.21 (a). Nanowires are clearly identifiable and in between them the surface appears rather disordered with subparts of the wetting layer reconstruction found in some areas.

Depositing Si on such nanowire samples and annealing the sample during or after the Si deposition at 400 °C or 450 °C, respectively, lead to rather similar surface characteristics [see figures 7.21 (b and c)]. Presumably crystalline Si forms, but the surface is very rough. Especially noticeable are troughs, in which structureless protrusions may be observed [see yellow arrows in figures 7.21 (b and c)]. Those protrusions are likely Dy silicide nanowires due to their similar appearance. While some nanowires may be covered by Si, one may still conclude that the Si crystallises preferentially in between the nanowires. This is not unexpected since the lattice constants of the silicide do not match exactly the one of bulk Si. The Si above the nanowires would be strained, which is energetically unfavourable and not the case for Si epitaxy in between the nanowires. In agreement with this Si growth model is the observation that the troughs are as deep as the thickness of the deposited Si layer or even deeper.

Another result of the work on capping Dy silicide wires is that one should not use too high annealing temperatures. For the preparation shown in figure 7.21 (d) a higher annealing temperature of 500 °C was used when compared to the Si capping procedure used for the sample shown in figure 7.21 (c). Some nanowires appear disrupted, although the thickness of the Si overlayer was reduced [red arrows in figure 7.21 (d)]. Thus, annealing temperatures well below 500 °C should be used, to prevent the destruction of nanowires already at low Si coverages.

While a decreasing Dy silicide nanowire density was observed with increasing thickness of the Si overlayer, it is unclear, if the nanowires remain stable inside a Si matrix or if the nanowires dissolve and the rare earth metal is distributed within the Si capping layer. Since the probability of the nanowire destruction increases with increasing annealing temperature, Tb silicide nanowire samples were overgrown by an about 5 nm thick amorphous Si layer at room temperature, the lowest achievable temperature at the TU Berlin setup. Cross sections of the resulting samples were then analysed using TEM methods to confirm if the nanowires survived this capping procedure. It should be noted that previous reports about TEM data on silicide structures on Si(001) mainly focussed on thicker structures, i.e. islands [432–434], so that the outcome of the TEM experiments presented here was uncertain.

Nevertheless, not only samples covered by an amorphous Si layer, but also crystallised Si

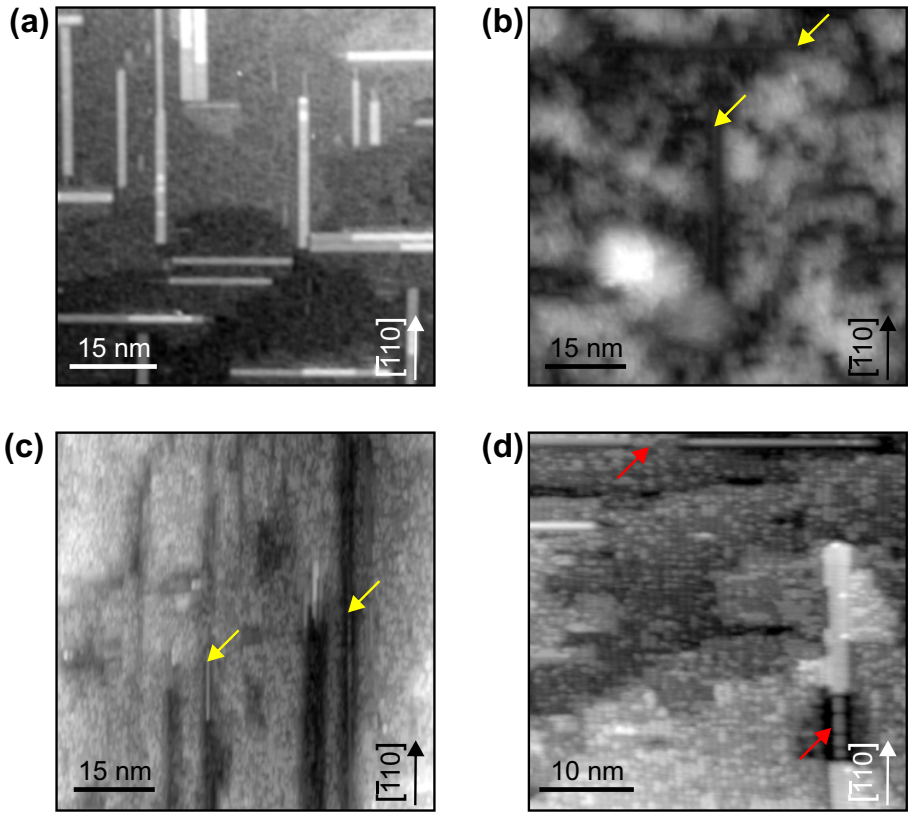

Figure 7.21.: STM images of the initial Si growth on Dy silicide nanowire samples, which were prepared on planar Si(001) substrates by deposition of 0.45 ML Dy and post-deposition annealing at 600 °C for 2 min. (a) Exemplary Dy silicide nanowire sample. (b) 0.3 nm Si deposited with the sample held at 400 °C. (c) 1.0 nm Si deposited at room temperature and 2 min annealed at 450 °C afterwards. (d) 0.5 nm Si deposited at room temperature and annealed for 2 min at 500 °C afterwards. The yellow arrows in (b and c) mark Tb silicide nanowires and the red ones in (d) indicate areas, where a nanowire may have been disrupted during the annealing of the Si layer. All STM images were taken with $V = -1.5$ V and $I = 100$ pA, except (a and b) with $V = -2.5$ V. Adapted from [431].

overlayers, again about 5 nm thick, were prepared by annealing at temperatures of 300 °C to 450 °C. Most of those samples were covered by an additional amorphous Si layer to protect nanostructures that may lie open in a trough of the crystallised Si cap. In total, 10 samples were grown for TEM studies. An overview on these samples is given in table 7.1. Of those 10 samples, 2 were studied by HRTEM and STEM and further 6 were studied by HRTEM only. Here, we concentrate on 2 samples with an amorphous Si cap (samples 1 and 8) and subsequently on 2 samples with a crystalline Si cap (samples 3 and 10). For these samples, the main aspects of the Si overgrowth can be nicely observed. These main aspects are briefly summarised after the individual samples are discussed.

The HRTEM studies were performed in the work group of Prof. Dr. Michael Lehmann (TU Berlin) by the students Paul Reiß and Jonas Heggemann, who were co-supervised by me and Dr. Tore Niermann, who also initiated the STEM experiments performed by Dr.

Table 7.1.: Overview on the samples prepared for TEM investigations, also showing if they were analysed by HRTEM or STEM. All nanowires were prepared by depositing a certain Tb amount (Θ_{Tb}) at room temperature and heating the sample for 2 min to the annealing temperature (T_{Tb}) afterwards. In general, the Si cap consists of two parts: a crystalline cap grown with a certain Si amount (Θ_{crys}) followed by an amorphous layer of a certain thickness (Θ_{amo}). To form the crystalline caps, the samples 2 and 3 (6, 9, and 10) were annealed after (during) the first Si deposition to the Si annealing temperature (T_{Si}).

	Nanowire sample			Si cap				
#	Substrate	Θ_{Tb}	T_{Tb}	Θ_{crys}	T_{Si}	Θ_{amo}	HRTEM	STEM
1	4° offcut	0.65 ML	600 °C	–	–	5.4 nm	Yes	Yes
2	4° offcut	0.65 ML	600 °C	5.4 nm	450 °C	5.4 nm	No	No
3	4° offcut	0.65 ML	600 °C	5.4 nm	450 °C	5.4 nm	Yes	Yes
4	Planar	0.70 ML	600 °C	–	–	4.0 nm	Yes	No
5	Planar	0.70 ML	600 °C	–	–	5.0 nm	Yes	No
6	4° offcut	0.70 ML	600 °C	5.0 nm	400 °C	–	Yes	No
7	Planar	1.75 ML	600 °C	–	–	5.0 nm	No	No
8	Planar	1.50 ML	575 °C	–	–	5.0 nm	Yes	No
9	Planar	0.90 ML	550 °C	5.0 nm	300 °C	3.0 nm	Yes	No
10	4° offcut	0.90 ML	550 °C	5.0 nm	350 °C	3.0 nm	Yes	No

Markus Andreas Schubert [IHP Frankfurt (Oder)]. In addition to the preparation and STM characterisation of the samples, mostly together with the students, my contributions lie within the interpretation and discussion of the data.

7.2.2. Nanowire samples capped by amorphous Si

Sample 1 used a vicinal substrate. Consequently, the nanowires mainly form parallel to each other, as is nicely seen with STM [see figure 7.22 (a)]. Due to the rather low Tb coverage and high annealing temperature (see table 7.1), the nanowires agglomerate in bundles and their density is rather low. The amorphous Si cap appears in STM as if the surface is covered by small Si clusters [see figure 7.22 (b)]. While the capping layer is generally rather homogeneous, there are elongated protrusions apparent. The apparent height of the protrusions varies monotonically along the length of the protrusion, similar as the apparent height of the nanowires, which also changes monotonically along their length due to the step misalignment. Thus, those protrusions indicate that nanowires are still intact under the amorphous Si layer.

Due to the low nanowire density, the probability to observe nanowires from the side, i.e. along [110], is low since TEM samples have to be thin. Thus, all TEM sample pieces of sample 1 were prepared in such a way that the cross sections of the nanowires are investigated, i.e. the electrons pass the sample along $[\bar{1}10]$.

Two HRTEM images presumably of nanowire cross sections are shown in figures 7.22 (c and d). Both images are dominated by a periodic structure at the bottom and an irregular

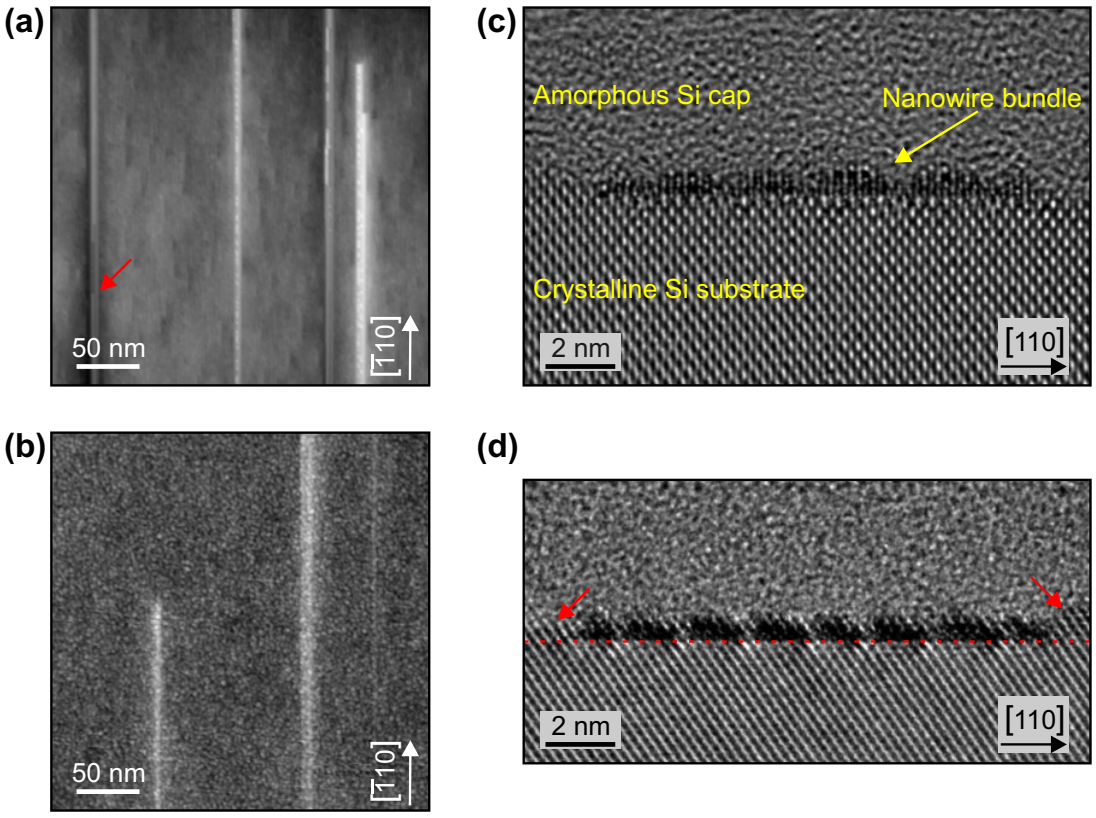

Figure 7.22.: STM and HRTEM images of sample 1. (a) The nanowire preparation as viewed in STM ($V = -1.5$ V and $I = 100$ pA). (b) STM image of the nanowire sample capped by 5.4 nm amorphous Si before the sample was moved out of the UHV ($V = -2.5$ V and $I = 100$ pA). (c and d) HRTEM images of the cross sections of nanowire bundles consisting of 6 and 8 nanowires, respectively. The images were taken with electrons accelerated by $V_{\mathrm{HRTEM}} = 300$ kV. In (d), the hatched red line indicates the basis of the nanowire bundle. The red arrows in (a and d) indicate areas, where nanowires may have grown into the substrate.

appearance at the top, corresponding to the Si substrate and the amorphous Si cap, respectively. At the interface between substrate and amorphous Si, there are darker appearing areas in the centre of the images, which are presumably the Tb silicide nanowires. These dark areas are divided into several substructures by notches in the dark areas, indicating that not single nanowires, but nanowire bundles may be imaged. The presence of nanowire bundles would agree nicely with the STM measurement on this sample. Taking into account that similar structures are found regularly at the interface between substrate and amorphous Si, it is concluded that these structures are indeed nanowires, i.e. the nanowires survived the capping by amorphous Si. The Si layer certainly influences the nanowire surface, but it is assumed that the inner structure of the nanowire is stable, so that structural information may be gained by HRTEM (see section 7.3).

Based on the HRTEM data, the average distance between the centres of neighbouring nanowires is about $6\, a_{\mathrm{Si}(001)}$ in good agreement with the STM and LEED results yielding

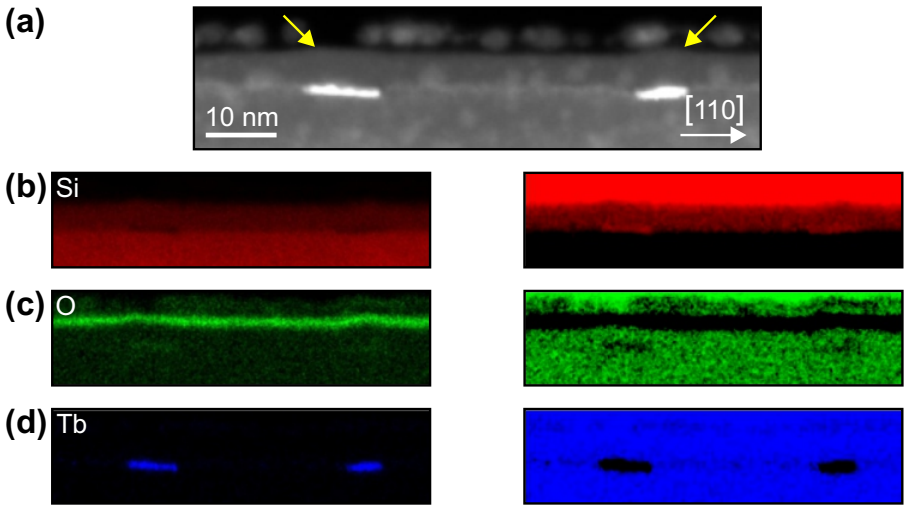

Figure 7.23.: STEM data of sample 1 taken with electrons accelerated by $V_{\mathrm{STEM}} = 200$ kV [435]. The images were taken simultaneously, i.e. they show exactly the same sample area. (a) HAADF image. (b to d) EDX images, i.e. maps of the distribution of Si (red), O (green), and Tb (blue), obtained by measuring the intensities of the characteristic X-rays Si-K_α, O-K_α, and Tb-L_α, respectively. In the left images, high intensity corresponds to high element content while the contrast is inverted and increased in the right images. The yellow arrows in (a) mark protrusions of the amorphous Si above the nanowires.

$5.7\,a_{\mathrm{Si}(001)}$ and $5.4\,a_{\mathrm{Si}(001)}$, respectively (see section 7.1.1). All nanowires of the bundles in figures 7.22 (c and d) have their basis at the same height, i.e. they formed on a single terrace, which is much wider than the average terrace width on the clean substrate. This agrees well with the STM observations made for nanowire growth on vicinal surfaces (see section 7.1.2). In figure 7.22 (d), crystalline Si is not only observed below the nanowire bundle, but also at the same height besides the nanowire bundle. Thus, the nanowire may have grown locally into the substrate, as also observed in STM (red arrows in figure 7.22).

A small discrepancy between HRTEM and STM measurements is that no clear indications for protrusions of the amorphous Si above a nanowire bundle was found in HRTEM, but such protrusions are evident in the HAADF image of sample 1 shown in figure 7.23 (a). Due to the high atomic number of Tb, the nanowire bundles are easily identifiable as the very bright bars in the HAADF image. Above the nanowire bundles, the amorphous Si, appearing homogeneously grey, shows small protrusions [yellow arrows in figure 7.23 (a)]. The slightly brighter horizontal stripe in the height of the nanowire bundles may be due to Tb structures on the surface, e.g. parts of the wetting layer, but the additional bright appearing spots are residues of the TEM sample preparation lying on the sample cross section. Those are not seen that clearly in HRTEM due to the different contrast mechanisms (see section 4.2).

Simultaneously with the HAADF data, also EDX images were taken [see figures 7.23 (b to d)]. In the Si content map, the crystalline Si substrate, the amorphous Si cap, and the Tb silicide nanowires can be nicely distinguished due to a decreasing Si density within this

sequence. There is a huge O density across the top of the sample since it is oxidised along the complete sample depth (along $[\bar{1}10]$ direction). Interestingly, the nanowires are also recognisable in the O content map indicating either that they are stronger, i.e. deeper, oxidised than the surrounding material or that the O density in the formed Tb silicide oxide is higher than in the formed Si oxide. Unsurprisingly, most of the Tb is located in the nanowires. There is additional Tb at the interface between substrate and amorphous Si, as expected from the HAADF data, but there is no Tb detectable in the amorphous Si, so that a dissolution of nanowires during the Si deposition at room temperature can be excluded. While it appears as if there is a small amount of Tb at the top of the sample, this signal stems from Fe, whose K_α-line lies energetically close to the L_α-line of Tb used for the mapping. This was clarified by measuring X-ray spectra over a wide energy range while scanning along the top of the sample and analysing the observed lines in detail.

Up to now only the cross sections of nanowires were analysed. To get information on the side view of nanowires, sample 8 used a planar substrate, which was densely covered by nanowires [see figure 7.24 (a)]. The amorphous Si layer again appears to consist of small Si clusters and preserves the morphology of the underlying surface [see figure 7.24 (b)].

For this sample, cross sections of the very wide nanowire bundles are routinely observed in HRTEM [see figure 7.24 (c)]. With about $5\,a_{\mathrm{Si}(001)}$, the average distance between the centres of neighbouring nanowires is again in good agreement with the STM and LEED results. There are also no obvious differences between the nanowire cross sections on vicinal and planar surfaces, supporting the assumption based on STM data that the same nanowires form [compare figures 7.22 (c and d) and 7.24 (c)].

Not all darker appearing wide areas at the interface between substrate and amorphous Si are divided into substructures, but there are also continuously appearing darker areas [see figure 7.24 (d)]. The height of these darker areas is the same as the one of nanowire cross sections. Thus, they are presumably side views through multiple nanowires. That only one nanowire contributes to a nanowire side view is rather improbable since such thin samples would not be stable under the electron beam. The continuous appearance of the side view shows that the nanowire does not fragment into multiple smaller parts upon Si capping at room temperature.

Interestingly, most nanowires of sample 8 appeared to be lying in a valley of crystalline Si and sometimes there appears to be crystalline Si even above nanowires [see yellow arrow in figure 7.24 (c)]. The Si atoms and clusters emitted from the evaporator and impinging on the surface may have sufficient thermal energy to arrange in a crystalline manner even when the sample is not additionally heated. This occurs most likely in areas without nanowires since crystalline Si grows unstrained there. The growth of well ordered Si on a nanowire is possible, but the observation of Si above a nanowire may also be caused by the electrons passing through a nanowire and crystalline Si in succession. Such a scenario also accounts for the different appearance of the Si above the nanowire. Thus, at most very few nanowires are embedded into crystalline Si, so that a sample has to be annealed to embed all nanowires in a crystalline Si matrix. Samples, whose Si caps were annealed, are presented in the following.

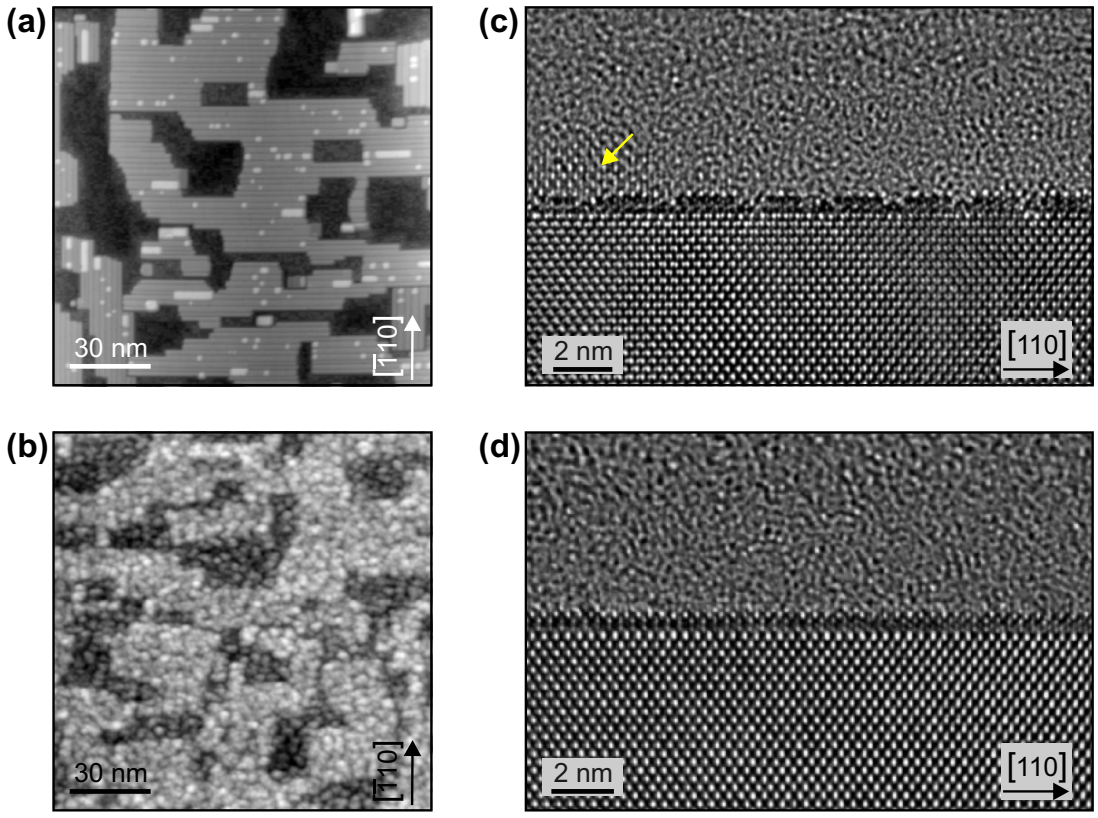

Figure 7.24.: STM and HRTEM images of sample 8. (a and b) STM images of the nanowire preparation and the 5.0 nm thick amorphous Si cap (both $V = -2.5$ V and $I = 100$ pA). (c) HRTEM image of the cross sections of nanowires ($V_{\mathrm{HRTEM}} = 300$ kV). The yellow arrow indicates an area where there may be crystalline Si above the nanowires. (d) HRTEM image presumably showing the side view through multiple nanowires ($V_{\mathrm{HRTEM}} = 200$ kV).

7.2.3. Nanowire samples capped by crystalline Si

Similar as for the preparation of nanowires, the sample may be annealed during or after the Si deposition to grow crystalline Si. Here, both annealing schemes are discussed with sample 3 being annealed at 450 °C after the Si deposition and sample 10 annealed at 350 °C during the Si deposition.

Since the same preparation parameters were used, the nanowire growth on sample 3 is similar to the one of sample 1 discussed above [see figure 7.25 (a)]. The main difference is that more minority domain nanowires formed on sample 3. The morphology of the Si cap drastically changed due to the annealing. Instead of the homogeneous cap of small clusters, larger protrusions and wide troughs dominate the surface appearance [see figure 7.25 (b)]. That the crystallisation of the amorphous Si was successful can already be deducted by the observation of Si dimer rows at the surface of the capping layer [see inset in figure 7.25 (b)]. The observation of the anisotropic troughs indicates that there may still be silicide nanowires below the crystalline cap, but no final conclusions can be drawn by STM alone.

Cross-sectional views of sample 3 along [$\bar{1}$10] are shown in the figures 7.25 (c to e). No

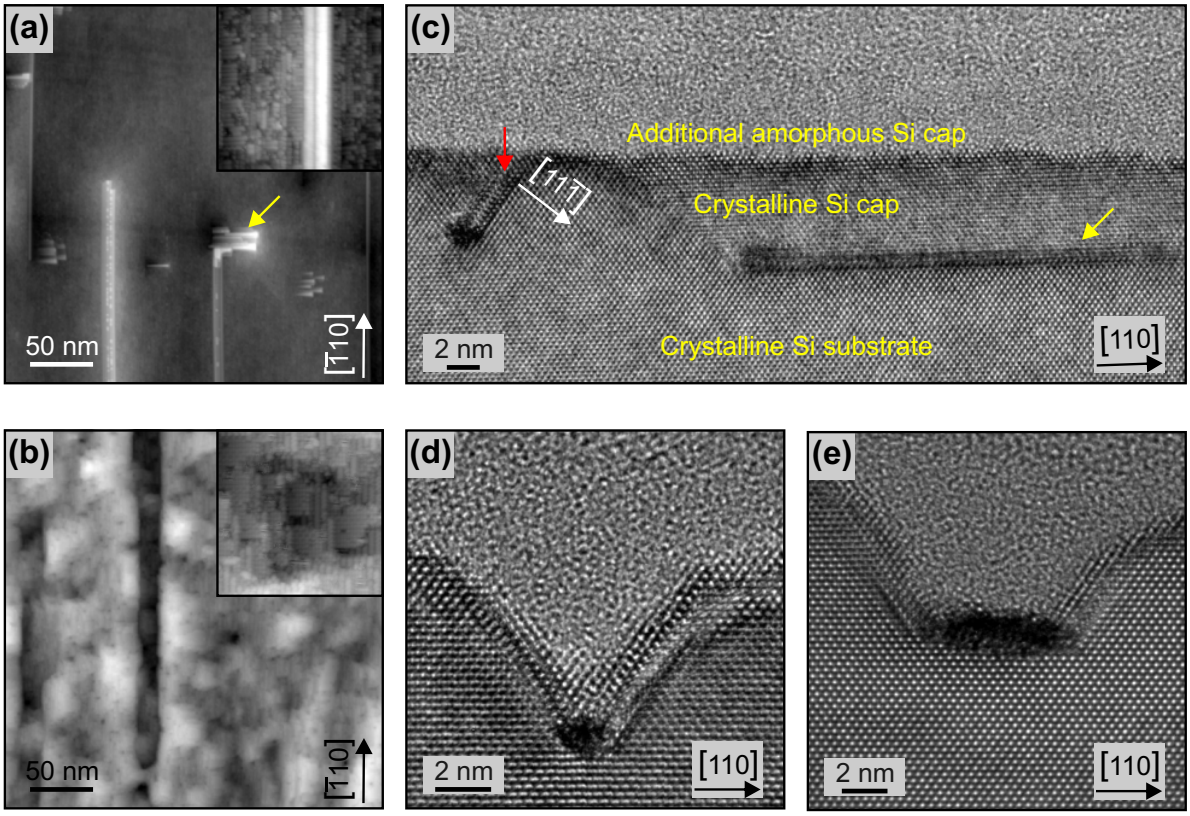

Figure 7.25.: STM and HRTEM images of sample 3 capped by 5.4 nm Si followed by annealing at 450 °C. (a and b) STM images (a) before and (b) after capping. The 25 nm wide insets show the presence of Si dimer rows. All STM images were recorded with $V = -1.5$ V and $I = 100$ pA. (c) HRTEM image showing on its left side a nanowire completely covered by crystalline Si. (d) HRTEM image of a nanowire embedded in crystalline Si that formed a through above the nanowire. (d) HRTEM image showing a nanowire, above which no Si crystallised. The electrons were accelerated by $V_{\mathrm{acc}} = 300$ kV for all HRTEM images. The yellow arrows in (a and c) mark presumably minority domain nanowires and the red one indicates a stacking fault in a {111} plane.

wide dark stripes with notches are observed in contrast to sample 1. Instead, three round dark structures and one stripe without notches are observed. Assuming that the Tb is again mainly found in the darker appearing areas, the wide nanowire bundles have transformed into the more compact, i.e. higher and narrower, round structures meaning that intensive material transport took place during the annealing. Such compacter structures have a much smaller interface area with their surrounding, may be less strained, and may also exhibit fewer stress on their surrounding reducing the total interface energy. The darker horizontal stripe in figure 7.25 (c) may stem from a minority domain nanowire and its continuous appearance is a first indication that the nanowires have not fragmented into smaller parts despite the material reorganisation.

In surface areas besides the nanowires, the amorphous Si recrystallised in phase with the substrate and without visible defects, i.e. the disordered surface morphology including

the wetting layer structures did not prevent the Si homoepitaxy. In contrast, troughs are often found in the crystalline Si cap above nanowires, sometimes even reaching down to the nanowires, in accordance with the STM observations [see figures 7.25 (b, d, and e)]. Even when a nanowire is completely covered, the crystalline Si is seldom defect-free in its vicinity. Often stacking faults or twins form in {111} planes with their origins at a nanowire [see red arrow in figure 7.25 (c)]. Stacking faults lead to a shift of the lattice while its orientation remains, and twins reverse the stacking order of lattice planes along a certain direction, i.e. change the orientation of the lattice. Here, the formation of twins and stacking faults in {111} planes agrees nicely with the energetically most favourable interface orientation between amorphous and crystalline Si leading to crystallisation fronts moving in $< 111 >$ directions [436].

The HAADF image of sample 3 shown in figure 7.26 (a) indicates that most of the Tb is found in the compact nanowires and that there are no other areas with high Tb content, i.e. the Tb at the interface between substrate and Si cap, which was observed for sample 1, segregated during the annealing. The EDX data reveal that the compact structures have a lower Si density and they may be more oxidised than the crystalline and amorphous Si similar to the nanowire bundles of sample 1 [see figures 7.26 (b and c)]. The compact structures also contain most of the Tb justifying the above assumption that they are Tb silicide structures [see figure 7.26 (d)].

Interestingly, the Tb distribution map shows that Tb is not only in the nanowires, but also very diluted in the crystalline Si cap [see figure 7.26 (d)]. This Tb may stem from the wetting layer, which was present before the annealing, or from the transformation of the nanowires. Due the very low Tb density at the resolution limit, no meaningful segregation profiles can be obtained to identify the source of Tb or to find out if the Tb distribution is as homogeneous as it appears in the Tb distribution map. There are no indications for segregation of Tb into the substrate or for an increased Tb content in the stacking faults. Thus, the stacking faults are not related to any kind of silicide formation.

During the nanowire preparation of sample 10, a higher Tb amount was deposited than during the nanowire preparation of sample 3 resulting in a higher nanowire density [see figure 7.27 (a)]. Similar to sample 1 and in contrast to sample 3, basically all nanowires form parallel to each other and very few are observed on minority terraces.

For sample 10, the crystalline Si cap was grown by Si deposition at elevated temperature. This capping layer is similarly rough as the crystalline cap of sample 3, but no comparable troughs are found [see figures 7.25 (b) and 7.27 (b)]. This observation may be related to the different annealing scheme or possibly also to the different nanowire preparation. Individual troughs above nanowires may not be as obvious since they may overlap due to the increased nanowire density. It cannot be excluded by STM that the nanowires dissolved during the Si capping, but the observation of Si dimer rows and the missing of Tb structures on the surface of the capping layer indicates the preservation of the nanowires and proves the crystallinity of the Si cap [see inset in figure 7.27 (b)].

That Tb silicide structures are still present after the capping procedure is indicated by the observation of darker appearing areas in cross-sectional HRTEM [see figures 7.27 (c and d)]. Due to the very similar appearance of these structures to the Tb silicide structures found for sample 3, e.g. they are much narrower and higher than the nanowire bundles observed beneath an amorphous Si cap, they are assumed to be Tb silicide structures. Often

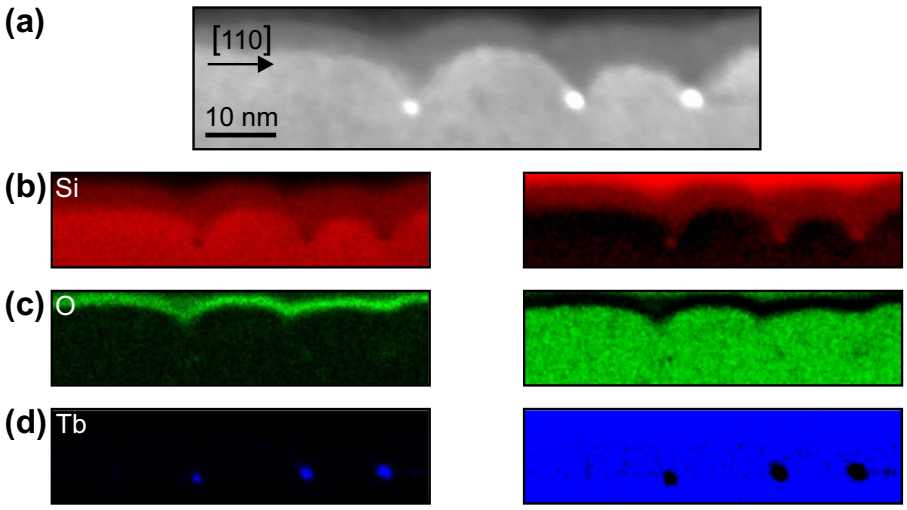

Figure 7.26.: STEM data of sample 3 (V_{STEM} = 200 kV) [435]. The same area is shown as (a) HAADF image and (b to d) EDX images, i.e. maps of the distribution of Si (red), O (green), and Tb (blue). In the left EDX images, high intensity corresponds to high element content while the contrast is inverted and increased in the right EDX images.

troughs are observed above these structure and stacking faults and twins may form at their boundaries, which is again similar to the observations for sample 3. However, such defects do not have to form in general, as seen for the Tb silicide structure marked by a yellow circle in figure 7.27 (d).

For sample 3, the troughs in the crystalline Si cap were always centred above a nanowire. In contrast, Tb silicide agglomerations are often found in the edges of broad troughs for sample 10 [see yellow arrows in figures 7.27 (c and d)]. While this difference may arise due to the different annealing scheme and temperature, no final conclusions should be made since the nanowire preparations of sample 3 and 10 were too different. The observation of wide troughs for sample 10 may be related to the high nanowire density compared to sample 3. Wide nanowire bundles or multiple nanowire bundles close together may prevent the growth of strain-free Si in a wide area. The crystalline Si protrusions next to the troughs are very high and may clearly exceed the nominally deposited Si amount. Thus, at least a part of the Si atoms that landed on the Tb silicide nanowires diffused to the surrounding Si during the Si deposition at elevated temperatures. The Tb silicide may self-assemble at the edge of a trough, but such an agglomeration may also be caused by the Si crystallisation. The Si crystallisation fronts are {111} planes, which may push the Tb silicide towards compacter structures during the crystallisation of pure Si planes, similar to a snowplough. This would also lead to the agglomeration of Tb silicide in the edge of a trough.

Due to the high nanowire density of sample 10, a reasonable amount of Tb silicide structures may also be observed in thin HRTEM samples that were prepared in such a way that the electrons pass the sample along [110]. Indeed, darker appearing areas, characteristic for Tb silicide structures, are observed in HRTEM images of such samples (see figure 7.28). These areas are very wide and continuous indicating that there are nanowires that did

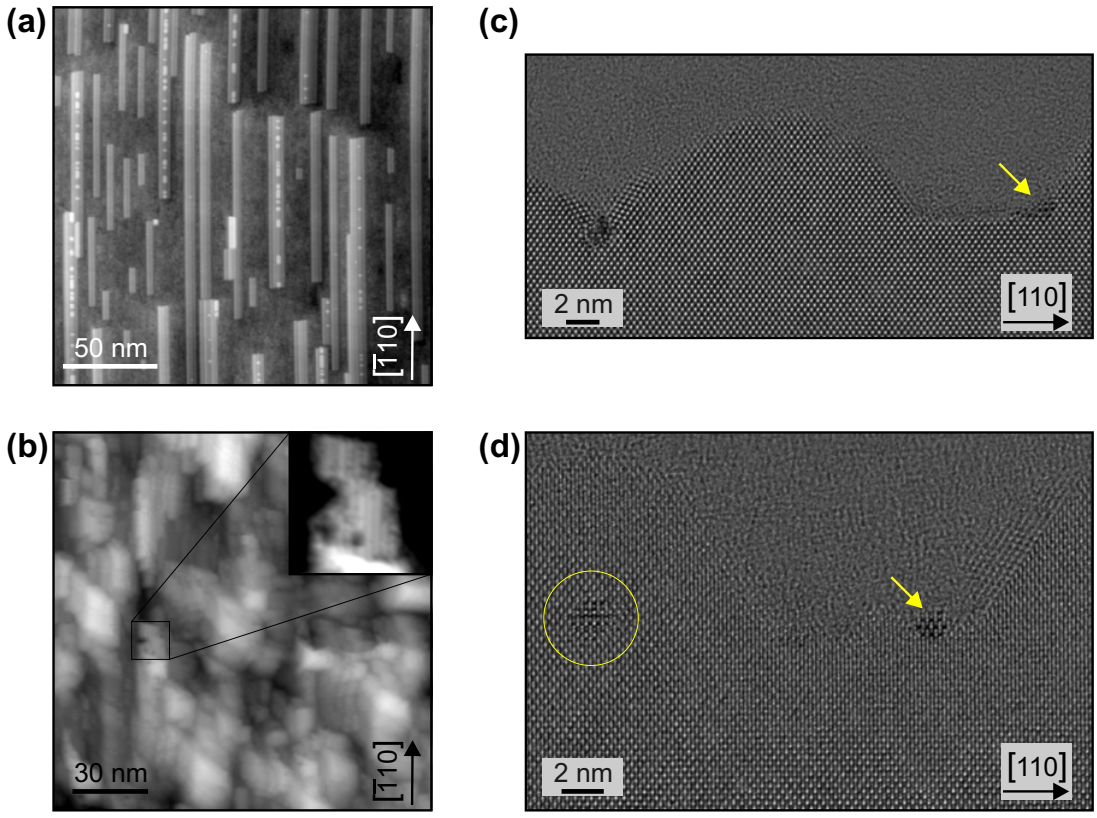

Figure 7.27.: STM and HRTEM images of sample 10 capped with 5.0 nm Si at 350 °C. (a and b) STM image of the nanowire preparation (both $V = -1.5$ V and $I = 100$ pA). (b) STM image of the crystalline Si cap ($V = -2.5$ V and $I = 100$ pA). While structures are imaged multiple times due to the tip shape, there are Si dimer rows resolved, as it is shown in the contrast enhanced inset. (c and d) HRTEM images of nanowire cross sections ($V_{\mathrm{HRTEM}} = 300$ kV). The yellow arrows mark Tb silicide accumulations in the edges of troughs and the yellow circle indicates a Tb silicide structure that is embedded defect-free in the surrounding crystalline Si.

not fragment into smaller parts. Although their appearance varies along their length, one cannot generally conclude that the structure of the nanowire changes along their length, since usually also the appearance of the substrate changes, e.g. indicating a variation of the sample thickness. The thin HRTEM samples are still thicker than the width of a compact nanowire, as revealed from figure 7.28 (b) by the imaging of multiple nanowires at different terraces. Thus, their appearance in side-view HRTEM images is always also influenced by the Si in front of and/or behind the nanowires making a detailed structural analysis impossible.

In contrast, the image of nanowire cross sections may be generated by electrons exclusively passing through the nanowire structures. Thus, structural information may be gained from such HRTEM images with sufficient resolution.

Already the uncapped rare earth silicide nanowires are assumed to consist of Si rich silicides due to the large Si reservoir in form of the substrate and the direct formation of Si

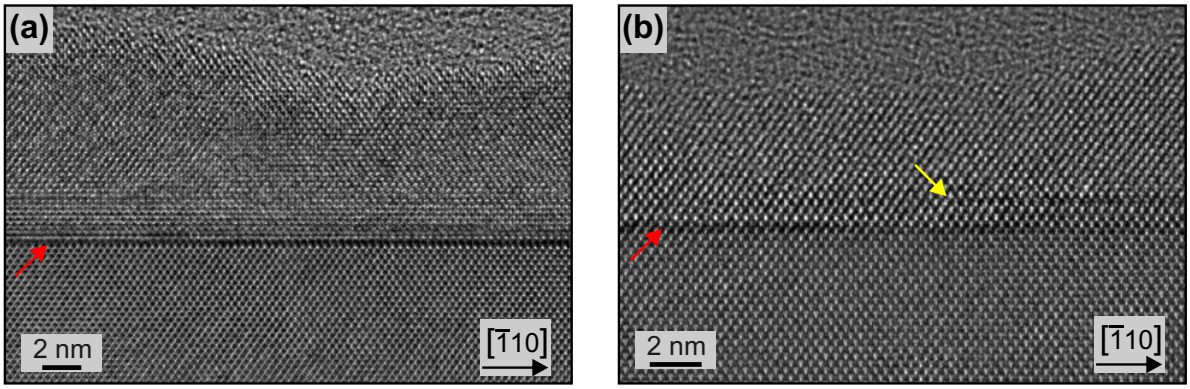

Figure 7.28.: (a and b) HRTEM images of sample 10 taken with the electron beam parallel to [110] (both $V_{\mathrm{HRTEM}} = 300$ kV). The red arrows mark wide darker appearing areas found across the entire HRTEM images and the yellow arrow indicates a darker area that starts in the image.

rich silicides even for the annealing of thick rare earth layers on clean Si surfaces [304, 305]. This argumentation should especially be valid for silicide structures embedded in a Si matrix.

The idealised structures of the Si richest rare earth silicides are already shown in figure 5.8 (b), but for an easier comparison with the HRTEM data, their projections along the expected viewing axes are shown in figures 7.29 (a and b). Those axes are characterised by Si-Si bonding arrangements in the silicide that are similar to the ones in crystalline Si. Other alignments between silicide and substrate are improbable since they would not fit structurally in the surrounding Si matrix leading to much larger strain.

While two different appearances may be found for the hexagonal structure depending on the orientation of the silicide, the tetragonal silicide always has the same appearance [see green guides to the eyes in figures 7.29 (a and b)]. All these different appearances are observed in cross-sectional HRTEM data of the compact nanowires embedded in crystalline Si [see figures 7.29 (c to e)]. Thus, the formation energies of the different structures may be rather similar. This is especially interesting regarding the orientation of the hexagonal silicide. Based on different lattice mismatches for the different axes, the exclusive growth of a specific orientation may have been expected, but is not observed.

In general, nanowires do not show only one single appearance, but a mixture of the different appearances may be observed. Furthermore, the inner structures of the nanowires often appear distorted making a designation to one of the structures impossible. Such distortions arise due to the stress from the surrounding crystalline Si or by the formation of Si vacancies in the silicide, which are typical for Si-rich bulk rare earth silicides [273]. While the centre of a compact nanowire may be clearly imaged by HRTEM, the interface between nanowire and crystalline Si usually appears fuzzy, indicating that the interface varies along the thickness of the sample while the interior of a nanowire may be periodic on this length scale.

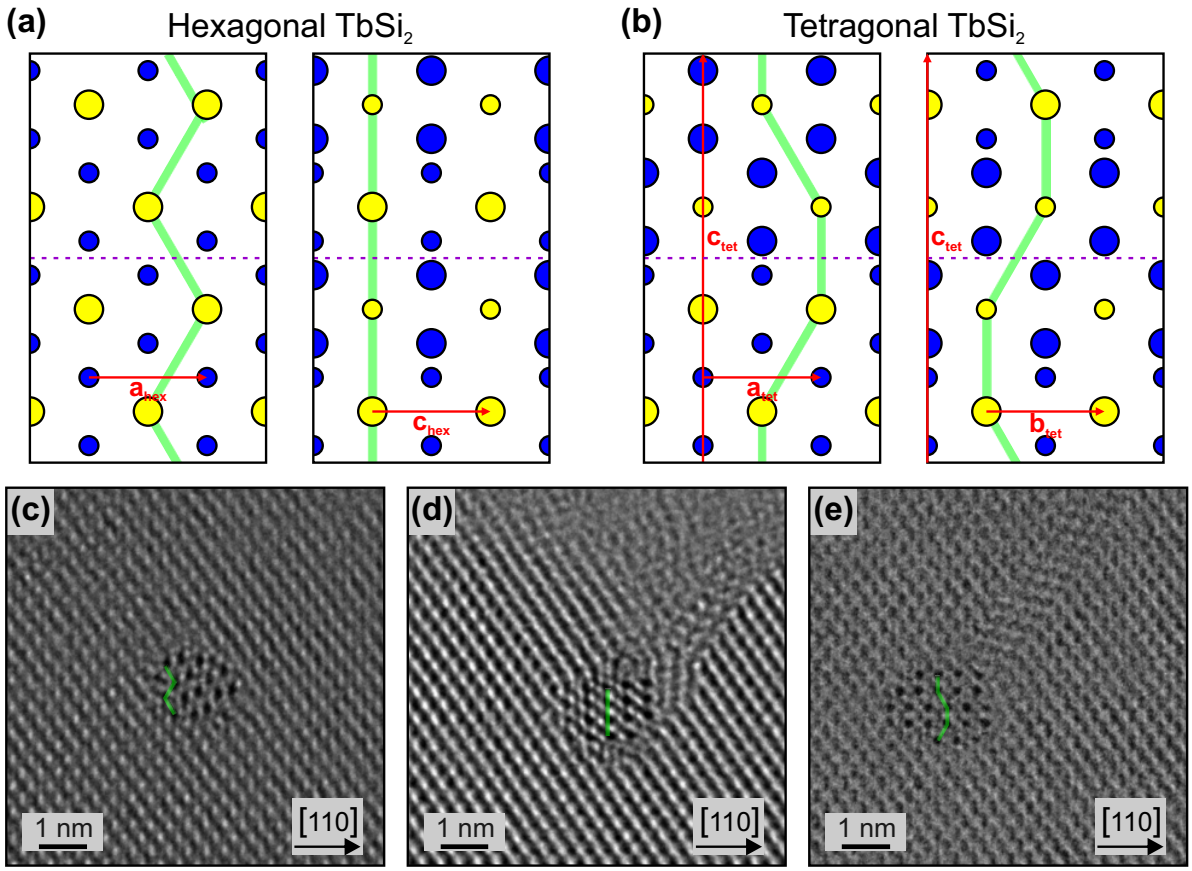

Figure 7.29.: (a and b) Schematic structure models of the idealised (a) hexagonal and (b) tetragonal $TbSi_2$ structures, from left to right viewed along c_{hex}, a_{hex}, b_{tet}, and a_{tet}. Si and Tb atoms are coloured blue and yellow, respectively, while large and small atoms lie in different depths, but are not discernible by HRTEM. The green lines are guides to the eyes connecting sites that should appear similar in HRTEM and the hatched purple lines indicate heights of two silicide layers. (c to e) Detailed HRTEM images of sample 10 showing symmetries expected for $TbSi_2$ structures as illustrated by the green guides to the eyes (all images obtained with $V_{HRTEM} = 200$ kV).

7.2.4. Summary of Tb silicide nanowire overgrowth by Si

A schematic overview on the overgrowth of Tb silicide nanowires by Si is given in figure 7.30. When the Si deposition begins, there are nanowires, possibly agglomerated in bundles, on the well ordered crystalline substrate, which is usually at least partly covered by a wetting layer [see figure 7.30 (a)].

If the sample is not annealed during this deposition, a homogeneous amorphous Si layer forms [see figure 7.30 (b)]. This amorphous Si layer certainly influences the surface of the silicide structures, but presumably not their inner structure since there is no segregation of Tb into it and the existence of nanowire bundles is still clearly observed.

Annealing a sufficiently thick amorphous Si layer leads to the embedding of nanowires in a crystalline Si matrix [see figure 7.30 (c)]. During the annealing, the nanowires of nanowire bundles agglomerate to compact structures that are narrower and higher than the initial

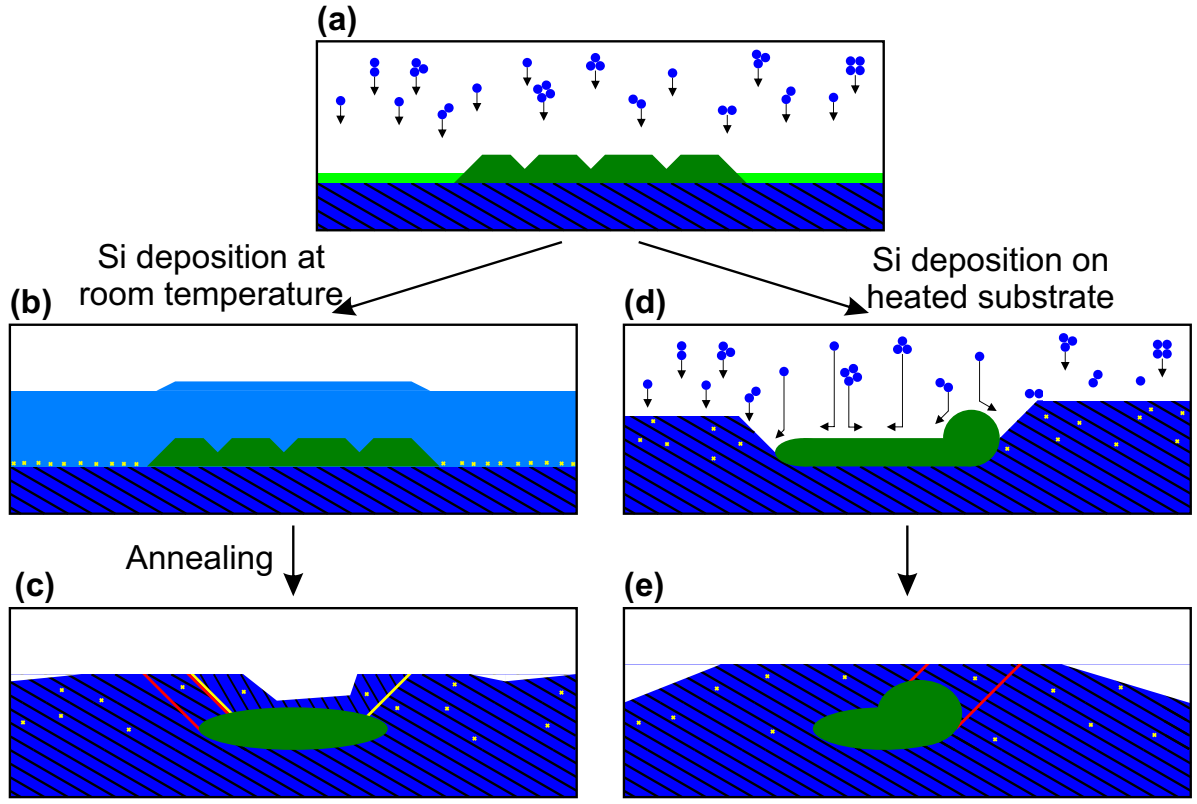

Figure 7.30.: Schematic diagram of the overgrowth of Tb silicide nanowires by Si with or without annealing after or during the Si deposition. Tb silicide is shown in dark green, the wetting layer in light green, crystalline Si in dark blue, amorphous Si in light blue, Si atoms as small blue circles, and Tb atoms as yellow crosses. The segregation of Tb atoms into the crystalline Si cap by annealing during the Si deposition is only presumed. Red and yellow lines indicate stacking faults and twins, respectively. Their influence on the orientation of the crystalline Si is indicated by the changed hatching of the crystalline Si.

nanowire bundles. Such a structural change upon embedding in a crystalline matrix is known from other systems, e.g. InAs quatum dots on GaAs(001) change their form from pyramidal to truncated pyramids upon embedding in a crystalline GaAs matrix [437–439].

The compact Tb silicide structures still have cross sections in the nm regime and extend over long distances, so that they can still be identified as nanowires. While the Si far away from the nanowires crystallises in perfect order with respect to the substrate, stacking faults and twins are frequently observed at nanowires. Furthermore, troughs often form above the nanowires leading to a rough surface appearance of the crystalline Si cap.

When the sample is annealed during the Si deposition, the deposited Si preferentially chemisorbs besides the nanowires, so that the nanowires may lie in a trough [see figure 7.30 (d)]. Inside such troughs, Tb silicide agglomerations are often observed in their edges. For sufficient Si coverages, nanowires may be completely embedded in Si [see figure 7.30 (e)]. Again, nanowire bundles become compact nanowires during the embedding, probably without disruption along their length, and stacking faults and other defects are

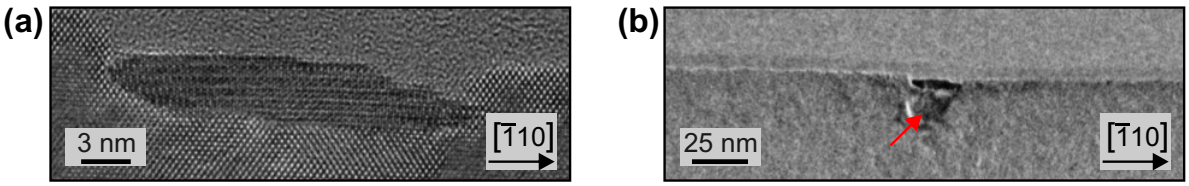

Figure 7.31.: HRTEM images of sample 5 (both $V_{\mathrm{HRTEM}} = 300$ kV). The red arrow marks a large defect in the Si substrate.

observed in the vicinity of the nanowires.

In general, the compacter nanowires appear to consist of hexagonal and tetragonal $TbSi_2$. Terbium is not only located in the nanowires, but also at the interface between Si cap and substrate for an amorphous Si cap and very diluted in crystalline Si caps. The wetting layer structures dissolve, but it is unclear if the compact nanowires contain as much or possibly even more Tb than the nanowires before capping. Comparing the areas of cross sections of the nanowire bundles before the capping, calculated by their apparent width in STM and an assumed height of two monolayers (see section 7.3), with the ones observed for the compact nanowires, they are in the same range, typically about 3 nm^2. Nevertheless, no definitive answer can be given due to the large variations in the cross sections and the small sample size.

The samples analysed by STEM never showed a measurable Tb concentration in the substrate. Thus, Tb does not segregate into the substrate during the nanowire preparation. However, Tb segregation during the flash annealing used to recover a clean substrate after Tb deposition cannot be excluded since the nanowire preparations on the TEM samples 1 and 3 were the first ones on these substrates.

Nanowires are the dominant, but not the only Tb silicide structures, which are observed in HRTEM. Figure 7.31 (a) shows an island found in TEM sample 5. In the area close to the island, no nanowires are observed [see figure 7.31 (b)]. Islands of similar size were sometimes also observed with HRTEM in other samples, especially when the annealing temperature during the nanowire preparation was high. Their dimensions agree well with the ones found by STM for a high annealing temperature (see section 7.1), but the island shown in figure 7.31 may be a part of a huge island since this substrate was already used for other nanowire preparations before the TEM sample preparation. An indication for this may be the large defect in the Si substrate below the island [red arrow in figure 7.31 (b)].

The experiments conducted here on the overgrowth of Tb silicide nanowires by Si are only a first step. It was shown that it is possible to embed Tb silicide nanowires in a crystalline Si matrix, but there are still many open questions, which should be addressed in future studies, e.g. if Tb segregates into the substrate during flash annealing or if the compact nanowires have similar properties as the surface nanowires. The properties of Tb silicide nanowires on Si(001) will be the focus in the remaining chapter, starting with their atomic structure in the next section.

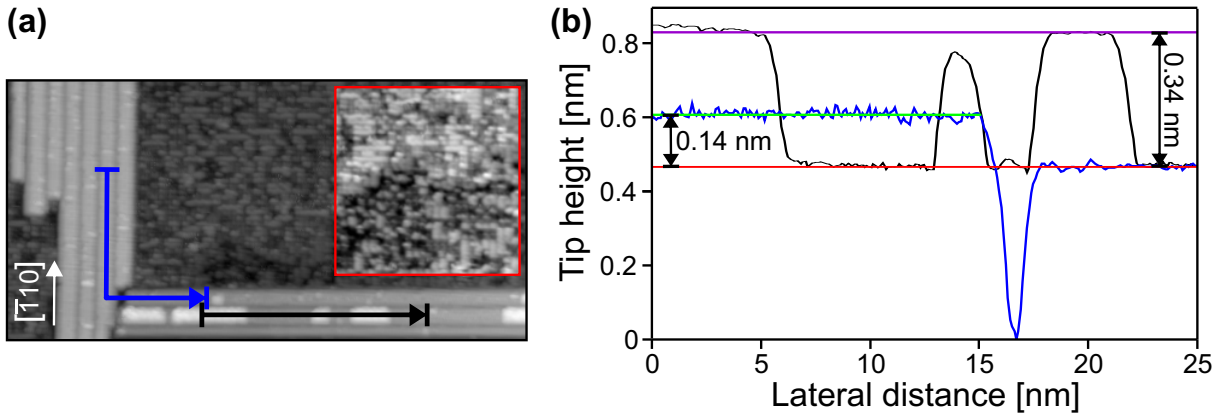

Figure 7.32.: (a) STM image of nanowire bundles that are seperated by a single step (planar substrate with 0.90 ML Tb annealed at 600 °C, $V = -1.5$ V, and $I = 100$ pA) (b) Height profiles along the lines marked in (a). The height was calibrated by taking a height histogram of the area marked by a red box in (a) and adjusting the difference between the maxima from the lower and upper terrace to the nominal step height on Si(001).

7.3. Atomic structure analysis

The atomic structure of the compact nanowires embedded in crystalline Si was already discussed based on HRTEM data. The inner structure of the surface nanowires will now also be determined using HRTEM data by assuming that it does not change by an amorphous Si cap. The surface of the Tb silicide nanowires on Si(001) certainly changes during the capping with Si, but is accessible by the surface science techniques STM and LEED. The results of these techniques are presented first and already reveal some information on the inner structure of the nanowires.

7.3.1. Scanning tunnelling microscopy and low energy electron diffraction

In section 7.1, the lateral dimensions of Tb silicide nanowires as observed by STM were reported, but additional structural information may be gained by STM, e.g. their orientation with respect to the original Si surface. The wetting layer rows run perpendicular to the Si dimer rows. Thus, the nanowires are also perpendicular to the Si dimer rows since they form parallel to the rows of the wetting layer.

Two nanowire bundles that are separated by a single step are shown in figure 7.32 (a). The height difference between both nanowires of 0.14 nm agrees well with the Si(001) step height of 0.136 nm indicating that the nanowires have the same structure [see blue graph in figure 7.32 (b)]. This agrees well with the similar general appearance of all nanowires as structureless elongated protrusions.

While perpendicular nanowires may appear touching, they do not grow together as is seen by trenches between them [see figure 7.32 (a)]. Thus, the atomic structures of the nanowires will not fit structurally together in perpendicular directions if there is a height displacement

of one Si(001) step, either because the structure has no corresponding symmetry such as hexagonal $TbSi_2$, or because the Si(001) step height does not coincide with the step height of the silicide. This step height can be determined by measuring the height of additional layer segments on the nanowires. Such a measurement is exemplified by the black graph in figure 7.32 (b), and the step height is determined to be (0.32 ± 0.02) nm clearly deviating from the Si(001) step height. Thus, no conclusions on the structural symmetry are possible based on the avoided merging of perpendicular nanowires. However, the determined step height of the nanowires agrees very well with the step heights of the $TbSi_2$ structures expected based on the lattice parameters of the bulk silicides with Si vacancies:

$$s_{\mathrm{hex}} \approx a_{\mathrm{hex}} \cdot \sin 60^\circ = 0.333 \text{ nm and } s_{\mathrm{tet}} \approx c_{\mathrm{ort}}/4 = 0.334 \text{ nm} \tag{7.1}$$

assuming orientations as shown in figures 7.29 (a and b). Such a good agreement is a clear indication for a $TbSi_2$ structure of the nanowires.

The surfaces of rare earth silicide nanowires are known to show various reconstructions in STM with the most often reported ones being a row-like appearing 2×1 and a c(2×2) [312, 313, 316, 330]. Since it is possible to cover nearly the complete Si(001) substrate with nanowires, not only STM may be used to study the surface of nanowires, but also LEED.

A LEED image of a surface with densely packed nanowires is shown in figure 7.33 (a). In addition to the spots induced by the bundle formation [red arrows in figure 7.33 (a)], which were already discussed in section 7.1, there are spots on the main axes in the centre between the main spots indicating a $\times2$ ordering on the surface [blue arrows in figure 7.33 (a)]. Since most of the sample is covered by nanowires [see figure 7.9 (b)], it can be concluded that neither the few small islands observed in addition to the nanowires nor the disordered appearing surface in between the silicide structures induce these spots. The only other regions that may be responsible for the $\times2$ LEED spots are the areas surrounding huge islands, which are possibly on the surface since the substrate was used for one nanowire preparation beforehand. However, those areas are very small compared to the surface area covered by nanowires and only few huge islands should be formed after only one Tb deposition, so that an assignment of the $\times 2$ LEED spots to the nanowire surface is the most convincing.

Indeed, rows with separations by 0.8 nm, being close to $2\,a_{\mathrm{Si(001)}} = 0.768$ nm, are observed on nanowire surfaces in STM images with high resolution [see figure 7.33 (b)]. The appearance of these rows is similar to the one of the 2×1 reconstruction on the bare Si(001) surface, and such a reconstruction of the nanowire surfaces nicely agrees with the LEED observations. The LEED image shows a two-domain 2×1 reconstruction since the nanowire grow in two domains on the planar substrate. Other $\times2$ reconstructions, e.g. a c(2×2), can be excluded since no spot was observed at the position marked by a green arrow in figure 7.33 (a) for any electron energy.

While a resolved nanowire surface appears row-like most of the time, those rows meander quite often indicating multiple local atomic arrangements with similar formation energies [see figures 7.33 (b and c)]. The only exception are very thin nanowires, which lie between grooves that are separated by $4\,a_{\mathrm{Si(001)}}$ [see both parts of figure 7.33 (c)]. These nanowires show two straight rows that are separated by less than $2\,a_{\mathrm{Si(001)}}$, which is the dominant separation observed on wider nanowires. Furthermore, the very thin nanowires appear

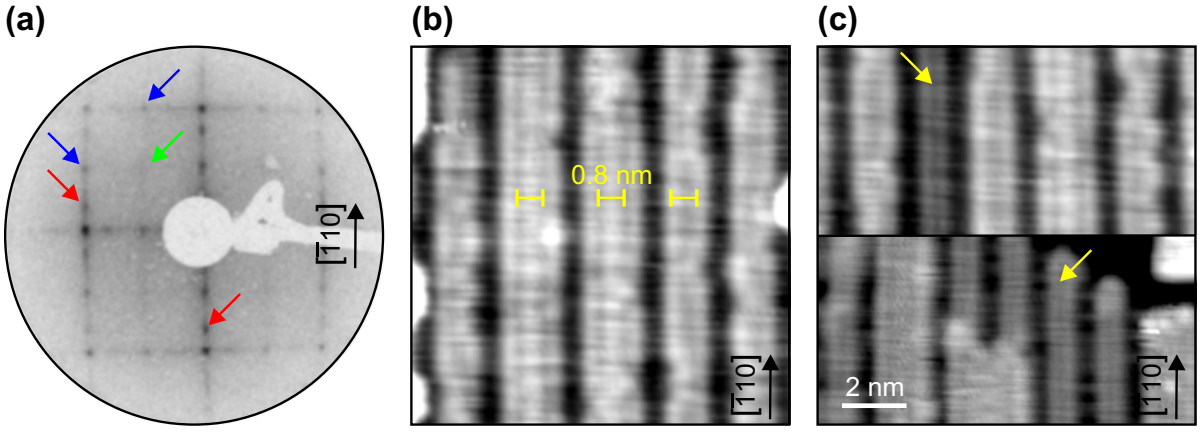

Figure 7.33.: (a) LEED image of a planar Si(001) sample covered by 1.85 ML Tb and annealed at 550 °C ($E_{\mathrm{kin}} = 50$ eV). Another LEED image and an STM image of this preparation are shown in figure 7.9. The blue arrows indicate ×2 spots on the main axes, the green one a position, where a spot is expected for a c(2×2) reconstruction, and the red arrows mark additional spots due to the bundle formation, which do not coincide with integer ordering. (b) Detailed STM image showing the surface of Tb silicide nanowires of a nanowire bundle (planar substrate with 2.20 ML Tb annealed at 600 °C). (c) STM image of narrow Tb silicide nanowires with a stable surface reconstruction, some of which are marked by yellow arrows [upper part same preparation as in (b), lower part planar substrate with 2.20 ML Tb annealed at 500 °C]. All STM images were taken with $V = -1.5$ V and $I = 100$ pA.

slightly lower than the other nanowires. Since the apparent height difference is only about 0.03 nm, which is much smaller than the step height, the narrow nanowires consist most likely of the same amount of silicide layers as the other nanowires. The observed small difference may be caused by a different surface reconstruction of the thin nanowires leading to different electronic properties.

Interestingly, very thin nanowires also showed exclusive properties for Y silicide nanowires [80]. Charge ordering at low temperatures was observed for nanowires with a width of $3\,a_{\mathrm{Si(001)}}$, but not for wider nanowires. These narrow Y silicide nanowires also showed rows on their surface, but they were about $2\,a_{\mathrm{Si(001)}}$ apart in contrast to the observations made here.

It should be noted that also some Tb silicide nanowires with a c(2×2) surface reconstruction were observed in STM. Those nanowires are very scarce, so that they do not influence the LEED image remarkably and are typically very broad, e.g. like the nanowire in the centre of the lower part of figure 7.33 (c). Such nanowires may be dominant for other rare earth metals, which form broad silicide nanowires preferentially. Furthermore, a distorted c(2×2) structure may be observed on longer stripes of an additional layer on top of a nanowire.

A dense packing of nanowires does not only enable the analysis of the nanowires by LEED, but also permits an estimation of the Tb content of the nanowires based on STM data. This was conducted for the preparations with a total Tb coverage of 2.20 ML (see figure 7.8). Since such a high coverage of about 2 ML is needed to nearly fill the entire

surface with nanowires, the Tb content of the nanowires is expected to be in the order of 2 atoms per unit cell of the unreconstructed Si(001) surface. Taking a closer look, not only nanowires formed in these measurements. Nanowire areas with an additional layer and small islands, which formed in addition to the nanowires, have a higher Tb content than the usual nanowires. In contrast, the areas appearing disordered in between the nanowires and the about $1\,a_{\mathrm{Si}(001)}$ wide grooves in nanowire bundles are expected to have a lower Tb content than the nanowires. Assuming these differences to be ± 1 Tb atom per unit cell of the unreconstructed Si(001), the Tb content of the nanowires is (3 ± 1) atoms per 1×1 cell. The rather large error is caused i.a. by the large uncertainty of the quartz crystal microbalance (20%) and does not take into account that the observed Tb coverage may be less than the deposited one, e.g. due to the nearby presence of huge islands.

Based on this Tb content and assuming any of the two $TbSi_2$ structures, the nanowires are 2 to 4 layers high. Taking into account the step heights of the silicides, this corresponds to nanowire heights of 0.7 to 1.3 nm. The apparent height of small nanowire bundles with respect to the surrounding surface is easily measured by STM. While it is depending on the tunnelling conditions and is certainly influenced by electronic effects, it is on average 0.4 nm [see blue graph in figure 7.32 (b)], i.e. smaller than even the lowest nanowire height derived from the nanowire Tb content of two silicide layers. Thus, if the structure of the nanowires is based on one of the $TbSi_2$ structures, the nanowires grow partly into the surface and the lower end of the Tb content estimation appears more convincing. Such a height of two layers would also agree well with an earlier estimation based on ARPES data [75]. Unfortunately, theory work only focussed on silicide structures with a single layer height up to now [80, 274, 325, 327, 330]. Consequently, it cannot give additional insight.

Of course, the nanowires may have a completely different structure, which is not based on a $TbSi_2$ structure and may explain the above observations. Thus, more information on the inner structure of the nanowires is needed to develop a structure model. For this purpose, HRTEM images of nanowire bundles covered by amorphous Si are analysed in detail now.

7.3.2. High resolution transmission electron microscopy

The following experimental HRTEM images were taken by the students Paul Reiß and Jonas Heggemann while the HRTEM simulations were performed by Dr. Tore Niermann. The simulations are necessary since a direct interpretation of the HRTEM data is in general not possible (see section 4.2). Only the symmetry of a structure is directly derivable from a HRTEM image, but even this is not trivial, e.g. the images shown in figure 7.34 (a) are of the same nanowire bundle on TEM sample 1, but were taken with different defocus settings leading to strongly varying visual impressions.

In the upper part of figure 7.34 (a), mainly the central nanowire of a nanowire bundle is distinguishable. The appearance of this nanowire is dominated by vertical stripes which seem not only to repeat periodically with $1\,a_{\mathrm{Si}(001)}$ along [110], but also show brighter areas with a similar periodicity along [001]. In the lower part of figure 7.34 (a), all three nanowires of the bundle appear as two layers of dark spots that are shifted with respect to each other along [110], i.e. no periodicity along [001] is apparent. In between the individual nanowires of the bundle, dark appearing areas that do not fit in the layers of the nanowires are observed [yellow arrows in figure 7.34 (a)]. Furthermore, the central nanowire shows

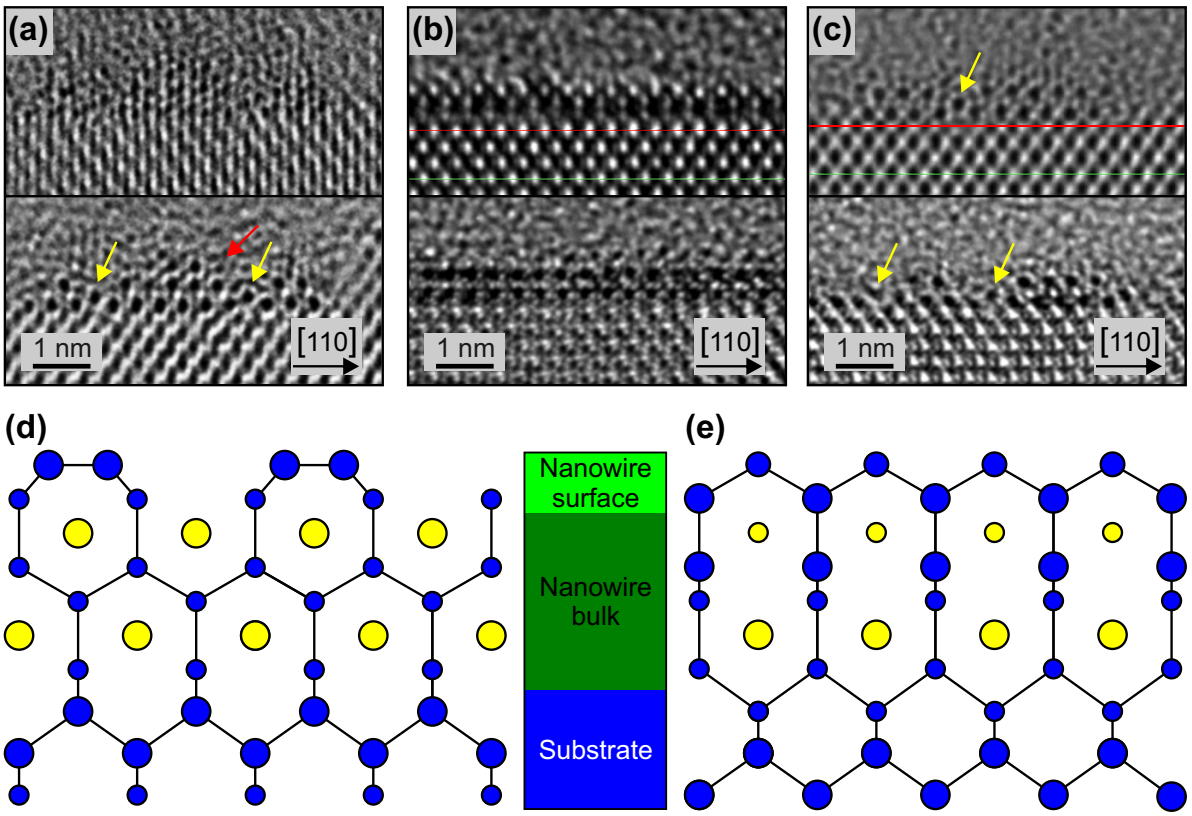

Figure 7.34.: (a) Cross-sectional HRTEM images of sample 1 showing the same Tb silicide nanowire bundle for different defocus settings ($V_{\mathrm{HRTEM}} = 300$ kV). (b and c) HRTEM images of the (b) side view and (c) cross-sectional view of Tb silicide nanowires of sample 8 (upper parts $V_{\mathrm{HRTEM}} = 200$ kV, lower parts $V_{\mathrm{HRTEM}} = 300$ kV). (d and e) Structure model of two silicide layers high TbSi on Si(001) viewed in the two perpendicular directions used for simulations. The Tb atoms (yellow) form a zigzag chain in (d) and are vertically stacked in (e). Si atoms are coloured blue, while large and small atoms lie in different depths, but are not discernible by HRTEM. The red arrow in (a) indicates the growth of an additional layer, while the yellow arrows in (a and c) mark presumably higher lying Tb atoms in the grooves between nanowires of a bundle. The red and green horizontal lines in (b and c) are guides to the eyes marking the interface Si layer directly beneath the nanowires and a Si layer of the substrate, respectively.

a partial third layer that lays directly above the second one, again not agreeing with a short periodicity of the nanowire structure along [001] [red arrow in figure 7.34 (a)]. Such contradicting observations as between the upper and lower part of figure 7.34 (a) may arise in HRTEM, especially when taking into account that the sample may bend with time or simply move under the electron beam leading to changing imaging axes. This shows that great care has to be taken when interpreting HRTEM data. Here, the first impression of vertical stripes is more consistent with the up-to-now assumed structure model, but it cannot be decided by these two HRTEM images alone, which impression is the correct or at least the more probable one.

Taking also into account further images of nanowire bundles, it is the side view that is often dominated by vertical arrangements of similarly appearing structures [see figure 7.34 (b)], while the cross-sectional view often shows two layers shifted with respect to each other [see figure 7.34 (c)]. These appearances of the nanowires are not consistent with the up-to-now assumed structure model. Instead, they agree with a model where the atomic structure of the nanowires is rotated by 90° if the nanowires have a $TbSi_2$ structure. Before the atomic structure is further discussed in detail, some general aspects have to be mentioned.

The HRTEM images of figures 7.34 (a and c) are of nanowires on a vicinal and planar substrate, respectively. Since the nanowire images may appear very similar, it can again be proposed that the same nanowires form on planar and vicinal surfaces. The smallest nanowires observed in HRTEM have a width of $3\,a_{\mathrm{Si}(001)}$, e.g. the outer ones of the nanowire bundle seen in figure 7.34 (a), agreeing well with STM observations [see section 7.1]. The structure of these narrow nanowires appears in HRTEM identical to the one of wider nanowires indicating that the slightly lower apparent height of the narrow nanowires in STM originates from their surface.

Typically, a nanowire appears to consist of two silicide layers and only occasionally an additional layer is observed on top. This agrees nicely with the findings by STM, in which a height of two layers is within the estimated range of nanowire heights and an additional layer is sometimes observed on the nanowires. It should be noted that for two layers the hexagonal and tetragonal $TbSi_2$ structure cannot be distinguished. This is obvious in figures 7.29 (a and b), in which the idealised $TbSi_2$ structures are shown. Starting at the bottom of these structure models, the hexagonal and tetragonal structure are exactly the same up to their centres [hatched purple lines in figure 7.29 (a and b)], which correspond to two silicide layers.

The substrate usually appears nicely periodic, e.g. the spots along the green lines in figures 7.34 (b and c), which do not necessarily have to coincide with Si atom positions, appear all very similar. Similarly, the uppermost Si double layer directly beneath the nanowire structure is imaged as very similarly appearing spots in side view, although there may be a very small undulation in [001] direction [compare to the horizontal red line in figure 7.34 (b)]. In contrast, the Si double layer at the interface between substrate and nanowire appears irregular in cross-sectional images [see red line in figure 7.34 (c)]. While all spots directly below the nanowires appear with reduced height compared to those of lower substrate layers, there is also a further variance in their appearance, especially, but not only beneath grooves [see yellow arrows in figure 7.34 (c)]. These difference in homogeneity between side and cross-sectional view may be caused by strain indicating that low strain is present along the long nanowire axis, but that there is large strain leading to lattice distortions in perpendicular direction.

In one viewing direction, the lowest Si atom of the nanowire and the uppermost one of the substrate form a vertical Si pair. Since the cross-sectional view revealed a different appearance at the interface between nanowire and substrate, it is assumed that these vertical pairs are seen in this direction. This assumption and the above mentioned apparent 90° rotation of the structure model with respect to the up-to-now generally accepted $TbSi_2$ orientation leads to the initial structure models shown in figures 7.34 (d and e) used for HRTEM image simulations. Based on the areas of substrate, nanowire bulk, and nanowire surface defined in these figures, these models illustrate that the nanowire shares a vertical

Si pair with the substrate only in cross-sectional view. In general, the same inner nanowire structure can also be realised with the lowest Si layer of the nanowire moved to the position of the topmost substrate layer shown here. To verify or falsify the alignment of the nanowire with the substrate assumed in the models is one of the aims of the following HRTEM image simulation.

Simulations were carried out for one defocus series showing the cross section of nanowires and for one showing a nanowire bundle from the side. Exemplary images of these defocus series are shown in figures 7.35 (a and e). By HRTEM image simulations, it is aimed to reconstruct the nanowire images of the defocus series using the sample parameters previously determined for the substrate, e.g. sample thickness and orientation. Unfortunately, the sample parameters for the nanowires and the substrate may be generally different, e.g. the effective sample thickness of the nanowires may be reduced due to a stronger oxidation, which may be the case here (see EDX data in section 7.2). In addition, the sample bends during the defocus series leading to a changing imaging axis during the acquisition, which is not reproduced by the simulations. Furthermore, the HRTEM image simulations are made based on the so-called weak phase-object approximation, which may not be applicable for Tb atoms due to their high atomic number. Based on these uncertainties, no final results may be expected, but nevertheless indications for or against a certain structure model are possible .

A comparison between measured and simulated data is shown in figures 7.35 (b to d) for the cross-sectional view and in figures 7.35 (f to h) for the side view. In the simulated images, the approximate atom positions of the structure models are overlayed on the right. The shown sections vary since the sample drifted during the defocus series making the image extraction of exactly the same nanowire areas impossible. Thus, all simulated images are individually aligned to the measured ones based on the substrate pattern. Comparing the appearances of the substrate in the simulation and the measured image gives an indication on the reliability of the simulation. In the measured images some noticeable structures, e.g. bright spots, are marked by coloured ellipses. These ellipses are also overlaid at the corresponding positions on the simulated images for an easier comparison.

Starting with the cross-sectional view, in addition to the dumbbells of the Si substrate the measured HRTEM image in figure 7.35 (b) is dominated by two bright spots in the nanowire region (green and blue), while a third spot above (red) is not always visible and also changes its position with respect to the other spots. At the top of the nanowire, there is a double spot structure (yellow) that may be periodic, but does not have a constant appearance as expected due to the interaction with the amorphous Si cap.

The lower two spots are nicely reproduced by the left simulated image, which is based on the structure model projection with the Tb atoms forming a zigzag chain [see figure 7.34 (d)]. There is no spot directly at the position of the one marked red, but slightly below as is also observed at other positions in the measured data. The topmost marked structure is not well reproduced possibly because of the neglected influence of the amorphous Si cap in the the simulation and the generally not perfect order of the nanowire surface [see figures 7.33 (b and c)]. The simulations show an additional spot slightly up shifted between the dumbbells of the Si substrate. No intensity is found at this position in the measurement, but an even higher intensity is apparent there in the simulation using the structure model projection with the vertical stacking of Tb atoms [see figure 7.34 (e)]. Furthermore, none of the marked

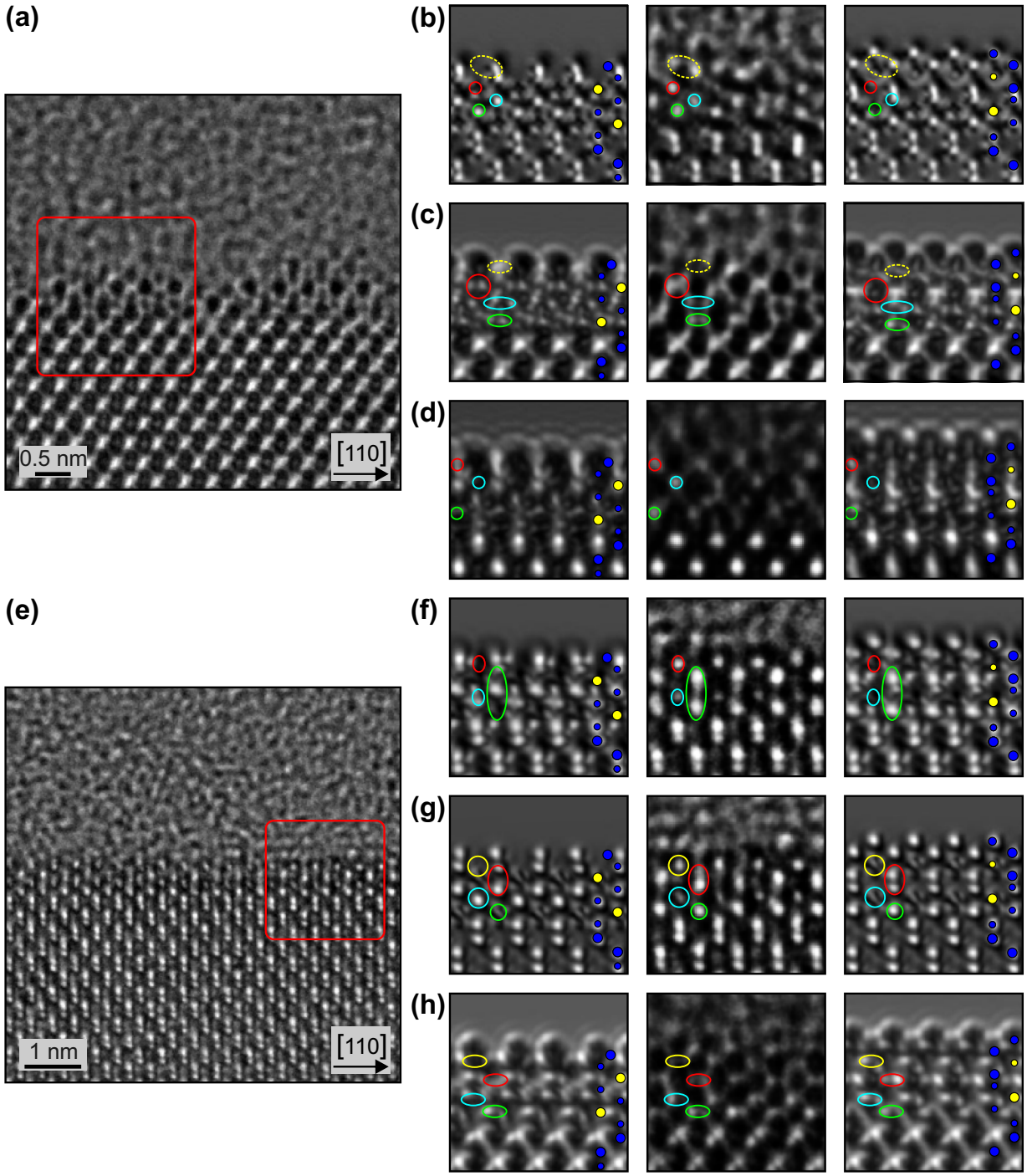

Figure 7.35.: Comparison between HRTEM and simulated data. (a and e) Cross-sectional and side view of nanowire bundles as observed for sample 8 in HRTEM, respectively ($V_{\mathrm{HRTEM}} = 300$ kV). Areas from inside the red squares are compared for various defocus settings to simulated data in (b to d) and (f to h). There, the left and right images are the simulations using the structure model projections of figures 7.34 (d and e), respectively, while the central images show slightly smoothed and contrast enhanced HRTEM images.

local intensity maxima are reproduced using this vertical Tb stacking projection, indicating that the Tb zigzag chain projection is more likely for the cross section of the nanowires.

This impression of the first comparison is confirmed by the next one for images with an increased defocus setting [see figure 7.35 (c)]. In the measured image, four sites with horizontal spot pairs are marked, the uppermost (yellow) appearing rather strongly varying again. The simulation using the Tb zigzag chain projection reproduces these intensity maxima rather well, although the detailed spot positioning may be slightly off, e.g. the left spot of the pair marked blue is shifted upwards. The lowest spot pair is also observed for the simulation using the vertical Tb stacking projection, but the other ones not. Especially at the height of the red marker, the highest simulated intensity is observed where none is found in the measured image. Both simulations do not reproduce the very dark areas observed in the measured image in between the intensity maxima. This problem is also present for the substrate region, i.e. possible explanations include a slightly different imaging geometry of the simulations compared to the measurement.

A changing imaging geometry in the measurement, e.g. due to sample bending, is most likely also the reason for the strong disagreement between both simulated images and the measured image for a further increased defocus setting [see figure 7.35 (d)]. Of course, it cannot be excluded that the differences stem from discrepancies between the simulated and real atomic structure.

In the measured side view HRTEM image shown in figure 7.35 (f), the Si substrate appears as uneven dumbbells and the area of the nanowire is characterised by four bright spots, two above the dumbbell of the topmost substrate layer (blue and red) and two brighter ones laterally shifted by half a lattice constant (green). Neither simulation reproduces the substrate appearance perfectly, with both showing an intense additional spot between dumbbells, which is not as prominent in the measured image. In general, the left simulated image based on the Tb zigzag chain projection does not agree well with the measured HRTEM image, e.g. a high intensity is observed in the centre of the green ellipse in the simulation, while the measured image shows intensity maxima at the two ends of this ellipse. In contrast, these two spots are observed in the simulation using the vertical Tb stacking projection shown on the right. As in the measured image, also two spots are observed above the topmost dumbbell of the Si substrate in this simulated image, but their vertical positions do not agree with the experimental data.

Interestingly, the side view HRTEM image measured with an increased defocus setting and shown in figure 7.35 (g) is rather well reproduced by both simulations. In all three images, the substrate appears as dumbbells with a bit of additional intensity in between them. Four sites with high intensity are observed in the measurement and also the simulations show increased intensity approximately at these sites. Furthermore, there are no additional sites with high intensity in the simulated images when excluding the nanowire surface, which is in reality often not as periodic as the simulated structure and may be changed by the amorphous Si cap in the measurement. This similar appearance of different models nicely demonstrates that a structure determination is not possible based on a single HRTEM image.

Further increasing the defocus changes the appearance of the substrate drastically, but the rather good agreement between measured and simulated images remains for the substrate area [see figure 7.35 (h)]. In contrast, discrepancies are apparent for the nanowire. Four

horizontal spot pairs are marked in the measured HRTEM image. Only the lowest one is also observed in the simulation using the Tb zigzag chain projection while there may even be intensity minima at the other positions, but all spot pairs are apparent in the simulation using the vertical Tb stacking projection. There is additional intensity in between the spot pairs in the right simulated images, but a similar small disagreement is observed for the substrates. Thus, the agreement is as good as one may expect it for the correct structure.

Summarising the comparison between measured and simulated HRTEM images, the Tb zigzag chain projection may be favoured as the atomic structure of Tb silicide nanowires seen in cross section while the vertical Tb stacking projection better corresponds to the side view. The agreement in side view is surprisingly good, especially, when taking into account that multiple nanowires, grooves, and possibly also the neighbouring Si capping layer contribute to the HRTEM image. The agreement in cross section is not as compelling, but sometimes the nanowire surface appeared relatively unaffected by the Si capping and produced reoccurring motives in measured images. This was not observed in side view, probably since amorphous Si is present in this height between individual nanowires of a bundle.

While it cannot be proven without doubt that the structure model projections of figures 7.34 (d and e) show the right structures for the cross section and the side view of the nanowires, respectively, by the simulations of HRTEM images shown here, these simulations partially indicate this assignment and certainly cannot exclude it. Assuming a $TbSi_2$ stoichiometry of the nanowires, the simulations show that the Tb atoms are seen above each other in side view while they form a zigzag chain in the nanowire cross section. Based on the simulations [see figure 7.35 (c)], the positions of the Tb atoms approximately coincide with the distinctive round dark areas that are often observed on nanowire HRTEM images [see figures 7.34 (a and c)]. Furthermore, the alignment with respect to the substrate has to be as in the simulated structure model, i.e. nanowires share vertical Si pairs with the substrate in cross section.

7.3.3. Nanowire structure model

The basic structure model for Tb silicide nanowires on Si(001) proposed here is shown in figure 7.36. It is based on the structure of the Si-richest silicides and the assumption of an ideal $TbSi_2$ stoichiometry, i.e. no Si vacancies form for nanowires in contrast to the observations made for the bulk silicides. As indicated by STM and HRTEM, the typical nanowire has a height of two Tb layers. The Tb atoms are vertically stacked in side view and form a zigzag chain in cross-sectional view as seen by HRTEM, i.e. the nanowire structure is rotated by 90° with respect to the up-to-now widely accepted model [75, 77, 78, 81, 85, 312]. The nanowires do not form on top of the surface, but are slightly buried in agreement with the apparent heights observed by STM. This is indicated in figure 7.36 by the height of the surrounding Si dimers. The rows of these Si dimers run perpendicular to the nanowires.

The surface of the nanowires is assumed to be Si terminated because of the Si surplus during their formation, similar to the observation for the $TbSi_2$ monolayer on Si(111) [361, 362]. As for the clean Si(001) surface, the number of dangling bonds at the uppermost nanowire Si atoms can be reduced by dimer formation. For nanowire base widths that are even multiples of $a_{Si(001)}$ these dimers may form rows along the wires, i.e. a 1×2 structure

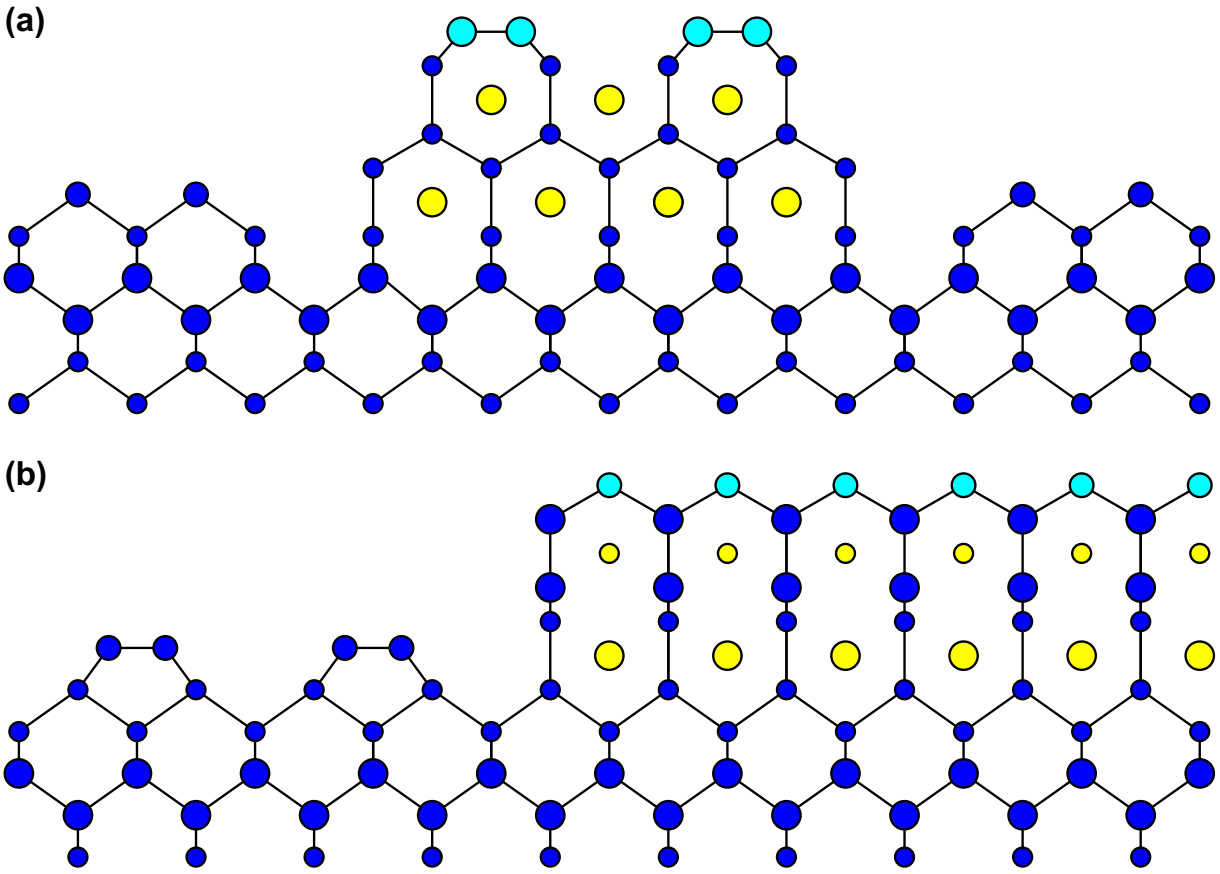

Figure 7.36.: (a) Cross-sectional and (b) side view of the structure model for Tb silicide nanowires proposed here. Si and Tb atoms are coloured blue and yellow, respectively, while large and small atoms lie in different depths. Cyan circles denote nanowire surface dimers. The shown nanowire surface structure of Si dimer rows is only applicable for nanowire base widths that are even multiples of $a_{\mathrm{Si}(001)}$.

agreeing with the LEED observations [see figure 7.37 (a)]. For other nanowire widths, undimerised Si atoms would remain on the nanowire surface for a 1×2 structure.

Si dimer rows that run perpendicular to the nanowires, i.e. a 2×1 structure, would also agree with the LEED observations [see figure 7.37 (b)]. Such rows could form independently of the nanowire width, but do not agree with the STM measurements, in which linear structures along the nanowires are dominantly observed. Also independent of the nanowire width is the formation of a $\mathrm{c}\,(2\times2)$ structure, which may be formed for both dimer orientations [see figures 7.37 (c and d)]. Such a structure was only observed for wide Tb silicide nanowire, but may be the dominant one for other rare earth elements, e.g. it is observed for Ho silicide nanowires by STM and LEED [429].

Interestingly, no indications for a $\times2$ ordering was observed with LEED for silicide nanowires of Dy, the rare earth metal lying between Tb and Ho in the periodic table, although earlier studies observed rows on the nanowire surface using STM [312, 415]. This may be caused by the missing of the long range order needed for LEED due to a too low nanowire density, since a coverage of only 1.2 ML Dy was used, or due to a too irregular

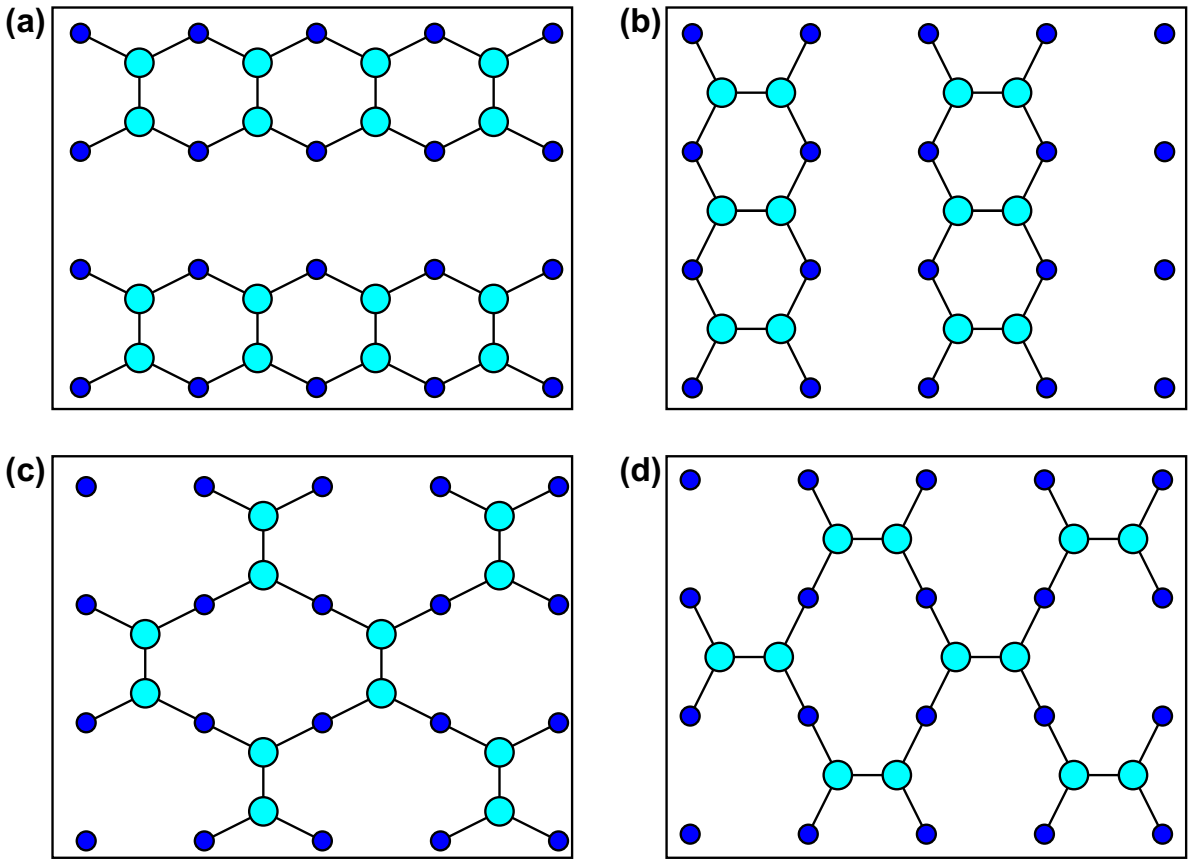

Figure 7.37.: Possible surface structures of Tb silicide nanowires with a dimerisation of the topmost Si atoms. (a) 1×2 and (b) 2×1 reconstruction. (c and d) Models of c(2×2) reconstructions with different dimerisation directions. In all images, the long nanowire axis is horizontal.

surface structure of the nanowires.

That the surface of the nanowires is in general not perfectly ordered was also observed for Tb silicide nanowires in STM [see figures 7.33 (b and c)]. The only exception are narrow Tb silicide nanowires that lie between grooves of nanowire bundles separated by $4\,a_{\mathrm{Si(001)}}$ [see figure 7.33 (c)]. These grooves were also observed in HRTEM and their width is in most cases $1\,a_{\mathrm{Si(001)}}$. Thus, the narrow nanowires have a base width of $3\,a_{\mathrm{Si(001)}}$, which corresponds to the minimum width for nanowires in this work and also for other rare earth silicide nanowires [330]. Only for Dy silicide nanowires even narrower nanowires are reported [316]. All $3\,a_{\mathrm{Si(001)}}$ wide silicide nanowires showed the same structure as wider nanowires in HRTEM, e.g. see figure 7.34 (a), so that the inner structure of these narrow nanowires should at least be similar, and the characteristic surface appearance is only based on a different surface structure.

No two Si dimer rows that run along the narrow nanowire fit on the surface of the nanowire when excluding a five-time coordination of Si atoms. Si dimers may be rotated by 90°, as illustrated in figure 7.37 (b), but then a $\times2$ periodicity is expected along the nanowires, which is not observed in STM. The rather drastic change in atomic structure

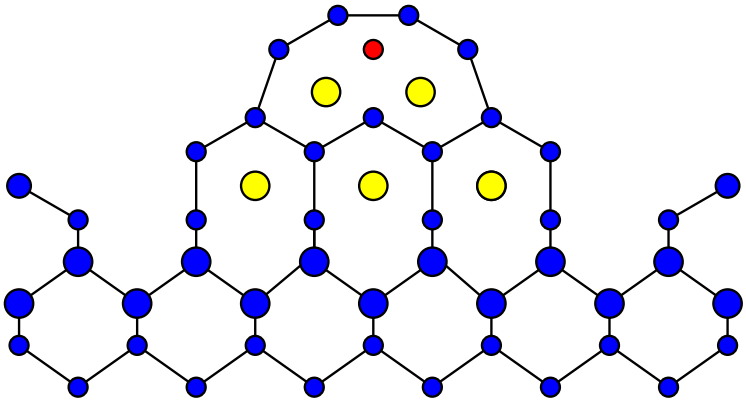

Figure 7.38.: Cross-sectional view of a structure model for narrow Tb silicide nanowires with a width of only $3\,a_{\mathrm{Si}(001)}$ based on the formation of Si vacancies (highlighted red). Silicon and Tb atoms are coloured blue and yellow, respectively, while larger and smaller atoms lie in different depths.

for Tb silicide nanowires proposed here clearly shows that further structural ideas should not be excluded easily. There may be Si vacancies in the surface layers of the narrowest nanowires, leading to a more compact nanowire structure (see figure 7.38). Bulk $TbSi_2$ structures are well known for their formation of Si vacancies and while no direct proof for them was found experimentally, they also cannot be excluded beyond doubt. The nanowire height may be nearly unchanged by the Si vacancies and two lines along the nanowires may be observed at the two topmost atoms.

Not included in any of the structure models are relaxation effects, e.g. a varying height of the Tb atoms of a horizontal layer, a buckling of the nanowire surface dimers, or a dimerisation at the nanowire side flanks. All given examples are likely to occur to reduce strain in the nanowires while keeping bond lengths close to their optimum values or to lower the number of dangling bonds. The resulting changes in the atomic structure are hard to estimate without theoretical calculations since neither STM nor HRTEM images may give further insight at the current resolution level, which is already remarkably high. Thus, the structure model proposed in figure 7.36 is certainly not the final one, but especially the fundamental change of silicide orientation with respect to the nanowire axes found here may help on the way to completely uncover the atomic structure of rare earth silicide nanowires.

7.3.4. Atomic structure of the wetting layer

The Tb induced wetting layer always appears much lower than the silicide nanowires in STM. Thus, it is unlikely that the wetting layer is a multi layer structure like the nanowires, so that any kind of passivation, e.g. by amorphous Si, should have a large influence on its atomic structure. Consequently, no indication for the wetting layer were found in HRTEM measurements, and the following structure analysis is based on LEED and STM data alone.

The wetting layer may cover the complete planar Si(001) substrate, if moderate annealing temperatures are used [see section 7.1, especially figure 7.5 (a)]. A LEED image of such a closed wetting layer is shown in figure 7.39 (a). There are two different periodicities

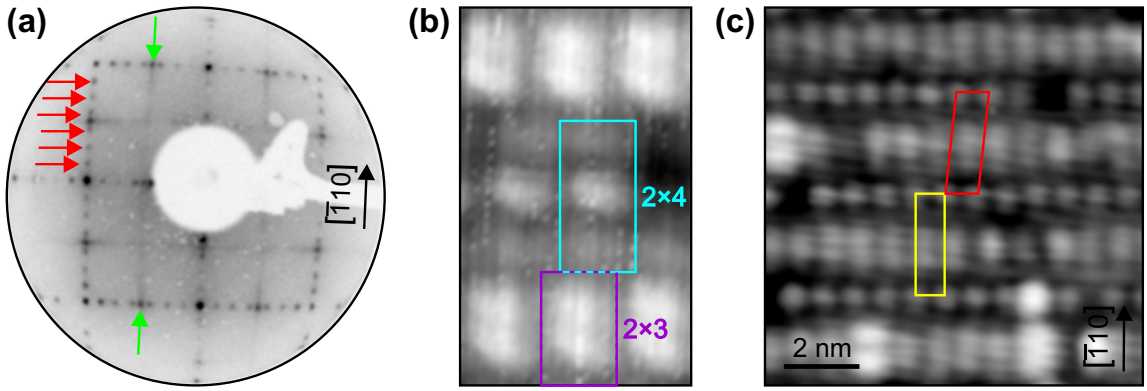

Figure 7.39.: (a) LEED image of a Si(001) substrate covered by a closed wetting layer and few single nanowires (0.70 ML Tb annealed at 450 °C and $E_{\mathrm{kin}} = 50$ eV). (b) Detailed STM image of the wetting layer with the two different subunits highlighted by frames (0.50 ML Tb annealed at 600 °C, $V = -1.0$ V, and $I = 1$ nA). (c) STM image of the wetting layer with the rectangle and the parallelogram marking the two different unit cells (0.50 ML Tb annealed at 500 °C, $V = -1.0$ V, and $I = 200$ pA).

observed, which overlie each other due to the formation of two perpendicular domains on planar substrates. There are intense spots in the centre between neighbouring ×1 spots of the Si bulk, e.g. marked by green arrows in figure 7.39 (a). In addition, six further equidistant spots are observed on the axes between ×1 spots [red arrows in figure 7.39 (a)]. Thus, the wetting layer has a ×2 and a ×7 periodicity. It does not form a well ordered 2×7 reconstruction since only streaks, but no distinct spots are observed on the axes between ×2 spots, e.g. between the green arrows in figure 7.39 (a). The reason for this is found by a detailed look at the real space structure with STM.

The wetting layer has not only one 2×7 unit cell since it is build up from smaller subunits, which cover areas of $2\times3\,a^2_{\mathrm{Si(001)}}$ and $2\times4\,a^2_{\mathrm{Si(001)}}$. The structures of these subunits that appear bright in STM at low tunnelling voltage are shifted by $1/2\,a_{\mathrm{Si(001)}}$ with respect to each other in the direction of the ×2 periodicity [see figure 7.39 (b)]. The shifts or neighbouring subunits of the same type may be in the same direction leading to a locally rectangular unit cell [yellow in figure 7.39 (c)] or in opposite directions resulting in a locally parallelogram-like unit cell [red in figure 7.39 (c)]. There is no preference of a specific unit-cell type even for high annealing temperatures of 600 °C indicating negligible energy differences between both types. Furthermore, there are no indications for long range order, e.g. an alternation between both unit cell types, so that only the ×2 periodicity along the wetting layer rows and the ×7 periodicity in the perpendicular direction, but no well-ordered 2×7 reconstruction are observed with LEED.

Crucial for the discussion of a possible atomic structure of the wetting layer is the content of Tb atoms in a unit cell. The STM image of the surface completely covered by the wetting layer shows a preparation with a nominal Tb coverage of (0.48 ± 0.10) ML [see figure 7.5 (a)]. In addition to very few, short nanowire segments also some dark wires were observed for this preparation. Thus, the experimental Tb coverage is assumed to be slightly higher than the ideal Tb coverage for an exclusive wetting-layer formation. Taking into account that a

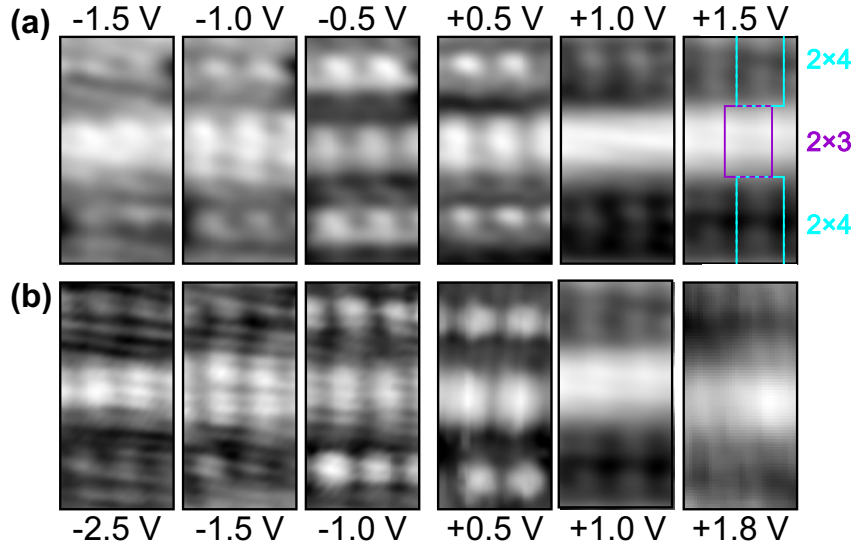

Figure 7.40.: Tunnelling voltage dependent appearance of the wetting layer in STM. (a) Taken at exactly the same position, by scanning the same line multiple times at different voltages and (b) at other positions, where the observed structure may be more detailed [all images taken with $I = 100$ pA, except for negative voltages in (b), there $I = 200$ pA].

wetting-layer unit cell should contain an integer number of Tb atoms, the exact coverage for a closed wetting layer film could be 0.43 ML corresponding to 6 Tb atoms in every unit cell. This agrees nicely with observations made by Preinesberger *et al.* for the Dy induced wetting layer, but contradicts the assumption of Liu and Nogami of only 5 rare earth atoms per unit cell [331, 333]. Similar to the estimation of the Tb content of the nanowires, further uncertainties arise, e.g., due to the possible presence of huge islands nearby. Still, a Tb content of 5–6 Tb atoms in a unit cell is going to be discussed in the following.

While 2×3 subunits are usually only observed in 2×7 structures, 2×4 subunits also form independently of the 2×7 reconstruction at low Tb coverages or after the formation of nanowires, when the Tb concentration is reduced in their vicinity. Thus, the density of Tb atoms in a 2×4 subunit should be smaller than in a 2×3 subunit, i.e. the number of Tb atoms in a 2×4 subunit has to be 3 or lower, though 3 is only possible for a total Tb content of 6 in a wetting layer unit cell.

That the individual 2×4 subunits, which may lie in Si dimer rows [332], are the same as in the 2×7 reconstruction is seen in their characteristic voltage dependent appearance in STM [332, 333]. The 2×4 subunits typically appear as three maxima [see figure 7.39 (b)], whose relative intensities vary with the tunnelling voltage [see figure 7.40]. In filled states images, the central maximum always appears brighter than the outer two. The same appearance is observed at low positive tunnelling voltages, but the contrast inverts at higher positive voltages.

The appearance of the 2×3 subunit is also voltage dependent. With increasing absolute value of negative tunnelling voltage, the maximum widens until it may even appear with a central depression before it shrinks again. At the same time, the apparent height of the 2×3 subunit increases with respect to the one of the 2×4 subunit. A similar apparent height

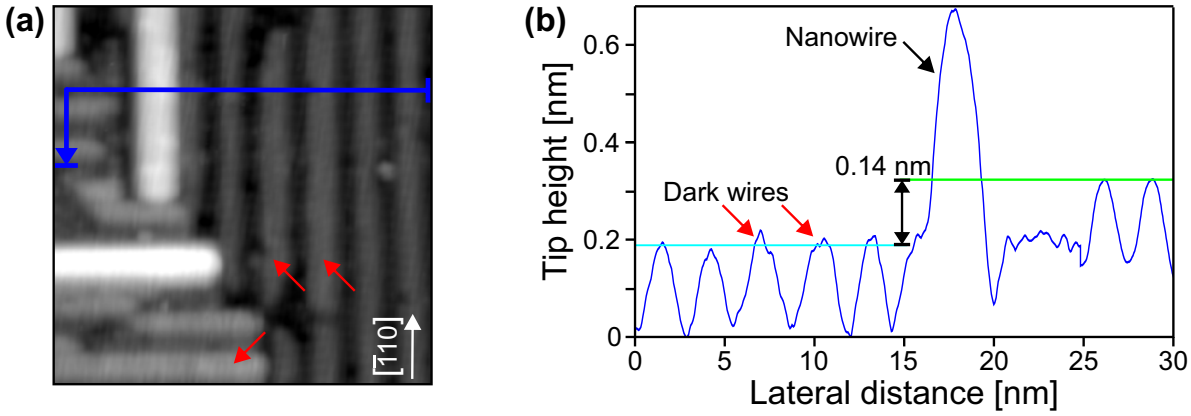

Figure 7.41.: (a) STM image of a similar sample area as already shown in figure 7.1 (b), but obtained with different tunnelling conditions (0.70 ML Tb annealed at 450 °C, $V = +1.5$ V, and $I = 250$ pA). Most of the area is covered by the wetting layer, but there are also some nanowires and some dark wires (marked by red arrows). (b) Tip height profile along the blue line in (a).

increase of the 2×3 subunit is found for positive tunnelling voltages. In general, height differences measured in STM match the actual ones better for high absolute values of the tunnelling voltage [440]. Thus, the atomic structure of the 2×3 subunit may be higher than the one of the 2×4 subunit, but has fewer states close to the Fermi level leading to a decreased apparent height for low absolute values of the tunnelling voltage.

In addition to the apparent height, also the overall appearance of the 2×3 subunit changes with increasing positive tunnelling voltage. Similar as the 2×4 subunit, the 2×3 subunit appears the same for low absolute values of the tunnelling voltage independent of the voltage polarity, but the individual maxima of neighbouring 2×3 subunits connect to form a continuous stripe at higher voltages. Such a rather structureless appearance is very similar to the one that is observed for dark wires or even nanowires independent of the tunnelling conditions. Interestingly, the typically observed height difference between 2×3 subunits and dark wires, e.g. seen in figure 7.1 (b), vanishes when the 2×3 subunits appear as a continuous structure. This is already apparent in the STM image shown in figure 7.41 (a), but also confirmed by the tip height profile crossing several 2×3 subunits and two dark wires in figure 7.41 (b). Thus, one may assume structural similarities between 2×3 subunits and dark wires.

In addition to the voltage dependent appearance of the 2×3 subunits, the main difference between 2×3 subunits and dark wires are their widths. The dark wires are always wider, which is nicely seen in the tip-height profile in figure 7.41 (b), but also by shifts of the 2×4 subunits of the wetting layer, e.g. indicated by green hatched lines in figure 7.1 (b). The dark wires are an intermediate structure between 2×3 subunits and nanowires, with the most obvious difference to nanowires being the apparent heights of the structures [329]. Again assuming structural similarities, one may want to describe the dark wires as an only one layer high $TbSi_2$ structure since the nanowires have a height of two silicide layers. However, the observed height difference between dark wires and nanowires is clearly larger than one step height of $TbSi_2$ [see figure 7.41 (b)]. Thus, further structural differences

should be considered.

Combining all the above structural information into one conclusive structure model is non-trivial, especially the shift of the maxima of the different subunits of a wetting layer unit cell is hard to include in a model. No structure model discussed in the literature is completely convincing, even including those proposed for rare earths, which do not form nanowires, but for which also 2×3 and 2×4 structures are observed [331–334, 441].

Well-ordered surface clusters were observed for even lower temperatures than needed for the formation of the wetting layer (see section 7.1). While no conclusions may be drawn on the atomic structures of the clusters, the diffusion of rare earth atoms to the energetically most favourable binding sites without further structural modification of the substrate should result in a structure with one of the lowest activation energies needed. Thus, if such a structure is induced by rare earth metals, it will be more probable for the clusters than for the wetting layer.

More energy is needed for displacements of Si dimers by rare earth atoms since the dimer bond and back bonds of the dimer atoms to the substrate have to be broken. Such substitutions are the main structural motive of the model for the 2×4 subunit proposed by Liu *et al.*, in which three neighbouring dimers of a Si dimer row are replaced by rare earth atoms [332]. This agrees well with the apparent height of the 2×4 subunits with respect to Si dimer rows [332], but Liu *et al.* also proposed only 5 rare earth atoms per wetting layer unit cell contradicting the above made assumption of a higher rare earth atom density in the 2×3 subunits than in the 2×4 subunits [333]. A further structural motive is the formation of Si cages surrounding rare earth atoms as it is observed in the $TbSi_2$ nanowires. Since the wetting layer forms in the same temperature regime, such cages may be viable, but no multilayer structures should form due to the low Tb content in the wetting layer.

A possible atomic structure of the wetting layer is shown in figure 7.42. The structure of the 2×4 subunit is based on Si dimer substitutions, similar to the model by Liu *et al.*, but only 2 instead of 3 dimers are replaced by rare earth atoms. Thus, the Tb density is lowered and a difference between outer and inner maxima of the 2×4 subunits is expected in agreement with the experiments. That the inner maxima appear higher at negative tunnelling voltages and the contrast inverts for high positive voltages is in agreement with the higher electronegativity of Si, leading to a concentration of filled states at the Si atoms [336, 337].

No complete cage formation is assumed for the structure of the 2×3 subunits since there has to be a structural difference between the lateral positions marked by I and II in figure 7.42 (b), because a maximum is observed only at one of those positions. Furthermore, no complete $TbSi_2$ layer is expected for the 2×3 subunits since nanowires are more than one step height higher than the 2×3 subunits. The high Si structure at position I appears improbable at first glance, but there are 12 dangling bonds at these Si atoms, which may be saturated by 12 electrons from the four neighbouring Tb atoms leaving those in their optimum trivalent state. Such a complete saturation of the main 2×3 structure agrees well with the reduced apparent height of the structure at low absolute values of the tunnelling voltage. At larger absolute values of the tunnelling voltage, the topography of the 2×7 superstructure dominates the appearance of the STM images leading to a higher appearance of the 2×3 subunits.

That the 2×3 subunits are still visible in STM at low absolute values of the tunnelling

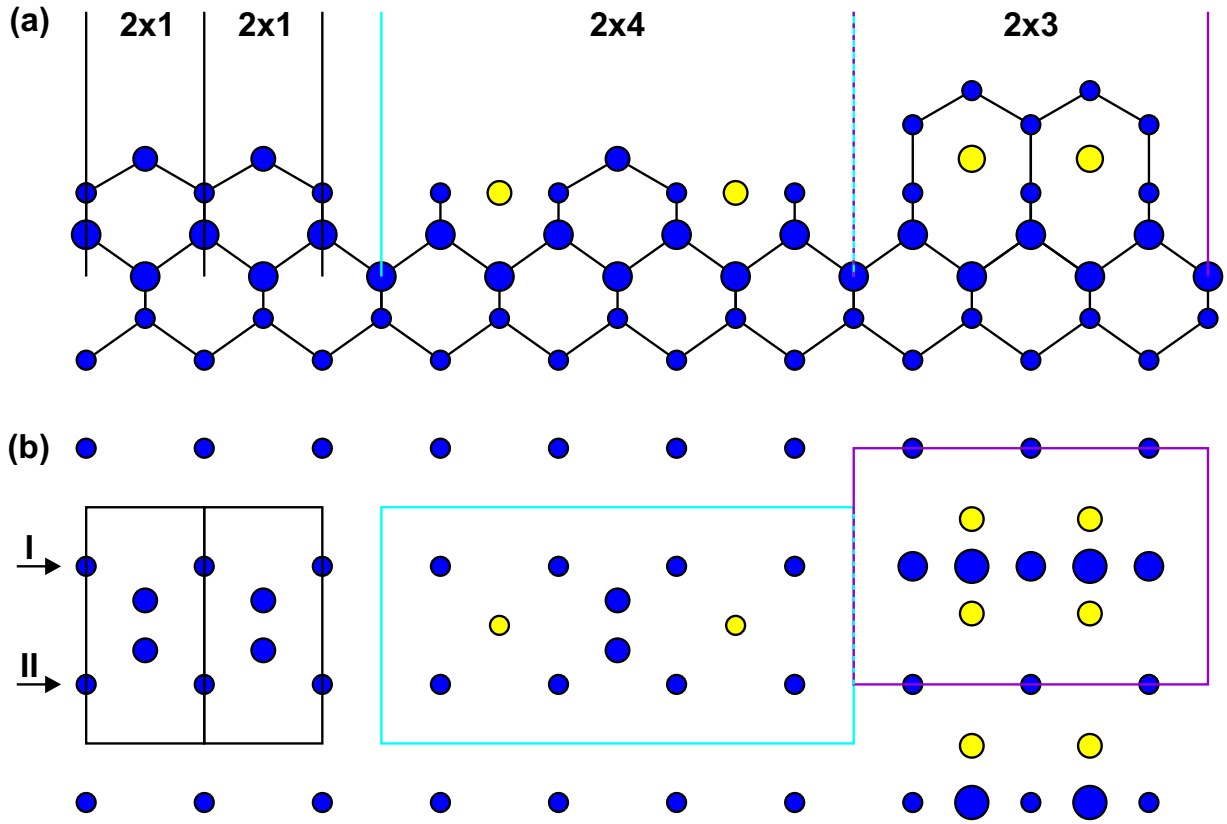

Figure 7.42.: Possible structure model of the wetting layer in (a) viewed along the wetting layer rows and in (b) in top view with Si dimers of the clean Si(001) surface shown for comparison. Si atoms are coloured blue and Tb atoms yellow while the size of the atoms is indicative for the depth in which they lay. I and II mark two lateral positions that have to appear differently in 2×3 subunits. A the left side, the clean Si(001)2×1 surface is shown for comparison.

voltage may be related to the atomic structure at position II where additional dangling bonds are situated. These dangling bonds may be partially saturated by an electron transfer from the main 2×3 structure, so that the main 2×3 structure is not completely saturated any more. Nevertheless the dangling bonds of the Si atoms at position II may never be observed in STM since the Si atoms lie structurally too low. The appearance of the 2×3 subunits as a continuous stripe at high positive tunnelling voltages may be related to a empty state delocalised over the complete subunit area.

Based on the proposed structure of the 2×3 subunits, a dark wire may have a similar structure only with one additional partial Tb silicide cage in ×3 direction. Such a structure may then stress the substrate in a way that the formation of a complete two layer $TbSi_2$ structure is possible without having to overcome large energy barriers leading to the observation of dark wires only for low annealing temperatures. Such proposed structural similarities between wetting layer and nanowires nicely agree with the observation of a rather universal silicide peak with RAS (see section 7.1).

As mentioned at the beginning of the discussion of the wetting layer structure model

proposed here, it should only be seen as a possibility, which agrees with all the experimentally derived structural information. Certainly, there are many more models that also agree with the information in a similar way, but without support by theoretical calculations, with which the stability and energetic differences between structure models can be assessed, any further discussion is not constructive at this point. Nevertheless, the proposed structure model may be an interesting input for future studies.

Analysing the atomic structure of Tb silicide structures is one of the main aspects of this thesis. The other one is the electronic structure, which is covered in the following section.

7.4. Electronic properties

In the previous section, an atomic structure of the nanowires based on $TbSi_2$ was proposed. This assumption may not only be tested by a direct structural analysis, but also indirectly by probing the electronic structure of the nanowires. The $TbSi_2$ monolayer on Si(111) is well known for the shift of the Fermi level to a position close to the conduction band minimum of the substrate. Such a characteristic shift should be rather independent of the orientation of the substrate, i.e. occur in a similar manner for $TbSi_2$ nanowires on Si(001). This and other aspects will be addressed in the following using XPS data of the Si-2p core level, before the electronic structure is analysed in detail using STS and ARPES to probe if the nanowires are indeed quasi-one-dimensional metals. This section concludes with a presentation of transport measurements performed in Hannover [416].

7.4.1. Core-level photoemission spectroscopy

All Si-2p core level spectra shown in the following are normalised to equal heights and were obtained at room temperature so that no photovoltage or charging effects have to be considered, allowing an analysis of the bend bending. Still, additional low temperature measurements were used to check the spectral composition found for room temperature measurements with higher resolution. As reference for the nanowire samples, clean samples will be analysed first, while a discussion of the Si-2p spectral components from the nanowires will be presented subsequently before the influence of other silicide structures, e.g. the wetting layer, on the nanowire Si-2p spectra is elucidated. The possible influence of the sample vicinality is probed by using substrates with 4° and 6° offcut towards [110].

The clean substrates

Figure 7.43 (a) shows Si-2p XPS spectra of clean substrates with varying vicinality taken with a photon energy of $h\nu = 200$ eV. The spectra appear remarkably similar with only the shoulder at high kinetic energy getting less pronounced with increasing offcut angle. While the resolution is not as good as in the literature data [see figure 5.3 (d)], all spectra can be fitted well using the components discussed in the literature [228].

First of all, there is the component of the Si bulk (B), which dominates all spectra and also has a slightly smaller Gaussian width than the other spectral components. Since the dimers are buckled, two components, one of the upper dimer atoms (S_u) and one of the

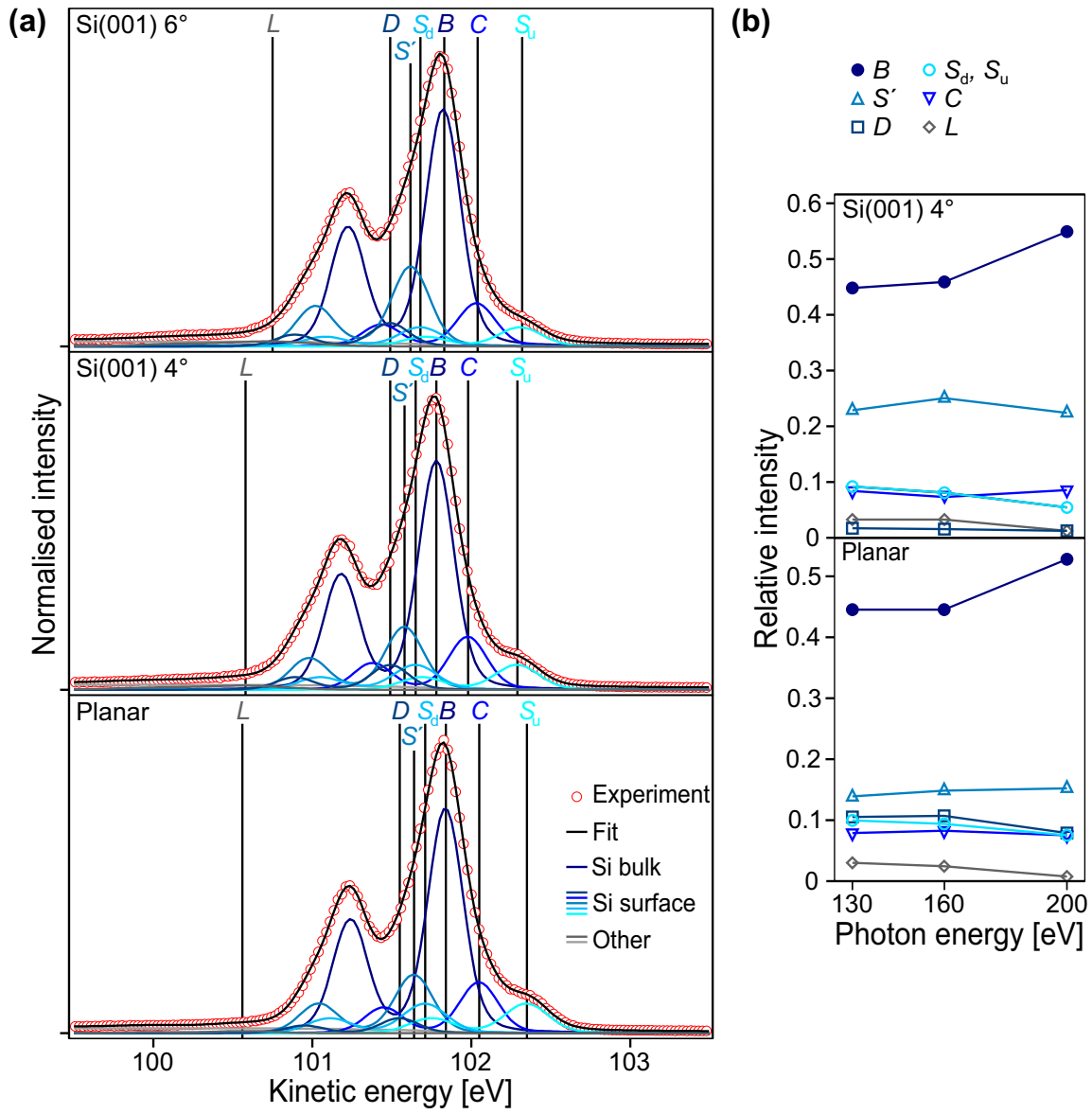

Figure 7.43.: (a) Si-2p spectra of clean n-type Si(001) substrates with different offcut angles obtained at room temperature ($h\nu = 200$ eV). (b) Exemplary intensity dependence of the Si-2p spectral components on the photon energy for clean Si(001) surfaces.

lower dimer atoms (S_d), with different core-level shifts can be related to the Si dimers. There is an equal number of upper and lower dimer atoms. Thus, the intensities of there two components is assumed to be equal. The dimer reconstruction of the surface leads to strain in lower layers and a non bulk-like atomic and bonding arrangement, i.e. a different chemical environment. Consequently, additional spectral components (S' and C) are observed in the Si-2p spectra. Furthermore, there are two spectral components with typically rather low intensities (D and L), which may be related to defects, but whose origins are still under debate [228].

Such an assignment of the spectral components is nicely reflected in their intensity variation

Table 7.2.: Overview on the derived absolute kinetic energies of the Si-bulk component ($h\nu = 200$ eV) and the core-level shifts of the other components for the Si-2p XPS spectra of clean substrates shown in figure 7.43 (a), with the respective peak labelling and literature values for comparison [228]. In addition, the average core-level shifts of all measurements including low temperature measurements are given with their standard deviations. All values are in eV.

	L	D	S'	S_d	B	C	S_u
Planar	-1.28	-0.29	-0.20	-0.13	101.84	0.21	0.51
4° offcut	-1.20	-0.29	-0.23	-0.13	101.78	0.20	0.51
6° offcut	-1.08	-0.34	-0.20	-0.15	101.83	0.21	0.49
Average	-1.20 ± 0.08	-0.33 ± 0.05	-0.22 ± 0.02	-0.14 ± 0.01	101.82	0.20 ± 0.02	0.49 ± 0.02
Literature	-1.34	-0.30	-0.22	-0.13		0.22	0.49

depending on the used photon energy [see figure 7.43 (b)]. Photon energies of 200 eV, 160 eV, and 130 eV approximately correspond to kinetic energies of the photoelectrons of 100 eV, 60 eV, and 30 eV. Taking into account that the minimum of the inelastic mean free path of electrons in Si lies at rather low energies [145], the surface sensitivity of Si-2p spectra increases with decreasing photon energy for the photon energy range used here. Consequently, the relative intensity of the Si-bulk component increases when the photon energy is increased from 130 eV to 200 eV while the relative intensities of the surface dimer components decrease. The other spectral components show a not as easily identifiable dependence of the relative intensities on the surface sensitivity, indicating that their origins are neither at the topmost surface atoms nor deeply in the Si bulk, also agreeing with their structural assignment. It should be noted that the error of the relative intensities, as obtained by the fitting procedure, is in general lower than the heights of the symbols used to indicate the relative intensities.

Comparing the obtained core-level shifts of the different spectral components with respect to the Si-bulk component, only a very small variance is found for the different samples, e.g. they are independent of the sample offcut or the measurement temperature. This is seen by comparing the core-level shifts for the three spectra shown in figure 7.43 (a) and also by the small standard deviations obtained for the average core-level shifts of all Si-2p spectra of clean substrates (see table 7.2). The independence on the temperature is expected, but new atomic sites at double steps are introduced for vicinal samples. The concentration of these may be too low since there are still 5 to 6 Si dimers for every double step on substrates with 6° offcut, and their core-level shifts are probably too close to one of the already included spectral components, so that no additional spectral components have to be introduced for them during the fitting procedure. In agreement with this is the very similar absolute energetic position of the Si-bulk component for all clean substrates indicating a similar surface band bending independent of any offcut.

A small dependence on the offcut angle is seen in the core-level shift of the L-component, which has a much larger Gaussian width than all other components and is complicated to asses correctly due to its low intensity. Its core-level shift seems to increase with increasing offcut angle, which also makes the energetic position of the D-component less certain. Since the origin of the L-component is unknown, no speculations regarding the possible reasons

for the shift in energetic position will be made. Nevertheless, the core-level shifts found here agree very well with the ones reported in the literature (see table 7.2). The literature values are within the standard deviations of the respective average core-level shifts for all spectral components excluding the L-component.

Tb silicide nanowires

The formation of Tb silicide nanowires has a drastic influence on the Si-2p spectra [compare figure 7.43 (a) and figure 7.44 (a)]. The spectra are much broader and spectral weight seems to be shifted to lower kinetic energies. Before the spectra are analysed, some general remarks have to be made. In contrast to the clean substrates, on which only one surface structure is found excluding defects, the nanowire samples contain a mixture of different structures ranging from uncovered substrate areas over wetting layer structures and nanowires possibly to islands (see figure 7.45). Since we are mainly interested in the signal from the nanowires, preparation conditions resulting in a high surface coverage with nanowires were chosen for the samples, whose spectra are shown in figure 7.44 (a). Many different spectral components corresponding to different atomic sites were already identified for the spectra of the clean substrate. Even more are expected for Tb silicide nanowires, e.g. there are nanowire surface Si atoms, silicide bulk Si atoms, Si atoms at the nanowire sides, etc. Due to this manifold of different Si atom sites, even when not including possible strain effects, one cannot expect to be able to fully assign all spectral components, but major contributions should be identifiable, the influence of the substrate offcut should be observable, and one may be able to asses the change in band bending upon nanowire formation.

Figure 7.44 (a) shows Si-2p spectra of nanowire samples that used the same substrates as in figure 7.43 (a). Now, there are larger differences between the spectra with a shoulder at lower kinetic energies becoming stronger with increasing offcut angle, but these differences can be related to the relative intensity of a single spectral component, as will be shown in the following. While spectra of a certain photon energy may be described by fewer components, one always has to assume 6 main components when taking into account that all Si-2p spectra of a specific sample must have the same spectral composition. Sometimes, an additional component (L^*) with low intensity and large Gaussian width has to be included at low kinetic energies, but will not be discussed in detail, similarly to the L-component of the spectra of the clean Si(001) surfaces.

Of the 6 main components, the B- and the R_1-component always show a decreasing relative intensity with increasing surface sensitivity [see figure 7.44 (b)], i.e. they are related to Si atoms in the bulk of the nanowire or of the substrate. Due to the lower electronegativity of the Tb atoms compared to Si atoms [336,337], charge transfers from Tb atoms to Si atoms in the silicide. Thus, the core levels of Si atoms close to Tb atoms have a lower binding energy and consequently their photoelectrons a higher kinetic energy. Such an assignment is in agreement with other XPS studies on rare earth silicides on Si surfaces [65, 69–71].

In contrast to these bulk components, the R_4-component always shows an increasing intensity with increasing surface sensitivity. Thus, the photoelectrons leading to this component definitely stem from Si atoms at the surface of the nanowires. The R_2- and R_3-components cannot be clearly assigned to bulk or surface atomic sites since their intensity changes are not always monotone with changing surface sensitivity [see R_2-component in

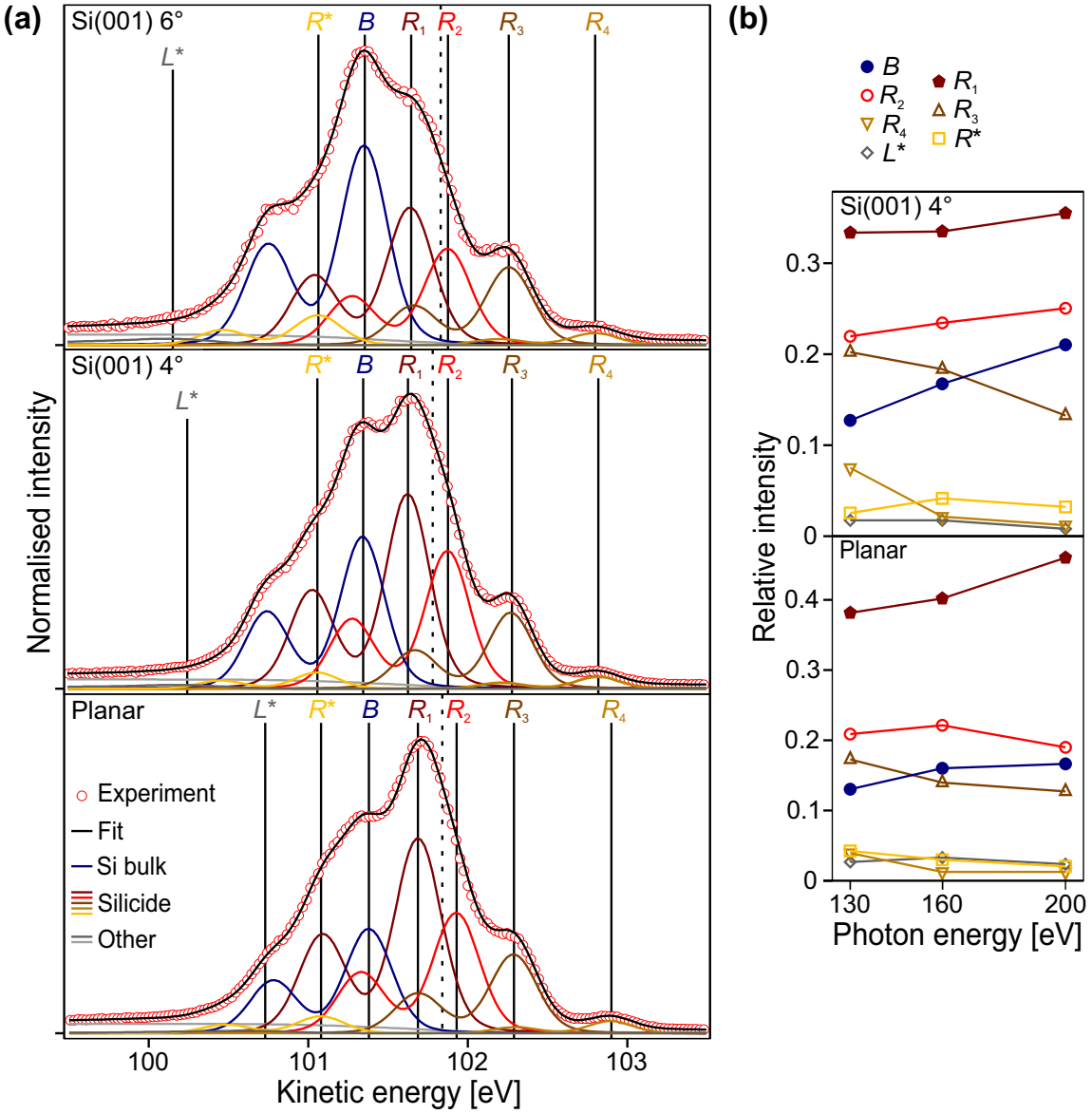

Figure 7.44.: (a) Si-2p spectra of samples with a high surface density of the nanowires using the same substrates, of which Si-2p spectra are shown in figure 7.43 (a) ($h\nu = 200$ eV). The nanowire samples were prepared by deposition of 1.7 ML and 1.5 ML Tb on the planar and vicinal samples, respectively, and annealing at 550 °C. The hatched lines illustrate the positions of the Si-bulk components of the clean substrates. (b) Exemplary intensity dependence of the Si-2p spectral components on the photon energy for nanowire samples on substrates with 0° and 4° offcut. For these data, 1.5 ML and 1.2 ML Tb were deposited on the planar and vicinal sample, respectively, while both samples were annealed at 550 °C.

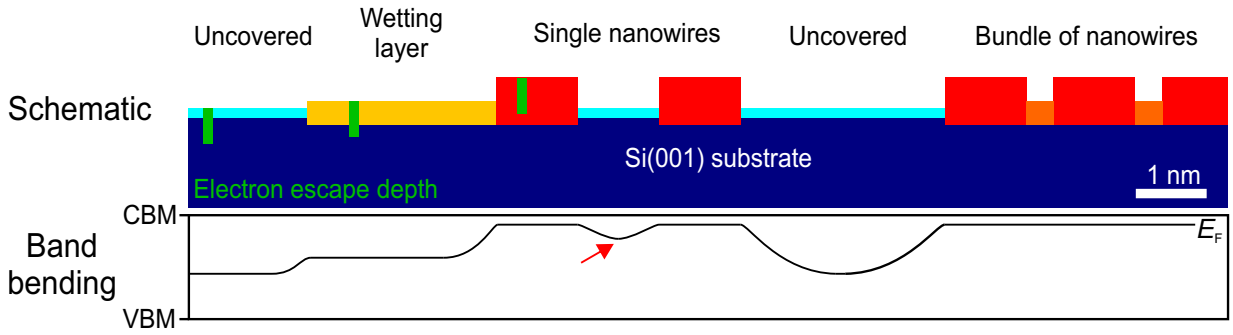

Figure 7.45.: Illustration of a Si(001) surface partly covered by the Tb silicide structures that are typically observed on nanowire samples. In addition, the influence of these structures on the local band bending is shown. In the vicinity of the nanowires, the band bending of the clean substrate and of the wetting layer is screened by the high density of states of the metallic nanowires. Typical lateral screening lengths on Si(001) are in the order of 1 nm [442, 443]. Consequently, the Fermi-level position is significantly dominated by the one of the nanowires in large surface areas when the nanowires form a dense network. This is seen, e.g., between the single nanowires (red arrow). Additionally, a photoelectron escape depth of 0.5 nm, about the inelastic mean free path of electrons with a kinetic energy of 100 eV in Si [145], is marked for the various surface structures.

figure 7.44 (b)], but the R_2-component behaves more often bulk-like, while the intensity of the R_3-component more often changes like the one of a surface component. Such a non-monotone intensity variation may arise when multiple Si atom sites from the surface and from deeper layers lead to a similar core-level shift that cannot be resolved as two separate components with XPS.

Similarly to the R_2- and R_3-components, the R^*-component likely stems from multiple Si sites or from an atomic site neither directly at the surface nor deep in the bulk due to its non-monotone intensity change with surface sensitivity [see figure 7.44 (b)]. This component is shifted to lower kinetic energies, which is unexpected for Si atoms close to Tb atoms. Thus, it may not origin from Si atoms in the silicide nanowires, but from Si atoms in the vicinity of the nanowires, whose atomic configuration was slightly changed due to strain by the silicide formation, similar to the S'-component of the Si-2p spectra of the clean substrates.

Comparing the observed core-level shifts of these spectral components with respect to the Si-bulk component, one finds a very good agreement not only between the spectra shown in figure 7.44 (a), but also with further measurements (see table 7.3). With the exception of the R^*-component, no core-level shift of a component comes close to one known from the clean substrate, showing that they are related to the formation of the Tb silicide structure. Furthermore, the intensities (I) of the components R_1-, R_2- and R_3-components have rather similar ratios for all samples, e.g. $I(R_1) : I(R_2) : I(R_3)$ is about $5 : 3 : 2$ for $h\nu = 200$ eV (see figure 7.44). No perfect agreement between all samples may be expected due the variations in nanowire growth, e.g. the formation of more or less bundled wires, but such similar intensity ratios and the very small variance in the core-level shifts clearly show that the same nanowires form on planar and vicinal samples. This is in very good

Table 7.3.: Overview on the derived absolute kinetic energies of the Si-bulk components for the Si-2p spectra of the nanowire samples shown in figure 7.44 (a) and the derived Si-2p core-level shifts of the spectral components with respect to the Si-bulk component for these specific spectra and for the average of all Si-2p spectra of nanowire samples together with its standard deviation. Literature values are given for comparison using data of Dy silicide nanowires [215]. All values are in eV and "—" assigns non-observed components.

	L^*	R^*	B	R_1	R_2	R_3	R_4
Planar	-0.65	-0.30	101.38	0.29	0.55	0.89	1.52
4° offcut	-1.10	-0.29	101.35	0.28	0.53	0.93	1.47
6° offcut	-1.20	-0.29	101.36	0.29	0.52	0.90	1.44
Average	-1.0 ± 0.3	-0.30 ± 0.02	101.36	0.29 ± 0.01	0.54 ± 0.02	0.90 ± 0.03	1.46 ± 0.05
Literature	—	-0.28		0.30	0.61	1.10	1.50

agreement with the already discussed STM and HRTEM data. The rather pronounced differences in the Si-2p spectra of nanowire samples might indicate structural differences [see figure 7.44 (a)], but taking a closer look at their decomposition it becomes clear that the differences mainly arise due to the increasing relative intensity of the Si-bulk component with increasing offcut angle. This behaviour is not unexpected since lower Tb coverages had to be used for the nanowire preparation on the vicinal samples.

In addition to the core-level shifts of the spectral components with respect to the Si-bulk component, tables 7.2 and 7.3 also include the energetic positions of the Si-bulk components. By calculating the differences between these kinetic energies of the bare substrates and the respective nanowire samples, the band bending change upon nanowire formation can be estimated. For the clean n-type Si(001) substrates, the Fermi level lies (0.48 ± 0.02) eV above the valence band maximum [215–217], and the shift by (0.45 ± 0.01) eV due to the nanowire growth leads to Fermi level position of about 0.93 eV above the valence band maximum. Such a Fermi level position very close to the conduction band minimum is characteristic for the $TbSi_2$ monolayer on Si(111), which is Si vacancy free, indicating that the Tb silicide nanowires on Si(001) have a similar atomic structure, possibly also without Si vacancies. This is in very good agreement with the atomic structure model for the nanowires proposed in this work (see section 7.3).

Taking a closer look, the derived Fermi-level position of the Tb silicide nanowires on Si(001) lies slightly lower than the one of the $TbSi_2$ monolayer on Si(111) at about 1.05 eV above the valence band maximum [69]. This small deviation may be related to the different growth modes. On Si(111), large $TbSi_2$ patches in between extended clean surface areas are observed leading to the observation of two substrate bulk Si-2p components, one shifted and an unshifted one [69]. The silicide nanowires on Si(001) are higher (about 0.7 nm, see section 7.3) than the monolayer structure on Si(111) (about 0.4 nm, see section 5.4) leading to a decreased intensity of the completely shifted Si-bulk component. Furthermore, the surface areas in between nanowires are disordered and for high nanowire coverages much narrower than in between the monolayer patches on Si(111) [compare figures 5.17 (a) and 7.8], resulting in relatively large contributions from surface areas close to the nanowires. There, the band bending of the uncovered surface is almost completely screened by the high

density of states of the metallic nanowires (see red arrow in figure 7.45). In addition, such screening processes are also expected for the wetting layer, which may be present on the nanowire samples and exhibit a Fermi level position in between that of the clean surface and that of the nanowires (see below and figure 7.45). Thus, the average Si-bulk component of the nanowire samples is expected to shift to higher kinetic energies as compared to the one directly under the nanowires. Furthermore, it should have a larger Gaussian width than the one of the clean surfaces, consistent with our findings. This view is also supported by the lack of a dominant contribution at the kinetic energy of the Si-bulk component of the clean surfaces [see figure 7.44 (a)].

A very similar Si-2p spectra composition as presented here for Tb silicide nanowires was found for Dy silicide nanowires [215]. There, also 6 main components were observed and assigned in a similar way to the bulk of the substrate, the surface of the nanowires, and the bulk of the nanowires. Even the derived core-level shifts of the various spectral components are rather similar for Dy and Tb silicide nanowires, again illustrating the chemical similarity of the different trivalent rare earth metals (see table 7.3). The only disagreement between the Si-2p spectra of Tb and Dy silicide nanowires is the observation of the R^*-component exclusively for low Dy coverages, which led to its assignment to the wetting layer. For Tb silicide nanowire sample, the R^*-component is present also for high nanowire coverages [see figure 7.44 (a)]. This discrepancy shows that further information on the Si-2p spectra of other rare earth silicide structures is needed for a better understanding.

Wetting layer and islands

The formation of the wetting layer in large areas is easily checked by LEED. The upper part of figure 7.46 (a) shows a Si-2p spectrum for a sample that showed the characteristic $\times 2$ and $\times 7$ spots of the wetting layer in LEED. Since the wetting layer is a submonolayer structure, the component with the largest intensity is the one of the Si bulk. Comparing the kinetic energy of this component to the one of the clean substrate, indicated as hatched line in figure 7.46 (a), a comparatively small band bending change of about 0.20 eV is deduced. Thus, the Fermi level is about 0.68 eV above the valence band maximum, which is much lower than observed for the silicide nanowires, as also depicted at the bottom of figure 7.45.

Due to this different bend bending, the kinetic energies of the wetting-layer components are not at the absolute positions observed for nanowire components, but instead the core-level shifts of the three wetting-layer components R^*, R_1, and R_2 with respect to the Si-bulk component agree nicely with the corresponding ones of the nanowire samples (see tables 7.3 and 7.4). This clearly indicates that structural similarities should exist between wetting layer and nanowires, which is in nice agreement with the RAS data and the discussed structure model (see sections 7.1 and 7.3). In contrast to the clear intensity differences of these spectral components for the case of the nanowire samples, these three components have a rather similar intensity for the wetting layer when a photon energy of 200 eV is used, indicating different occurrences of structural motives [see figures 7.46 (a and b)]. Furthermore, additional structural elements are expected for the nanowires due to the missing of the R_3- and R_4-component for the wetting layer.

In addition to the up-to-now discussed components of the wetting layer Si-2p spectra, there are two other ones observed. The one at low kinetic energy (L^*) always has a large

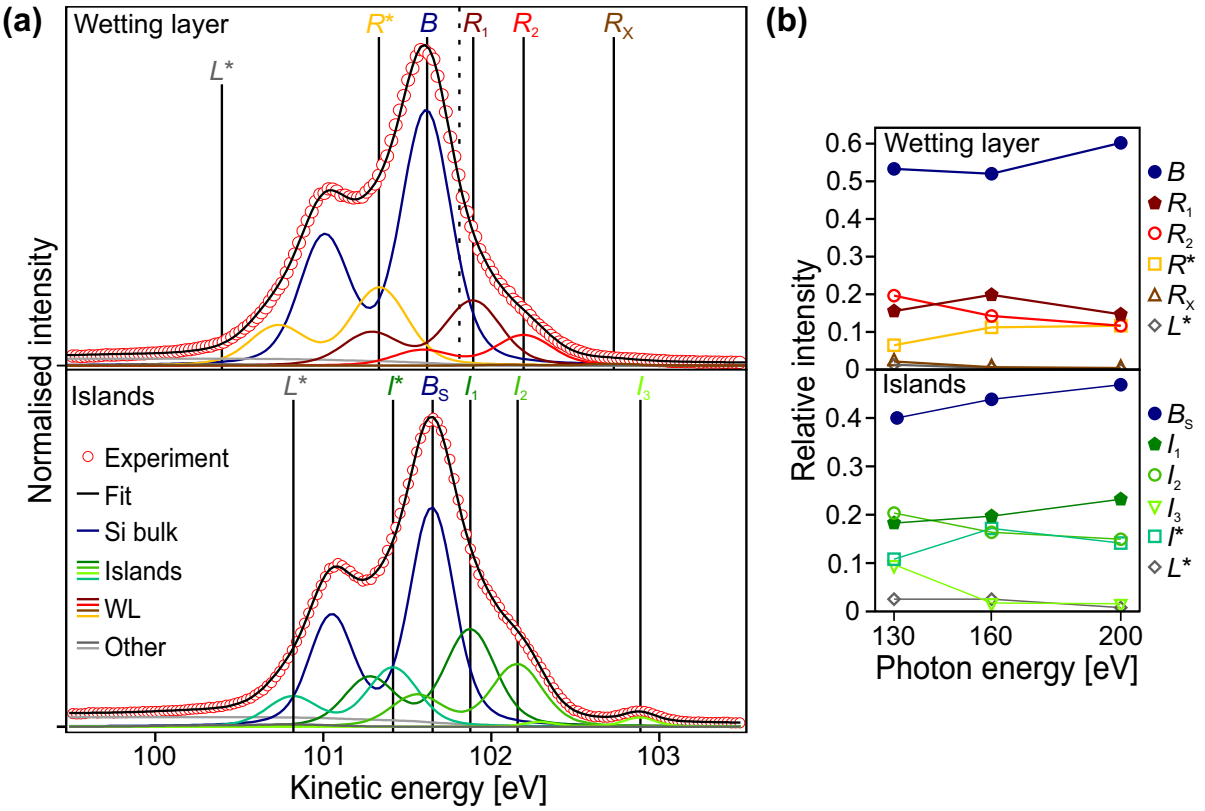

Figure 7.46.: (a) Si-2p spectra of planar samples completely covered by the wetting layer (upper part) and with a high surface density of Tb silicide islands (lower part). The hatched line in the upper part indicates the position of the Si-bulk component of the same substrate without wetting layer. (b) Dependence of the relative intensities of the Si-2p spectral components of the wetting layer and of the islands on the used photon energy. The preparation conditions for the wetting layer were in (a) 0.5 ML Tb annealed at 500 °C and in (b) 0.4 ML Tb annealed at 450 °C. The island sample was prepared by depositing 4.6 ML Tb and annealing at 700 °C.

Table 7.4.: Overview on the average Si-2p core-level shifts of the spectral components with respect to the Si-bulk component for the wetting layer together with their standard deviations. All values are in eV.

	L^*	R^*	R_1	R_2	R_X
Wetting layer	-1.1 ± 0.1	-0.30 ± 0.02	0.30 ± 0.02	0.54 ± 0.02	1.17 ± 0.02

Gaussian width and low intensity, as already observed for the clean and nanowire covered surface. Due to its unknown origin, this component is not discussed here. There is also a very small component at high kinetic energy (R_X). This component lies approximately at the kinetic energy of the R_4-component of the nanowire samples. Similarly to the R_4-component, the R_X-component shows an increasing intensity with increasing surface sensitivity. Thus, it most likely stems from nanowires that may have formed rarely. In contrast to the other nanowire components, it may be resolved due to is rather separate

Table 7.5.: Overview on the derived Si-2p core-level shifts of the spectral components with respect to the shifted Si-bulk component for Si-2p spectra of the island sample shown in figure 7.46 (a). All values are in eV.

	L^*	I^*	I_1	I_2	I_3
Islands	−0.7	−0.23	0.23	0.50	1.24

position at high kinetic energy. Of course the Si-2p spectra of the nanowires may also be influenced by the wetting layer, but taking into account that all spectral components that stem from the wetting layer have a much smaller intensity than the Si-bulk component, the effect of occasional wetting layer structures on the nanowire spectra should be negligible.

Other structures that may influence the nanowire Si-2p spectra are islands since they may form already at rather low temperatures for high Tb coverages [see figure 7.8 (a)]. The lower part of figure 7.46 (a) shows a Si-2p spectrum of a sample with high island density [see similar preparation in figure 7.10 (c)]. The island Si-2p spectrum appears surprisingly similar to the one of the wetting layer. Even a similar number of spectral components is found, but distinctly different core-level shifts with respect to the Si-bulk component are derived (see tables 7.4 and 7.5).

The determination of the Si-bulk component for the island sample is not trivial. Presumably, the larger part of the surface is covered by multilayer high islands, but there are still sizeable areas showing the clean Si(001) surface [see figure 7.10 (c)]. Two components (B_S and I_1) show a clear increase with increasing photon energy indicating that they stem from bulk Si atoms. Since most of the surface is covered by islands, the component with higher intensity might be related to the islands, but the opposite is proposed here. The component with lower kinetic energy is assigned to the Si bulk while the other one is assumed to stem from the bulk of the silicide islands as is in agreement with the expectation due to the lower electronegativity of Tb compared to Si [336, 337]. The large intensity of the Si-bulk component may be related to the about 70% higher Si atom density in crystalline Si than in hexagonal or tetragonal $TbSi_2$ with Si vacancies or the formation of larger clean surface areas than observed in figure 7.10 (c).

That the islands consist of these bulk silicides is in agreement with the STM measurements presented here, but also directly observed in HRTEM measurements [432–434]. For such bulk Tb silicides with Si vacancies, the Fermi-level position is expected to move towards the conduction band, but not as drastically as for the stoichiometric $TbSi_2$ [69]. However, there should only be a negligible amount of photoelectrons stemming from below the islands due to their large height. Nevertheless, the component assigned to the Si bulk is shifted to lower kinetic energy compared to the one of clean substrates presumably due to the large density of defects on the clean surface areas, which may be induced by Tb.

That the islands have a different structure than the nanowires is also seen in the differences of the core-level shifts of the silicide components (see tables 7.3 and 7.5), but there are also similarities between the data of the different silicide structures. With increasing kinetic energy, the spectral components with positive core-level shifts (I_1, I_2, and I_3) stem from sites closer to the surface, a trend that was also observed for the nanowires. In addition, there are also a component (I^*) that may be related to the strained Si surrounding the islands

and a component (L^*) with low intensity and large Gaussian width at low kinetic energies. It should be noted that the errors of the core-level shifts for the islands are assumed to be rather large since only a single sample was studied and the core-level shifts are close to the ones also observed on the clean surface, which is present next to the nanowires.

The $p_{3/2}$-part of the I_3-component lies well isolated from the rest of spectral weight leading to a precise determination of the Gaussian and Lorentzian widths of this component. The derived Gaussian width is much smaller than the ones of the other components, a reminder that not all components are resolved in the XPS study presented here. Nevertheless, this study clearly showed that there are similarities between the silicide nanowires and the wetting layer and differences to silicide islands.

In the discussion of the band bending, it was assumed that the nanowires are metallic. If that is indeed the case will be analysed in the following by STS.

7.4.2. Scanning tunnelling spectroscopy

Taking a look at the literature, the general electronic structures of the various rare earth silicide structures on Si(001) seem well understood. The wetting layer is semiconducting while the nanowires are metallic and one may safely assume that the islands are metallic, since they are in principle large clusters of the metallic bulk silicide phases [75, 81–85, 275, 276, 315, 330, 331, 432, 433]. However, detailed studies on the wetting layer and the silicide islands are missing, and more in depth studies on nanowires show a rather heterogeneous picture (see section 5.4).

Beginning with the wetting layer, average STS point spectra taken on the 2×3 subunits are depicted in figure 7.47. It should be noted that no atomically resolved STS measurements are possible with the used set-up due to the rather large temperature fluctuations in the laboratory, in the order of 1 °C between day and night, leading to considerable thermal drift. This is seen in the shift of the wetting layer row during the acquisition of one STS spectrum in the inset in figure 7.47 (a).

While the black and red I-V spectra, which cover together a rather large voltage range, show negligible slope around $V = 0$ indicating semiconducting behaviour, the normalised differential conductance, which approximately resembles the density of states, reveals states very close to the Fermi level, which corresponds to $V = 0$, and drops only directly at $V = 0$ to zero indicating a (semi-)metallic characteristics. This unexpected finding is proven by the STS measurement shown in blue in figure 7.47 (a), in which the tip was presumably closer to the surface than for the other measurements. This small voltage range I-V curve clearly shows a finite slope at $V = 0$, which is only possible if both tip and analysed sample structure are metallic. However, the strongly voltage dependent appearance of the wetting layer indicates that these metallic states are localised and may not lead to a lateral conduction. Such an interpretation of the STS data obtained here agrees well with the ARPES data reported for the Dy induced wetting layer, where non-dispersing intensity is observed close to the Fermi level [85].

In contrast, the nanowires of Gd, Dy, and Er silicide are well known to form electron bands crossing the Fermi level [75, 84, 85]. States at the Fermi level are also found for Tb silicide nanowires using STS. This is exemplarily seen in figure 7.48 for a single wire on a Si(001) substrate with 6° offcut. While the slope at $V = 0$ may be rather small, the

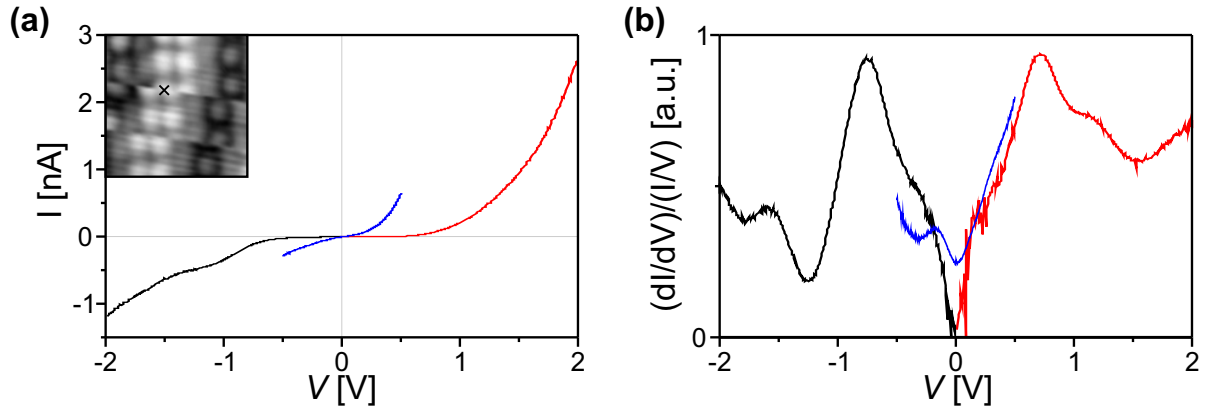

Figure 7.47.: (a) I-V and (b) normalised differential conductance spectra measured on the 2×3 subunits of the wetting layer. The stabilisation conditions of the tip before the measurement were: $I = 0.1$ nA at $V = -1.0$ V and approach of the tip to the sample by $\Delta z = 50$ pm for the black graph, $I = 0.05$ nA, $V = +0.5$ V, and $\Delta z = 75$ pm for the red graph, and $I = 0.5$ nA, $V = -1.5$ V, and $\Delta z = 50$ pm for the blue graph. The inset in (a) shows an STM image of a 3.5 nm wide area together with one measurement position marked as black cross ($V = -1.0$ V and $I = 0.1$ nA). The shift of the wetting layer rows arises during one STS point spectrum due to thermal drift and piezo-creep effects.

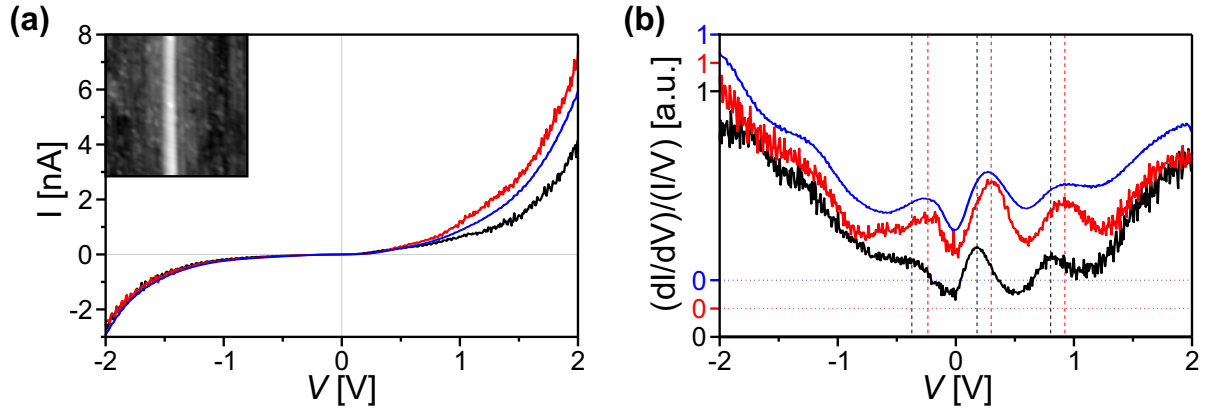

Figure 7.48.: (a) I-V and (b) normalised differential conductance spectra measured on a single nanowire. The stabilisation conditions of the tip prior to the measurement were $I = 0.1$ nA, $V = -1.5$ V, and $\Delta z = 100$ pm for all measurements. The red and black curve are point spectra taken at positions 2 nm apart while the blue curve shows an average spectrum. The inset in (a) shows an STM image of a 25 nm wide area with the investigated nanowire ($V = -1.5$ V and $I = 0.1$ nA). The hatched and dotted lines in (b) are guides for the eyes.

normalised differential conductance is well above zero in the entire measured voltage range proving the metallic character of the nanowires. Unfortunately, the measured spectra may vary rather strongly even when obtained on the same nanowire, a problem also observed in the literature data (see section 5.2).

Taking a look at the red and black *I-V* spectra in figure 7.48 (a), which were measured on the same nanowire at positions 2 nm apart, they appear rather similar in the negative voltage range, but deviate for positive voltages. The discrepancy between both measurements becomes even more pronounced for the differential conductance [see figure 7.48 (b)]. There, the spectra appear similar at a first glance, but the positions of the local maxima differ significantly. While a small tip change cannot be excluded, no indications for it are seen in the measured STM image. Thus, the difference may be related to a change of the nanowire structure, e.g. the surface structure may have changed, as often observed (see section 7.3). A variation of the surface atomic structure may lead to a slightly different electronic structure of the surface and consequently different STS data, although the surface structure of the investigated nanowire is not resolved in STM [see inset in figure 7.48 (a)]. Another possibility could be a small width change, which cannot always be easily detected for single nanowires due to their exposed presence outshining their surrounding in STM images. This last problem is not as prominent in bundled nanowires, so that further information may be obtained despite the variation of STS spectra of the same nanowire.

Figures 7.49 (a and b) show STS data of nanowires of different widths, which are all observed in nanowire bundles. The spectra of the narrowest nanowire are shown in black and those of the widest one in blue. Interestingly, structures in the normalised differential conductance occur at rather similar voltages for all three nanowires, but these structures widen with increasing width of the nanowire, e.g. the local maximum at about -0.3 V appears sharper for narrower nanowires. In addition, also local minima, e.g. at about -0.8 V or around about $+1.5$ V, are less pronounced the wider the investigated nanowire is. Very similar results are often obtained, e.g. also for the STS data shown in figure 7.49 (c and d). The red and blue spectra were obtained above a narrow and a wide nanowire, respectively [see inset in figure 7.49 (c)]. Again, a rather similar appearing normalised differential conductance is found, but the local structures are much wider and less pronounced for the wider nanowire. That the spectra appear in general rather similar independent of the nanowire width again indicates that all nanowires have the same structure including the general surface structure. The smoothing of the spectra with increasing nanowire width indicates that additional states develop when the nanowire gets wider.

Comparing the spectra of the different nanowires in figures 7.48 and 7.49, it becomes obvious that not only the individual STS spectra of a single nanowire vary, but also the average STS spectra may differ strongly. The main reason for this is the tip, which changes with every approach. The strong influence of the tip is also seen when the red spectra are compared to the black spectra in figures 7.49 (c and d). Both are average spectra of the same nanowire, but a drastic tip change occurred between the two STS measurements, as also revealed by a different appearance of the surface structures, which surround the nanowire bundle. In the normalised differential conductance, the local maxima for positive voltages are shifted while the negative voltage ranges appear completely different with the exception of the local maxima at about -0.2 V. This large variety prevents a more detailed analysis, e.g. of the influence of the bundling in general or of small changes due to an embedding in the wetting layer, but fits to the already reported variation of STS data for other rare earth metal silicide nanowires (see section 5.4). If the electronic structure changes with the rare earth metal or if all rare earth silicide nanowires have in general the same electronic structure cannot be decided based on the present STS data.

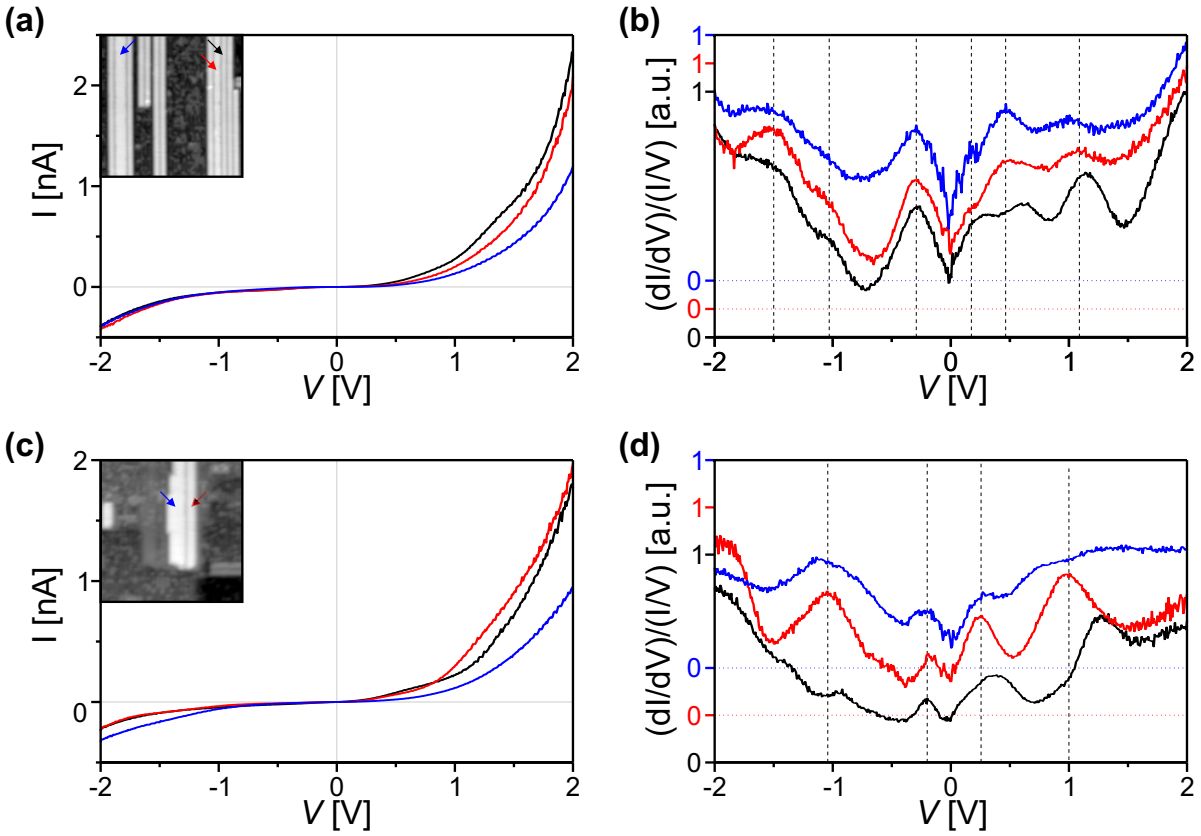

Figure 7.49.: (a) I-V and (b) normalised differential conductance spectra measured on nanowires of nanowire bundles. From black over red to blue, the nanowires get wider, see arrows in the inset in (a), which shows an STM image of a 37 nm wide area with the investigated nanowires ($V = -2.5$ V and $I = 0.1$ nA). (c) I-V and (d) normalised differential conductance spectra measured on nanowires of a nanowire bundle. The black and red curve are measured on a narrow nanowire while the blue curve is from a wide nanowire, see arrows in the inset in (c), which shows an STM image of a 25 nm wide area with the investigated nanowire bundle ($V = -2.5$ V and $I = 0.1$ nA). The stabilisation conditions of the tip were $I = 0.1$ nA and $V = -2.5$ V for all measurements with (a and b) $\Delta z = 100$ pm and (c and d) $\Delta z = 75$ pm. In (b and d), the hatched and dotted lines are guides for the eyes.

Lastly, the islands were analysed using STS. Three measurements, which are nominally different only due to changing distances between tip and island, are shown in figure 7.50. There is a clear slope of the I-V spectra at $V = 0$ especially for the tip closer to the island and all normalised differential conductances are well above zero across the entire measured voltage range. Thus, the islands are metallic, similar to the nanowires. Interestingly, although nanowires and islands presumably consist of $TbSi_2$ with a Si dimer surface structure, the spectra are substantially different. In nearly all STS measurements of nanowires, the normalised differential conductance shows a local maximum or at least a shoulder at about -0.2 V to -0.3 V (see figures 7.48 and 7.49). Such a structure is completely missing in all acquired spectra of islands (see figure 7.50). This difference may be related to the Si

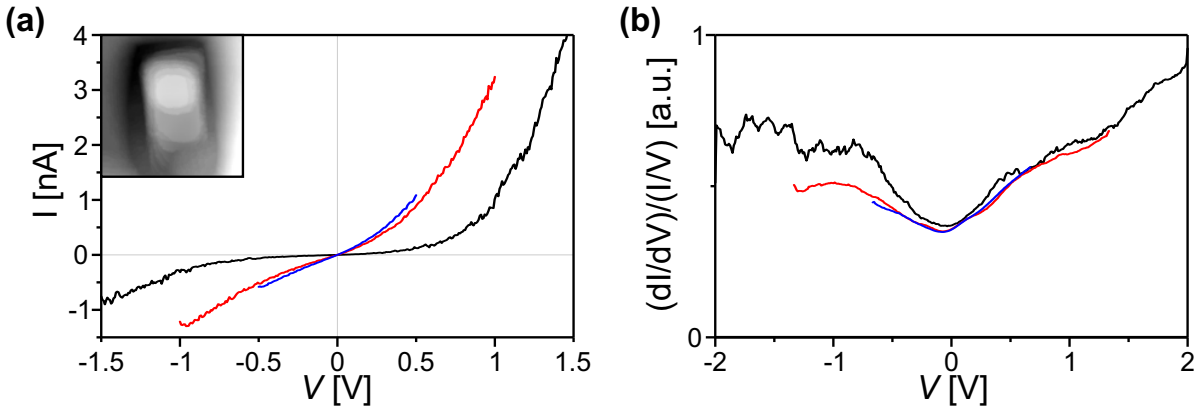

Figure 7.50.: (a) I-V spectra and (b) normalised differential conductance measured on an island. The stabilisation conditions of the tip prior to the measurement were for all measurements $I = 0.1$ nA and $V = -1.5$ V, but the tip approached to the sample by $\Delta z = 50$ pm for the black graph, $\Delta z = 75$ pm for the red graph, and $\Delta z = 100$ pm for the blue graph. The inset in (a) shows an STM image of a 250 nm wide area with the island, and all STS measurements shown here were performed on its topmost surface ($V = -1.5$ V and $I = 0.1$ nA).

vacancies, which probably do not form in the nanowires, and the different dimensionality of the investigated Tb silicide structures.

A metallic behaviour and indications for a reduced dimensionality of the nanowires were found using STS. For a conclusive determination of the dimensionality of the nanowires, ARPES results are discussed in the following.

7.4.3. Angle resolved photoemission spectroscopy

Both XPS and ARPES measurements were performed at the same station using the same samples, i.e. also the ARPES samples always contained a mixture of various surface structures. This does not prevent the assignment of observed bands to the nanowires, since no dispersing bands were found for the wetting layer alone in agreement with the literature and island formation is unlikely for the preparations discussed in the following due to their low Tb coverages or low annealing temperatures [85]. But the incomplete coverage of the surface with nanowires leads to a reduced intensity of the nanowire bands and a significant diffuse background from the other surface structures. This problem gets worse since vicinal samples, on which nanowires form dominantly in a single domain, have to be used to differentiate between the dispersion parallel and perpendicular to the nanowires. On such vicinal samples, the maximum nanowire coverage is reduced compared to planar samples (see section 7.1).

Furthermore, not every nanowire must have exactly the same electronic structure, e.g. a variation with the nanowire width was observed by STS. Since a global assembly of different nanowires is measured, all these different electronic structures overlap leading to a broadening of bands and possibly even the non-observation of certain bands that only stem from specific nanowires. In addition, the ARPES data may vary from sample to

sample depending on what kind of nanowires formed preferentially. Further variations from sample to sample may be expected due to varying nanowire densities or changes in bundling behaviour by different annealing temperatures if there are interactions between neighbouring nanowires.

Despite these problematic circumstances regarding the analysis of the electronic structure of the $TbSi_2$ nanowires on Si(001), it was possible to obtain ARPES data showing clear bands after some data processing. That such data processing is necessary is exemplarily demonstrated for the three-dimensional ARPES data cuboid of a nanowire sample shown in figure 7.51 (a). The highest intensity is found between binding energies of about 1.5 eV and 4.0 eV, so that the bands are hardly visible in the interesting part close to the Fermi level. This large intensity may stem from the valence bands of the Si substrate, the nanowires, and the other surface structures, but also the Tb-4f emission is known to lie in this energy region [444, 445].

In figure 7.51 (a), both $k_\parallel$ and $k_\perp$ lie parallel to the surface plane and describe the momentum of the photoelectrons parallel and perpendicular to the step edges and consequently to the majority of the nanowires, respectively [see figure 7.51 (b)]. During the measurement, binding energy-$k_\parallel$ intensity images were acquired while $k_\perp$ is changed step by step, i.e. the $k_\perp$ axis also corresponds to a time axis. With increasing $k_\perp$, there is a significant increase of rather diffuse intensity at a binding energy of about 5.5 eV to 6.5 eV [see purple arrow in figure 7.51 (a)], which is related to oxidised Tb silicide leading to the conclusion that the Tb silicide nanostructures react with O from the rest gas with time [446]. That the samples indeed oxidise during the often time consuming ARPES measurements was tested using XPS. Before the ARPES measurement, only Si peaks are observed in the overview XPS spectra in figure 7.51 (c). Afterwards, there is an additional albeit small peak stemming from O. That the O peak has such a low intensity and that no Tb lines are clearly observed is related to the large photoelectron escape depths by the 800 eV photons leading to a small signal from the surface compared to the one of the Si substrate bulk. No data of samples with very large O adsorption will be presented in the following, but it should be kept in mind that the samples change during a measurement.

Before the ARPES data of $TbSi_2$ nanowires are analysed in detail, the influence of the substrate on the apparent band structure is determined. Figure 7.52 shows dispersion plots of a clean Si(001) substrate with 6° offcut and of the same substrate covered with a nominally rather low density of nanowires. The dispersion plots of the clean substrate are dominated by bands of the Si bulk [see figure 7.52 (a)]. In addition, there is also a broad band (marked by the red arrows) that lies partially in the bulk band gap (valence-band maximum is marked by inside ticks on the binding energy scale). This band stems from the Si dimer rows [225]. It disperses perpendicular to, but not parallel to the step edges, in agreement with the formation of Si dimer rows perpendicular to the step edges as observed by STM (see section 5.1).

Despite the presumably low nanowire density due to the rather low Tb coverage, almost all of the Si bulk bands and also the surface state vanish upon nanowire preparation [see figure 7.52 (b)]. The silicide structures disrupt the surface, so that no well-defined band of the Si dimer rows forms, although Si dimer rows may still be observed locally. In addition to a reduced intensity of the Si bulk bands due to the additional material on the surface, the non homogeneous band bending by the multitude of surface structures leads to a washing out

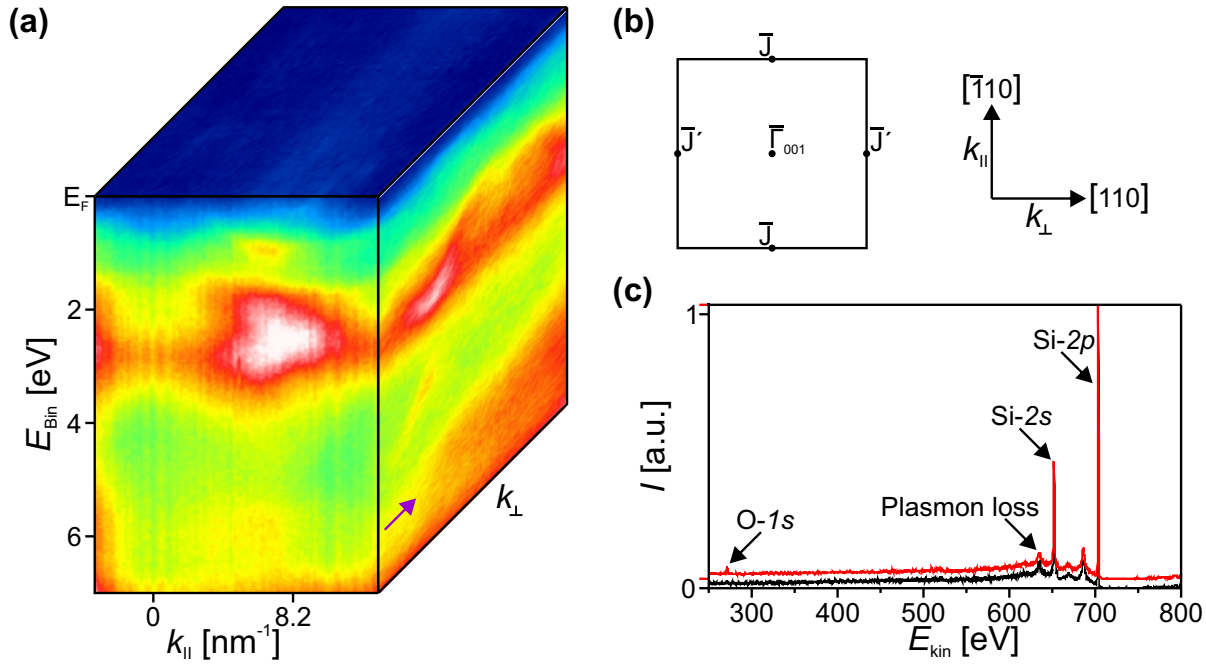

Figure 7.51.: (a) Exemplary three-dimensional ARPES data cuboid obtained for a nanowire sample ($h\nu = 62$ eV). The nanowires were prepared on a Si(001) substrate with 6° offcut towards [110] by depositing 1.1 ML Tb and annealing at 600 °C (sample 1). The purple arrow indicates an oxide peak, whose intensity increases with time, i.e. increasing $k_\perp$. For all nanowire samples, the Fermi level could be estimated and was checked frequently by measurements of the Fermi edges of the Mo sample holders or of the Au piece on the manipulator. (b) Illustrations of the first Brillouin zone based on a 1×1 surface structure with high symmetry points and of the corresponding directions. $\overline{\mathrm{J}}$ and $\overline{\mathrm{J}}'$ are 8.2 nm^{-1} away from the Brillouin zone centre $\overline{\Gamma}_{001}$. Since all vicinal samples have the same offcut direction, the long nanowire axis is along $[\bar{1}10]$ and the short one parallel to [110] for most nanowires. (c) Overview XPS spectra before (black) and after (red) an ARPES measurement of a Tb silicide nanostructure sample ($h\nu = 800$ eV). The spectra are shifted to each other for better visibility with the lower and upper coloured ticks at the axis of the intensity corresponding to 0 and 1, respectively. The measurements lie about 2 h apart.

of these bands. Nevertheless, one Si bulk band is still clearly visible even if it is broadened. It is shifted to higher binding energies by about 0.4 eV, in agreement with the band bending change observed by XPS (yellow arrows in figure 7.52). Since all Si bulk bands are affected by this band bending change, also the valence band maximum shifts to higher binding energies. Bands that are observed at lower binding energies than the Si bulk valence-band maximum lie in the band gap of the substrate and, consequently, can be assigned to the nanowires.

Detailed and contrast-enhanced dispersion plots of this nanowire sample are shown in figures 7.53 (a and b). Starting with analysing the dispersion perpendicular to the nanowires, there are dispersing bands even in the substrate band gap, e.g. see the band marked by a yellow arrow in figure 7.53 (a). Nevertheless, most bands disperse only

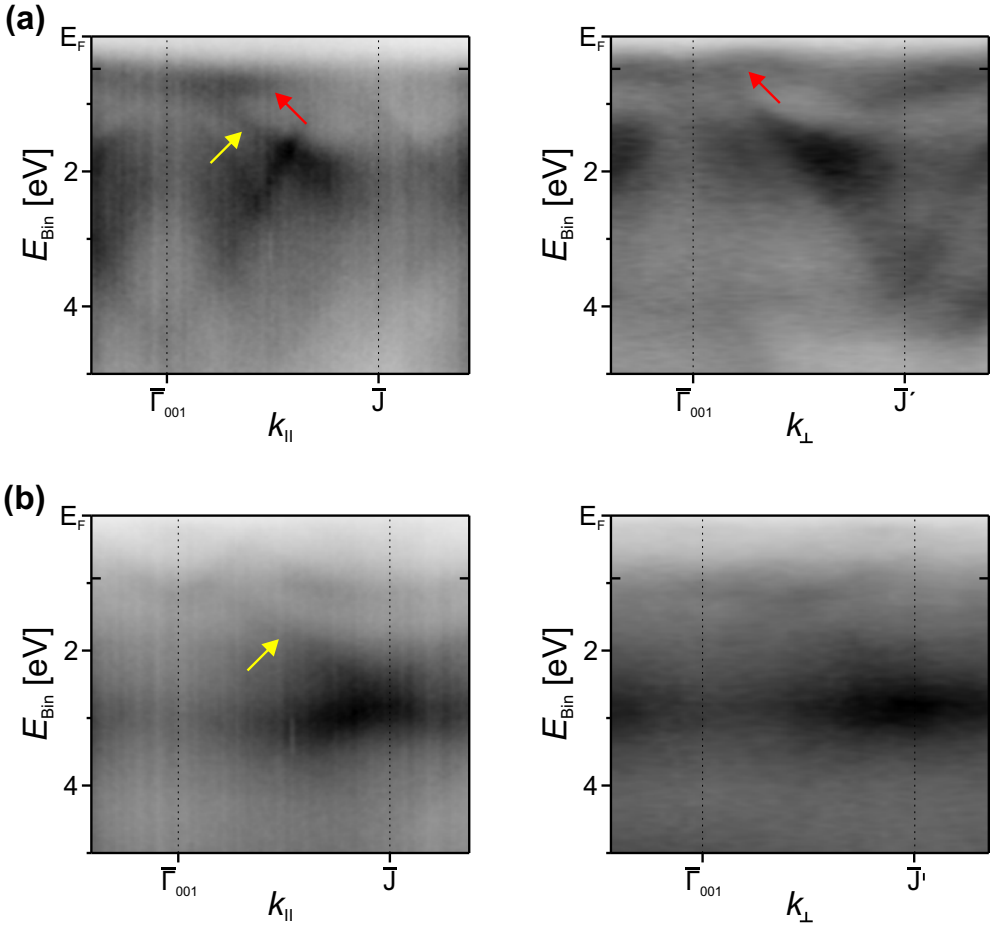

Figure 7.52.: Dispersion plots of the electronic bands parallel (left) and perpendicular (right) to the step edges of (a) a clean vicinal n-type Si(001) substrate and of (b) the same substrate with nanowires ($h\nu = 62$ eV), being the same nanowire ARPES data as in figure 7.51, i.e. sample 1. The red arrows mark the band of the Si dimers on the clean Si substrate and the yellow arrows indicate a Si substrate bulk band, which is observed for both the clean and the nanowire sample. The inside ticks on the binding energy scale correspond to the valence-band maxima of the Si substrate.

slightly, e.g. no strongly dispersing band is observed at the boundary of the Brillouin zone ($k_{\parallel} = 8.2$ nm^{-1}). Especially at the Fermi level, one does not find dispersing bands, although there are rather strong intensity modulations with $k_{\perp}$. Thus, the nanowires have not a purely one-dimensional electronic structure, which is of course expected, but they may still be quasi-one-dimensional if the Fermi surface shows oscillating contours instead of closed lines despite the few bands dispersing perpendicular to the nanowires. It is even possible that two-dimensional bands at higher binding energies turn into quasi-one-dimensional ones close to the Fermi level [447].

In contrast to the dispersion plots perpendicular to the nanowires, many strongly dispersing bands are easily seen parallel to the nanowires in figure 7.53 (b). Comparing the various shown cuts, pronounced intensity variations with $k_{\perp}$ are apparent in agreement with the observations in the perpendicular direction. Concentrating on the region marked by

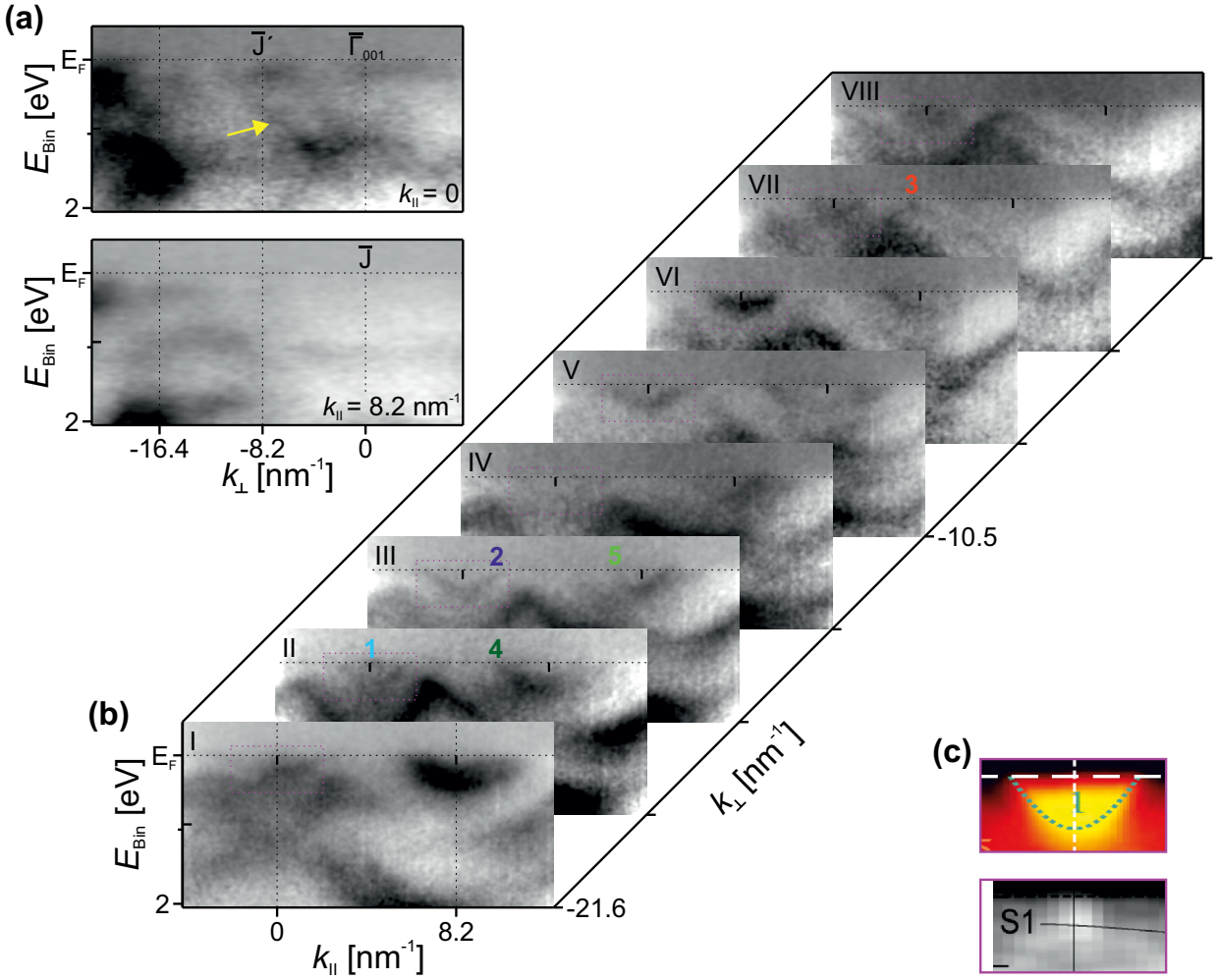

Figure 7.53.: (a and b) Detailed dispersion plots close to the Fermi level (a) perpendicular and (b) parallel to the nanowires of the fully processed ARPES data that were already introduced in figure 7.51 (a) (sample 1, $h\nu = 62$ eV). The yellow arrow marks a dispersing band and the coloured numbers indicate bands that reach or cross the Fermi level. Dotted magenta rectangles highlight the range discussed in the text. The nominally same ranges of the reported Dy (upper part) and Gd (lower part) silicide nanowire data are shown in (c) for comparison [84, 85]. The inside ticks in (a and b) indicate the substrate valence band maximum.

magenta rectangles in figure 7.53 (b), i.e. the one close to the Fermi level around $k_{\|} = 0$, the intensity reduces from panel I until there is nearly no intensity observed any more in panel IV. Afterwards the intensity increases rapidly up to panel VI before diminishing again. These intensity changes are not caused by bands moving into and out of this region, but by the loss and decrease of intensity of apparently the same bands. If the intensity would only diminish with $k_{\perp}$, the reasons for the intensity change could be the oxidation of the nanowires, but intensity increases do not agree with such an explanation. Thus, matrix element effects are the most likely candidates for the intensity variations.

Taking a closer look at the dispersing bands, there are two bands reaching or crossing the

Fermi level around $k_{\parallel} = 0$ [labelled 1 and 2 in figure 7.53 (b)]. The first band only appears as a local intensity maximum, which fills the parabola of the second band. Most of the times, the resolution is not sufficiently high to resolve these two bands individually (see panels I or VII), but a reduced intensity between them is seen in panel II of figure 7.53 (b). The existence of the second band nicely agrees with observations made for Dy and Er silicide nanowires, for which similar parabolic bands were reported [85]. Interestingly, the parabolas appear rather filled in the literature data, as seen in figure 7.53 (c), so that also band 1 may be present, but not distinguishable. In contrast, the first band was observed for Gd silicide nanowires, but not the second band [see figure 7.53 (c)] [84]. While the first band was never observed alone in the study presented here in contrast to the Gd silicide nanowire data, the different appearing band dispersions for the various rare earth metals may be related to matrix element effects and not to fundamentally different electronic structures.

A very nice agreement between the band structures of nanowires from different rare earth silicides is the observation of two parabolas around the edge of the Brillouin zone (bands 4 and 5 around $k_{\parallel} = 8.2$ nm^{-1}) [84, 85]. While they appear as a broad single band in panel I of figure 7.53 (b), similar to early findings for Dy silicide nanowires [319], a wider and a narrower parabola are clearly distinguished in the two following panels. In addition, there is another band reaching the Fermi level at approximately $k_{\parallel} = 3.7$ nm^{-1}, which is only visible in the panels VII and VIII [labelled 3 in figure 7.53 (b)]. This band was not reported in previous nanowire studies [84, 85, 319], but a band crossing the Fermi level at about the $k_{\parallel}$-value of the third band was predicted based on ARPES data for the two-dimensional $RESi_2$ monolayer on Si(111) [75]. A schematic overview on the dispersions of these bands crossing or reaching the Fermi level is shown in figure 7.54 (a) while the Fermi surface obtained for the up-to-now discussed ARPES data of Tb silicide nanowires is depicted in figure 7.54 (b).

Band 1 is only shown as a filled ellipse in the schematics, since it will be unclear if it has hole-like or electron-like characteristics. In the dispersion plots, it is only a local intensity maximum, and no continuous band reaches this maximum from higher binding energies indicating an electron-like dispersion. But such bands may be masked by the surrounding parabola of the second band, and no two lines are discernible as Fermi contours, which would be expected for an electron-like parabola. A high intensity on the Fermi surface is only observed for large negative values of $k_{\perp}$ for the first band [light blue ellipse in figure 7.54 (b)]. Its Fermi contour is a single rather straight line, which is also quite broad, so that its double structure or small oscillations may be masked. Thus, an assignment as electron-like or hole-like is not possible for the first band.

Band 2 is clearly electron-like, and two faint lines can be detected as Fermi contour for this band. The lines are symmetric to the $k_{\parallel} = 0$ axis and appear almost straight, but are slightly convex around $\overline{\mathrm{J}'}$ [see dark blue ellipse in figure 7.54 (b)]. Thus, they clearly indicate a quasi-one-dimensional electronic structure of the nanowires. Due to the oscillation of the dispersion, the band parameters effective mass (m^*) and binding energy of the bottom of the band (E^{B}) change with $k_{\perp}$, so that only average values can be determined conclusively. For the up-to-now discussed ARPES data, this average effective mass is $(0.25 \pm 0.05)\ m_0$, and the bottom of the band is at (0.25 ± 0.05) eV for band 2 (see table 7.6). The binding energy of the bottom of the band and the effective mass of the band vary with $k_{\perp}$. The errors of the averages given above correspond to the variances of the energy of the bottom

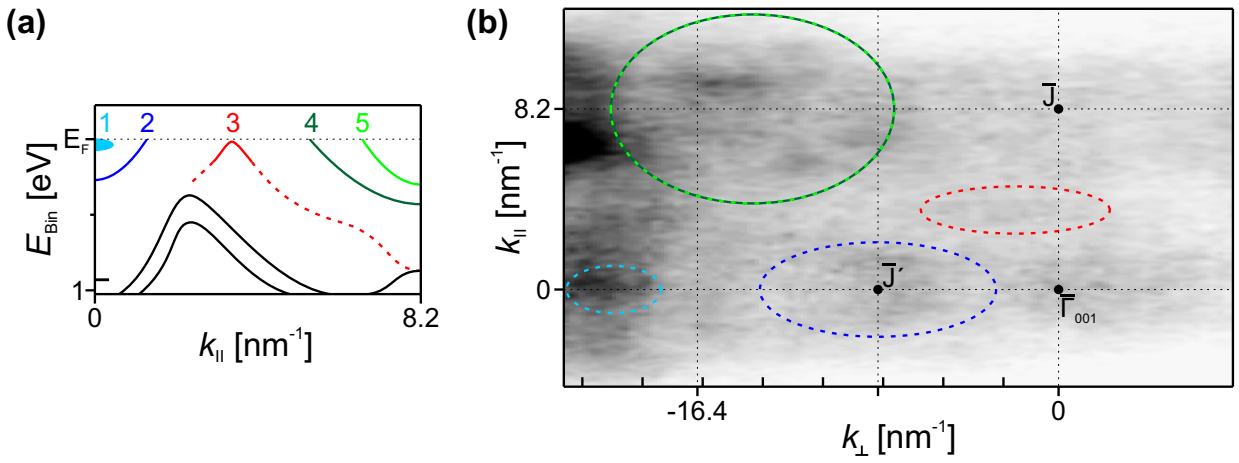

Figure 7.54.: (a) Schematic of the dispersion curves close to the Fermi level parallel to the nanowires with the $k_\perp$-averaged binding energies and $k_\parallel$-values as derived for the ARPES data shown in figure 7.53. The dashed dispersion segments are not unambiguously detectable. The black bands are drawn exemplarily for a multitude of similarly dispersing bands not reaching the Fermi level. The inside tick indicates the substrate valence band maximum. (b) Fermi surface obtained for the nanowire sample 1 ($h\nu = 62$ eV). The ellipses highlight areas of interest. The inside ticks on the $k_\perp$-scale mark the values at which the dispersion plots of figure 7.53 (b) were taken.

Table 7.6.: Overview on the $k_\perp$-averaged binding energies of the bottoms of the bands (E^B in eV) and the effective masses (m^* in m_0) for the parabolic bands 2, 4, and 5 around $k_\parallel = 0$ and $k_\parallel = 8.2$ nm^{-1} compared to the values reported in the literature [84, 85].

	E_2^B	m_2^*	E_4^B	m_4^*	E_5^B	m_5^*
Sample 1 (figure 7.53)	0.25 ± 0.05	0.25 ± 0.05	0.45 ± 0.05	0.7 ± 0.1	0.30 ± 0.05	0.4 ± 0.1
Sample 2 [figure 7.55 (a)]	0.31 ± 0.05	0.24 ± 0.05	0.4 ± 0.1	1.0 ± 0.5	0.3 ± 0.1	0.2 ± 0.1
Sample 3 (figure 7.56)	0.24 ± 0.05	0.19 ± 0.05	0.43 ± 0.05	0.6 ± 0.1	—	—
$GdSi_2$ nanowires	—	—	—	0.91 ± 0.05	—	0.63 ± 0.05
$DySi_2$ and $ErSi_2$ nanowires	0.38 ± 0.05	0.2 ± 0.1	0.53 ± 0.05	1.1 ± 0.2	0.26 ± 0.05	1.0 ± 0.3

of the band and the effective mass. In general, the minimum errors are estimated to 0.05 m_0 and 0.05 eV, which may appear rather large, but the intensity variations of the bands may lead to an under- or over-representation of the dispersion at certain $k_\perp$-values in the $k_\perp$-averages.

Band 3 may be observable on the Fermi surface at the lowest $k_\perp$-values, but is only clearly discernible in the area marked by a red ellipse in figure 7.54 (b). There its Fermi contour appears rather straight, but also quite broad, so that oscillations may be masked. Its dispersion close to the Fermi level appears like two rather straight lines forming a kink just at the Fermi level [see figure 7.53 (b) panel VII]. Thus, it has clearly a hole-like characteristics, but no evaluation of the effective mass close to the Fermi level is performed, since the fitting of a kink by a parabola is not justified. With higher resolution ARPES data, one may expect this band to show a curvature at its top while the presence of a small gap at the Fermi level is also possible, as depicted in figure 7.54 (a).

Both bands 4 and 5 situated around $k_{\parallel} = 8.2$ nm^{-1} have clear electron-like dispersions appearing as parabolas with positive curvatures. Similarly to the observations made for the dispersions of these bands, they appear as a single very broad and very intense maximum at the lowest $k_{\perp}$-values of the measured Fermi surface, but well separated at larger $k_{\perp}$-values, e.g. in the area marked by green ellipses in figure 7.54 (b). Their Fermi contours are strongly disrupted in general, as already observed for the other bands, but the band 5 clearly appears as a slightly oscillating line on the Fermi surface for $k_{\parallel}$-values larger than 8.2 nm^{-1} in the highlighted area. Thus, a quasi-one-dimensional electronic structure of the nanowires is again indicated. Band 4 has not only a larger $k_{\perp}$-averaged binding energy of its band bottom, $E_4^{\mathrm{B}} = (0.45 \pm 0.05)$ eV compared to $E_5^{\mathrm{B}} = (0.30 \pm 0.05)$ eV, but is also characterised by a larger $k_{\perp}$-averaged effective mass than the band 5, $m_4^* = (0.7 \pm 0.1)\ m_0$ compared to $m_5^* = (0.4 \pm 0.1)\ m_0$, leading to the observation of the forth band in a larger $k_{\parallel}$-segment.

The signal of the bands at the Fermi surface is in general rather low compared to the background noise for the ARPES data of sample 1 discussed up to now. A higher intensity of these bands was observed for sample 2 [see figure 7.55 (a)], which used a slightly larger Tb coverage leading to a presumably increased nanowire density. Due to this higher amount of Tb silicide structures on the surface, the electronic bands of the bulk Si substrate are too weak to use them to calibrate the measured ARPES data. Thus, the centre of the Brillouin zone is set to agree with the observations made for sample 1.

In general, a band dispersion very similar to the one found for sample 1 is observed for sample 2 [see figure 7.55 (a)], so that the same nomenclature is used. There are an electron-like parabolic band around $k_{\parallel} = 0$ and two electron-like parabolic bands around $k_{\parallel} = 8.2$ nm^{-1}, which dominate the dispersion plot and have the highest intensity on the Fermi surface. Furthermore, the Fermi contours of these bands are oscillating lines, which is best seen for band 2 for $k_{\perp} < 8.2$ nm^{-1} [see blue hatched line in figure 7.55 (a)], confirming the observations made for sample 1. Also apparent are strong intensity variations with $k_{\perp}$, e.g. band 2 vanishes for $k_{\perp} > 8.2$ nm^{-1}, while at the same time intensity of band 3 appears on the Fermi surface.

The only band that is not observed for sample 2 is the first band at $k_{\parallel} = 0$. This may be related to the different preparation parameters leading to a reduced ratio of the nanowires mainly responsible for the observation of this band. The rather broad appearance of the bands around $k_{\parallel} = 8.2$ nm^{-1} may also be caused by a different nanowire assembly, which may be more inhomogeneous. This broadness of bands 4 and 5 of sample 2 leads to quite large errors in the determination of their band parameters when compared to the results for sample 1 and for band 2 of sample 2 (see table 7.6).

An interesting detail found in the dispersion plot shown in figure 7.55 (a) are two nearly parallel dispersing bands at higher binding energies (marked by red arrows). That these bands do not only disperse very similarly with $k_{\parallel}$, but also with $k_{\perp}$ is seen in the ARPES data of sample 3 [see figure 7.56 (a)]. They clearly disperse in both $k_{\parallel}$-direction and-$k_{\perp}$ direction and the one at lower binding energy can be unambiguously assigned to the nanowire since it is observed in the band gap of the Si bulk. Thus, the nanowire bundles have also two-dimensional bands in addition to the one-dimensional ones observed at the Fermi level. Their contours at a constant energy are described by anisotropic ellipses, e.g. highlighted by yellow dashed lines in figure 7.56 (c) for the band at lower binding energy. Interestingly,

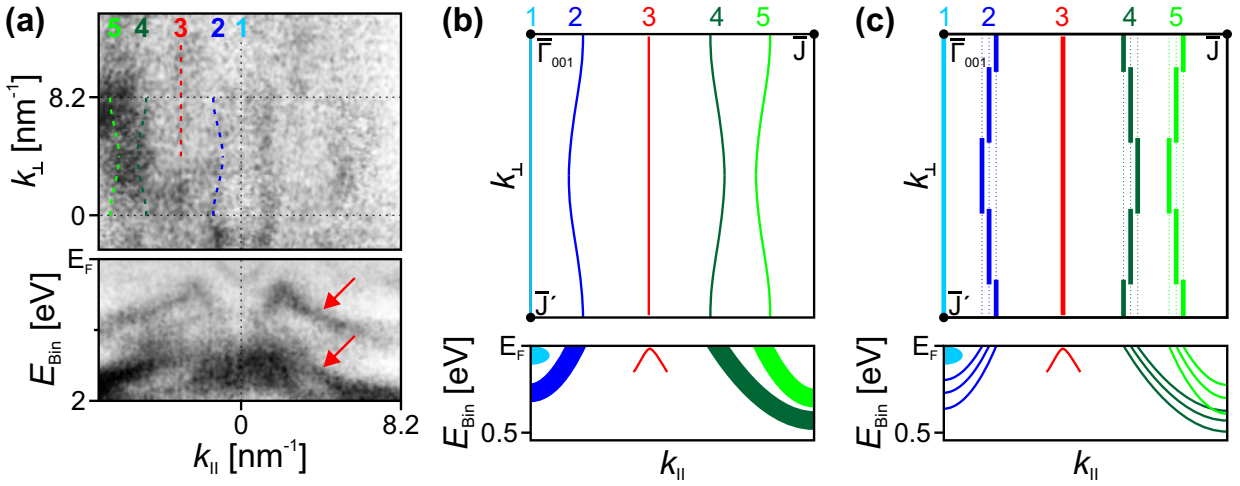

Figure 7.55.: (a) Fermi surface (top) and dispersion close to the Fermi level parallel to the nanowires (bottom, $k_\perp = -2.4$ nm^{-1}) for a nanowire sample prepared by deposition of 1.2 ML Tb on a Si(001) substrate with 6° offcut and annealing at 550 °C (sample 2, $h\nu = 62$ eV). The coloured dashed lines are guides to the eyes and the red arrows indicate almost parallel bands. (b and c) Schematics of possibilities for the observation of oscillating Fermi contours (top) and the corresponding average band dispersion parallel to the nanowires (bottom). In (b), the bands vary with $k_\perp$ leading to the oscillations and a broad and continuous average band dispersion. In (c), oscillations occur due to the observation of different bands, e.g. stemming from nanowires with different widths, with changing $k_\perp$ due to matrix-element effects. The average dispersion is then described by multiple bands, which are distinct. In both illustrations, the effective masses of the bands are set constant and only the binding energies of the bottoms of the bands are varied.

only ellipses elongated in $k_\perp$-direction are observed, while there are no corresponding ellipses elongated in $k_\parallel$-direction although a k-area larger than the first Brillouin zone is covered by the ARPES data. Such anisotropic two-dimensional bands indicate an anisotropic atomic structure in agreement with the structure model proposed in section 7.3.

Comparing the ARPES data of the sample 3 to those of the other samples, significant similarities are found. Bands 2 and 4 are clearly observed in the dispersion plots and their contours are easily distinguished on the Fermi surface [see figures 7.56 (b and c)]. In addition, the parabola of band 2 appears sometimes completely filled indicating the presence of band 1 [see panels V and VI in figure 7.56 (b)]. Another indication for band 1 is observed on the Fermi surface, on which a large intensity is observed directly at $k_\parallel = 0$ for $k_\perp$ around 12 nm^{-1} [see figure 7.56 (c)]. At the expected $k_\parallel$-values for bands 3 and 5 no clearly increased intensity is found on the Fermi surface. On first view, these bands also appear to be missing in the dispersion plots, but for some $k_\perp$-values possible traces of these bands are observed [see circles in panel II of figure 7.56 (b)]. Due to the very low intensity of band 5, the $k_\perp$-averaged effective masses and $k_\perp$-averaged binding energies of the bottoms of the bands could only be determined for bands 2 and 4 (see table 7.6).

In contrast to the previously discussed samples is the observation that the Fermi contours

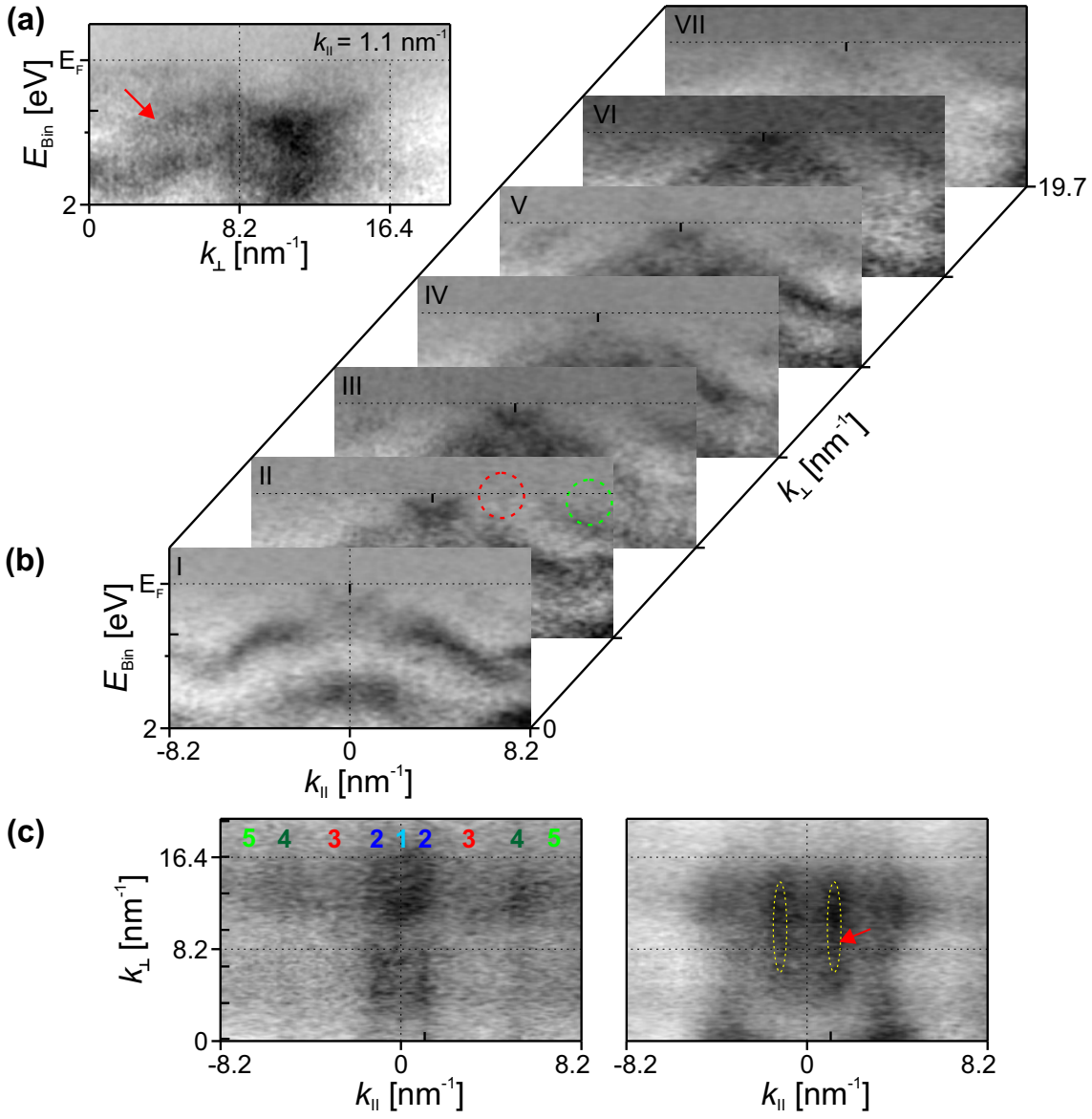

Figure 7.56.: ARPES data of a nanowire sample prepared by deposition of 1.5 ML Tb on a Si(001) substrate with 4° offcut and annealing at 550 °C (sample 3, $h\nu = 62$ eV). (a and b) Detailed dispersion data close to the Fermi level (a) perpendicular and (b) parallel to the nanowires. (c) Energy surfaces at the Fermi level (left) and at $E_{\mathrm{Bin}} = 0.7$ eV (right). The zero of $k_{||}$ is in agreement with the data of sample 1, while the zero of $k_\perp$ is arbitrary, since neither substrate bands nor clear oscillations of the band contours at the Fermi level are observed. The inside ticks on the scales indicate the positions for which slices of the three-dimensional data set are shown. The red arrows in (a and c) mark the same band, the coloured hatched circles in (b) indicate traces of bands 3 and 5, and the hatched yellow ellipses in (c) highlight two-dimensional energy contours.

appear straight without any obvious oscillations. Since the Tb coverage was even higher for sample 3 than for the other two, the absence of such oscillations cannot be caused by a lower nanowire density resulting in a reduced coupling between neighbouring nanowires. Rather, the oscillations may be masked by the broad appearance of the Fermi contours. This broad appearance may again be related to a different nanowire composition for this sample, which is most likely also the reason for the other differences found between the ARPES data of the various samples.

While further ARPES data not shown here may again slightly differ in the appearance of the band structure, all typical variations are already observed for samples 1 to 3, e.g. varying broadness of observed bands, Fermi contours with different strengths of their oscillations, or very low intensities for certain bands. Despite of the varying appearance of the band structure in the ARPES data, all bands reaching or crossing the Fermi level show quasi-one-dimensional characteristics. This band structure at the Fermi level determines the physical properties of a structure, e.g. transport properties, and one-dimensional phenomena may be observed for a structure even if bands at higher binding energies show two-dimensional characteristics [447]. Thus, the Tb silicide nanowires are still denoted quasi-one-dimensional.

That the differences in the ARPES data of the different samples are only caused by different nanowire ensembles of the same nanowire structures is nicely seen by the band parameters shown in table 7.6. For all three samples, the determined band parameters agree nicely with each other. There are small variations as one may expect, e.g. due to the influence of the intensity variations, but all error intervals at least overlap, while most of the time even all determined values are within the error intervals of the respective other samples. Taking a closer look, both the binding energies of the bottom of the bands and the effective masses increase from band 2 over band 5 to band 4.

Comparing the band parameters determined for Tb silicide nanowires with the values reported for other rare earth silicide nanowires, significant differences are found especially for the effective masses of the bands around $k_{\parallel} = 8.2$ nm^{-1} (see table 7.6). These differences are most likely not the result of the probing of different nanowire ensembles, but indicate an influence of the used rare earth metal on the details of the electronic structure of rare earth silicide nanowires. Nevertheless, there are not only differences, e.g. the trend of an increasing effective masses from band 2 over band 5 to band 4 is observed independently of the used rare earth metal.

Furthermore, the general electronic structure of five bands crossing or reaching the Fermi level is consistent with all up-to-now reported band structures for rare earth silicide nanowires. The apparent differences can be easily explained by the matrix element effects observed in this thesis. Prior studies analysed the band dispersion parallel to the nanowires only for certain $k_{\perp}$-values, so that some bands may not have been observed at all, since they are only measurable for other $k_{\perp}$-values. Thus, it may also be assumed that all rare earth silicide nanowires have a quasi-one-dimensional electronic structure at the Fermi level, as was already presumed in the reports on the other rare earth silicide nanowire, but conclusively proven here for Tb silicide nanowires.

Figure 7.55 (b) summarises the observed band structure with the average band parameters of all three samples discussed above. On the Fermi surface, the contours of bands 2, 4, and 5 are oscillating. The maximum $k_{\parallel}$-value of band 2 is reached for $k_{\perp} = 0$ as observed for sample 1 and the oscillations of bands 4 and 5 are known relative to the one of band 2

from sample 2 [see figures 7.54 (b) and 7.55 (a)]. Due to these oscillations, the dispersions of these bands parallel to the nanowire varies, which is the reason for their depictions as broad bands in the schematic dispersion plot. While band 3 is distinctly hole-like close to the Fermi level, its dispersion for higher binding energies was resolved only once for a very small $k_\perp$-range, so that only its dispersion close to the Fermi level is included in the schematic. In contrast, it is completely unknown if band 1 has a electron-like or hole-like characteristic leading to its depiction as blob in the schematic dispersion plot. A similarity between bands 1 and 3 is that no oscillations of their Fermi contours could be resolved. It should be noted that this non-observation may be a resolution problem.

Taking into account the observation of rather straight Fermi contours and the matrix element effects, indicated by the intensity variations of the bands, the strong oscillations of some Fermi contours may not be caused by strong interactions between nanowires, e.g. within a nanowires bundle, or between nanowires and the substrate, but instead by the observations of different subbands at different $k_\perp$. This is illustrated in figure 7.55 (c). A labelled band may not be a single band, but consist of a multitude of rather similar subbands, which are slightly different, e.g. for different nanowire widths. Their alternating observation with $k_\perp$ due to matrix element effects may lead to a rather continuous appearance of a single oscillating band.

Assuming such a band structure, one may easily explain why the bands around $k_\parallel = 8.2$ nm^{-1} appear sometimes as one very broad band when a large number of subbands of the bands 4 and 5 are seen simultaneously [see panel I of figure 7.53 (b)]. Furthermore, a complete oscillation of the Fermi contour of band 2 is clearly observed with half the extension of the Brillouin zone [see figure 7.55 (a)]. Assuming a single continuous band 2, this indicates an atomic structure with $\times$2-periodicity along the nanowires, which was not observed in real space up to now [see section 7.3]. Such a discrepancy does not arise with the band structure that assumes subbands. However, a $\times$2-periodicity may actually be present on the nanowire, e.g. by dimerisation of the side facets, which is predicted by theoretical studies [448]. Thus, both proposed scenarios are in agreement with the ARPES data presented here.

Using STS, a very local measurement technique, the metallic character of the nanowires was proven. Based on ARPES, a globally averaging technique, this result could be extended to show that the Tb silicide nanowires are quasi-one-dimensional metals. Although both techniques probe the filled states of the nanowires, it is refrained from a direct comparison of both data sets, since the large variations in both ARPES dispersion and STS peak positions make a detailed comparison meaningless.

In the following, results obtained by the last experimental technique used to analyse Tb silicide nanowires on Si(001), transport measurements, are presented. With these measurements, it is probed if the Tb silicide nanowires are conducting as one may expect from their band structure observed here.

7.4.4. Transport measurements

The transport measurements took place in the work group of Prof. Dr. Herbert Pfnür and Prof. Dr. Christoph Tegenkamp at the Leibniz Universität Hannover and were mainly conducted and analysed by Frederick Edler and Ilio Miccoli, with me assisting during parts

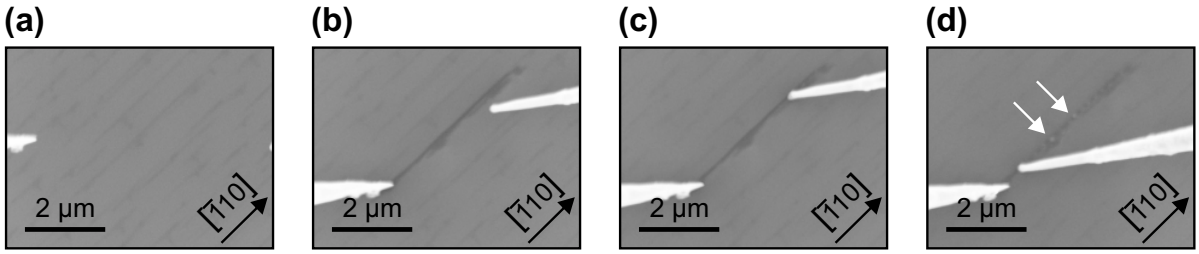

Figure 7.57.: Sequence of top-view SEM images showing the contacting procedure of a Tb silicide nanowire during a transport measurement. (a) No contact between the STM tips and the nanowire, (b) one tip in contact with the nanowire, and (c) two tips in contact with the nanowire. (d) The second tip is moved stepwise towards the first tip to determine the nanowire resistivity. The arrows in (d) mark prior contacting positions, where the nanowire was modified. For all images, an acceleration voltage of $V_{\mathrm{SEM}} = 15$ kV and an emission current of $I_{\mathrm{SEM}} = 1$ nA were used. From [416].

of the experiments, especially in the beginning when the preparation procedure had to be adjusted to lead to the formation of long and well-separated nanowires. The need for long nanowires led to the use of vicinal substrates, while rather low Tb coverage and high annealing temperatures were used in order to obtain large distances between the nanowires. For all measurements discussed here, the nanowires were prepared by deposition of about 0.8 ML Tb on p-type Si(001) substrates with 4° offcut towards [110], which were held at 700 °C during the Tb deposition.[1]

No prefabricated probe array, but a 4-tip STM was used for the transport measurements. The 4-tip STM is combined with an SEM for reliable tip positioning. The steps of the contacting of a nanowire as observed with SEM are shown in figure 7.57. In the SEM images, the STM tips appear white, i.a. since they are tilted with respect to the incident electron beam, while the Si(001) sample appears grey. Taking a closer look, the appearance of the sample is not homogeneous, but there are darker stripes, which are the Tb silicide nanowire bundles [see figure 7.57 (a)]. The most likely reason for the nanowire contrast are different local work functions.

When an STM tip contacts a nanowire bundle, the complete bundle changes its appearance in SEM [see figure 7.57 (b)]. The appearance change arises due to the potential change of the nanowire by the tip. The influence on the complete length of the nanowire bundle already indicates conductivity along the nanowire bundle. The tip may contact the entire bundle and not an individual nanowire since the radius of the tip apex (about 50 nm) is typically considerably larger than the width of an individual nanowire (about 2 nm), but nanowires in a nanowire bundle are certainly also electrically connected or at least strongly interacting. Otherwise, the apparent width of a contacted nanowire region could only stay constant or reduce with increasing distance from the contact point of the tip. Taking a closer look at the contacted nanowire in figure 7.57 (b), it increases its width several times when moving from the lower left, where it is connected to an STM tip, to the upper right,

[1] The temperature measurement setup at the transport measurement station in Hannover is different from the one used at all other setups, e.g. the emissivity is adjusted to the measured temperature. Thus, the temperature of 700 °C given here corresponds to a lower one at the other setups.

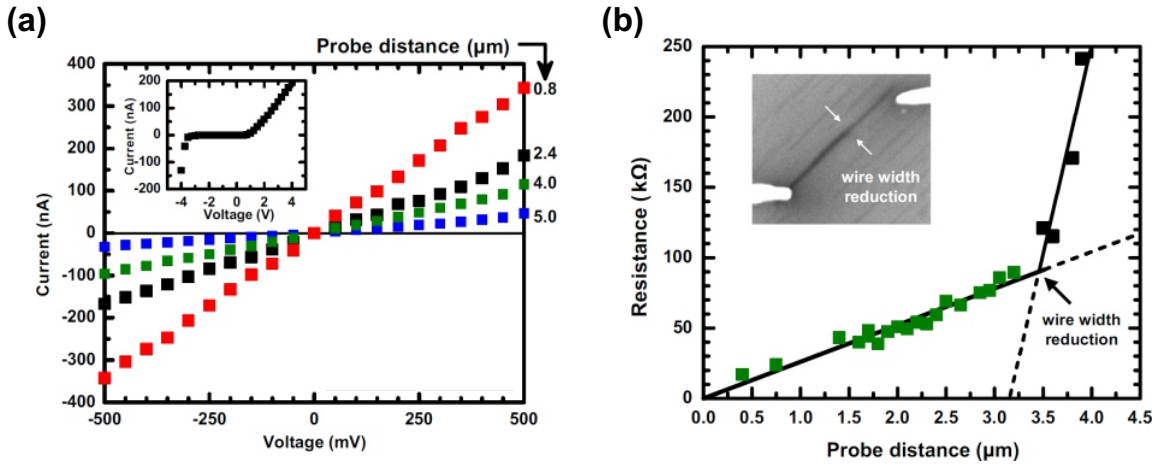

Figure 7.58.: (a) I-V curves between two probes, i.e. STM tips, contacted to a nanowire with varying distances between them. The curves were obtained during the measurement depicted in figure 7.57. The inset shows an I-V curve with the second tip not positioned on the same nanowire as the first one, but on the substrate. (b) Nanowire resistance-probe spacing diagram obtained in a two-point probe arrangement for the nanowire shown in the inset SEM image ($V_{\mathrm{SEM}} = 15$ kV and $I_{\mathrm{SEM}} = 1$ nA). The position, where the width of the nanowire changes, is highlighted in both diagram and SEM image. From [416].

proving the strong interactions in a nanowire bundle.

Now, the nanowire bundle may be contacted with a second STM tip [see figure 7.57 (c)], and the nanowire resistance may be determined by measuring the dependence of the current between the probes on their potential difference. That the second tip is on the same nanowire can be easily determined by the obtained I-V curve since a clear linear characteristics is always observed when both tips are in contact to the same nanowire [see figure 7.58 (a)]. In contrast, a Schottky-type characteristics is found when one tip is on the substrate [see inset in figure 7.58 (a)]. Such a characteristic may stem from the Schottky contact between the semiconducting Si substrate and the metallic W tip connected to it, but there is also a Schottky contact between the metallic silicide nanowire and the substrate. Interestingly, the height of the Schottky barrier between rare earth silicide nanostructures and p-type Si substrates, which should be rather high due to the Fermi-level position observed here, is effectively rather small, i.a., because of tunnelling effects [323, 449, 450].

The linear I-V curves for transport measurements with two probes in contact with the same nanowire bundle clearly prove a finite diffuse electron transport in the Tb silicide nanowires and the formation of ohmic contacts between the probes and the nanowires. Thus, the metallic character of the silicide nanowires is confirmed once again. The slopes of these curves give the conductances of the probed nanowire bundle sections. The conductance clearly increases with decreasing distance between the two probes on the same nanowire bundle [see figure 7.58 (a)].

A peculiarity of the transport measurements reported here is that the distance between the probes could only be decreased, since the contacting changes the morphology of the nanowires [see figure 7.57 (d)]. While the visible residues of the contacting process lead to an

easier estimation of probe distances by SEM, the previously contacted areas are characterised by an increased resistance when compared to clean nanowire sections. This is also one of the main reasons for employing two-point-probe instead of four-point-probe measurements. The typical problem that arises by using only two probes is the additional resistance contribution not related to the probed species, e.g. due to the contacts. That these additional resistances are negligible, i.e. that the two-point-probe measurements are dominated by the resistance of the nanowire bundle sections, is seen when the determined resistance, the inverse of the conductance, of a nanowire bundle section is plotted in dependence on the distance between the two probes. Such a graph is exemplarily shown in figure 7.58 (b). The best fit to the data for probe distances below 3.25 μm is a line that crosses the origin of the axes, which is only possible for negligible additional resistances.

That the resistance depends linearly on the probe spacing clearly shows a one-dimensional electron transport in the silicide nanowire bundles, while additional conductance channels, e.g. a two-dimensional one of the surrounding surface or a three-dimensional one of the Si substrate, can be excluded (see section 4.4). Thus, the Schottky barrier between Tb silicide nanowire and substrate is sufficiently large to decouple the nanowires from the substrate, leading to an electron transport exclusively through the nanowire bundle.

The slope of the linear resistance increase changes for probe distances larger than 3.25 μm for the measurement shown in figure 7.58 (b). This change can be related to an inhomogeneity of the nanowire bundle. In SEM, a reduction of the nanowire bundle width is apparent in the area that corresponds to a probe distance of about 3.25 μm [see inset in figure 7.58 (b)]. Excluding nanowire bundles with such inhomogeneities, the resistance per length of the studied nanowire bundles varies between 0.03 MΩ/μm and 1 MΩ/μm. To calculate the resistivity from these values, the areas of the nanowire bundle cross sections have to be estimated. The resolution of the SEM is too low for this purpose, but using the high-resolution tip of the 4-tip STM to obtain images of the previously contacted nanowire bundles, the required accuracy is achievable.

Figure 7.59 (a) shows an overview STM image with two nanowire bundles, $w1$ and $w2$, on which transport measurements were conducted. In agreement with SEM images, evidence for morphology changes of the nanowire bundles and their surroundings is observed at the contacting positions. More detailed STM images of the two nanowire bundles $w1$ and $w2$ are shown in figures 7.59 (b and c), respectively. Their appearances as rather wide structures with grooves and occasionally segments of an additional layer nicely match the ones known for rare earth silicide nanowires as measured with the STM setup at the TU Berlin, e.g. see section 7.1, proving the growth of the same Tb silicide nanowires.

Since the additional layer is heavily disrupted, it is assumed that only the two continuous silicide layers of the nanowires are responsible for the electron transport. Thus, the height of the nanowire cross section is always assumed to be 0.66 nm corresponding to two times the step height of the hexagonal $TbSi_2$. An exact determination of the nanowire width is not possible due to the use of a vicinal surface and the widening of the Si(001) terraces by the nanowire bundles leading to a very steep flank at one bundle side. Still, the bundle widths were approximated by the full widths at half the effective nanowire height. This process is illustrated in the tip height profiles in figures 7.59 (b and c) with the horizontal red lines marking the effective heights and the vertical dashed lines indicating the assumed bundle sides, resulting in widths of about 18 nm and 30 nm for $w1$ and $w2$, respectively.

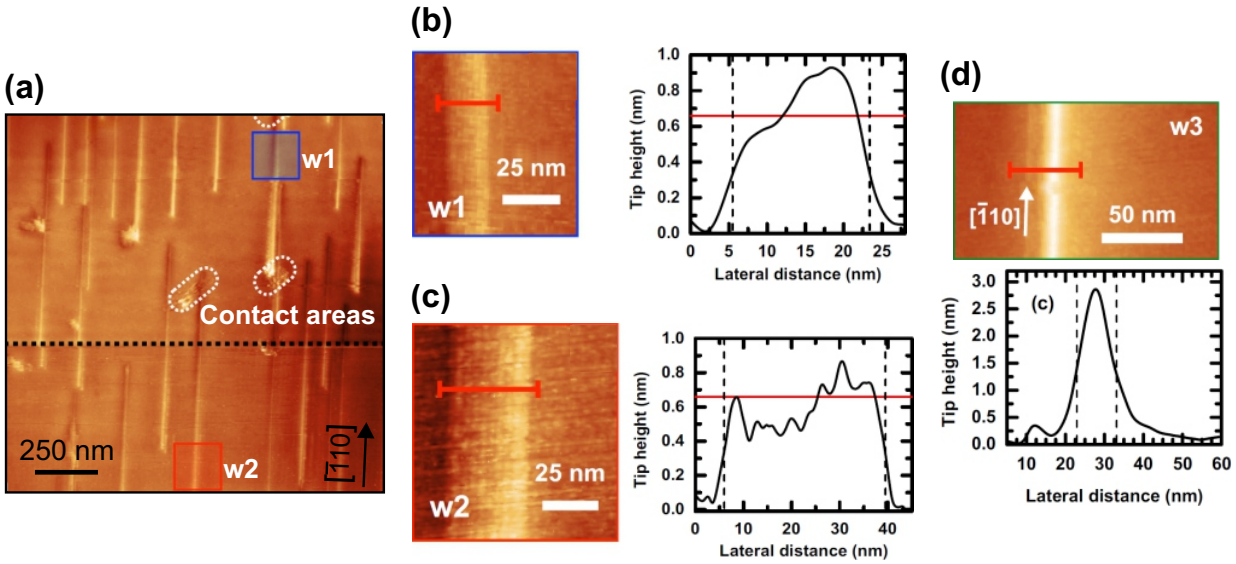

Figure 7.59.: (a) Overview STM image on a sample area containing two nanowires $w1$ and $w2$, which were previously analysed with two-point probe measurements. This image is composed of two images, which were joined at the dotted line. (b and c) Detailed STM images of the two nanowires $w1$ and $w2$, respectively, and corresponding tip height profiles. (d) STM image and tip height profile of an uncharacteristically high nanowire $w3$. The red lines in the STM images in (b to d) indicate the courses of the tip height profiles while the red lines in the tip height profiles in (b and c) mark the estimated average height of the nanowire bundles. All STM images were taken with $V = +2$ V and $I = 100$ pA. From [416].

Calculating the resistivities of the nanowire bundles using the measured resistances per length and the determined areas of the nanowire cross sections leads to values of about 1100 $\mu\Omega$cm for the majority of the nanowires. Such a resistivity of the nanowires is more than ten times larger than the resistivity measured for a 12 nm thin Tb silicide film on Si(111) (90 $\mu\Omega$cm) [276]. Confinement effects may play a role in this resistivity increase, but the difference of the silicide structure has to be taken into account too. The 12 nm thin film consists of the silicide with Si vacancies, which is electronically different from the silicide with ideal $TbSi_2$ stoichiometry of the nanowires. This is, e.g., evident from the different band bending changes observed for the two silicide structures on Si(111) [69].

It should be noted, that also nanowire structures were observed, which do not fit to the above discussed majority of observed nanowires. One of these nanowires ($w3$) is shown in figure 7.59 (d). No indication of bundle formation is observed for this nanowire, and its apparent height of nearly 3 nm, as observed in the tip height profile, is much higher than one may expect, even when taking into account the possibility of step bunching around the nanowire. Such nanowires may even reach apparent height of up to 9 nm and show resistivities down to 150 $\mu\Omega$cm, when using their apparent height in the calculations. Thus, they may represent a different, up to know not reported kind of Tb silicide nanowire species, which formed due to the rather extreme preparation conditions.

The transport data on Tb silicide nanowires confirmed assumptions based on the STS

and ARPES data. The nanowires are electrically conducting, although they typically show a rather large resistivity. Further information on the transport measurements, including an in-depth discussion of the influence of the nanowire size on its resistivity, is available in reference [416].

7.5. Conclusion

In this chapter, Tb silicide nanowires on Si(001) were studied in detail. Their formation nicely agrees with the studies using other rare earth metals [78]. In contrast to previous assumptions on the atomic structure, it could be demonstrated that the Tb silicide nanowires are formed from hexagonal $TbSi_2$, but with its c_{hex}-axis parallel to the long nanowire axis. Due to the chemical similarity of the rare earth elements, this new structural orientation of the silicide should also be present in the nanowires formed using other rare earth elements.

The Tb silicide nanowires are two silicide layers high, have typical widths of about 2 nm, and may reach lengths exceeding 1 μm when vicinal substrates are used. Such nanowires on vicinal samples are identical to the ones on planar substrates. The nanowires tend to form bundles, with wider bundles observed for higher annealing temperatures. The nanowire growth is preceded for lower annealing temperatures or lower Tb coverages by the formation of a wetting layer. These two growth regimes can be differentiated by RAS. Too high annealing temperatures or Tb coverages lead to the formation of Tb silicide islands.

No indications for structural changes upon the overgrowth of Tb silicide nanowires with Si at room temperature are found. In contrast, the Tb silicide rearranges by Si deposition at higher temperatures or by annealing of an amorphous overlay, procedures required to form a crystalline Si cap. The rearranged silicide structures may still be extended nanowires, but have a more compact cross section.

The nanowires have a finite density of states at the Fermi level, i.e. they are metallic. Similar to the $TbSi_2$ monolayer on Si(111), the Fermi level is pinned by the nanowires close to the Si conduction band minimum. While two-dimensional bands are observed at higher binding energies, the electronic structure of the nanowires close to the Fermi level is characterised by quasi-one-dimensional bands. These bands may show clearly oscillating contours on the Fermi surface, but may also vanish for certain momenta parallel to the surface due to matrix element effects. With this observation, the contradictions in reported electronic structures for nanowires containing other rare earth metals could be resolved, so that one may assume a similar electronic structure for all rare earth silicide nanowires on Si(001).

As expected from the finding of dispersing bands and the observed Fermi-level pinning, the Tb silicide nanowires are conducting, while showing sufficient decoupling from p-type substrates to prevent electron transport through the substrate. Interestingly, the entire nanowire bundle and not only individual nanowires seem to contribute to the conductance, even when not all nanowires of a bundle may be contacted.

8. Tb silicide nanowires on vicinal Si(111)

Vicinal Si(111) substrates are used to confine the $TbSi_2$ monolayer structure, which may result in nanowire formation. If this is indeed the case is discussed in the first section of this chapter (section 8.1). Interestingly, while mostly the same silicide structures form, there are large morphology differences depending on the offcut direction. From this STM study, the dominant formation of the $TbSi_2$ monolayer and the $2\sqrt{3}\times2\sqrt{3}$R°30 superstructure is proposed.

This proposal is confirmed by an analysis of the electronic structures of the formed Tb silicide structures using STS, XPS, and ARPES, which is presented in section 8.2. In this section only the general ARPES results are discussed while a detailed analysis of the confinement effects of the $TbSi_2$ monolayer follows subsequently in section 8.3. In addition to these influences on the two-dimensional structure, also the emergence of a quasi-one-dimensional band is observed with ARPES on Si(335) covered by Tb silicide nanostructures. This electronic structure and possible corresponding silicide structures are discussed in the section covering confinement effects, before this chapter concludes with a summary of the main results in section 8.4.

As a preparation for the study on Tb silicide nanostructure on Si(hhk) substrates, which are vicinal to Si(111), their growth was first studied on planar Si(111). The previously reported results [361], which are partially presented in the first part of this thesis (see section 5.4.2), were nicely reproduced, e.g. including the diffusion of Tb into the Si bulk. Thus, there is no section dedicated to these initial studies. Instead, this chapter fully concentrates on Tb silicide nanostructures on Si(hhk) with some of the information obtained on planar substrates, e.g. STS spectra, used for comparison.

8.1. Growth analysis

The preparation parameters for the $TbSi_2$ monolayer on planar Si(111) are well known. Annealing temperatures of about 500 °C and Tb coverages slightly exceeding 1 ML have to be used to obtain closed films. These parameters are the starting point for the following growth study on vicinal Si(111) substrates. While the annealing temperature was only varied moderately, the Tb coverage range was extended well into the submonolayer regime. The reason for this is seen in the following discussion on the growth of Tb silicide structures on Si(hhk) substrates with $h > k$.

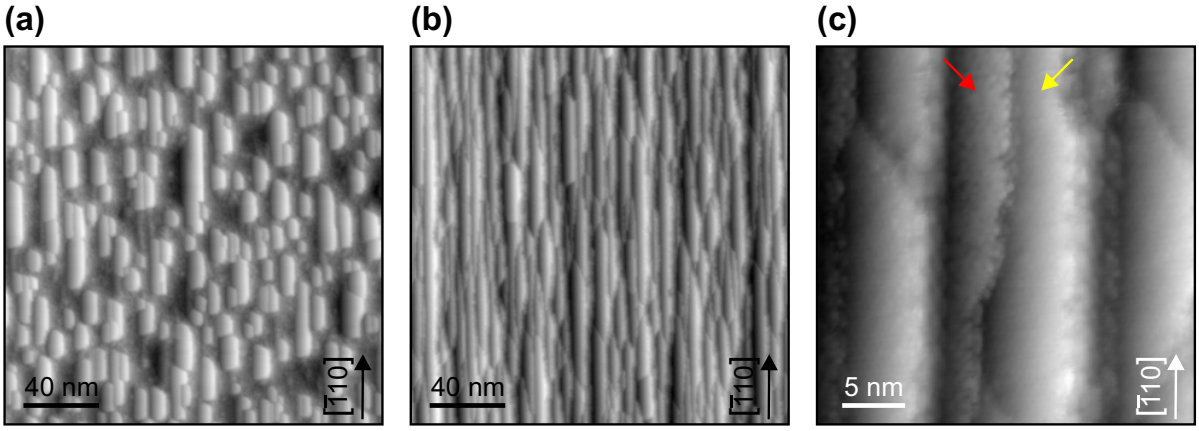

Figure 8.1.: (a) STM image of Tb silicide nanostructures on Si(775), which were prepared with the typical preparation parameters for the $TbSi_2$ monolayer on Si(111) (1.25 ML Tb annealed at 500 °C, $V = -2.5$ V, and $I = 100$ pA). (b) Overview and (c) detail STM image of a sample prepared by depositing 0.65 ML Tb on a clean Si(775) surface and annealing at 500 °C (both taken with $V = -1.5$ V and $I = 100$ pA). The yellow arrow marks a terrace presumably covered by the $TbSi_2$ monolayer while the red one indicates a terrace presumably showing the Tb induced $2\sqrt{3}\times2\sqrt{3}$R30° superstructure.

8.1.1. Si(775) and Si(553)

The clean Si(775) surface shows rather wide Si(111) terraces alternating with areas dominated by step sequences (see section 5.1). These Si(111) terraces, which extend over large distances in $[\bar{1}10]$ direction, are intended as agglomeration areas for the forming Tb silicide to obtain nanowires. Initially, amorphous Tb is deposited at room temperature on the entire clean surface. Afterwards, the sample is annealed leading to the formation of silicides. The Si required for the silicide formation stems from the substrate, i.e. the surface structure may change drastically during the annealing. Thus, the formation of nanowires on the original Si(111) terraces of the clean Si(775) substrate may not be realised.

Indeed, when the preparation parameters that lead to the formation of a closed $TbSi_2$ film on planar Si(111) are applied using a Si(775) substrate, no nanowires form [see figure 8.1 (a)]. Instead, islands with rather low aspect ratios are observed showing only a small elongation along $[\bar{1}10]$. Their appearance is rather structureless similar as observed for the metallic Tb silicide mono- or multilayers on planar Si(111) substrates. The growth of these silicide structures is further indicated by the inclination of the island surfaces by $-10° \pm 2°$ with respect to the average surface orientation, in good agreement with the nominal offcut angle of the substrate of $-8.5°$. Straight or round edges are characteristic for the Tb silicide mono- or multilayer, respectively, but both kind of edges are observed for the found islands, most of the time even on the same island. Thus, an assignment of a Tb silicide structure to the islands based on the STM data is not possible.

While all islands are formed on Si(111) terraces, as is apparent from their uniform inclination, they are not all situated on the same Si(111) terraces that are observed on clean Si(775) substrates. In contrast, new broad Si(111) terraces have formed during the silicide formation, also disrupting the initial ones. Silicide structures on different terraces

cannot grow together since the step height of the silicide, $c_{\mathrm{hex}} = 0.415$ nm, does not fit to the step height of Si in [111]-direction, $s_{\mathrm{Si(111)}} = 0.314$ nm. Due to the disruption of the initial Si(111) terraces and the impossibility of merging silicide structures, no structures expanding over large distances, but only rather compact island are observed.

Increasing the Tb coverage may lead to even denser island growth leading to even shorter elongations. In contrast, a lower Tb coverage may lead to the preservation of long sections of the initial Si(111) terraces since the silicide forms at fewer locations. An overview image of a preparation, for which only a submonolayer amount of Tb was deposited on the clean Si(775) substrate, is shown in figure 8.1 (b). Si(111) terraces expanding over 200 nm are found, but their widths usually vary strongly in the course of the terraces. In general, the widths of the terraces are reduced, and no wide silicide islands are formed. This reduced width is desirable, since it indicates the growth of narrower silicide structures, but therefore these silicide structures are also harder to discern.

There are at least two different kinds of terraces. One has a rather structured appearance, which is reminiscent of the $2\sqrt{3}\times2\sqrt{3}\mathrm{R}^{\circ}30$ superstructure [see red arrow in figure 8.1 (c)], while the other appears structureless meaning that it may be covered by the $TbSi_2$ monolayer structure [see yellow arrow in figure 8.1 (c)]. The formation of a Tb silicide multilayer is unlikely for the present case of submonolayer Tb coverages.

While a part of the terraces may be covered by the Tb silicide monolayer, even these terraces are characterised by the width variations. Thus, it is apparent that no well defined nanowires with long sections of constant widths are formed. To differentiate them from well-defined nanowires, the Tb silicide structures observed here are denoted stripes. While the width of the stripes is inhomogeneous, they only achieve widths of about 8 nm at their widest part. Thus, the widths of the Tb silicide monolayer is considerably reduced when compared to the extensions on planar surfaces. This may already lead to electronic confinement effects. In contrast, the lengths of the stripes of at least 25 nm and reaching values of 200 nm and more will prevent a strong confinement in this direction.

The growth of Tb silicide structures on Si(553) is in general rather similar to the one on Si(775). Islands that are identifiable as Tb silicide mono- or multilayer form on Si(111) terraces for preparation parameters typical used for the growth of a closed $TbSi_2$ monolayer film on planar Si(111) [see figure 8.2 (a)]. The indications are again the appearance of the islands and their inclination to the average surface, here $-11^{\circ} \pm 2^{\circ}$ compared to the nominal value of -12.3°. In contrast to the islands on Si(775), the islands on Si(553) are more elongated in $[\bar{1}10]$ direction, but only few reach a length of 100 nm.

In addition to using a lower Tb coverage, annealing during the Tb deposition may also lead to longer islands. In this case, silicide structures already start forming during the deposition, and subsequently deposited Tb may preferentially attach to these structures instead of forming new silicide structures, similar as only an incomplete coverage of a Si(001) surface with Tb silicide nanowires is achievable by annealing during the Tb deposition (see section 7.1). Since the growth of fewer silicide structures would lead to rather wide islands for Tb coverages about or above 1 ML, both approaches, submonolayer Tb deposition and simultaneous annealing, were combined.

However, the resultant surface morphology, seen in figure 8.2 (b), is very similar to the ones observed for submonolayer amounts of Tb and post deposition annealing [see figures 8.1 (b) and 8.2 (c)]. Elongated Si(111) terraces are formed. There are again at

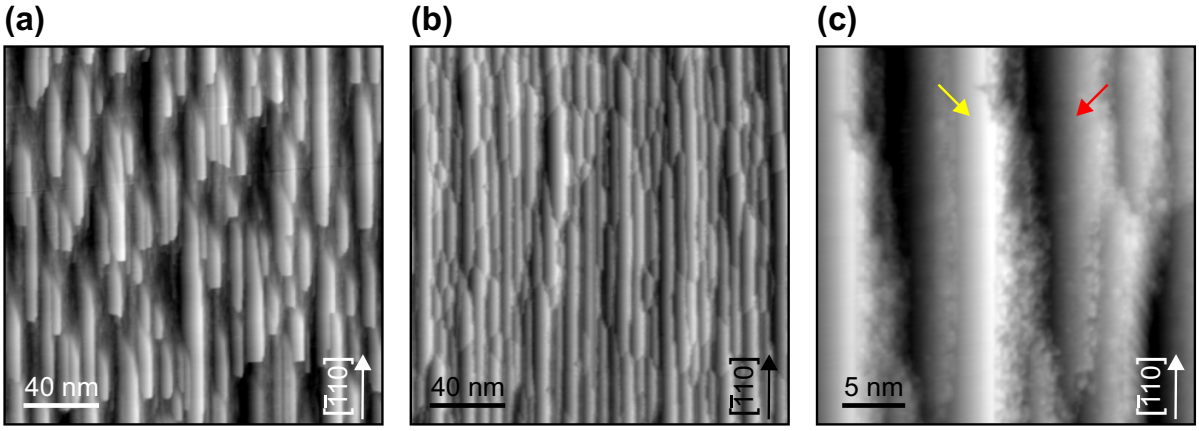

Figure 8.2.: (a) STM image of Tb silicide nanostructures on Si(553) (1.25 ML Tb annealed at 500 °C). (b) STM image of a sample prepared by depositing 0.65 ML Tb on the clean surface held at 450 °C. (c) Detailed STM image (0.65 ML Tb annealed at 500 °C). All STM images were taken with $V = -1.5$ V and $I = 100$ pA. The yellow arrow marks a terrace presumably covered by the $TbSi_2$ monolayer while the red one indicates a terrace presumably showing the Tb induced $2\sqrt{3}\times2\sqrt{3}$R30° superstructure.

least two different types of terraces, one presumably covered by the structureless $TbSi_2$ monolayer [see yellow arrow in figure 8.2 (c)], and one with structure motives similar to the one of the $2\sqrt{3}\times2\sqrt{3}$R°30 superstructure [see red arrow in figure 8.2 (c)].

The terraces and consequently the grown silicide structures are again characterised by strong width variations, so that silicide stripes instead of well-defined nanowires form. Due to the larger offcut angle of the Si(553) surface compared to Si(775), these stripes are in general narrower on the Si(553) substrate showing maximum widths of about 6.5 nm in average. Interestingly, the lengths of the stripes on Si(775) and on Si(553) are very similar, indicating that the low Tb coverage may limit the growth of the stripes.

Already the clean Si(hhk) substrates with the opposite offcut direction strongly differ from the up-to-now discussed substrates. Thus, one may observe different silicide morphologies for $h < k$, e.g. $TbSi_2$ nanowires, which is studied in the following.

8.1.2. Si(557) and Si(335)

Similar to the growth study on Si(hhk) substrates with $h > k$, also the one using Si(hhk) surfaces with $k > h$ begins with the $TbSi_2$ monolayer preparation on the substrate with the smaller offcut angle, i.e. the Si(557) surface. An STM image of such a preparation is shown in figure 8.3 (a). Now, highly elongated Tb silicide islands are observed. They show well-defined edges, have very high aspect ratios, and in general widths below 10 nm. Thus, the growth of Tb silicide nanowires was successful on Si(557).

Similar as the stripes and islands on Si(775) and Si(553), the nanowires appear structureless, do not merge, and show inclinations indicating their growth on Si(111) terraces, here $+9° \pm 2°$ compared to the nominal value of $+9.5°$. In addition, most nanowires show straight edges at their ends [see figure 8.3 (c)]. Thus, one may assume that the nanowires

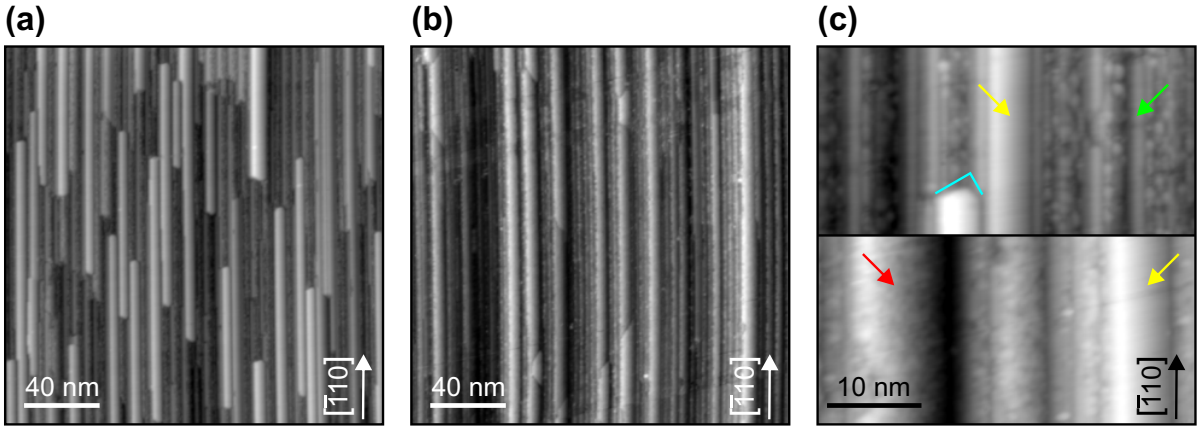

Figure 8.3.: (a) Overview STM image of a $TbSi_2$ monolayer preparation on Si(557) (1.35 ML Tb annealed at 500 °C, $V = -1.5$ V, and $I = 100$ pA). (b) STM image of a sample prepared by depositing 0.70 ML Tb on the clean surface and annealing at 500 °C ($V = +1.5$ V, $I = 100$ pA). (c) Detailed STM images of 1.35 ML Tb (top) and 0.70 ML Tb (bottom) annealed at 500 °C (top $V = -1.5$ V, bottom $V = +1.5$ V, and both $I = 100$ pA). The yellow arrows mark terraces presumably covered by the $TbSi_2$ monolayer, while the red one indicates a terrace presumably showing the Tb induced $2\sqrt{3}\times2\sqrt{3}$R30° superstructure, and the green one highlights a nanoline. The light blue line illustrates dominant edge courses expected for the $TbSi_2$ monolayer.

consist of the $TbSi_2$ monolayer. The typical length of the nanowires is about 100 nm, but some are much longer. The average width of the nanowires is only (3.6 ± 0.3) nm, i.e. the $TbSi_2$ monolayer is strongly confined.

In addition to the nanowires, even narrower extended structures are observed, which are termed nanolines in this thesis and were never observed on Si(775) or Si(553) [see green arrow in figure 8.3 (c)]. While these nanolines typically appear to be several 10 nm long in overview images, they are often segmented when analysed in detail, e.g. the nanoline marked by the green arrow in figure 8.3 (c) is disrupted slightly below the arrowhead. Still, they have large aspect ratios since their widths are exceptionally small, usually below 1 nm. Due to this narrowness, the inclination of the nanolines with respect to the surface normal cannot be determined, since the convolution of the real structure with the tip shape masks such small structures. Thus, it is unknown if the nanolines are formed on Si(111) terraces, on a different facet, or on a step edge, and it remains unclear if the nanolines are very narrow nanowires or a distinctly different structure type. It is even not determinable by STM if the nanolines are Tb silicide structures or a pure Si structure, e.g. Si(337) facets show a similar appearance in STM [261]. While such steep facets were not observed on clean substrates, the step bunching needed to compensate the much wider Si(111) terraces formed during Tb nanostructure growth may lead to their formation.

Using a lower Tb coverage, the average expansion of the Si(111) terraces in $[\bar{1}10]$ direction increases strongly. This is seen in figure 8.3 (b), in which several terraces span the complete vertical extension of the image, i.e. they are longer than 200 nm. Unfortunately, now more terraces appear to be covered by the $2\sqrt{3}\times2\sqrt{3}$R30° superstructure [see figure 8.3 (c)], and

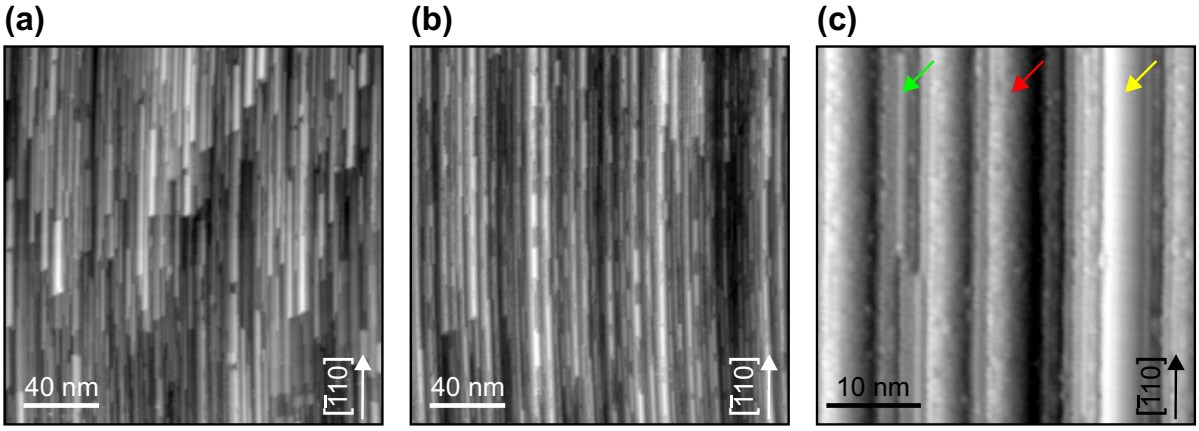

Figure 8.4.: (a) STM image of a Si(335) surface covered by 1.35 ML Tb, which was annealed at 500 °C ($V = -1.5$ V and $I = 100$ pA). (b) STM image of a sample prepared by depositing 0.70 ML Tb on the clean Si(335) surface and annealing at 500 °C ($V = -1.5$ V and $I = 100$ pA). (c) Detailed STM image of 0.65 ML Tb annealed at 500 °C on Si(335) ($V = -1.5$ V and $I = 100$ pA). The yellow arrow marks a terrace presumably covered by the $TbSi_2$ monolayer, while the red one indicates a terrace presumably showing the Tb induced $2\sqrt{3}\times2\sqrt{3}$R30° superstructure, and the green one highlights a nanoline.

sections with the $TbSi_2$ monolayer are often rather short with of lengths only a few 10 nm. Interestingly, no nanolines were observed for the submonolayer Tb coverage preparation.

Moving to the Si(335) substrate, which has the same offcut direction as the Si(557) substrate, but a larger nominal offcut angle of +14.4°, a similar growth is observed for the typical $TbSi_2$ monolayer preparation [see figure 8.4 (a)]. Nanowires with straight edges, which presumably consist of the $TbSi_2$ monolayer due to their appearance in STM, form on Si(111) terraces (determined inclination angle of $+15° \pm 2°$). The main differences to the nanowire growth on Si(557) is that the nanowires are narrower on Si(335) with an average width of only (2.5 ± 0.5) nm due to the larger offcut angle with respect to Si(111), and that the nanowire growth is not as homogeneous on Si(335). While nanowires with lengths surpassing 200 nm are observed, there are many nanowires which are only a few 10 nm long.

In addition to the nanowires, also nanolines and, when submonolayer Tb coverages are used, also Si(111) terraces presumably covered by the $2\sqrt{3}\times2\sqrt{3}$R30° superstructure are observed [see figure 8.4 (c)]. Similar to the observations made for Si(557) substrates, not only the $2\sqrt{3}\times2\sqrt{3}$R30° superstructure is found for submonolayer Tb coverages, but the nanowires are also often rather short [see figure 8.4 (b)]. In contrast to the results on Si(557), nanolines are definitely present for low Tb coverages on Si(335) [see figure 8.4 (c)].

It should be noted that no reconstruction that appears like a chain of protrusions, which was observed for Dy deposition on Si(557) [73], is found in this thesis. This chain-like reconstruction formed best for Dy coverages below 0.5 ML and for annealing temperatures around 650 °C. Preparation parameters in this range were not employed here, since this work focusses on the analysis of the confined $TbSi_2$ monolayer structure, and this monolayer forms dominantly for higher coverages and lower temperatures.

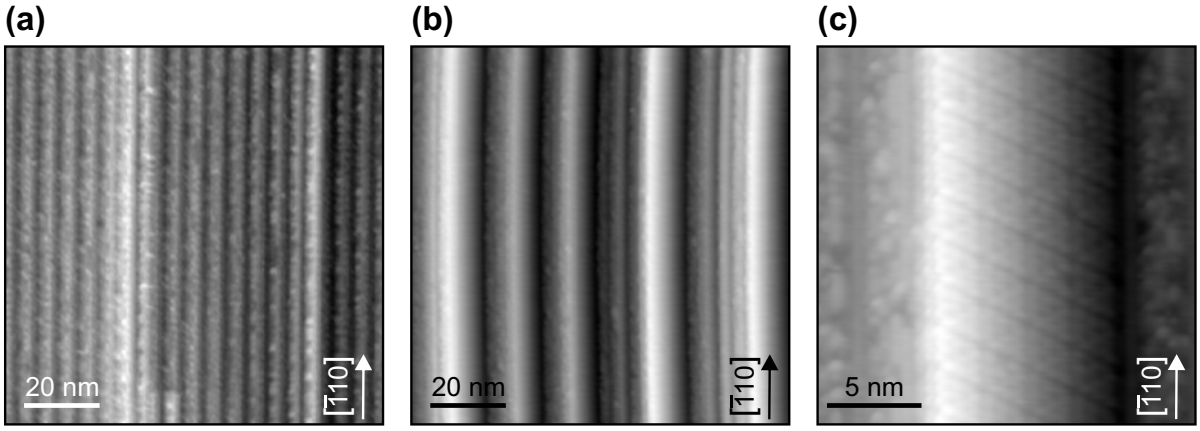

Figure 8.5.: (a) Overview STM image of a Si(557) substrate before the first Tb deposition ($V = -1.5$ V and $I = 100$ pA). (b) Large scale and (c) detailed STM image of the same Si(557) substrate as in (a) after the total deposition of about 4 ML Tb over the course of three Tb silicide nanostructure preparations and flash annealing to clean the sample [(b) $V = -2.5$ V, (c) $V = -1.5$ V, and both $I = 100$ pA].

Using the preparation parameters optimised for the formation of a closed $TbSi_2$ monolayer on Si(111), one may expect that also the Si(hhk) surfaces would be nearly completely covered by the $TbSi_2$ monolayer. While the surface coverage was found to be rather high and multilayer structures could not be excluded for Si(hhk) substrates with $h > k$, the surface coverage by the $TbSi_2$ monolayer is surprisingly low for Si(hhk) substrates with $h < k$, especially for Si(557) [see figure 8.3 (a)]. This indicates an even stronger Tb diffusion into the Si bulk than for the planar surface at least for Si(hhk) substrates with $h < k$. The influence of this Tb diffusion is discussed in the following.

8.1.3. Influence of Tb diffusion into the Si bulk

The Tb diffusion into the Si bulk directly changes the morphology of clean Si(hhk) substrates. Figure 8.5 (a) shows an overview STM image of a clean Si(557) substrate before the first Tb deposition. A very regular alternation of narrow Si(111) terraces and steps is observed even on this large scale. Most Si(111) terraces have the width of only one Si(111)7×7 unit cell, and very rarely one is sufficiently wide to host two unit cells [see figure 5.6 (d)].

This substrate was then used for three Tb silicide nanostructure preparations with a Tb coverage of 1.35 ML each. In between these preparations, the substrate was cleaned by flash annealing. After the third preparation, the Si(557) substrate was once more cleaned by flash annealing and the resulting surface was analysed by STM. The overview STM image in figure 8.5 (b) reveals wide terraces alternating with step bunches. The wide terraces are Si(111) facets, which is proven by the observation of the well-known Si(111)7×7 reconstruction, as seen in the STM image in figure 8.5 (c). The shown terrace is four 7×7 unit cells wide, i.e. much wider than all Si(111) terraces found before the first preparation with Tb.

While the sample used to obtain the STM images shown in figure 8.5 was heated by a

current flowing perpendicular to the steps, a similar observation of wider Si(111) terraces after Tb preparations was also made for a sample that was heated by a current parallel to the steps. Thus, this step bunching is not related to electromigration, but presumably to the Tb diffusion into the Si bulk. A part of the Tb in the Si bulk may diffuse back to the surface during the cooling of the sample to room temperature. While no indications for the $2\sqrt{3}\times2\sqrt{3}$R30° submonolayer structure were found here, in contrast to the observations made on planar Si(111) [384], small amounts of Tb at the surface may lead to the wider Si(111) terraces, e.g. by stabilising steeper or wider step structures, which have to be compensated to obtain the nominal surface orientation on average. An indication for such Tb induced faceting may be the observation of disordered step structures, e.g. left of the wide Si(111) terrace in figure 8.5 (c).

This change of surface morphology of the supposedly clean substrates after prior preparations and the presence of a Tb reservoir in the Si bulk lead to a dependence of the Tb silicide nanostructure formation on prior preparations. In figure 8.6 (a), the first and second preparation on a Si(557) surface are compared. Both preparations used the same nominal Tb amount and during the second one (top image) a lower annealing temperature was applied than in the first one [bottom image and figure 8.3 (a)]. Nevertheless, there are many nanowires for the second preparation that are much wider, broader than 6 nm, than the nanowires of the first preparation. This contradicts the expectations of smaller, including narrower, structures forming at lower annealing temperatures, but agrees with the formation of wider silicide structures due to both initially wider Si(111) terraces and a higher actual Tb coverage. There does not have to occur Tb diffusion out of the Si bulk during preparation, but a decreased Tb diffusion into the Si bulk, since it already contains some Tb would also lead to an increased Tb coverage on the surface of the second preparation.

Similar observations can be made for the Si(335) substrates. Figure 8.6 (b) shows a Si(335) substrate with the typical $TbSi_2$ monolayer preparation subsequently performed two times. The second preparation (top image) leads to wider nanowires than found in the first one (bottom image), here (3.4 ± 0.3) nm compared to (2.5 ± 0.5) nm, but there are also some positive effects observed. The nanowire growth is much more homogeneous for the second preparation, which is directly seen in the STM images and also indicated by the reduced variance of the average nanowire width.

Using multiple preparations, it is possible to achieve the homogeneous growth of even thinner nanowires. This is seen in figure 8.6 (c), in which a sample is shown that was used three times for the same preparation, here the deposition of 0.65 ML Tb and annealing at 500 °C. The average width of the nanowires was found to be (2.3 ± 0.5) nm for this preparation, which is in the range of the widths of individual $TbSi_2$ nanowires on Si(001). Thus, one may expect the observation of a quasi-one-dimensional electronic structure for these narrow nanowires on Si(335). Interestingly, in contrast to the first preparations on Si(hhk) samples with submonolayer Tb coverages, no Si(111) terraces with the $2\sqrt{3}\times2\sqrt{3}$R30° superstructure are observed any more for the shown third preparation. Instead, the surface in between the nanowires is dominated by nanolines and step structures.

On Si(hhk) substrates with $h > k$, the growth studies focussed on finding preparation parameters to obtain anisotropic Tb silicide structures, so that no systematic results regarding the influence of the reuse of substrates are available. In general, a higher surface coverage by Tb silicide structures is observed for Si(hhk) substrates with $h > k$ compared

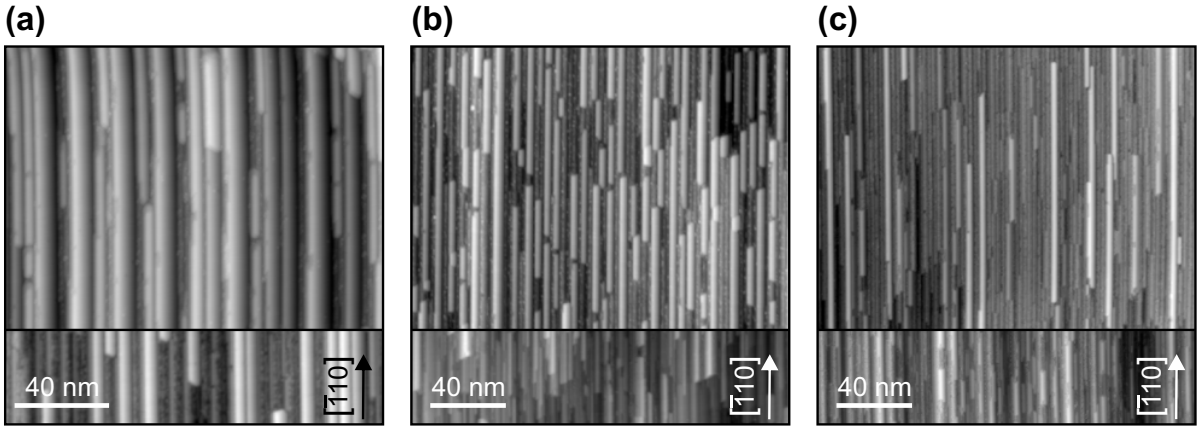

Figure 8.6.: Influence of reusing Si(hhk) substrate, i.e. of flash annealing a formerly Tb covered substrate. (a) STM image of a once reused Si(557) substrate with 1.35 ML Tb annealed at 450 °C ($V = +1.5$ V and $I = 100$ pA). (b) STM image of a once reused Si(335) substrate with 1.35 ML Tb annealed at 500 °C ($V = +2.0$ V and $I = 100$ pA). (c) STM image of a twice reused Si(335) substrate with 0.65 ML Tb annealed at 500 °C ($V = -2.5$ V and $I = 100$ pA). The bottom parts of (a), (b), and (c) show sections of the STM images of the figures 8.3 (a), 8.4 (a), and 8.4 (b), respectively, for comparison.

to those with $h < k$ when the same preparation parameters are used [compare figures 8.1 (a) and 8.2 (a) with figures 8.3 (a) and 8.4 (a)]. Thus, the Tb diffusion into the Si substrate may be influenced by the different surface morphologies of the two offcut directions, but further studies are needed for well-founded conclusions.

Up to now, the Tb silicide structures were only analysed by STM, which led to comprehensible assumptions regarding the formed structures, but further affirmation by other methods is still needed. The assignment of the $TbSi_2$ monolayer structure to the nanowires is mainly build on the observation of straight edges, which are also possible for multilayer Tb silicide even if they are uncommon. Furthermore, the dimensionality of the electronic structure of the nanowires with widths down to 2.3 nm is still unknown. Thus STS, XPS, and ARPES results on the Si(hhk) nanowire samples are presented in the following.

8.2. Electronic properties

The Tb silicide nanowires and stripes on Si(hhk) surfaces are characterised by a structureless appearance for typical tunnelling conditions. Thus, one may expect a metallic behaviour as it is also known for the Tb silicide mono- and multilayer on planar substrates. In order to test this expectation, STS experiments are performed. Using STS, an identification of the silicide structures should also be possible, since characteristic spectra are reported for the different structures on planar substrates (see section 5.4). Similarly, the growth of the $TbSi_2$ monolayer also leads to characteristic XPS and ARPES signatures (see section 5.4).

Of these three methods, STS and ARPES are also sensitive to changes in the electronic structure due to confinement effects. Thus, they are ideal methods to characterise such

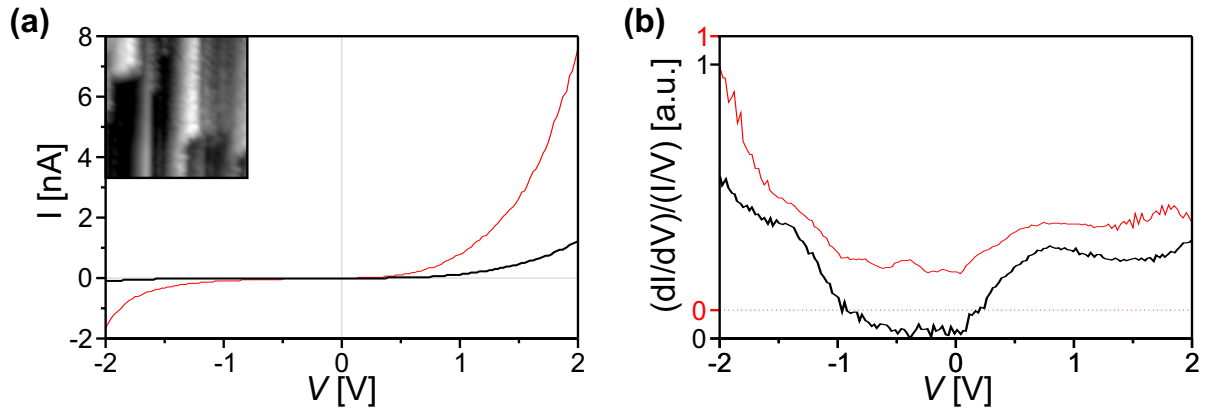

Figure 8.7.: (a) I-V and (b) normalised differential conductance spectra measured on a terrace of a Si(335) sample presumably covered by the $2\sqrt{3}\times2\sqrt{3}$R30° superstructure in black and of the $2\sqrt{3}\times2\sqrt{3}$R30° submonolayer structure on a planar Si(111) sample in red. The stabilisation conditions were $I = 100$ pA, $V = +1.0$ V, and $\Delta z = 0$ for the measurement on Si(335) and $I = 100$ pA, $V = -1.5$ V, and $\Delta z = 50$ pm for the Si(111) measurement. The analysed terrace of the Si(335) sample is in the centre of the 30 nm wide STM image shown as inset in (a) ($V = +1.0$ V, and $I = 100$ pA). The analysis procedure introduced in reference [113] had to be used for the data of the Si(335) sample due to a wide range, in which only a small tunnelling current was measured.

changes. However, STS and ARPES data can only be used to verify the formation of a structure but not for falsification, since deviations may be caused by confinement effects. In contrast, XPS is not so sensitive to electronic changes, which are not accompanied by changes of the atomic structure, with the exception of the Fermi-level position, allowing a more reliable structure identification. In the following, the general results using these methods are presented beginning with the STS data and ending with the ARPES data.

8.2.1. Scanning tunnelling spectroscopy

Preparations of Tb silicide nanostructures on Si(hhk) substrates that used only a submonolayer coverage of Tb often resulted in the formation of Si(111) terraces with a rough surface appearance. The black curves in figure 8.7 show an STS measurement on such a terrace of a Si(335) substrate. In the same figure, an STS measurement of the $2\sqrt{3}\times2\sqrt{3}$R30° superstructure on a planar Si(111) substrate is presented as red curves. While the I-V-curves show strong differences probably due to the very different stabilisation conditions prior to the STS measurement, the normalised differential conductances of these two measurements nicely agree with each other.

The main discrepancy between both measurements is that finite values of the normalised differential conductance are observed for the superstructure on the planar substrate in the wide voltage range, in which the normalised differential conductance is close to zero for the silicide structure on the vicinal substrate. This difference is easily explained by the stabilisation conditions. The tip was rather far away from the sample during the measurement on the vicinal substrate leading to a wide voltage range with very low

tunnelling current [see figure 8.7 (a)]. Thus, it is safe to assume that the Si(111) terraces with a rough appearance are covered by the $2\sqrt{3}\times2\sqrt{3}$R30° superstructure.

For this $2\sqrt{3}\times2\sqrt{3}$R30° superstructure, the STS measurements reported here are in general in rather good agreement with the previously reported data [see figure 5.16 (c)]. With local maxima or shoulders in the normalised differential conductance at about −1.5 V, −0.5 V, +0.25 V, and +0.75 V, the course of all spectra are similar. However, the previous STS measurements show a rather sharp dip to zero at the Fermi level in the normalised differential conductance indicating a very low density of states at the Fermi level [384]. Furthermore, theory even predicts a band gap for the extended $2\sqrt{3}\times2\sqrt{3}$R30° superstructure [362]. In reality, the $2\sqrt{3}\times2\sqrt{3}$R30° superstructure forms domains. The triangular domains are rather small even on the planar substrate with base lengths typically below 5 nm [see figure 5.16 (a)]. The domain walls may alter the electronic structure of the $2\sqrt{3}\times2\sqrt{3}$R30° superstructure, e.g. leading to an increased density of states at or close to the Fermi level. Consequently, STS spectra may be rather strongly influenced by the spectroscopy location leading to discrepancies in different experimental data sets and with theoretical predictions for the extended superstructure.

The vicinal and planar samples, on which the STS measurements were performed for the $2\sqrt{3}\times2\sqrt{3}$R30° superstructure, were also used for STS measurements on the Tb silicide nanowires on Si(335) and the Tb silicide mono- and multilayer on Si(111). The STS results of two nanowires are shown in figures 8.8 (a and b). In the STM image of the nanowires, shown in figure 8.8 (c), it is observed that the first nanowire with a width of about 2.1 nm [black curves in figures 8.8 (a and b)] is much wider than the second one with a width of about only 1.0 nm [red curves in figures 8.8 (a and b)]. Interestingly, the normalised differential conductance appears similar for both nanowires, which indicates also a similar atomic structure.

For comparison, the normalised differential conductances of the Tb silicide mono- and multilayers on Si(111) are presented in figure 8.8 (d). The STS spectrum of the $TbSi_2$ monolayer is in rather good agreement with the reported spectrum of this silicide that is seen in red in figure 5.18 (a) and agrees well with the experimental STS data of other $RESi_2$ monolayers [370, 373, 374, 384]. Unfortunately, such good agreement is not found between any STS spectrum of the nanowires on Si(335) and the STS spectra of the $TbSi_2$ monolayer or the Tb_3Si_5 multilayer on Si(111), although the spectra of $2\sqrt{3}\times2\sqrt{3}$R30° superstructures showed a nice conformity for the very same preparations and tips. However, there is one similarity between the nanowire spectra and the $TbSi_2$ monolayer spectrum in the position of the minima of the normalised differential conductance at small positive sample voltages. This is an indication for $TbSi_2$ nanowires, but cannot be conclusive since the STS spectra deviate significantly in the remaining voltage range.

Even taking into account further nanowire STS data obtained for other preparations and different tips, a part of which is illustrated in figure 8.9, a good agreement with any of the STS data reported here or previously on silicide structures on planar substrates is never observed for a wide voltage range [see figures 5.18 (a) and 8.8 (d)]. Thus, it cannot be determined by STS if the nanowires consist of a $TbSi_2$ monolayer, but it also cannot be excluded, since the large variety of different STS spectra clearly shows the strong influence of the tip on the measured STS data. Spectra may appear similar for rather different nanowires, e.g. the nanowires discussed in figure 8.8, and may be completely different for

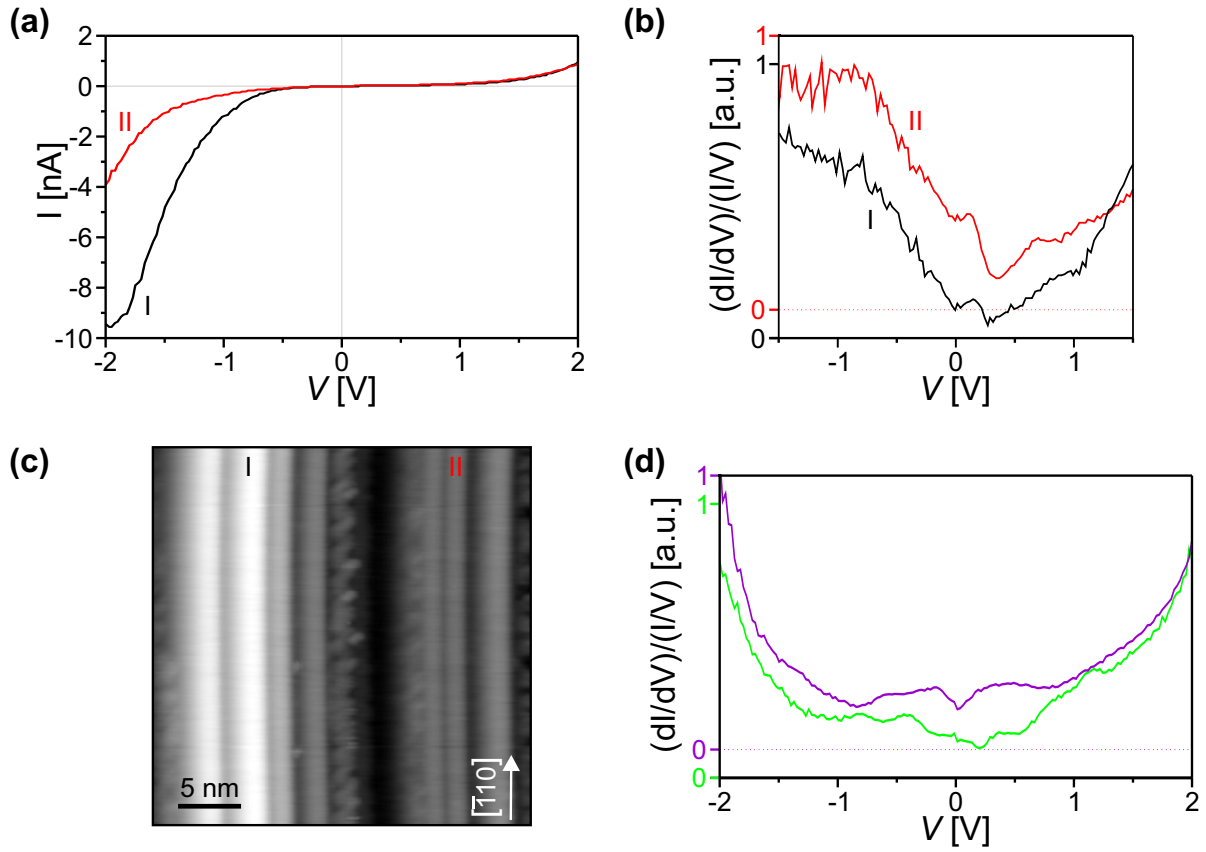

Figure 8.8.: (a and b) STS data, I-V curve in (a) and normalised differential conductance in (b), for two nanowires with varying widths observed for the same Si(335) sample that is discussed in figure 8.7 ($I = 100$ pA, $V = +1.0$ V, and $\Delta z = 0$). A reduced voltage range is shown in (b) since current saturation effects, see black curve in (a), distorted the data for negative voltages with high absolute values. (c) STM image showing the two nanowires, which are marked by I and II in the colours of the graphs in (a and b) ($V = +1.5$ V and $I = 100$ pA). (d) Normalised differential conductance as measured for the Tb silicide monolayer (green) and multilayer (purple) on planar Si(111) ($I = 100$ pA, $V = -1.5$ V, and $\Delta z = 50$ pm). The measurements were performed using the sample that was also used for the STS measurement on Si(111) shown in figure 8.7.

rather similar nanowires, e.g. the STS data shown in black in figures 8.8 and 8.9 are of long nanowires that have similar widths. Thus, no systematic changes with the nanowire width are evident for nanowires on Si(335), in contrast to the STS data on Tb silicide nanowires on Si(001). Nevertheless, all nanowires on Si(hhk) substrates showed a finite normalised differential conductance at $V = 0$ and many also a clear positive slope of the I-V-curve at $V = 0$, e.g. the red and blue curves in figure 8.9 (a). Thus, the nanowires on Si(hhk) are metallic, which agrees with a Tb silicide mono- or multilayer structure of the nanowires.

The narrow nanowire shown in figure 8.8 (c) is only about 1 nm wide. Thus, it has a width also typically observed for nanolines. It was identified as nanowire since it showed a straight side in the tip-height profile, which is not observed for nanolines (see section 8.1). Similar to

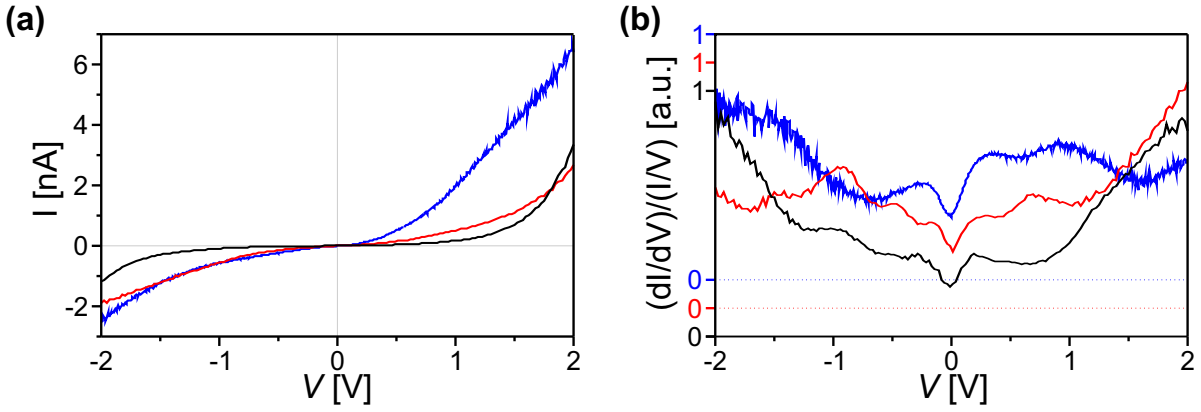

Figure 8.9.: STS data of nanowires on Si(335) taken at different days, i.e. different preparations and also different tips. The widths of the investigated nanowires were about 2.2 nm (black spectra), 1.4 nm (red spectra), and 2.6 nm (blue spectra) while the respective stabilisation conditions were $I = 100$ pA, $V = -1.5$ V, and $\Delta z = 50$ pm (black spectra), $I = 100$ pA, $V = -1.0$ V, and $\Delta z = 50$ pm (red spectra), and $I = 100$ pA, $V = -1.5$ V, and $\Delta z = 100$ pm (blue spectra).

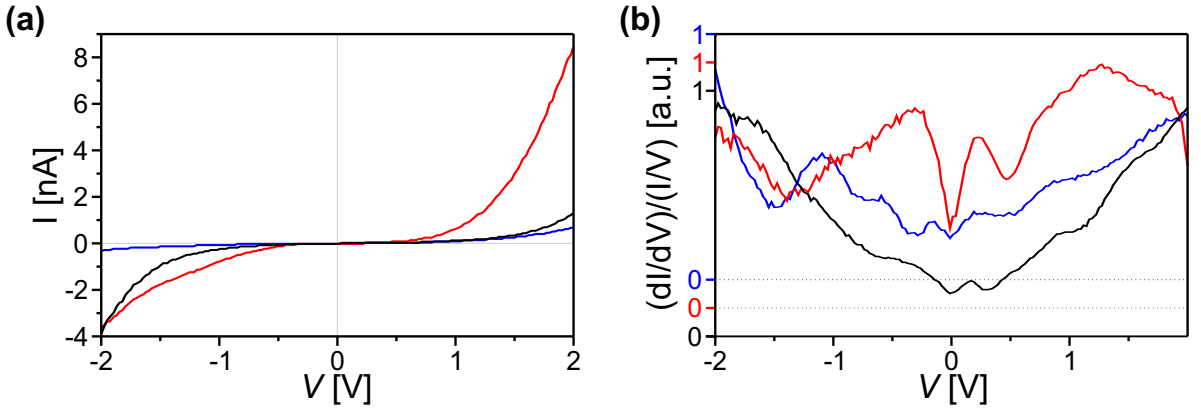

Figure 8.10.: (a) I-V curves and (b) derived normalised differential conductance curves for nanolines on Si(335) for different preparations and tips. All nanolines had widths of about 1.0 nm and the stabilisation parameters were $I = 100$ pA, $V = -1.5$ V, and $\Delta z = 100$ pm (black spectra), $I = 100$ pA, $V = -1.5$ V, and $\Delta z = 125$ pm (red spectra), and $I = 100$ pA, $V = +1.5$ V, and $\Delta z = 50$ pm (blue spectra).

nanowires, STS spectra obtained on nanolines show a wide variety (see figure 8.10). Again the differences between individual spectra are most likely caused by tip effects, especially since the analysed nanolines show a similar width, so that the width can be excluded as an influencing factor.

While spectra of nanolines may show similarities to the ones of nanowires, as e.g. the black coloured curves of the normalised differential conductance in figures 8.9 and 8.10, they cannot be used as conclusive prove of a similar atomic structure of nanolines and nanowires, since such similarities are practically unavoidable in large sets of strongly varying spectra. However, a common property between nanolines and nanowires is their metallic behaviour. For the nanolines, their metallicity is evident by the curves of the normalised differential

conductance in figure 8.10 (b), which stay well above zero and show no extended voltage range with low values.

Similar to STM, STS showed debatable indications for the formation of Tb silicide nanowires on Si(hhk) with the $TbSi_2$ monolayer structure. In the following, this is further analysed with XPS, a method not relying on the rather unstable tips present in STM and STS.

8.2.2. Core-level photoemission spectroscopy

Similar to the shown XPS data on nanowires on the Si(001) surface, all Si-2p core level spectra for Tb silicide nanostructures on Si(hhk) depicted here are normalised to equal heights and were obtained at room temperature, so that they should not be influenced by photovoltage or charging effects. For comparison, not only the samples with nanostructures were analysed, but also the clean substrates.

A Si-2p spectrum of a clean Si(557) substrate is shown in the lower part of figure 8.11. It can be fitted reasonably well using the known spectral composition of the planar Si(111)7×7 reconstruction [256], but most components have a rather low intensity, while the Si bulk component strongly dominates the spectrum [compare to figure 5.5 (c)]. This is in good agreement with the reduced surface area of the 7×7 reconstruction on this vicinal substrate compared to the planar one. Since a large number of spectral components is already considered for the 7×7 reconstruction, no additional components are needed due to presence of the step structure between the Si(111) terraces. The step structure may induce the uncharacteristically strong C_1 component, which is situated at a slightly lower kinetic energy than the Si bulk component [compare with figure 5.5 (c)].

After the preparation of Tb silicide nanowires on the same Si(557) substrate using slightly more than 1 ML Tb, the Si-2p spectra changes strongly [see upper part of figure 8.11]. On the first view, it does not resemble the known Si-2p spectra of the Tb silicide mono- or multilayer on Si(111), which are shown in figure 8.12 for comparison. But the Si-2p spectrum of the nanowires on Si(557) has the same spectral composition as the $TbSi_2$ monolayer on planar Si(111) with one additional component at high kinetic energy, which is drawn in purple in figure 8.11. This additional component lies about 0.40 eV higher in kinetic energy than the main silicide component. Thus, it should not be related to the second silicide component of the Tb_3Si_5 multilayer (orange in figure 8.12) or the other component at high kinetic energy of the Tb silicide mono- or multilayer spectra, which are shifted by about 0.33 eV and 0.49 eV with respect to the main silicide component, respectively. The origin of the well-known other component at high kinetic energy is unclear, but it may be related to defects in the silicide layers, substrate areas covered by Tb induced submonolayer superstructures, or even 7×7 reconstructed areas devoid of Tb [69].

In addition to the additional component, the main difference between the nanowire spectrum and the $TbSi_2$ monolayer spectrum on Si(111) is the much larger intensity of the component originating from the uncovered Si substrate. This observation is in good agreement with the STM experiments, in which a reduced surface coverage was observed on Si(557) in comparison to preparations with the same parameters using planar Si(111) substrates [see figure 8.3 (a)]. In contrast, the intensity of the completely shifted Si bulk component, i.e. the one stemming from below the nanowires, is rather low compared to the

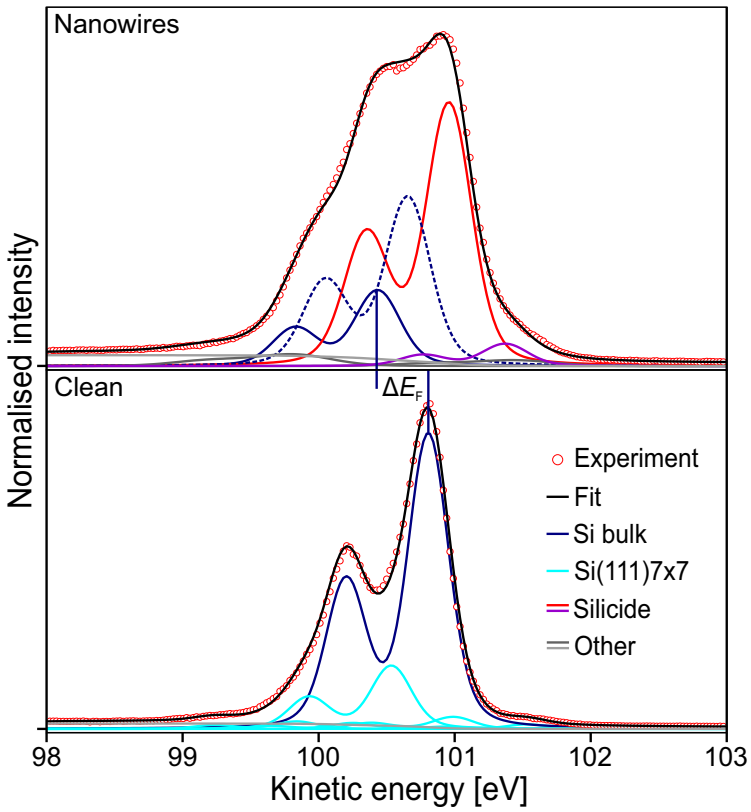

Figure 8.11.: Si-2p spectra of a clean Si(557) substrate and the same substrate covered by 1.15 ML Tb annealed at 500 °C ($h\nu$ = 200 eV). The hatched Si bulk component of the nanowire spectrum corresponds to uncovered Si substrate areas. The nanowire growth is expected to be similar to the one shown in figure 8.3 (a).

intensity of the silicide component. Possible reasons for this include the nanowire growth on Si(111) terraces that are inclined to the surface normal and whose influence on the Fermi-level position of neighbouring areas may be reduced due to the steps surrounding the Si(111) terraces. While it is not possible to exactly determine the Fermi-level position in the Si band gap since no usable reference data of clean Si(111) substrates are available, the shift of the Fermi level upon nanowire growth of $\Delta E_\mathrm{F} \approx 0.37$ eV is in the same range as observed for $TbSi_2$ formation on Si(111), where $\Delta E_\mathrm{F} \approx 0.33$ eV is observed [69]. The slightly larger shift for the nanowires may be related to an initial Fermi-level position closer to the valence band for clean Si(557) substrates, e.g., due to the step structure in between Si(111) terraces.

The good agreement between the Si-2p spectra of the nanowires on Si(557) and the $TbSi_2$ monolayer on Si(111), especially in the spectral composition, clearly indicates the formation of $TbSi_2$ nanowires confirming the expectations by STM. Si-2p spectra of nanowires or stripes prepared on the other Si(hhk) substrates by using submonolayer amounts of Tb can be well fitted using the same spectral composition as found for the nanowires on Si(557) (see figure 8.13). Thus, the nanowires and stripes on Si(335), Si(775), and Si(553) may also consist of $TbSi_2$.

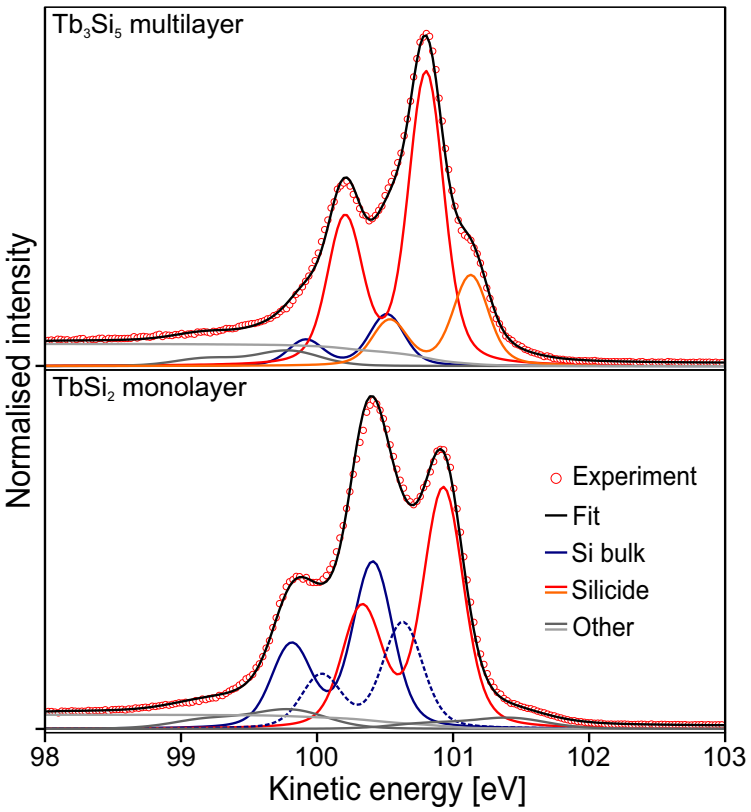

Figure 8.12.: Si-2p spectra of the $TbSi_2$ monolayer and Tb_3Si_5 multilayer on planar Si(111) for comparison with the XPS data of the vicinal samples ($h\nu = 200$ eV). The monolayer was prepared by deposition of 1.15 ML Tb and annealing at 500 °C while 4.25 ML Tb were annealed at 500 °C for the multilayer. The hatched Si bulk component of the monolayer spectrum corresponds to uncovered Si substrate areas.

The additional component, depicted in purple in the XPS spectra, is observed for all substrates. Thus, it cannot stem from nanolines, which are only observed for Si(hhk) substrates with $h < k$. The only common surface structure on substrates of both offcut directions, which was apparent in STM (see section 8.1), is the one assigned to the $TbSi_2$ monolayer, which forms the stripes or nanowires. Consequently, the additional component is presumably related to the $TbSi_2$ structures. For both offcut directions, the intensity of this component is higher for the substrates with increased offcut. With increasing offcut angle, the $TbSi_2$ nanostructures get narrower. The atomic structure does not change with a width decrease, but the relative contribution of the edges is increased for narrower structures. Thus, the additional silicide component may be related to the edges of the nanostructures.

Furthermore, it may be directly related to the straight edges in $[\bar{1}10]$-direction since its intensity is quite low for the preparation using the Si(775) substrate. The stripes showed only short straight segments for this preparation [see figures 8.1 (b and c)], in contrast to the stripes on Si(553) [see figures 8.2 (b and c)], and especially in contrast to the nanowires on Si(557) and Si(335) (see figures 8.3 and 8.4). While such edges are also apparent for the $TbSi_2$ monolayer on planar Si(111), the ratio of edge atoms to inner atoms is very low for

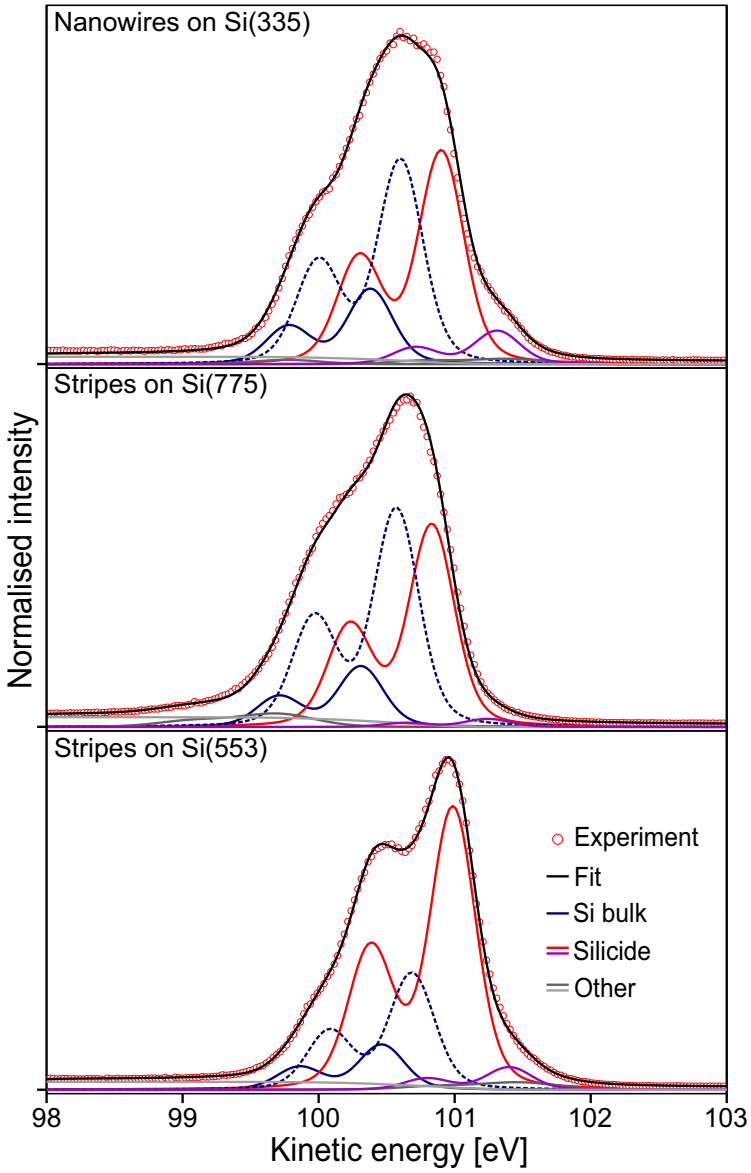

Figure 8.13.: Si-2p spectra of Tb silicide nanostructure preparations on various Si(hhk) surfaces using submonolayer Tb coverages ($h\nu$ = 200 eV). All Tb layers were annealed at 500 °C, but 0.70 ML, 0.55 ML, and 0.65 ML Tb were deposited on the Si(335), Si(775), and Si(553) substrates, respectively. STM images of similar preparations are seen in figures 8.4 (b), 8.1 (b), and 8.2 (b) using Si(335), Si(775), and Si(553) substrates, respectively. The hatched Si bulk components correspond to uncovered substrate areas. The spectrum of the Tb silicide stripes on Si(553) was shifted by 1 eV to lower kinetic energies in order to compensate for a presumably faulty setting of the analyser work function during this measurement.

extended films, leading to a very small intensity of an edge-related Si-2p spectral component making it indistinguishable.

A strong main silicide component is found in the Si-2p spectrum of the stripe preparation on Si(553) (see bottom part of figure 8.13). This is unexpected for the low amount of deposited Tb and may indicate a reduced Tb diffusion into the Si bulk in agreement with the observations by STM (see section 8.1). Unfortunately, the intensity of the Si bulk component of the silicide covered area is uncharacteristically small compared to the intensity of the main silicide component even for a preparation on a vicinal substrate (compare with respective parts in figures 8.11, 8.12, and 8.13). This inconsistency may raise some doubt regarding the correctness of the present assignment of the Si-2p spectral components, so that some final proof for the formation of a $TbSi_2$ monolayer on the vicinal substrates is still needed. This is given in the following discussion of the ARPES data obtained for nanowire and stripe samples.

8.2.3. Angle resolved photoemission spectroscopy

Close to the Fermi level, the band structure of the $TbSi_2$ monolayer on planar Si(111) is characterised by highly anisotropic electron pockets at the $\overline{\mathrm{M}}$-points and a hole pocket at the $\overline{\Gamma}_{111}$-point of the first Brillouin zone (see section 5.4). The corresponding bands are nicely resolved in dispersion plots and on the Fermi surface while dispersing bands at higher binding energies are partially masked by the non-dispersing Tb-4f core-levels. Thus, the analysis of ARPES data concentrates on the region close to the Fermi level in the following. All reported electronic structures of the rare earth disilicide monolayer are very similar [67, 69, 360, 362, 364], and a similar electronic structure was also observed for rather wide $DySi_2$ nanowires on Si(557) [73, 74]. Consequently, the observation of the characteristic bands described above is expected at least for wide $TbSi_2$ nanowires.

Wide nanowires formed especially when a substrate was reused for multiple preparations. Figure 8.14 shows the ARPES data for such a second preparation of nanowires on Si(557) using the typical $TbSi_2$ monolayer preparation. Shown are dispersion plots along high symmetry directions in (a and b) and the Fermi surface in (c). The high symmetry directions used here coincide with the direction (a) perpendicular and (b) parallel to the step edges and accordingly to the nanowires. The Fermi surface is oriented in a way that the momentum component parallel to the nanowires ($k_\parallel$) is vertical and the one perpendicular to the nanowires ($k_\perp$) is horizontal. The distinction of the momentum components in the directions perpendicular and parallel to the nanowires is easily possible despite the sixfold symmetry of the Brillouin zone and consequently of the ARPES data. Based on the substrate structure, the direction of the step edges corresponds to a $\overline{\mathrm{K}}_{111}$-$\overline{\mathrm{K}}$-direction in reciprocal space. Since the samples were oriented in the way that the step edges were either approximately vertical or approximately horizontal to the entrance slit of the hemispherical analyser, the step direction is easily assigned in the ARPES data.

Comparing the ARPES data obtained for wide nanowires on Si(557) to the ARPES data of the $TbSi_2$ monolayer on Si(111) [see figures 5.18 (b and c)], a very good agreement between both is found. There are parabolic electron pockets at the $\overline{\mathrm{M}}$-points characterised by a high effective mass in $\overline{\Gamma}_{111}$-$\overline{\mathrm{M}}$-direction and a low one in $\overline{\mathrm{K}}$-$\overline{\mathrm{M}}$-direction [see figures 8.14 (a and b)]. This strong anisotropy of the effective mass leads to an elliptical appearance of

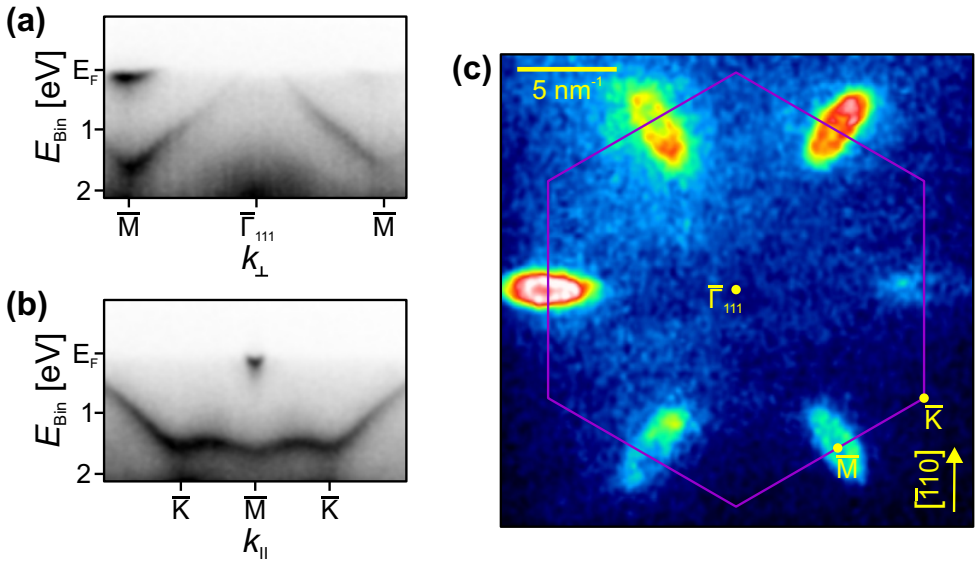

Figure 8.14.: ARPES data of a Si(557) substrate, on which Tb silicide nanowires were prepared by the typical $TbSi_2$ monolayer preparation for the second time (1.15 ML Tb annealed at 500 °C and $h\nu = 100$ eV). In (a and b), dispersion plots perpendicular and parallel to the long nanowires axis, respectively, are shown, while the Fermi surface is presented in (c). The dispersion plot in (a) intersects both horizontal ellipses observed in (c) while only the left ellipse is cut in (b). The purple hexagon in (c) marks the first Brillouin zone. An STM image of a similar preparation is seen in the upper part of figure 8.6 (a).

these electron pockets on the Fermi surface [see figure 8.14 (c)].

In contrast to the electron pockets, the expected hole pocket is not observed on the Fermi surface around the $\overline{\Gamma}_{111}$-point. This is caused by matrix-nelement effects leading to a vanishing intensity of the corresponding bands at the Fermi level. That these bands are also present for the nanowires is clearly observed in the dispersion plots. Similarly, the strong intensity variation of the electron pockets on the Fermi surface can be assigned to matrix-element effects.

The observation of the band structure of the $TbSi_2$ monolayer for the nanowire samples is a compelling proof for the formation of $TbSi_2$ nanowires since no other structure with an appearance similar to the one of the $TbSi_2$ monolayer is observed by STM on nanowire samples (see section 8.1). Not only wide nanowires consist of $TbSi_2$, also narrower nanowires show the band structure of $TbSi_2$. Figure 8.15 shows ARPES data of a nanowire sample prepared by deposition of a submonolayer amount of Tb on a Si(335) substrate, the combination of preparation parameters that leads to the narrowest nanowires (see section 8.1). The orientation of the Fermi surface and the directions, for which dispersion plots are presented, are the same as in figure 8.14.

The highly anisotropic electron pockets and the bands leading to the hole pocket are clearly observed in the dispersion plots [see figures 8.15 (a and b)] and the electron pockets are also distinguishable as anisotropic ellipses at the $\overline{\text{M}}$-points on the Fermi surface [see figure 8.15 (c)]. Thus, narrow nanowires are also $TbSi_2$ structures.

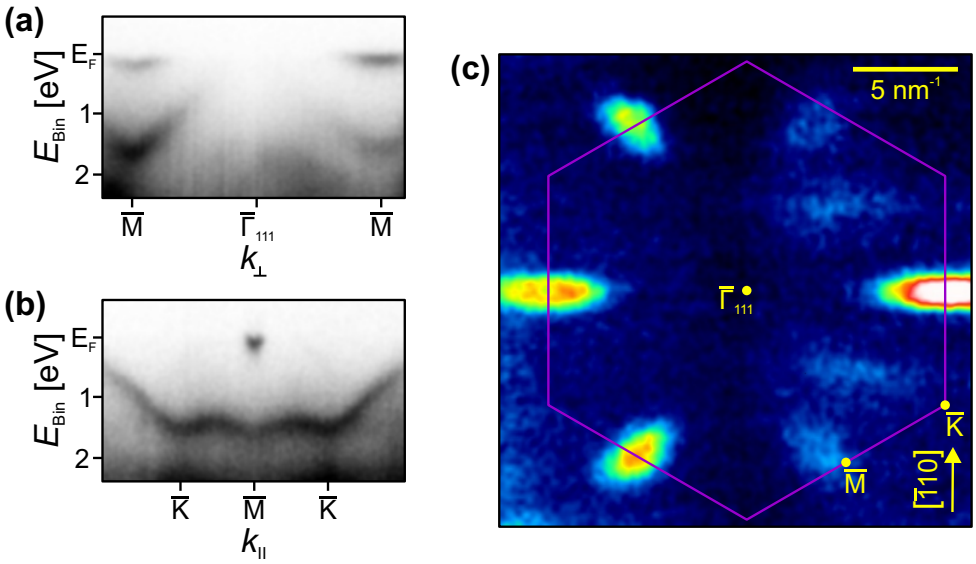

Figure 8.15.: Dispersion plots (a) perpendicular and (b) parallel to the long nanowires axis, and (c) Fermi surface of the nanowire preparation on Si(335), for which the Si-2p spectrum is shown in figure 8.13. The ARPES data were obtained with $h\nu = 100$ eV. The dispersion plot in (a) intersects both horizontal ellipses observed in (c) while only the left ellipse is cut in (b).

Taking a detailed look at the ARPES data, differences between the electronic structures of narrow nanowires and of the extended two-dimensional film, which is very well reproduced by wide nanowires, become apparent. The bands in the dispersion plot perpendicular to the nanowires are blurred in the ARPES data of narrow nanowires [compare figures 8.14 (a) and 8.15 (a)]. Interestingly, while the dispersion parallel to the nanowires may also be slightly broadened for the narrow nanowire sample, this effect is much less pronounced than for the perpendicular direction [compare figures 8.15 (a and b)].

For wide nanowires or the extended two-dimensional film, all electron pockets have similar extensions on the Fermi surface and areas with reduced intensity are found in their centres [see figures 5.18 (b) and 8.14 (c)]. The situation is different for narrow nanowires [see figure 8.15 (c)]. Here, the horizontally oriented ellipses appear rather similar to the ones of the extended film, but the other four are not as anisotropic any more and show their maximum intensities in their centres. These effects cannot be attributed to matrix element effects, but may be caused by the confinement of the electrons in the $TbSi_2$ to smaller widths. Especially the variations of the electron pockets are analysed in detail in the following section 8.3. In this section, also the emergence of the additional intensity on the Fermi surface, observed in figure 8.15 (c) in the right half of the Brillouin zone, will be discussed.

The nanowires on Si(hhk) substrates with $h < k$ are $TbSi_2$ nanostructures. Now, the stripes formed on Si(hhk) substrates with $h > k$ are analysed. Dispersion plots and the Fermi surfaces for preparations of stripes on a Si(775) substrate and on a Si(553) substrate are shown in the figures 8.16 and 8.17, respectively. Again, the orientation of the Fermi surfaces and the directions, for which dispersion plots are presented, are the same as in figure 8.14.

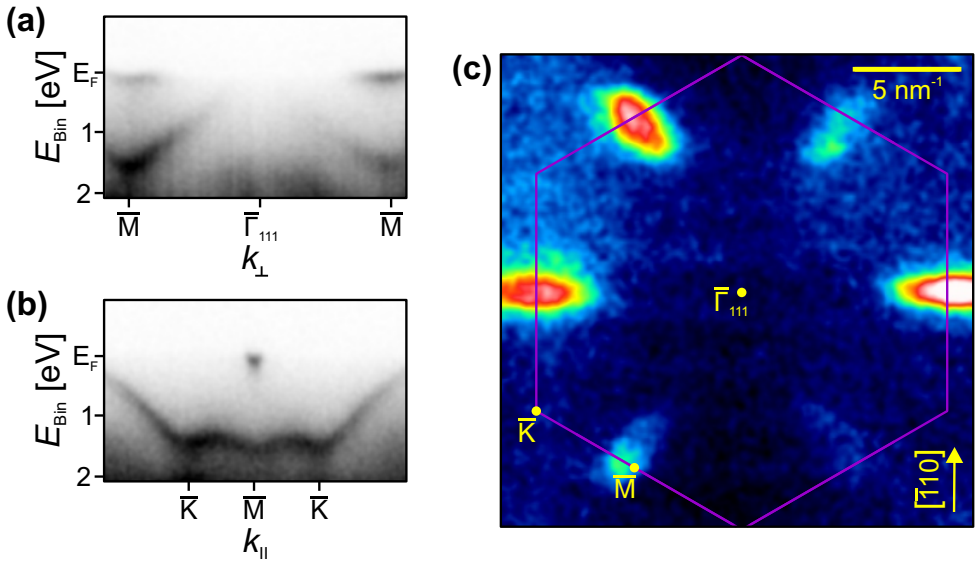

Figure 8.16.: ARPES data of the Tb silicide stripe preparation on Si(775) ($h\nu = 100$ eV), whose Si-2p spectrum is shown in figure 8.13. In (a and b), dispersion plots perpendicular and parallel to the stripe elongation, respectively, are shown while the Fermi surface is presented in (c). The dispersion plot in (a) intersects both horizontal ellipses observed in (c) while only the right ellipse is cut in (b).

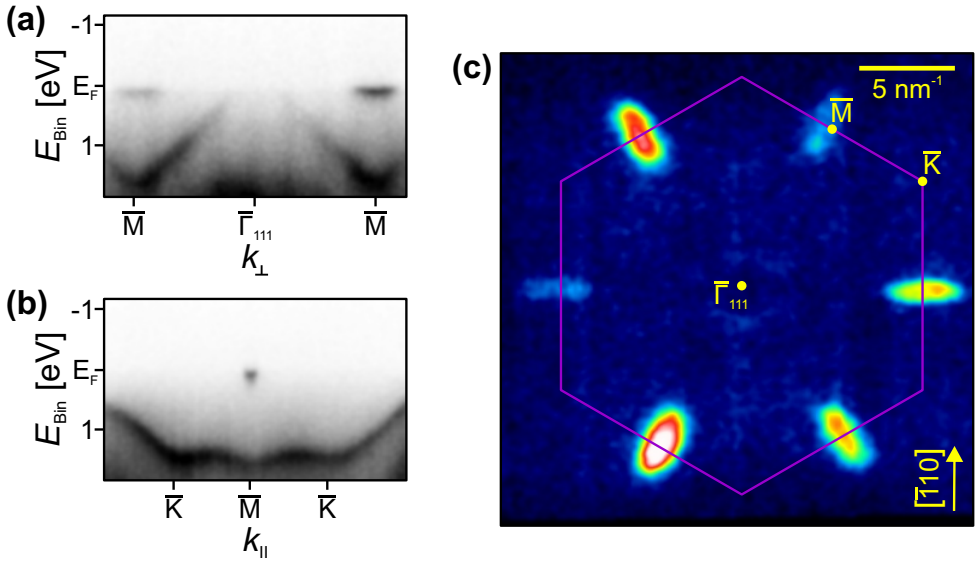

Figure 8.17.: ARPES data of the Tb silicide stripe preparation on Si(553) ($h\nu = 100$ eV), whose Si-2p spectrum is shown in figure 8.13. In (a and b), dispersion plots perpendicular and parallel to the stripe elongation, respectively, are shown while the Fermi surface is presented in (c). The dispersion plot in (a) intersects both horizontal ellipses observed in (c) while only the right ellipse is cut in (b).

In general, the electronic structure of the $TbSi_2$ monolayer is also observed for the stripe samples. There are anisotropic electron pockets at the $\overline{\text{M}}$-points seen in the dispersion plots

[see figures 8.16 (a and b) and 8.17 (a and b)] and on the Fermi surfaces [see figures 8.16 (c) and 8.17 (c)]. In addition, the bands forming the hole pocket around the $\overline{\Gamma}_{111}$-point are present in the dispersion plots showing a course as is known for the $TbSi_2$ monolayer on planar Si(111) [see figure 5.18 (b)]. The hole pocket is even visible, albeit faintly, on the Fermi surface for the stripe sample on the Si(553) substrate. Similar as for the nanowires on Si(hhk) substrates with $h < k$, there is no other structure observed in STM that may be assigned to the $TbSi_2$ monolayer. Consequently, the stripes are formed by $TbSi_2$. Moreover, no additional bands that cannot be related to the $TbSi_2$ monolayer are found in the ARPES data obtained for stripes on Si(775) and Si(553) in contrast to the measurements on narrow nanowires on Si(335).

While the bands in the dispersion plots also appear slightly blurred for the stripes, any anisotropy of this broadening of the electronic structure is at least not as pronounced as it is observed for the narrow nanowires on Si(335). In contrast, an inhomogeneous appearance of the electron pockets on the Fermi surface is found similar to the observations made for narrow nanowires on Si(335). In the data of the stripes on Si(775), there is only one non-horizontal electron pocket with considerable intensity. The ellipse of this electron pocket appears to have a similar width as the horizontal ones, but is shorter. In contrast, no large length differences are observed for the elliptical appearances of the electron pockets for the stripes on Si(553), but the horizontal ellipse with considerable intensity is much narrower than the non-horizontal ones. Thus, there are also confinement effects for the stripes, which are included in the discussion in the following section.

8.3. Confinement effects

The electronic band structure of narrow nanowires and stripes showed effects that may be related to their confinement to small widths. First the anisotropic broadening of the band structure and the inhomogeneous appearance of the electron pockets on the Fermi surface are analysed. Afterwards, the additional intensity on the Fermi surface is discussed, which was exclusively observed for nanowire preparations using submonolayer amounts of Tb on Si(335).

8.3.1. The broadening of the electronic structure

The band structures of the two-dimensional $TbSi_2$ film and of the wide $TbSi_2$ nanowires are characterised by sharp bands in the dispersion plots [see figure 5.18 (b) and 8.14 (a and b)]. Neither the $TbSi_2$ band structure of narrow nanowires nor the one of stripes show such sharp bands [see (a and b) in figures 8.15, 8.16, and 8.17]. Interestingly, this broadening of the $TbSi_2$ band structure is predominantly perpendicular to the step edges, especially for the narrow nanowires, i.e. the direction of the enhanced broadening coincides with the direction, in which the nanostructures have a limited extension.

The Fermi contours of the electron pockets are ellipses. These ellipses appear filled most of the time for the narrow nanowires and stripes in contrast to the wide nanowires and the extended two-dimensional film, for which local intensity minima are observed in the centres of the ellipses. This filled appearance is easily explained by taking the broadening

of the band structure into account since it leads to increased intensities in the centres of the electron pockets.

Taking a closer look at the ellipses found on the Fermi surfaces of the narrow nanowire and the stripe preparations [see (c) in figures 8.15, 8.16, and 8.17], the horizontal ellipses that have their long axis perpendicular to the step edges are longer and narrower than the non-horizontal ellipses. This inhomogeneous appearance is differently developed for the various measurements, e.g. the difference in width is more pronounced than the length variation in the ARPES data of stripes on Si(553) shown in figure 8.17, but is in general observed in ARPES data of narrow nanowires or stripes, including ARPES data not illustrated here.

Assuming an anisotropic broadening that is stronger perpendicular to the step edges and accordingly to the nanostructures, such an inhomogeneous appearance of the electron pockets is expected. This is illustrated by the schematic in figure 8.18 (a) depicting the Fermi contours of the electron pockets and a broadening only perpendicular to the nanostructures. The resulting Fermi surface agrees well with the experimental findings showing longer and narrower horizontal ellipses than non-horizontal ones.

The confinement mainly of the width of the nanostructures is assumed to be the reason for the anisotropic broadening. A smaller nanostructure leads to a better defined initial position of the photoelectron that is emitted from the nanostructure. A more precisely known initial position leads to a larger uncertainty of the initial momentum after Heisenberg's uncertainty principle [451], resulting in $\Delta k \Delta x \gtrsim 2\pi$. Since the width of the Brillouin zone of a structure is about $2\pi/a$ with a the lattice constant of the structure, a considerable broadening (Δk) of the band structure observed by ARPES is expected if the extension of the structure (Δx) amounts to only a few lattice constants. The nanowires and stripes are mainly restricted in the direction perpendicular to the step edges of the Si(hhk) substrates, so that the broadening is dominant in this direction.

Based on this explanation, one expects a stronger broadening for narrower structures, i.e. the broadening should be stronger for the nanostructures on the substrates with larger absolute values of the offcut angles, since steeper offcut angles lead to narrower nanostructures (see section 8.1). This is already qualitatively observed for the nanowires on Si(hhk) substrates with $h < k$. The wide nanowires on Si(557) show a rather sharp band structure very similar to the one of the $TbSi_2$ film on planar substrates while the band structure of the narrow nanowires on Si(335) is strongly broadened.

Intensity profiles taken on the Fermi surface confirm these visual impressions. Figure 8.19 (a) shows intensity profiles cutting horizontal electron pockets of the nanowire ARPES data obtained using a Si(557) substrate in black and using a Si(335) substrate in red. Both electron pockets show a higher intensity closer to the centre of the Brillouin zone, but the electron pocket of the Si(557) data is sharper. Interestingly, the intensity profile of the electron pocket for the narrow nanowires on Si(335) is rather well described by a convolution of the intensity profile of the wide nanowires on Si(557) with a Gaussian profile that uses the average width of the narrow nanowires Δx for determining Δk as full width at half maximum [blue graph in figure 8.19 (a)]. Such a correspondence agrees well with the assumption of a broadening based on Heisenberg's uncertainty principle and that the wide nanowires reproduce the electronic structure of the extended $TbSi_2$ monolayer on Si(111). However, such a correspondence is not always observed as the analysis of non-horizontal electron pockets in figure 8.19 (b) shows. There the convolution of the intensity profile

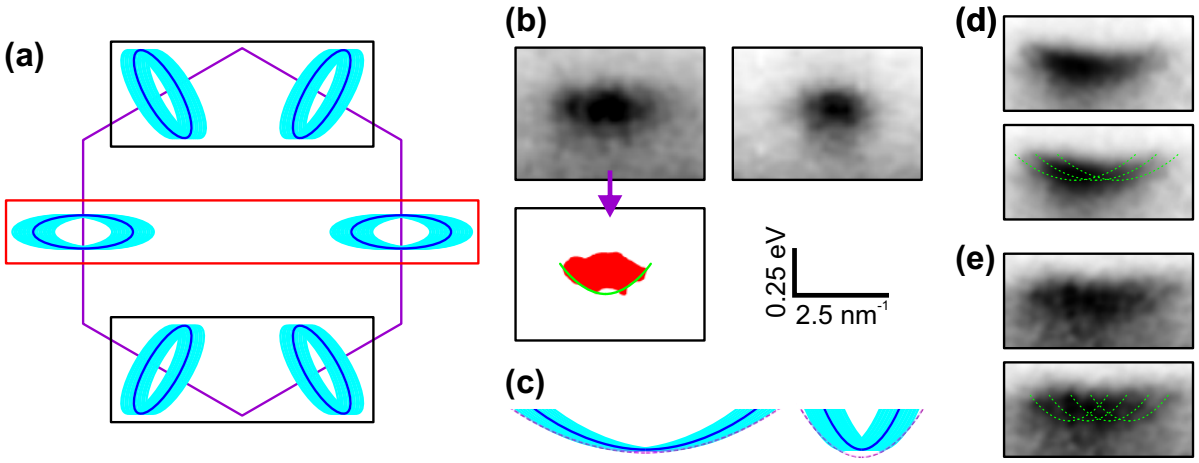

Figure 8.18.: (a) Schematic of the broadening of the elliptical appearance of the electron pockets on the Fermi surface for narrow nanowires and stripes. The original Fermi contour is shown in dark blue while the broadening is illustrated in light blue. After the broadening, the two horizontal ellipses, marked by the red rectangle, differ from the non-horizontal ellipses, marked by black boxes. (b) Dispersion plots of a non-horizontal electron pocket of the ARPES data on narrow nanowires on Si(335) shown in figure 8.15. On the left, the original dispersion data along the long axis are shown (upper image) and as a two-tone image with fit parabola (lower image), while the original dispersion data along the short ellipse axis are illustrated on the right. (c) Schematic of a broadened parabola illustrating that the difference between the fit (hatched purple line) of the broadened band structure (light blue) and the original dispersion (dark blue line) is larger for lower effective masses, i.e. for narrower parabolas. (d and e) Dispersion plots of parabolas that appear to consist of multiple parabolas. The upper images show the original data and the lower images the same images with parabolas overlaid. The plots in (d and e) are parts of the ARPES data already shown in figures 8.14 and 8.16, respectively. The scales given in (b) are also applicable to (d and e).

of the wide nanowires on Si(557) with the same Gaussian profile as above leads to an overestimation of the electron pocket width for the narrow nanowires on Si(335).

In the following, the broadened dispersions of the electron pockets are analysed quantitatively. Such an analysis is possible in a rather straight forward way for wide nanowires by fitting parabolas to the dispersing bands in the direction along the long and short ellipse axes. For the ARPES data shown in figure 8.14, one obtains on average effective masses of about 0.74 m_0 for the long axis and about 0.13 m_0 for the short axis. These values are in good agreement with the effective masses for the $TbSi_2$ monolayer on Si(111) derived here, which are about 0.94 m_0 for the long axis and 0.15 m_0 for the short axis.

The analysis is more complex for the ARPES data of narrow nanowires and stripes. Most electron pockets do not show distinguishable bands in dispersion plots, but appear blurred [see upper two images in figure 8.18 (b)]. It is not possible to derive the original effective mass of the band due to the blurring, but one may extract apparent effective masses. This is illustrated in the two images on the left in figure 8.18 (b). An arbitrary intensity threshold

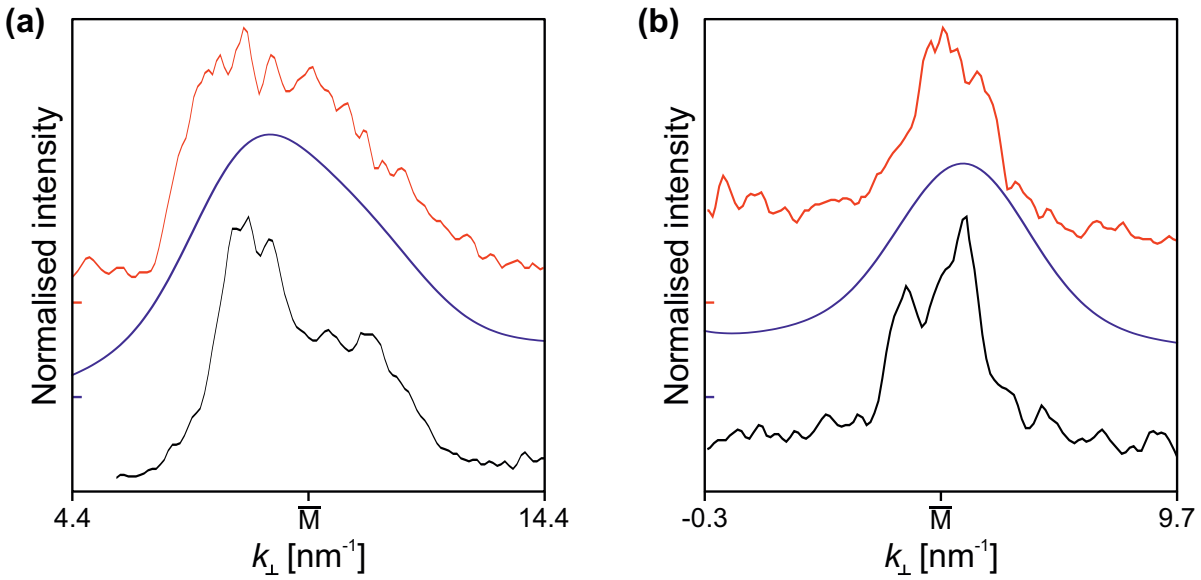

Figure 8.19.: Intensity profiles taken in the direction perpendicular to the nanowires on the Fermi surfaces, which are shown in figures 8.14 (c) and 8.15 (c). The most intense (a) horizontal and (b) non-horizontal electron pockets of the ARPES data using the Si(557) (black graphs) and using the Si(335) (red graphs) are cut. The blue graphs are convolutions of the graphs obtained for the Si(557) data with a Gaussian profile that has a full width at half maximum of 2.5 nm^{-1}, which corresponds to a by STM determined average width of the nanowires of 2.5 nm for a preparation similar to the one used for the Si(335) ARPES data.

is chosen and the original dispersion plot is depicted as a two-tone image with every data point shown in the first or the second colour if the corresponding intensity value is below or above the threshold, respectively. The lower contour of the electron pocket is fitted to a parabola, from which the apparent effective mass is derived. This apparent effective mass is in general larger than the effective mass of the original dispersion since it is influenced by the broadening [see figure 8.18 (c)].

Due to the dominant broadening perpendicular to the nanostructures, mainly the long axes of the horizontal electron pockets and the short axes of the non-horizontal electron pockets are influenced by the broadening [see figure 8.18 (a)]. This should lead to considerable differences when the apparent effective masses of the horizontal electron pockets are compared to the ones of the non-horizontal electron pockets. Since the influence of the broadening is stronger for lower original effective masses [see figure 8.18 (c)], we expect the largest deviations in the apparent effective masses for the short axis of the electron pockets.

A direct comparison of all derived apparent effective masses of an ARPES measurement is rather confusing, e.g. the apparent effective masses are for the ARPES measurement shown in figure 8.15: $m^*_{\mathrm{short},1} \approx 0.08\ m_0$, $m^*_{\mathrm{long},1} \approx 0.71\ m_0$, $m^*_{\mathrm{short},2} \approx 0.08\ m_0$, and $m^*_{\mathrm{long},2} \approx 0.62\ m_0$ for the horizontal electron pockets and $m^*_{\mathrm{short},3} \approx 0.15\ m_0$, $m^*_{\mathrm{long},3} \approx 0.44\ m_0$, $m^*_{\mathrm{short},4} \approx 0.20\ m_0$, and $m^*_{\mathrm{long},4} \approx 0.33\ m_0$ for the non-horizontal electron pockets with sufficient intensity for an analysis. Thus, an anisotropy factor α is defined, which is given

Table 8.1.: Overview on the derived anisotropy factors for nanowire and stripe samples. For Si(557) substrates, wide nanowires and nanowires with a medium width were prepared by deposition of more than 1 ML Tb on an already once used substrate and of a submonolayer of Tb on a new substrate, respectively. Only preparations with depositions of submonolayer amounts of Tb are included for Si(335), Si(775), and Si(553). For the preparations on Si(557) and Si(775), only a single ARPES measurement each was analysed while the average of multiple measurements is given for the $TbSi_2$ nanostructure samples using Si(335) and Si(553) substrates.

	$Si(557)_{wide}$	$Si(557)_{medium}$	Si(335)	Si(775)	Si(553)
α_{short}	0.8	0.4	0.5	0.7	0.5
α_{long}	0.9	0.8	1.6	1.0	1.3

by the ratio of the average apparent effective masses:

$$\alpha = \overline{m^*}_{horizontal} / \overline{m^*}_{non-horizontal}. \tag{8.1}$$

Anisotropy factors $\alpha > 1$ imply that the electron pockets oriented perpendicular to the step edges are stronger broadened, which is expected for the long axes while factors $\alpha < 1$ are derived for a stronger broadening of the non-horizontal electron pockets. The error of the calculated anisotropy factors is estimated to $\Delta\alpha = 0.2$, which corresponds to the maximum deviation from $\alpha = 1$ obtained for ARPES data of the two-dimensional $TbSi_2$ film on Si(111), for which no anisotropic broadening is expected. An overview on the anisotropy factors for both the long and the short axes of the electron pockets is shown in table 8.1 for the various ARPES measurements.

The anisotropy factors derived for wide nanowires on Si(557) correspond to no anisotropy within the estimated error. This agrees well with all previous observations, which showed always a nice agreement between the band structure of the two-dimensional $TbSi_2$ film on Si(111) and the one of the wide $TbSi_2$ nanowires on Si(557). In contrast, a preparation of nanowires with a medium width on a new Si(557) substrate by using a submonolayer amount of Tb leads to the observation of a $TbSi_2$ band structure with anisotropic broadening. While the anisotropy factor of 0.8 for the long axes of the electron pockets is still consistent with no anisotropy at all, the anisotropy factor of 0.4 clearly indicates that the horizontal electron pockets are narrower than the non-horizontal ones. These findings agree well with the expectation of mainly a horizontal broadening that leads to larger differences in the apparent effective masses for the short axes of the electron pockets.

For even narrower nanowires, i.e. for nanowire preparations on new Si(335) substrates using submonolayer amounts of Tb, the anisotropic broadening is not only apparent for the short axes of the electron pockets, but also for the long axes with an anisotropy factor of 1.6. This factor confirms the visual impression that the horizontal electron pockets are elongated compared to the non-horizontal ones [compare figure 8.15] (c). Nevertheless, the anisotropy is more pronounced for the short axes as expected with an anisotropy factor of 0.5. With decreasing width of the nanowires on Si(hhk) substrates with $h < k$, an anisotropy was first observed for the short axes of the electron pockets and subsequently for both axes indicating a stronger confinement for reduced nanowire width.

For the case of the stripes on Si(hhk) substrates with $h > k$, it is observed that wide $TbSi_2$ stripes on Si(775) show a small anisotropic broadening only for the short axes of the electron pockets (see table 8.1). Interestingly, the inhomogeneity of the electron pockets is visually more apparent for the long axes on the Fermi surface shown in figure 8.16 (c). In contrast, significant broadening is observed for both the short and the long axes of the electron pockets for the narrower $TbSi_2$ stripes on Si(553) although only the width differences are visually apparent on the Fermi surface shown in figure 8.2 (c) (see table 8.1).

First of all, these findings for the stripes nicely confirm the result for nanowires on Si(hhk) substrates with $h < k$ that narrower nanostructures lead to stronger confinement and stronger anisotropic broadening. This is again more apparent for the direction characterised by a lower effective mass of the electron pocket. Nevertheless, it is rather unexpected that the stripes, which have maximum widths similar to the widths of wide nanowires on Si(557), show a confinement that is similar in strength to the one observed for the much narrower nanowires. This may be related to the inhomogeneous widths of the stripes. They tend to have extended narrow regions, especially at their ends, even though their maximum widths are rather large. These narrow regions may then lead to the observed strong anisotropic broadening.

An issue that has to be considered is the rather low number of analysable ARPES measurements. This low number may play a role in the observation of an unexpectedly strong confinement for stripes. Certainly, it prevents the finding of a more precise correlation between the average nanowire width as observed in STM and the strength of anisotropic broadening. Furthermore, the assumption that the broadening is related to the confinement of the width of the nanostructures leads to a consistent explanation of the ARPES results without contradictions. However, other possible causes cannot be excluded with the present ARPES data, e.g. an apparent broadening of the electronic structure may also be the result of an electronic coupling between the nanostructures. Such a coupling would result in an additional reciprocal lattice vector based on the average distance between nanowires, possibly leading to replica of the original electronic structure. Indeed, some electron pockets appear to consist of multiple parabolas [see figures 8.18 (d and e)], but such an appearance may be related to the quality of the ARPES data. It is quite hard to imagine such a coupling between the rather well separated $TbSi_2$ nanostructures, especially between stripes (see section 8.1). However, more detailed ARPES data are required to resolve this issue.

The anisotropic broadening of the $TbSi_2$ band structure is not the only possible confinement effect found in the ARPES measurements presented here. There is also the emergence of additional bands that cannot be related to the two-dimensional electronic structure of $TbSi_2$, which is discussed in the following.

8.3.2. The quasi-one-dimensional structure

Using the preparation conditions of the narrowest observed nanowires, i.e. when depositing only submonolayer amounts of Tb on Si(335) substrates, and analysing such samples with ARPES leads to the additional observation of an electronic structure not related to the one of the two-dimensional $TbSi_2$ monolayer. This is already seen on the Fermi surface shown in figure 8.15 (c), but even more apparent in the contrast optimised version of the same ARPES data in figure 8.20 (a). Since this additional electronic structure is also characterised

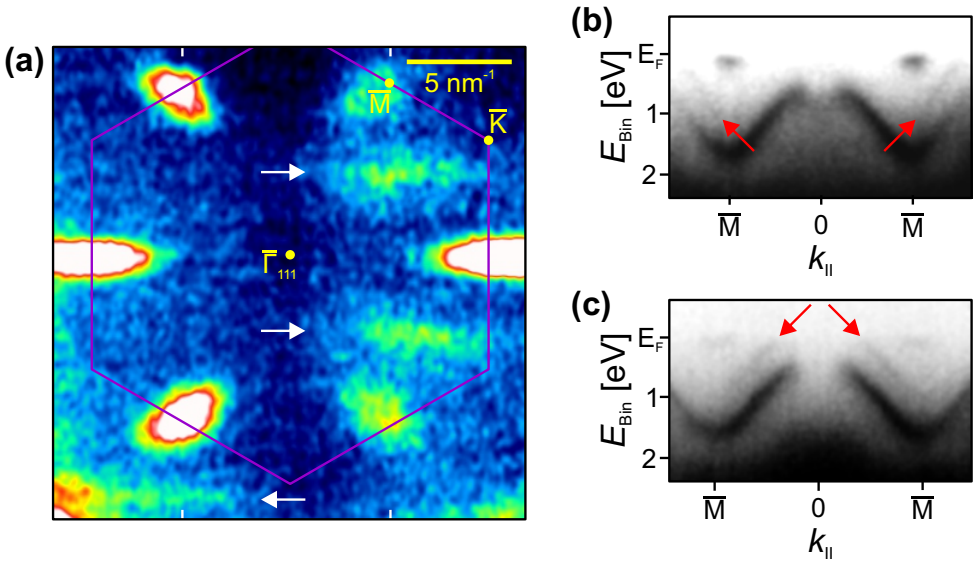

Figure 8.20.: Further features of the ARPES data that were already presented in figure 8.15. (a) Fermi surface shown with an intensity scale that highlights the additional horizontally oriented features marked by white arrows that are not caused by a two-dimensional $TbSi_2$ structure. (b and c) Dispersion plots taken between (b) the two left and (c) the two right white inner ticks in (a). The red arrows mark the additional bands of the quasi-one-dimensional electronic structure.

by an intensity at the Fermi level, it describes a further metallic nanostructure in addition to the $TbSi_2$ nanowires that show a laterally confined two-dimensional electronic structure.

The Fermi contours of the additional electronic structure, which are marked by arrows in figure 8.20 (a), are lines with a small curvature, which does not lead to a closing of the Fermi contours. Due to the surface sensitivity of the ARPES measurements, it is obvious that this electronic structure originates from a surface structure, i.e. a structure with very little height. Consequently, this electronic structure is a quasi-one-dimensional one. Since the lines on the Fermi surface run mainly horizontally, i.e. in the direction perpendicular to the step edges, the corresponding surface structure is confined in this direction and has its long axis along the step edges.

Before possibly corresponding surface structures are discussed, it should be noted that the quasi-one-dimensional structure observed by ARPES is not a measurement artefact. Although one may think it could be an artefact, e.g. due to its faintness, the quasi-one-dimensional structure is well reproducible. Similar preparations of narrow nanowires on Si(335) substrates lead to the observation of the same quasi-one-dimensional structure (see figure 8.21). Not only newly prepared Si(335) substrates were used, but the ARPES measurements were conducted during another beamtime at another beamline and the sample orientation was varied with respect to the analyser. Nevertheless, the quasi-one-dimensional structures are clearly visible on the energy surfaces at $E_{\mathrm{Bin}} = 0.2$ eV, which are shown here due to the stronger intensity of the quasi-one-dimensional bands compared to the Fermi surface. On the energy surfaces shown, these bands also appear more extended than on the Fermi surface, but unfortunately they are not well distinguishable across the complete

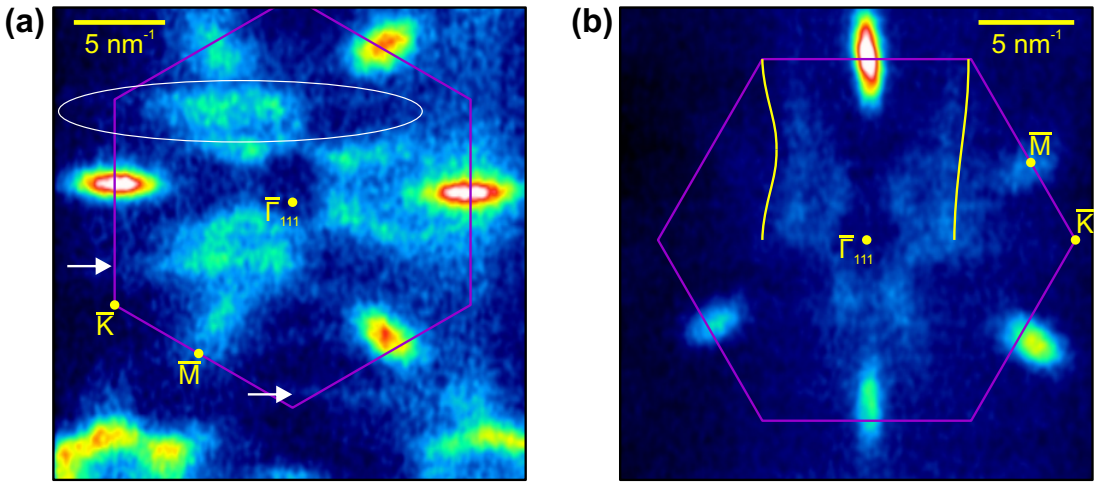

Figure 8.21.: (a) Energy surface at $E_{\mathrm{Bin}} = 0.2$ eV for a preparation of narrow nanowires by deposition of 0.85 ML Tb and annealing at 500 °C ($h\nu = 100$ eV). (b) Energy surface at $E_{\mathrm{Bin}} = 0.2$ eV of a narrow nanowire preparation by deposition of 0.60 ML Tb and annealing at 460 °C ($h\nu = 100$ eV). This measurement was conducted with an approximately 90° rotated sample compared to the data shown in (a) and in figure 8.20 (a). White coloured ellipses and arrows mark quasi-one-dimensional band contours. In (b) possible oscillations of the quasi-one-dimensional band contours are indicated in yellow.

first Brillouin zone. Thus, the periodicity of their possible oscillations is not determinable without doubt [see figure 8.21 (b)].

A surface structure fitting the expectations by the ARPES data, i.e. a metallic structure confined in the direction perpendicular to the step edges, are the $TbSi_2$ nanowires observed on the surface. While the wide and the majority of the narrow nanowires show the two-dimensional $TbSi_2$ band structure leading to its dominance in all ARPES data reported here, the narrowest nanowires may be characterised by a quasi-one-dimensional electronic structure. A debatable indication for a correlation between the $TbSi_2$ structure and the quasi-one-dimensional structure is given by the dispersion of the quasi-one-dimensional bands. Figures 8.20 (b and c) show dispersion plots parallel to the step edges taken at $k_\perp$-values corresponding to one half of the horizontal $\overline{\Gamma}_{111}$-$\overline{\mathrm{M}}$ distances. The dispersion of the quasi-one-dimensional bands is approximately parallel to the bands leading to the hole-pocket of the two-dimensional $TbSi_2$ structure. Such similarities in the electronic structure indicate similarities in the atomic structure. However, they do not prove an identical atomic structure.

Remembering the XPS data (see section 8.2.2), another structure agreeing with all above criteria comes to the mind: possible edge states of the nanowires, e.g. due to the dangling bonds of the Si atoms at the $TbSi_2$ edges. While nanowires certainly have a length and may have a width too large to lead to complete confinement to a lower dimension, a quasi-one-dimensional electronic structure may be expected for edge states. Furthermore, such edge states may have a similar, but energetically shifted dispersion as the corresponding two-dimensional structure, as is often observed for two-dimensional surface

states of three-dimensional bulk materials, e.g. in references [452, 453].

Similar to the intensity increase of the additional silicide component in Si-2p core-level spectra with decreasing width of the silicide nanostructures, which may be related to their edge atoms, edge states may become detectable when the nanostructures get sufficiently narrow. If there is such a correlation between XPS and ARPES data, the observation of such a quasi-one-dimensional electronic structure should also be possible for stripe samples on Si(553), since the intensity of the additional silicide component is also considerable for such samples (see figure 8.13). However, no indication for a quasi-one-dimensional structure is found in any of the available data for stripes on Si(553), but this may be related to a too low intensity or the meandering edges of the stripes preventing the formation of homogeneous edge states. Thus, edge states as origin for the quasi-one-dimensional electronic structure are a possibility and cannot be excluded based on the present data.

Since it is not clear if the nanolines are very narrow nanowires or not, they are discussed as an additional structure possibly responsible for the observation of the quasi-one-dimensional electronic structure in ARPES. The observation of the quasi-one-dimensional electronic structure for nanowire preparations on Si(335) and its missing in the ARPES data for samples using Si(hhk) substrates with $h > k$ agrees well with the formation of nanolines exclusively on Si(hhk) substrates with $h < k$ (see section 8.1). Using new Si(557) substrates, nanolines may be found for typical $TbSi_2$ monolayer preparations (see figure 8.3 (c)], but ARPES measurements using such samples were not successful. Due to the very similar growth of Tb silicide nanostructures on Si(hhk) substrates with $h < k$, one may expect a high surface density of nanolines on Si(557) for successive preparations using submonolayer amounts of Tb. Consequently, one may also expect the observation of the quasi-one-dimensional electronic structure for such preparations if it originates from nanolines, which was also not observed. However, such preparations clearly showed the electronic structure of two-dimensional $TbSi_2$ only once, although also well defined nanowires should form for such preparations. Thus, while there is a disagreement between the expectations based on the assumption that nanolines lead to the quasi-one-dimensional structure observed with ARPES, no definite conclusion is possible without sufficient further data, similarly as for the assumption of edge states as origin of the quasi-one-dimensional electronic structure.

While edge states and nanolines cannot be excluded without doubt and further possibilities may exist, no contradiction arises by the assumption that the narrowest nanowires lead to the observation of the quasi-one-dimensional electronic structure in ARPES. Thus, it is the most probable scenario at the moment. Assuming this and that the anisotropic broadening of the two-dimensional $TbSi_2$ structure is caused by the width confinement of the nanowires, an interesting picture about the confinement of two-dimensional $TbSi_2$ emerges. If the width of the two-dimensional $TbSi_2$ monolayer is reduced, the electronic structure will broaden. Further confinement of the $TbSi_2$ leads to a quasi-one-dimensional structure, but this structure is not characterised by the strongly broadened electronic structure of the two-dimensional $TbSi_2$, e.g. with intensity on the Fermi surface at the positions of the electron pockets. Interestingly, the quasi-one-dimensional electronic structure shows a similar, but energetically shifted dispersion as the two-dimensional $TbSi_2$ monolayer at certain $k_\perp$ [see figures 8.20 (b and c)]. Since there are no indications for a continuous crossover from the two-dimensional to the quasi-one-dimensional electronic structure, e.g. no bands dispersing in between the two- and one-dimensional ones are observed in ARPES

[see figure 8.20 (c)], there seems to be a well-defined critical width, at which the $TbSi_2$ nanowires abruptly become a quasi-one-dimensional metal.

8.4. Conclusions

The focus of this chapter were $TbSi_2$ nanostructures on vicinal Si(hhk) substrates. Previously reported results for Dy deposition on Si(557) were confirmed using Tb as rare earth metal and rather wide nanowires were grown, which are characterised by the two-dimensional electronic structure known from extended films on Si(111).

In contrast, no well-defined nanowires form on Si(hhk) substrates with $h > k$. While structures with rather low aspect ratios are observed for typical $TbSi_2$ monolayer preparation parameters, elongated nanostructures are found for submonolayer Tb coverages. These nanostructures do not show straight, but rough edges. In order to differentiate them from nanowires, they are denoted stripes. In addition to wide nanowires and stripes, also narrower nanowires were grown by using new Si(557) substrates and especially by moving from Si(557) to Si(335) substrates. The narrowest nanowires formed for submonolayer amounts of Tb on Si(335). All these structures are observed on Si(111) terraces of the vicinal substrates, but there are also nanostructures too narrow to assign them to a specific terrace orientation. These here denoted nanolines may be very narrow nanowires, but this is not certain.

Stripes and at least the majority of the nanowires are $TbSi_2$ nanostructures as proven by ARPES. This was also indicated by XPS not only by the spectral composition of the Si-2p spectra, but also by the strong shift of the Fermi level towards the conduction band minimum typical for $TbSi_2$. The Si-2p spectra also included an additional component, which is not observed for planar silicide preparations and may be related to the edges of the nanostructures. That the $TbSi_2$ structures confined to nanowires and stripes still show metallic behaviour was proven by STS for nanowires.

For both narrow nanowires and stripes, the band structure of extended $TbSi_2$ monolayers is reproduced in general. However, the band structure appears anisotropically broadened. This broadening could be quantified and is increased with decreasing width of the nanostructures. Only for preparations using submonolayer coverages of Tb and Si(335), a quasi-one-dimensional electronic structure was observed in addition to the two-dimensional one of $TbSi_2$. The corresponding surface structure is still under debate, but may be related to nanowire edges, to nanolines, or to the narrowest nanowires.

9. Summary and outlook

The main focus of this thesis was the investigation of Tb silicide nanowires, which form by self-organisation on Si substrates. Two different types of substrates were used: planar and vicinal Si(001) substrates and Si(hhk) substrates that are vicinal to Si(111). While the Tb silicide nanostructures on Si(hhk) substrates were studied using STM, STS, XPS, and ARPES, the nanowires on Si(001) substrates were investigated with even more methods thanks to collaborations within FOR1700 funded by the DFG and with the workgroup of Prof. Dr. Micheal Lehmann (TU Berlin).

It is known for 20 years that trivalent rare earth metals may induce the formation of silicide nanowires on Si(001). Thus, the formation of Tb silicide nanowires on Si(001) was expected and could be confirmed with this work. The growth of the nanowires was studied in detail. While single nanowires have widths about 2 nm, they tend to aggregate to wider structures in form of nanowire bundles. Their growth in length seems to be hindered only by other nanowires, step bunches, or a shortage of Tb supply, but not by strain. Typically, a 2×7 reconstructed wetting layer accompanies the nanowire formation and the dominance of one of the two structures can be differentiated by RAS on vicinal substrates. In addition to the nanowires and the wetting layer, islands, nanowire stumps, or small surface clusters may form. Islands are predominantly observed for large Tb coverages or high annealing temperatures while nanowire stumps are found for moderate Tb coverages and lower annealing temperatures than typically used for nanowire formation. The Tb silicide surface clusters form for even lower temperatures and very low Tb coverages. They tend to form rows, i.e. they are an interesting structure to investigate the transition from a zero-dimensional to a one-dimensional electronic structure.

In possible future devices using Tb silicide nanowires, e.g. as interconnects, the nanowires have to be embedded in a Si matrix, stimulating experiments on the overgrowth of the nanowires with Si. Deposition of amorphous Si does not appear to lead to changes of the inner nanowire structures since nanowire bundles consisting of multiple individual nanowires were well resolved in HRTEM. In contrast, more compact Tb silicide structures, which may still be as long as the nanowires before the structural change, form if an amorphous Si overlayer is annealed or Si is deposited on a heated substrate. Such procedures are necessary to embed the nanowires into crystalline Si. Not only the structure of the nanowires changes, but also the crystalline cap layer is never as homogeneous as an amorphous one. Instead, grooves above the Tb silicide structures and stacking faults are observed.

Since the structure of the nanowires remains stable during the deposition of amorphous Si, the HRTEM results can be used for an atomic structure analysis. As expected, the assumption of a hexagonal $TbSi_2$ structure is in agreement with the HRTEM data, but in contrast to previously proposed nanowire structure models, its c_{hex} axis is oriented along the nanowires and not perpendicular to them. Based on this observation, and STM and LEED data, a new structure model was proposed for the nanowires. Theoretical calculations on the

previous and the here proposed structure model are currently conducted in the workgroup of Prof. Dr. Simone Sanna (Justus-Liebig-Universität Gießen).

The metallic characteristics of the nanowires was confirmed by STS and XPS experiments, and they showed a similar band bending as known for $TbSi_2$ on Si(111) confirming the assumption of a $TbSi_2$ composition from the HRTEM data. In ARPES, the $TbSi_2$ nanowires show a quasi-one-dimensional metallic electronic structure, which is influenced by the probed nanowire ensemble and by matrix element effects. Especially, the matrix element effects are assumed to be responsible for discrepancies between previously reported band structures for rare earth silicide nanowires. Transport measurements also confirmed the metallic behaviour of the nanowires. Observations by SEM after contacting of a nanowire bundle indicate a strong electronic interaction between the individual nanowires of a bundle.

Up to now, the constitution of the nanowire ensemble probed by ARPES can only be estimated based on the used preparation parameters and the knowledge from growth investigations. Thus, the use of a combined STM-ARPES setup may allow a much better correlation between nanowire ensemble and observed electronic structure. Furthermore, low temperature studies appear promising to lead to new insights on physical phenomena unique for quasi-one-dimensional metallic systems.

In addition to the detailed analysis of the nanowires, it was also shown by STS and XPS that the wetting layer has a finite density of states at the Fermi level, but is characterised by a Fermi level closer to the centre of the Si band gap. Its atomic structure was discussed based on its strongly voltage-depended appearance in STM while the final structure determination requires theoretical calculations.

The Tb silicide nanowires on Si(001) presumably form due to an anisotropic lattice mismatch by self organisation. The concept behind the formation of nanowires on Si(hhk) substrates is different. The $TbSi_2$ monolayer forms two-dimensional films on planar Si(111). By using substrates vicinal to Si(111), this monolayer cannot grow as an unlimited film any more, but is disrupted by steps leading to narrow sections of the monolayer.

The Si(hhk) substrates with $h > k$ are fundamentally different from the ones with $h < k$. This is already observed for the clean surfaces, but also apparent in the growth of Tb silicide structures. Well defined nanowires with straight edges only form for $h < k$. In contrast for $h > k$, structures with low aspect ratios are observed for typical $TbSi_2$ monolayer preparations while stripes can be formed using submonolayer Tb coverages. These stripes show considerable aspect ratios, but have rough edges, which differentiates them from nanowires.

Both nanowires and stripes are $TbSi_2$ nanostructures as indicated by STM and XPS, e.g. by the observation of a strong shift of the Fermi level towards the Si conduction band minimum upon nanostructure formation, and finally proven by the observation of the two-dimensional $TbSi_2$ band structure in ARPES. While all general characteristics of the known $TbSi_2$ band structure are reproduced for nanowires and stripes, there are differences apparent in details for stripes and narrow nanowires. The band structure appears anisotropically broadened, which is related to the strong width confinement of the nanostructures.

Strong confinement of nanowires may also be responsible for the observation of an additional quasi-one-dimensional metallic electronic structure for preparations of the narrowest nanowires, but the corresponding surface structure is not known at the moment. Three

possibilities were discussed, narrowest $TbSi_2$ nanowires, edge states of these nanowires, which may also lead to an additional component in Si-2p core level spectra, and nanolines, which are very narrow nanostructures with unknown atomic structure. These nanolines are only observed for Si(hhk) substrates with $h < k$.

The investigations on the quasi-one-dimensional structure would also benefit from a combination of ARPES and STM in a single system, which would also help investigations on a better-defined correlation between the apparent anisotropic broadening and the width of the nanostructures. Moreover, theoretical calculations should allow to find out which nanostructures are responsible for the observed quasi-one-dimensional electronic structure. Another interesting project for the future would be an investigation of the Si overgrowth of the $TbSi_2$ films and nanowires on planar and vicinal Si(111) substrates. They may even prove more resistant to structural reorganisation during annealing due to the rather unstrained interfaces with the Si, as compared to the nanowires on Si(001).

Comparing the results of $TbSi_2$ nanowires on Si(001) and Si(hhk), some further interesting questions arise. A strong coupling between the in average about 2 nm wide nanowires in a bundle was observed for nanowires on Si(001). Even on vicinal substrates, such bundles easily reach widths of about 10 nm, but a quasi-one-dimensional and never a two-dimensional electronic structure was observed on the Fermi surface with ARPES. In contrast, confined two-dimensional electronic structures were found on Si(hhk) and only for samples with the narrowest nanowires, on average about 2.5 nm, a quasi-one-dimensional electronic structure is observed, which even may not be related to the nanowires. Thus on the hand, one may wonder if there is a strong influence of the silicide orientation with respect to the confinement directions on the dimensionality of $TbSi_2$ nanostructures leading to a quasi-one-dimensional electronic structure of nanowires on Si(001) for larger widths. On the other hand, the electronic correlations between nanowires on Si(001) may not be as strong as expected based on the combined SEM-transport experiments. Then, there may be a critical width of about 2 nm for confinement to one dimension independent on the silicide orientation and the majority of $TbSi_2$ nanowires on Si(001) are just sufficiently narrow for one-dimensional confinement.

In conclusion, the knowledge on rare earth silicide nanowires in general and on Tb silicide nanowires in particular was strongly expanded within this thesis. For instance, a 20 years old and widely accepted structure model was corrected, which was only possible by investigations with multiple methods illustrating the strength of collaborations. While the road to applications with Tb silicide nanowires may still be long, quasi-one-dimensional electronic structures were observed for both Si(001) and Si(hhk) substrates. These are especially promising for future studies, e.g., to explore the interesting world of one-dimensional physics.

Bibliography

[1] L. Boltzmann, Wien. Ber. **76**, 373 (1877).

[2] M. Planck, Ann. Phys. **309**, 553 (1901).

[3] B. J. Kim, H. Koh, E. Rotenberg, S.-J. Oh, H. Eisaki, N. Motoyama, S. Uchida, T. Tohyama, S. Maekawa, Z.-X. Shen, and C. Kim, Nat. Phys. **2**, 397 (2006).

[4] R. H. McKenzie, Nat. Phys. **3**, 756 (2007).

[5] R. Peierls, Helv. Phys. Acta **7-2**, 81 (1934).

[6] N. D. Mermin and H. Wagner, Phys. Rev. Lett. **17**, 1133 (1966).

[7] P. C. Hohenberg, Phys. Rev. **158**, 383 (1967).

[8] N. D. Mermin, Phys. Rev. **176**, 250 (1968).

[9] W. Kohn, Phys. Rev. Lett. **2**, 393 (1959).

[10] E. J. Woll and W. Kohn, Phys. Rev. **126**, 1693 (1962).

[11] R. E. Peierls, *Quantum Theory of Solids*, Oxford University Press, London 1955.

[12] S. Kagoshima, Jpn. J. Appl. Phys. **20**, 1617 (1981).

[13] T. Giamarchi, Physics **2**, 78 (2009).

[14] S. Tomonaga, Prog. Theoret. Phys. **5**, 544 (1950).

[15] J. M. Luttinger, J. Math. Phys. **4**, 1154 (1963).

[16] D. C. Mattis and E. H. Lieb, J. Math. Phys. **6**, 304 (1965).

[17] F. D. M. Haldane, J. Phys. C Solid State **14**, 2585 (1981).

[18] J. Voit, Rep. Prog. Phys. **58**, 977 (1995).

[19] J. Ferraris, D. O. Cowan, V. Walatka, and J. H. Perlstein, J. Am. Chem. Soc. **95**, 948 (1973).

[20] S. Coleman, Comm. Math. Phys. **31**, 259 (1973).

[21] A. N. Bloch, J. P. Ferraris, D. O. Cowan, and T. O. Poehler, Solid State Commun. **13**, 753 (1973).

[22] M. Dressel and C. Kuntscher, Kleine Bausteine für große Aufgaben, in *Wechsel-Wirkungen — Jahrbuch 2004*, Universität Stuttgart, 2004.

[23] T. Giamarchi, Chem. Rev. **104**, 5037 (2004).

[24] D. Jérome, Chem. Rev. **104**, 5565 (2004).

[25] H. Eisele, *The Atomic Composition of Semiconductor Quantum Dots and Related Nanostructures*, Habilitation thesis, TU Berlin, 2013.

[26] L. De Broglie, *Recherches sur la théorie des Quanta*, Phd thesis, Migration - université en cours d'affectation, 1924.

[27] S. Tarucha, T. Honda, and T. Saku, Solid State Commun. **94**, 413 (1995).

[28] M. H. Huang, S. Mao, H. Feick, H. Yan, Y. Wu, H. Kind, E. Weber, R. Russo, and P. Yang, Science **292**, 1897 (2001).

[29] Y. Tserkovnyak, B. I. Halperin, O. M. Auslaender, and A. Yacoby, Phys. Rev. Lett. **89**, 136805 (2002).

[30] L. J. Lauhon, M. S. Gudiksen, D. Wang, and C. M. Lieber, Nature **420**, 57 (2002).

[31] M. S. Gudiksen, L. J. Lauhon, J. Wang, D. C. Smith, and C. M. Lieber, Nature **415**, 617 (2002).

[32] O. M. Auslaender, H. Steinberg, A. Yacoby, Y. Tserkovnyak, B. I. Halperin, K. W. Baldwin, L. N. Pfeiffer, and K. W. West, Science **308**, 88 (2005).

[33] H. J. Fan, P. Werner, and M. Zacharias, Small **2**, 700 (2006).

[34] Y. Jompol, C. J. B. Ford, J. P. Griffiths, I. Farrer, G. A. C. Jones, D. Anderson, D. A. Ritchie, T. W. Silk, and A. J. Schofield, Science **325**, 597 (2009).

[35] X.-J. Wu, F. Zhu, C. Mu, Y. Liang, L. Xu, Q. Chen, R. Chen, and D. Xu, Coord. Chem. Rev. **254**, 1135 (2010).

[36] H. J. Joyce, Q. Gao, H. H. Tan, C. Jagadish, Y. Kim, J. Zou, L. M. Smith, H. E. Jackson, J. M. Yarrison-Rice, P. Parkinson, and M. B. Johnston, Prog. Quant. Electron. **35**, 23 (2011).

[37] J. K. Hyun, S. Zhang, and L. J. Lauhon, Annu. Rev. Mater. Res. **43**, 451 (2013).

[38] N. P. Dasgupta, J. Sun, C. Liu, S. Brittman, S. C. Andrews, J. Lim, H. Gao, R. Yan, and P. Yang, Adv. Mater. **26**, 2137 (2014).

[39] M. Bockrath, D. H. Cobden, J. Lu, A. G. Rinzler, R. E. Smalley, L. Balents, and P. L. McEuen, Nature **397**, 598 (1999).

[40] Z. Yao, H. W. Ch. Postma, L. Balents, and C. Dekker, Nature **402**, 273 (1999).

[41] S. Reich, C. Thomsen, and J. Maultzsch, *Carbon Nanotubes: Basic Concepts and Physical Principles*, Wiley-VCH, Weinheim 2004.

[42] J.-C. Charlier, X. Blase, and S. Roche, Rev. Mod. Phys. **79**, 677 (2007).

[43] S. Ilani and P. L. McEuen, Annu. Rev. Condens. Ma. P. **1**, 1 (2010).

[44] F. Wang, J. V. Alvarez, J. W. Allen, S.-K. Mo, J. He, R. Jin, D. Mandrus, and H. Höchst, Phys. Rev. Lett. **103**, 136401 (2009).

[45] T. Podlich, M. Klinke, B. Nansseu, M. Waelsch, R. Bienert, J. He, R. Jin, D. Mandrus, and R. Matzdorf, J. Phys. Condens. Matter **25**, 014008 (2013).

[46] L. Dudy, J. D. Denlinger, J. W. Allen, F. Wang, J. He, D. Hitchcock, A. Sekiyama, and S. Suga, J. Phys. Condens. Matter **25**, 014007 (2013).

[47] H. Ohnishi, Y. Kondo, and K. Takayanagi, Nature **395**, 780 (1998).

[48] A. I. Yanson, G. R. Bollinger, H. E. van den Brom, N. Agraït, and J. M. van Ruitenbeek, Nature **395**, 783 (1998).

[49] N. Agraït, A. L. Yeyati, and J. M. van Ruitenbeek, Phys. Rep. **377**, 81 (2003).

[50] H. W. Yeom, S. Takeda, E. Rotenberg, I. Matsuda, K. Horikoshi, J. Schaefer, C. M. Lee, S. D. Kevan, T. Ohta, T. Nagao, and S. Hasegawa, Phys. Rev. Lett. **82**, 4898 (1999).

[51] S. Chandola, K. Hinrichs, M. Gensch, N. Esser, S. Wippermann, W. G. Schmidt, F. Bechstedt, K. Fleischer, and J. F. McGilp, Phys. Rev. Lett. **102**, 226805 (2009).

[52] P. C. Snijders and H. H. Weitering, Rev. Mod. Phys. **82**, 307 (2010).

[53] S. Wippermann and W. G. Schmidt, Phys. Rev. Lett. **105**, 126102 (2010).

[54] J. N. Crain, A. Kirakosian, K. N. Altmann, C. Bromberger, S. C. Erwin, J. L. McChesney, J.-L. Lin, and F. J. Himpsel, Phys. Rev. Lett. **90**, 176805 (2003).

[55] J. N. Crain, J. L. McChesney, F. Zheng, M. C. Gallagher, P. C. Snijders, M. Bissen, C. Gundelach, S. C. Erwin, and F. J. Himpsel, Phys. Rev. B **69**, 125401 (2004).

[56] T. Lichtenstein, C. Tegenkamp, and H. Pfnür, J. Phys. Condens. Matter **28**, 354001 (2016).

[57] C. Blumenstein, J. Schäfer, S. Mietke, S. Meyer, A. Dollinger, M. Lochner, X. Y. Cui, L. Patthey, R. Matzdorf, and R. Claessen, Nat. Phys. **7**, 776 (2011).

[58] S. Meyer, J. Schäfer, C. Blumenstein, P. Höpfner, A. Bostwick, J. L. McChesney, E. Rotenberg, and R. Claessen, Phys. Rev. B **83**, 121411 (2011).

[59] N. de Jong, R. Heimbuch, S. Eliëns, S. Smit, E. Frantzeskakis, J.-S. Caux, H. J. W. Zandvliet, and M. S. Golden, Phys. Rev. B **93**, 235444 (2016).

[60] F. Hötzel, K. Seino, S. Chandola, E. Speiser, N. Esser, F. Bechstedt, and A. Pucci, J. Phys. Chem. Lett. **6**, 3615 (2015).

[61] R. Baptist, S. Ferrer, G. Grenet, and H. C. Poon, Phys. Rev. Lett. **64**, 311 (1990).

[62] P. Paki, U. Kafader, P. Wetzel, C. Pirri, J. C. Peruchetti, D. Bolmont, and G. Gewinner, Phys. Rev. B **45**, 8490 (1992).

[63] F. P. Netzer, J. Phys. Condens. Matter **7**, 991 (1995).

[64] I. Manke, H. J. Wen, A. Höhr, A. Bauer, M. Dähne-Prietsch, and G. Kaindl, J. Vac. Sci. Technol. B **13**, 1657 (1995).

[65] S. Vandré, T. Kalka, C. Preinesberger, I. Manke, H. Eisele, M. Dähne-Prietsch, R. Meier, E. Weschke, and G. Kaindl, Appl. Surf. Sci. **123-124**, 100 (1998).

[66] M. Dähne, S. Vandré, C. Preinesberger, S. Becker, W. Busse, and T. Kalka, Lanthanide-Silicide Films on Silicon Surfaces, in *Advances in Solid State Physics*, edited by Bernhard Kramer, Springer, Berlin Heidelberg 2001.

[67] C. Rogero, C. Koitzsch, M. E. González, P. Aebi, J. Cerdá, and J. A. Martín-Gago, Phys. Rev. B **69**, 045312 (2004).

[68] E. W. Perkins, I. M. Scott, and S. P. Tear, Surf. Sci. **578**, 80 (2005).

[69] M. Franz, S. Appelfeller, C. Prohl, J. Große, H.-F. Jirschik, V. Füllert, C. Hassenstein, Z. Diemer, and M. Dähne, J. Vac. Sci. Technol. A **34**, 061503 (2016).

[70] S. Vandré, T. Kalka, C. Preinesberger, and M. Dähne-Prietsch, Phys. Rev. Lett. **82**, 1927 (1999).

[71] S. Vandré, T. Kalka, C. Preinesberger, and M. Dähne-Prietsch, J. Vac. Sci. Technol. B **17**, 1682 (1999).

[72] Z. He, D. J. Smith, and P. A. Bennett, Appl. Phys. Lett. **86**, 143110 (2005).

[73] M. Wanke, K. Löser, G. Pruskil, and M. Dähne, Phys. Rev. B **79**, 155428 (2009).

[74] M. Wanke, M. Franz, M. Vetterlein, G. Pruskil, C. Prohl, B. Höpfner, P. Stojanov, E. Huwald, J. D. Riley, and M. Dähne, J. Appl. Phys. **108**, 064304 (2010).

[75] M. Dähne and M. Wanke, J. Phys. Condens. Matter **25**, 014012 (2013).

[76] C. Preinesberger, S. Vandré, T. Kalka, and M. Dähne-Prietsch, J. Phys. D Appl. Phys. **31**, L43 (1998).

[77] Y. Chen, D. A. A. Ohlberg, G. Medeiros-Ribeiro, Y. A. Chang, and R. S. Williams, Appl. Phys. Lett. **76**, 4004 (2000).

[78] Y. Chen, D. A. A. Ohlberg, and R. S. Williams, J. Appl. Phys. **91**, 3213 (2002).

[79] Y. Cui and J. Nogami, Surf. Sci. **605**, 2038 (2011).

[80] C. Zeng, P. R. C. Kent, T.-H. Kim, A.-P. Li, and H. H. Weitering, Nat. Mater. **7**, 539 (2008).

[81] J. Nogami, B. Z. Liu, M. V. Katkov, C. Ohbuchi, and N. O. Birge, Phys. Rev. B **63**, 233305 (2001).

[82] C. Ohbuchi and J. Nogami, Phys. Rev. B **66**, 165323 (2002).

[83] S. Qin, T.-H. Kim, Y. Zhang, W. Ouyang, H. H. Weitering, C.-K. Shih, A. P. Baddorf, R. Wu, and A.-P. Li, Nano Lett. **12**, 938 (2012).

[84] H. W. Yeom, Y. K. Kim, E. Y. Lee, K.-D. Ryang, and P. G. Kang, Phys. Rev. Lett. **95**, 205504 (2005).

[85] M. Wanke, K. Löser, G. Pruskil, D. V. Vyalikh, S. L. Molodtsov, S. Danzenbächer, C. Laubschat, and Mario Dähne, Phys. Rev. B **83**, 205417 (2011).

[86] G. Binnig and H. Rohrer, Rev. Mod. Phys. **59**, 615 (1987).

[87] G. Binnig, H. Rohrer, C. Gerber, and E. Weibel, Appl. Phys. Lett. **40**, 178 (1982).

[88] G. Binnig, H. Rohrer, C. Gerber, and E. Weibel, Phys. Rev. Lett. **49**, 57 (1982).

[89] R. E. Schlier and H. E. Farnsworth, J. Chem. Phys. **30**, 917 (1959).

[90] G. Binnig, H. Rohrer, C. Gerber, and E. Weibel, Phys. Rev. Lett. **50**, 120 (1983).

[91] K. Takayanagi, Y. Tanishiro, M. Takahashi, and S. Takahashi, J. Vac. Sci. Technol. A **3**, 1502 (1985).

[92] K. Takayanagi, Y. Tanishiro, S. Takahashi, and M. Takahashi, Surf. Sci. **164**, 367 (1985).

[93] T. Frängsmyr and G. Ekspong, editors, *Nobel Lectures, Physics 1981-1990*, World Scientific Publishing Co., Singapore 1993.

[94] J. Bardeen, Phys. Rev. Lett. **6**, 57 (1961).

[95] J. Tersoff and D. R. Hamann, Phys. Rev. Lett. **50**, 1998 (1983).

[96] J. Tersoff and D. R. Hamann, Phys. Rev. B **31**, 805 (1985).

[97] C. J. Chen, J. Vac. Sci. Technol. A **6**, 319 (1988).

[98] C. J. Chen, Phys. Rev. Lett. **65**, 448 (1990).

[99] C. J. Chen, Phys. Rev. B **42**, 8841 (1990).

[100] C. J. Chen, J. Vac. Sci. Technol. A **9**, 44 (1991).

[101] W. Sacks and C. Noguera, Phys. Rev. B **43**, 11612 (1991).

[102] W. Sacks and C. Noguera, J. Vac. Sci. Technol. B **9**, 488 (1991).

[103] W. Sacks and C. Noguera, Ultramicroscopy **42-44**, 140 (1992).

[104] W. Sacks, Phys. Rev. B **61**, 7656 (2000).

[105] R. Wiesendanger, *Scanning Probe Microscopy and Spectroscopy*, Cambridge University Press, Cambridge 1994.

[106] C. J. Chen, *Introduction to Scanning Tunneling Microscopy*, Oxford University Press, 2nd edition, New York 2008.

[107] C. J. Chen, *Introduction to Scanning Tunneling Microscopy*, Oxford University Press, New York 1993.

[108] R. M. Feenstra, J. A. Stroscio, and A. P. Fein, Surf. Sci. **181**, 295 (1987).

[109] R. M. Feenstra, J. A. Stroscio, J. Tersoff, and A. P. Fein, Phys. Rev. Lett. **58**, 1192 (1987).

[110] H. Haberland, *Clusters of Atoms and Molecules*, Springer Verlag, Berlin 1994.

[111] J. A. Stroscio, R. M. Feenstra, and A. P. Fein, Phys. Rev. Lett. **57**, 2579 (1986).

[112] N. D. Lang, Phys. Rev. B **34**, 5947 (1986).

[113] M. Prietsch, A. Samsavar, and R. Ludeke, Phys. Rev. B **43**, 11850 (1991).

[114] C. Hellenthal, R. Heimbuch, E. S. Sotthewes, K.and Kooij, and H. J. W. Zandvliet, Phys. Rev. B **88**, 035425 (2013).

[115] H. Hertz, Ann. Phys. **267**, 983 (1887).

[116] W. Hallwachs, Ann. Phys. **269**, 301 (1888).

[117] P. Lenard, Ann. Phys. **307**, 359 (1900).

[118] P. Lenard, Ann. Phys. **313**, 149 (1902).

[119] A. Einstein, Ann. Phys. **322**, 132 (1905).

[120] R. A. Millikan, Phys. Rev. **7**, 355 (1916).

[121] Y. Zhou, *Nobel Lectures, Physics 1901-1921*, Elsevier Publishing Company, Amsterdam 1967.

[122] C. G. Santesson, editor, *Les Prix Nobel en 1921-1922*, Nobel Foundation, Stockholm 1923.

[123] Y. Zhou, *Nobel Lectures, Physics 1922-1941*, Elsevier Publishing Company, Amsterdam 1965.

[124] J. G. Jenkin, R. C. G. Leckey, and J. Liesegang, J. Electron Spectrosc. **12**, 1 (1977).

[125] J. G. Jenkin, J. D. Riley, J. Liesegang, and R. C. G. Leckey, J. Electron Spectrosc. **14**, 477 (1978).

[126] S. D. Kevan, editor, *Angle-resolved photoemission: Theory and Current Applications*, Elsevier Science Publishers B.V., Amsterdam 1992.

[127] C. Nordling, E. Sokolowski, and K. Siegbahn, Phys. Rev. **105**, 1676 (1957).

[128] E. Sokolowski, C. Nordling, and K. Siegbahn, Phys. Rev. **110**, 776 (1958).

[129] U. Gelius, E. Basilier, S. Svensson, T. Bergmark, and K. Siegbahn, J. Electron Spectrosc. **2**, 405 (1973).

[130] C. N. Berglund and W. E. Spicer, Phys. Rev. **136**, A1044 (1964).

[131] N. V. Smith, M. M. Traum, and F. J. Di Salvo, Solid State Commun. **15**, 211 (1974).

[132] P. M. Echenique, R. Berndt, E. V. Chulkov, T. Fauster, A. Goldmann, and U. Höfer, Surf. Sci. Rep. **52**, 219 (2004).

[133] C. S. Fadley, J. Electron Spectrosc. **178-179**, 2 (2010).

[134] G. Schönhense, K. Medjanik, and H.-J. Elmers, J. Electron Spectrosc. **200**, 94 (2015).

[135] S. Hüfner, *Photoelectron Spectroscopy*, Springer, 2nd edition, Berlin 1996.

[136] C. N. Berglund and W. E. Spicer, Phys. Rev. **136**, A1030 (1964).

[137] G. D. Mahan, Phys. Rev. B **2**, 4334 (1970).

[138] G. Hollinger, Photoelectron Spectroscopies: Probes of Chemical Bonding and Electronic Properties at Semiconductor Interfaces, in *Semiconductor Interfaces: Formation and Properties*, edited by G. LeLay, J. Derrien, and N. Boccara, Springer-Verlag, Berlin Heidelberg 1987.

[139] M. P. Seah and W. A. Dench, Surf. Interface Anal. **1**, 2 (1979).

[140] D. R. Penn, Phys. Rev. B **13**, 5248 (1976).

[141] C. J. Powell, J. Electron Spectrosc. **47**, 197 (1988).

[142] S. Tanuma, C. J. Powell, and D. R. Penn, Surf. Interface Anal. **21**, 165 (1994).

[143] M. P. Seah, Surf. Interface Anal. **44**, 497 (2012).

[144] H. Shinotsuka, S. Tanuma, C. J. Powell, and D. R. Penn, Surf. Interface Anal. **47**, 871 (2015).

[145] T.-W. Pi, I.-H. Hong, C.-P. Cheng, and G. K. Wertheim, J. Electron Spectrosc.. **107**, 163 (2000).

[146] I. Campillo, J. M. Pitarke, A. Rubio, E. Zarate, and P. M. Echenique, Phys. Rev. Lett. **83**, 2230 (1999).

[147] S. Moser, J. Electron Spectrosc. **214**, 29 (2017).

[148] G. D. Mahan, *Many Particle Physics*, Kluwer Academic- Plenum Publishers, 3rd edition, New York 2000.

[149] J. W. Negele and H. Orland, *Quantum Many-particle Systems*, Westview Press, 2008.

[150] S. D. Kevan and E. Rotenberg, J. Electron Spectrosc. **117-118**, 57 (2001).

[151] A. Damascelli, Phys. Scr. **T109**, 61 (2004).

[152] G. Ertl and J. Küppers, *Low energy electrons and surface chemistry*, VCH, 2nd edition, Weihnheim 1985.

[153] C. J. Davisson and L. H. Germer, Nature **119**, 558 (1927).

[154] C. Davisson and L. H. Germer, Phys. Rev. **30**, 705 (1927).

[155] G. P. Thomson and A. Ried, Nature **119**, 890 (1927).

[156] G. P. Thomson, Nature **120**, 802 (1927).

[157] G. P. Thomson, P. Roy. Soc. A Math. Phys. **117**, 600 (1928).

[158] L. J. Clarke, *Surface crystallography: an introduction to low energy electron diffraction*, John Wiley & Sons Ltd, 1985.

[159] A. Kahn, Surf. Sci. Rep. **3**, 193 (1983).

[160] M. Henzler, Applications of Surface Science **11**, 450 (1982).

[161] W. Friedrich, P. Knipping, and M. Laue, Ann. Phys. **346**, 971 (1913).

[162] P. P. Ewald, Acta Crystallogr. A **25**, 103 (1969).

[163] E. A. Wood, J. Appl. Phys. **35**, 1306 (1964).

[164] M. A. Van Hove, W.-H. Weinberg, and C.-M. Chan, *Low-Energy Electron Diffraction*, Springer, Berlin 1986.

[165] E. Abbe, Arch. mikrosk. Anat. **9**, 413 (1873).

[166] Lord Rayleigh Sec. R. S., Philos. Mag. (Series 5) **42**, 167 (1896).

[167] M. Knoll and E. Ruska, Z. Phys. **78**, 318 (1932).

[168] E. Ruska, Z. Phys. **87**, 580 (1934).

[169] D. B. Williams and C. B. Carter, *Transmission Electron Microscopy Part 1: Basics*, Springer, New York 2009.

[170] D. McMullan, Scanning **17**, 175 (1995).

[171] *Scanning Electron Microscope A to Z*, Jeol Ltd., Tokyo 2009.

[172] T. E. Everhart and R. F. M. Thornley, J. Sci. Instrum. **37**, 246 (1960).

[173] W. C. H. Kuo, M. Briceno, and D. Ozkaya, Platin. Met. Rev. **58**, 106 (2014).

[174] B. J. Griffin, Scanning **33**, 162 (2011).

[175] J. Baringhaus, *Mesoscopic transport phenomena in epitaxial graphene nanostructures: A surface science approach*, Phd thesis, Gottfried Wilhelm Leibniz Universität Hannover, 2015.

[176] M. von Ardenne, Z. Phys. **109**, 553 (1938).

[177] P. D. Nellist, The Principles of STEM imaging, in *Scanning Transmission Electron Microscopy*, Springer, New York 2010.

[178] E. Rutherford J. R. S., Philos. Mag. (series 6) **21**, 669 (1911).

[179] W. H. Bragg and W. L. Bragg, P. Roy. Soc. A Math. Phys. **88**, 428 (1913).

[180] M. J. Casanove, N. Combe, F. Houdellier, and M. J. Hÿtch, Europhys. Lett. **91**, 36001 (2010).

[181] D. E. Aspnes and A. A. Studna, Phys. Rev. Lett. **54**, 1956 (1985).

[182] V. L. Berkovits, I. V. Makarenko, T. A. Minashvili, and V. I. Safarov, Solid State Commun. **56**, 449 (1985).

[183] A. Lastras-Martínez, J. Ortega-Gallegos, L. E. Guevara-Macías, O. Nuñez-Olvera, R. E. Balderas-Navarro, L. F. Lastras-Martínez, L. A. Lastras-Montaño, and M. A. Lastras-Montaño, J. Cryst. Growth **425**, 21 (2015).

[184] S. Nannarone, P. Chiaradia, F. Ciccacci, R. Memeo, P. Sassaroli, S. Selci, and G. Chiarotti, Solid State Commun. **33**, 593 (1980).

[185] W. Richter and J. F. McGilp, Philos. Trans. Roy. Soc. A Math. Phys. **344**, 453 (1993).

[186] *http://www.tcd.ie/Physics/research/facilities/oal/facilities/RAS.php*, retrieved 22 May 2017.

[187] A. Fresnel, Memoires de l'Academie des sciences **11**, 393 (1823).

[188] P. Weightman, D. S. Martin, R. J. Cole, and T. Farrell, Rep. Prog. Phys. **68**, 1251 (2005).

[189] R. C. Jones, J. Opt. Soc. Am. **31**, 488 (1941).

[190] G. Onida, W. G. Schmidt, O. Pulci, M. Palummo, A. Marini, C. Hogan, and R. Del Sole, Phys. Status Solidi A **188**, 1233 (2001).

[191] C. Hogan, N. McAlinden, and J. F. McGilp, Phys. Status Solidi B **249**, 1095 (2012).

[192] J. F. McGilp, Prog. Surf. Sci. **49**, 1 (1995).

[193] R. A. Serway, *Principles of physics*, Saunders College Pub., 2nd edition, London 1998.

[194] P. Hofmann and J. W. Wells, J. Phys. Condens. Matter **21**, 013003 (2009).

[195] M. Prietsch, Phys. Rep. **253**, 163 (1995).

[196] I. Miccoli, F. Edler, H. Pfnür, and C. Tegenkamp, J. Phys. Condens. Matter **27**, 223201 (2015).

[197] F. Wenner, Bulletin of the Bureau of Standards **12**, 469 (1916).

[198] P. Jaschinsky, *Kombinierte Rasterelektronen- und Mehr-Spitzen-Rastertunnelmikroskopie als Methode zur Ladungstransportmessung im Nanometerbereich*, Phd thesis, RWTH Aachen, 2007.

[199] P. Jaschinsky, J. Wensorra, M. I. Lepsa, J. Mysliveček, and B. Voigtländer, J. Appl. Phys. **104**, 094307 (2008).

[200] S. Yoshimoto, Y. Murata, K. Kubo, K. Tomita, K. Motoyoshi, T. Kimura, H. Okino, R. Hobara, I. Matsuda, S. Honda, M. Katayama, and S. Hasegawa, Nano Lett. **7**, 956 (2007).

[201] S. Korte, M. Steidl, W. Prost, V. Cherepanov, B. Voigtländer, W. Zhao, P. Kleinschmidt, and T. Hannappel, Appl. Phys. Lett. **103**, 143104 (2013).

[202] H. Marom, J. Mullin, and M. Eizenberg, Phys. Rev. B **74**, 045411 (2006).

[203] L. Sheng, D. Y. Xing, and Z. D. Wang, Phys. Rev. B **51**, 7325 (1995).

[204] S. Chatterjee and A. E. Meyerovich, Phys. Rev. B **81**, 245409 (2010).

[205] F. H. Nielsen and H. H. Sandstead, Am. J. Clin. Nutr. **27**, 515 (1974).

[206] J. Dabrowski and H.-J. Müssig, *Silicon Surfaces and Formation of Interfaces*, World Scientific Publishing Company, Singapur 2000.

[207] H. Ibach and H. Lüth, *Festkörperphysik*, Springer Verlag, 3rd edition, Berlin 1993.

[208] P. J. Mohr, B. N. Taylor, and D. B. Newell, Rev. Mod. Phys. **80**, 633 (2008).

[209] C. Kittel, *Einführung in die Festkörperphysik*, Oldenbourg Wissenschaftsverlag, 14th edition, München 2006.

[210] J. A. Stroscio and W. J. Kaiser, editors, *Scanning tunneling microscopy*, Academic Press, Inc., San Diego 1993.

[211] J. Dabrowski and M. Scheffler, Appl. Surf. Sci. **56-58**, 15 (1992).

[212] D. J. Chadi, Phys. Rev. Lett. **43**, 43 (1979).

[213] R. J. Hamers, R. M. Tromp, and J. E. Demuth, Surf. Sci. **181**, 346 (1987).

[214] K. Hata, Y. Shibata, and H. Shigekawa, Phys. Rev. B **64**, 235310 (2001).

[215] S. Vandré, *Growth and electronic structure of lanthanide silicides on Si(111) and Si(001)*, Wissenschaft und Technik Verlag, Berlin 2000.

[216] F. J. Himpsel, B. S. Meyerson, F. R. McFeely, J. F. Morar, A. Taleb-Ibrahimi, and J. A. Yarmoff, Core Level Spectroscopy at Silicon Surfaces and Interfaces, in *Proceedings of the International School of Physics "Enrico Fermi" CVIII - Photoemission and Absorption Spectroscopy of Solids and Interfaces with Synchrotron Radiation*, edited by M. Campagna and R. Rosei, Elsevier Science Publishers B.V., Amsterdam 1990.

[217] C. Kentsch, M. Kutschera, M. Weinelt, T. Fauster, and M. Rohlfing, Phys. Rev. B **65**, 035323 (2001).

[218] C. Preinesberger, *Rastertunnelmikroskopie an Lathanidsiliziden auf Si(001)*, Diploma thesis, TU Berlin, 1998.

[219] K. Hata, S. Yasuda, and H. Shigekawa, Phys. Rev. B **60**, 8164 (1999).

[220] X. R. Qin and M. G. Lagally, Phys. Rev. B **59**, 7293 (1999).

[221] K. Nagaoka, M. J. Comstock, A. Hammack, and M. F. Crommie, Phys. Rev. B **71**, 121304 (2005).

[222] K. Hata, S. Yoshida, and H. Shigekawa, Phys. Rev. Lett. **89**, 286104 (2002).

[223] D. Riedel, M. Lastapis, M. G. Martin, and G. Dujardin, Phys. Rev. B **69**, 121301 (2004).

[224] D. J. Chadi, Phys. Rev. Lett. **59**, 1691 (1987).

[225] L. S. O. Johansson, R. I. G. Uhrberg, P. Mårtensson, and G. V. Hansson, Phys. Rev. B **42**, 1305 (1990).

[226] J. Pollmann, R. Kalla, P. Krüger, A. Mazur, and G. Wolfgarten, Appl. Phys. A **41**, 21 (1986).

[227] J. Pollmann, P. Krüger, and A. Mazur, J. Vac. Sci. Technol. B **5**, 945 (1987).

[228] P. E. J. Eriksson and R. I. G. Uhrberg, Phys. Rev. B **81**, 125443 (2010).

[229] E. Landemark, C. J. Karlsson, Y.-C. Chao, and R. I. G. Uhrberg, Phys. Rev. Lett. **69**, 1588 (1992).

[230] H. Koh, J. W. Kim, W. H. Choi, and H. W. Yeom, Phys. Rev. B **67**, 073306 (2003).

[231] J. J. Lander, G. W. Gobeli, and J. Morrison, J. Appl. Phys. **34**, 2298 (1963).

[232] K. C. Pandey, Phys. Rev. Lett. **47**, 1913 (1981).

[233] R. M. Feenstra, W. A. Thompson, and A. P. Fein, J. Vac. Sci. Technol. A **4**, 1315 (1986).

[234] R. M. Feenstra and M. A. Lutz, Phys. Rev. B **42**, 5391 (1990).

[235] K. D. Brommer, M. Needels, B. Larson, and J. D. Joannopoulos, Phys. Rev. Lett. **68**, 1355 (1992).

[236] I. Štich, M. C. Payne, R. D. King-Smith, J-S. Lin, and L. J. Clarke, Phys. Rev. Lett. **68**, 1351 (1992).

[237] D. Vanderbilt, Phys. Rev. B **36**, 6209 (1987).

[238] J. L. Mercer and M. Y. Chou, Phys. Rev. B **48**, 5374 (1993).

[239] F. Bechstedt, A. A. Stekolnikov, J. Furthmüller, and P. Käckell, Phys. Rev. Lett. **87**, 016103 (2001).

[240] J. J. Lander, Surf. Sci. **1**, 125 (1964).

[241] P. A. Bennett and M. W. Webb, Surf. Sci. **104**, 74 (1981).

[242] R. S. Becker, J. A. Golovchenko, G. S. Higashi, and B. S. Swartzentruber, Phys. Rev. Lett. **57**, 1020 (1986).

[243] Y.-N. Yang and E. D. Williams, Phys. Rev. Lett. **72**, 1862 (1994).

[244] M. A. Kulakov, Surf. Sci. **372**, L266 (1997).

[245] J. Ortega, F. Flores, and A. L. Yeyati, Phys. Rev. B **58**, 4584 (1998).

[246] J. Ortega, A. L. Yeyati, and F. Flores, Appl. Surf. Sci. **123-124**, 131 (1998).

[247] J. E. Demuth, B. N. J. Persson, and A. J. Schell-Sorokin, Phys. Rev. Lett. **51**, 2214 (1983).

[248] R. I. G. Uhrberg, G. V. Hansson, U. O. Karlsson, J. M. Nicholls, P. E. S. Persson, S. A. Flodström, R. Engelhardt, and E.-E. Koch, Phys. Rev. B **31**, 3795 (1985).

[249] R. I. G. Uhrberg, G. V. Hansson, J. M. Nicholls, P. E. S. Persson, and S. A. Flodström, Phys. Rev. B **31**, 3805 (1985).

[250] R. J. Hamers, R. M. Tromp, and J. E. Demuth, Phys. Rev. Lett. **56**, 1972 (1986).

[251] R. Losio, K. N. Altmann, and F. J. Himpsel, Phys. Rev. B **61**, 10845 (2000).

[252] I. Barke, F. Zheng, A. R. Konicek, R. C. Hatch, and F. J. Himpsel, Phys. Rev. Lett. **96**, 216801 (2006).

[253] J. Mysliveček, A. Stróżecka, J. Steffl, P. Sobotík, I. Ošt'ádal, and B. Voigtländer, Phys. Rev. B **73**, 161302 (2006).

[254] R. Schillinger, C. Bromberger, H. J. Jänsch, H. Kleine, O. Kühlert, C. Weindel, and D. Fick, Phys. Rev. B **72**, 115314 (2005).

[255] M. D'angelo, K. Takase, N. Miyata, T. Hirahara, S. Hasegawa, A. Nishide, M. Ogawa, and I. Matsuda, Phys. Rev. B **79**, 035318 (2009).

[256] R. I. G. Uhrberg, T. Kaurila, and Y.-C. Chao, Phys. Rev. B **58**, R1730 (1998).

[257] C. J. Karlsson, E. Landemark, Y.-C. Chao, and R. I. G. Uhrberg, Phys. Rev. B **50**, 5767 (1994).

[258] G. Le Lay, M. Göthelid, T. M. Grehk, M. Björkquist, U. O. Karlsson, and V. Yu. Aristov, Phys. Rev. B **50**, 14277 (1994).

[259] J. J. Paggel, W. Theis, K. Horn, C. Jung, C. Hellwig, and H. Petersen, Phys. Rev. B **50**, 18686 (1994).

[260] M. T. Cuberes, A. Bauer, H. J. Wen, D. Vandré, M. Prietsch, and G. Kaindl, J. Vac. Sci. Technol. B **12**, 2422 (1994).

[261] A. A. Baski, S. C. Erwin, and L. J. Whitman, Surf. Sci. **392**, 69 (1997).

[262] A. Kirakosian, R. Bennewitz, J. N. Crain, T. Fauster, J.-L. Lin, D. Y. Petrovykh, and F. J. Himpsel, Appl. Phys. Lett. **79**, 1608 (2001).

[263] A. N. Chaika, D. A. Fokin, S. I. Bozhko, A. M. Ionov, F. Debontridder, T. Cren, and D. Roditchev, Surf. Sci. **603**, 752 (2009).

[264] L. J. Pedri, L. Toppozini, and M. C. Gallagher, Surf. Sci. **601**, 924 (2007).

[265] M. Kopciuszyński, P. Dyniec, R. Zdyb, and M. Jałochowski, Phys. Rev. B **91**, 235420 (2015).

[266] S. Hara, M. Yoshimura, and K. Ueda, Jpn. J. Appl. Phys. **47**, 6102 (2008).

[267] N. G. Connelly, T. Damhus, R. M. Hartshorn, and A. T. Hutton, editors, *Nomenclature of Inorganic Chemistry IUPAC recommendations 2005*, RSC Publishing, Cambridge 2005.

[268] G. B. Haxel, J. B. Hedrick, and G. J. Orris, *Rare Earth Elements—Critical Resources for High Technology*, U.S. Geological Survey, Reston 2002.

[269] F. Artizzu, F. Quochi, A. Serpe, E. Sessini, and P. Deplano, Inorg. Chem. Front. **2**, 213 (2015).

[270] T. G. Goonan, *Rare Earth Elements—End Use and Recyclability*, U.S. Geological Survey, Reston 2011.

[271] B. S. Van Gosen, P. L. Verplanck, K. R. Long, J. Gambogi, and R. R. Seal II., *The Rare-Earth Elements—Vital to Modern Technologies and Lifestyles*, U.S. Geological Survey, Reston 2014.

[272] G. Löffler, Phys. J. **16**, 51 (2017).

[273] M. V. Bulanova, A. N. Mikolenko, K. A. Meleshevich, G. Effenberg, and P. A. Saltykov, Z. Metallkd. **90**, 216 (1999).

[274] C. Eames, M. I. J. Probert, and S. P. Tear, Appl. Phys. Lett. **96**, 241903 (2010).

[275] K. Holtgrewe, *Dichtefunktionaltheorie von Substrat-stabilisierten Seltenerdsilizidnanodrähten*, Master thesis, Universität Paderborn, 2016.

[276] F. H. Kaatz, W. R. Graham, J. Van der Spiegel, W. Joss, and J. A. Chroboczek, J. Vac. Sci. Technol. A **9**, 426 (1991).

[277] S. Labroo and N. Ali, J. Appl. Phys. **67**, 4811 (1990).

[278] R. L. Schwoebel and E. J. Shipsey, J. Appl. Phys. **37**, 3682 (1966).

[279] G. Ehrlich and F. G. Hudda, J. Chem. Phys. **44**, 1039 (1966).

[280] B. Voigtländer, Surf. Sci. Rep. **43**, 127 (2001).

[281] T. Young, Philos. Trans. Roy. Soc. **95**, 65 (1805).

[282] E. Bauer, Z. Krist. Cryst. Mater. **110**, 372 (1958).

[283] E. Bauer, Z. Krist. Cryst. Mater. **110**, 395 (1958).

[284] F. C. Frank and J. H. van der Merwe, P. Roy. Soc. A Math. Phys. **198**, 205 (1949).

[285] F. C. Frank and J. H. van der Merwe, P. Roy. Soc. A Math. Phys. **198**, 216 (1949).

[286] F. C. Frank and J. H. van der Merwe, P. Roy. Soc. A Math. Phys. **200**, 125 (1949).

[287] M. Volmer and A. Weber, Z. phys. Chem. **119**, 277 (1926).

[288] I. N. Stranski and L. Krastanow, Sitzungsber. Akad. Wiss. Wien Abt. IIb **146**, 797 (1937).

[289] L. Goldstein, F. Glas, J. Y. Marzin, M. N. Charasse, and G. Le Roux, Appl. Phys. Lett. **47**, 1099 (1985).

[290] D. Bimberg, M. Grundmann, and N. N. Ledentsov, *Quantum Dot Heterostructures*, John Wiley & Sons, Chichester (1999).

[291] F. Braun, Ann. Phys. **229**, 556 (1875).

[292] F. Bloch, Z. Phys. **52**, 555 (1929).

[293] W. Mönch, *Electronic Properties of Semiconductor Interfaces*, Springer, Berlin 2004.

[294] F. Flores, Schottky Barrier and Band Line-up in Semiconductors, in *Semiconductor Interfaces: Formation and Properties*, edited by G. LeLay, J. Derrien, and N. Boccara, Springer, Berlin Heidelberg 1987.

[295] P. Debye and E. Hückel, Phys. Z. **24**, 185 (1923).

[296] V. Heine, Phys. Rev. **138**, A1689 (1965).

[297] J. Bardeen, Phys. Rev. **71**, 717 (1947).

[298] W. Mönch, J. Appl. Phys. **111**, 073706 (2012).

[299] R. T. Tung, Appl. Phys. Rev. **1**, 011304 (2014).

[300] W. Schottky, Naturwissenschaften **26**, 843 (1938).

[301] W. Schottky, Z. Phys. **113**, 367 (1939).

[302] S. M. Sze, *Physics of Semiconductors*, John Wiley & Sons, New York 1981.

[303] G. Brauer and H. Haag, Z. anorg. allg. Chem. **267**, 198 (1952).

[304] J. E. Baglin, F. M. d'Heurle, and C. S Petersson, Appl. Phys. Lett. **36**, 594 (1980).

[305] J. E. E. Baglin, F. M. d'Heurle, and C. S. Petersson, J. Appl. Phys. **52**, 2841 (1981).

[306] J. A. Knapp and S. T. Picraux, Appl. Phys. Lett. **48**, 466 (1986).

[307] R. Anderson, J. Baglin, J. Dempsey, W. Hammer, F. d'Heurle, and S. Petersson, Appl. Phys. Lett. **35**, 285 (1979).

[308] F. M. d'Heurle, J. Mater. Res. **3**, 167 (1988).

[309] K. N. Tu, R. D. Thompson, and B. Y. Tsaur, Appl. Phys. Lett. **38**, 626 (1981).

[310] H. Norde, J. de Sousa Pires, F. d'Heurle, F. Pesavento, S. Petersson, and P. A. Tove, Appl. Phys. Lett. **38**, 865 (1981).

[311] T. Kalka, C. Preinesberger, S. Vandré, and M. Dähne-Prietsch, Appl. Phys. A **66**, 1073 (1998).

[312] C. Preinesberger, S. K. Becker, S. Vandré, T. Kalka, and M. Dähne, J. Appl. Phys. **91**, 1695 (2002).

[313] Y. Chen, D. A. A. Ohlberg, G. Medeiros-Ribeiro, Y. A. Chang, and R. S. Williams, Appl. Phys. A **75**, 353 (2002).

[314] Q. Cai, J. Yang, Y. Fu, Y. Wang, and X. Wang, Appl. Surf. Sci. **190**, 157 (2002).

[315] D. Lee and S. Kim, Appl. Phys. Lett. **82**, 2619 (2003).

[316] B. Z. Liu and J. Nogami, J. Appl. Phys. **93**, 593 (2003).

[317] B. Z. Liu and J. Nogami, Nanotechnology **14**, 873 (2003).

[318] Q. Cai and W. Zhou, J. Phys. Condens. Matter **16**, 6835 (2004).

[319] C. Preinesberger, G. Pruskil, S. K. Becker, M. Dähne, D. V. Vyalikh, S. L. Molodtsov, C. Laubschat, and F. Schiller, Appl. Phys. Lett. **87**, 083107 (2005).

[320] B. C. Harrison and J. J. Boland, Surf. Sci. **594**, 93 (2005).

[321] W. Zhou, S. Wang, T. Ji, Y. Zhu, Q. Cai, and X. Hou, Jpn. J. Appl. Phys. **45**, 2059 (2006).

[322] W. Zhou, Y. Zhu, T. Ji, X. Hou, and Q. Cai, Nanotechnology **17**, 852 (2006).

[323] O. Kubo, Y. Shingaya, M. Aono, and T. Nakayama, Appl. Phys. Lett. **88**, 233117 (2006).

[324] T. Kobayashi, Phys. Rev. B **75**, 125401 (2007).

[325] V. Iancu, P. R. C. Kent, C. G. Zeng, and H. H. Weitering, Appl. Phys. Lett. **95**, 123107 (2009).

[326] C. Nisoli, D. Abraham, T. Lookman, and A. Saxena, Phys. Rev. Lett. **102**, 245504 (2009).

[327] A. Shinde, R. Wu, and R. Ragan, Surf. Sci. **604**, 1481 (2010).

[328] E. P. Rugeramigabo, C. Tegenkamp, H. Pfnür, T. Inaoka, and T. Nagao, Phys. Rev. B **81**, 165407 (2010).

[329] Y. Cui, J. Chung, and J. Nogami, J. Phys. Condens. Matter **24**, 045003 (2012).

[330] V. Iancu, P. R. C. Kent, S. Hus, H. Hu, C. G. Zeng, and H. H. Weitering, J. Phys. Condens. Matter **25**, 014011 (2013).

[331] C. Preinesberger, S. K. Becker, and M. Dähne, AIP Conf. Proc. **696**, 837 (2003).

[332] B. Z. Liu and J. Nogami, Surf. Sci. **488**, 399 (2001).

[333] B. Z. Liu and J. Nogami, Surf. Sci. **540**, 136 (2003).

[334] A. Shinde, J. Cao, W. Ouyang, R. Wu, and R. Ragan, Phys. Lett. A **373**, 3459 (2009).

[335] M. Kuzmin, P. Laukkanen, R. E. Perälä, R.-L. Vaara, and I. J. Väyrynen, Appl. Surf. Sci. **222**, 394 (2004).

[336] A. L. Allred, J. Inorg. Nucl. Chem. **17**, 215 (1961).

[337] E. J. Little Jr. and M. M. Jones, J. Chem. Educ. **37**, 231 (1960).

[338] G. Rossi, Surf. Sci. Rep. **7**, 1 (1987).

[339] F. A. d'Avitaya, A. Perio, J.-C. Oberlin, Y. Campidelli, and J. A. Chroboczek, Appl. Phys. Lett. **54**, 2198 (1989).

[340] J.-Y. Veuillen, S. Kennou, and T. A. Nguyen Tan, Solid State Commun. **79**, 795 (1991).

[341] P. Wetzel, L. Haderbache, C. Pirri, J. C. Peruchetti, D. Bolmont, and G. Gewinner, Phys. Rev. B **43**, 6620 (1991).

[342] F. H. Kaatz, J. Van der Spiegel, and W. R. Graham, J. Appl. Phys. **69**, 514 (1991).

[343] L. Stauffer, C. Pirri, P. Wetzel, A. Mharchi, P. Paki, D. Bolmont, G. Gewinner, and C. Minot, Phys. Rev. B **46**, 13201 (1992).

[344] O. Sakho, F. Sirotti, M. DeSantis, M. Sacchi, and G. Rossi, Appl. Surf. Sci. **56**, 568 (1992).

[345] D. B. B. Lollman, T. A. Nguyen Tan, J.-Y. Veuillen, P. Muret, K. Lefki, M. Brunel, and J. C. Dupuy, Appl. Surf. Sci. **65**, 704 (1993).

[346] G. Allan, I. Lefebvre, and N. E. Christensen, Phys. Rev. B **48**, 8572 (1993).

[347] P. Wetzel, S. Saintenoy, C. Pirri, D. Bolmont, and G. Gewinner, Phys. Rev. B **50**, 10886 (1994).

[348] L. Stauffer, A. Mharchi, S. Saintenoy, C. Pirri, P. Wetzel, D. Bolmont, and G. Gewinner, Phys. Rev. B **52**, 11932 (1995).

[349] T. P. Roge, F. Palmino, C. Savall, J. C. Labrune, P. Wetzel, C. Pirri, and G. Gewinner, Phys. Rev. B **51**, 10998 (1995).

[350] M. Lohmeier, W. J. Huisman, E. Vlieg, A. Nishiyama, C. L. Nicklin, and T. S. Turner, Surf. Sci. **345**, 247 (1996).

[351] C. H. Luo, G. H. Shen, and L. J. Chen, Appl. Surf. Sci. **113-114**, 457 (1997).

[352] R. Gunnella, J. Y. Veuillen, T. A. Nguyen Tan, and A. M. Flank, Phys. Rev. B **57**, 4154 (1998).

[353] C. Rogero, J. A. Martín-Gago, and J. I. Cerdá, Phys. Rev. B **74**, 121404 (2006).

[354] F. Timmer, R. Oelke, C. Dues, S. Sanna, W. G. Schmidt, M. Franz, S. Appelfeller, M. Dähne, and J. Wollschläger, Phys. Rev. B **94**, 205431 (2016).

[355] T. P. Roge, F. Palmino, C. Savall, J. C. Labrune, S. Saintenoy, P. Wetzel, C. Pirri, D. Bolmont, and G. Gewinner, Surf. Sci. **352**, 622 (1996).

[356] P. Wetzel, S. Saintenoy, C. Pirri, D. Bolmont, G. Gewinner, T. P. Roge, F. Palmino, C. Savall, and J. C. Labrune, Surf. Sci. **355**, 13 (1996).

[357] I. Manke, T. Kalka, H. J. Wen, M. Dähne-Prietsch, and G. Kaindl, Growth and electronic structure of epitaxial interfaces of Dy and Er silicides with Si(111), in *Proceedings of the 23th Int. Conf. on the Physics of Semiconductors*, edited by M. Scheffler and R. Zimmermann, World Scientific, Singapore 1996.

[358] J. A. Martín-Gago, J. M. Gómez-Rodríguez, and J. Y. Veuillen, Surf. Sci. **366**, 491 (1996).

[359] J. A. Martín-Gago, J. M. Gómez-Rodríguez, and J. Y. Veuillen, Phys. Rev. B **55**, 5136 (1997).

[360] M. Wanke, M. Franz, M. Vetterlein, G. Pruskil, B. Höpfner, C. Prohl, I. Engelhardt, P. Stojanov, E. Huwald, J. D. Riley, and M. Dähne, Surf. Sci. **603**, 2808 (2009).

[361] M. Franz, J. Große, R. Kohlhaas, and M. Dähne, Surf. Sci. **637-638**, 149 (2015).

[362] S. Sanna, C. Dues, W. G. Schmidt, F. Timmer, J. Wollschläger, M. Franz, S. Appelfeller, and M. Dähne, Phys. Rev. B **93**, 195407 (2016).

[363] A. Imai, H. Kakuta, K. Mawatari, A. Harasawa, N. Ueno, T. Okuda, and K. Sakamoto, Appl. Surf. Sci. **256**, 1156 (2009).

[364] P. Wetzel, C. Pirri, P. Paki, J. C. Peruchetti, D. Bolmont, and G. Gewinner, Solid State Commun. **82**, 235 (1992).

[365] L. Stauffer, A. Mharchi, C. Pirri, P. Wetzel, D. Bolmont, G. Gewinner, and C. Minot, Phys. Rev. B **47**, 10555 (1993).

[366] P. Wetzel, C. Pirri, P. Paki, D. Bolmont, and G. Gewinner, Phys. Rev. B **47**, 3677 (1993).

[367] M. H. Tuilier, P. Wetzel, C. Pirri, D. Bolmont, and G. Gewinner, Phys. Rev. B **50**, 2333 (1994).

[368] D. J. Spence, S. P. Tear, T. C. Q. Noakes, and P. Bailey, Phys. Rev. B **61**, 5707 (2000).

[369] S. Vandré, C. Preinesberger, W. Busse, and M. Dähne, Appl. Phys. Lett. **78**, 2012 (2001).

[370] I. Brihuega, P. Mallet, L. Magaud, S. Pons, O. Custance, J. M. Gómez-Rodríguez, and J.-Y. Veuillen, Phys. Rev. B **69**, 155407 (2004).

[371] C. Koitzsch, M. Bovet, M. G. Garnier, P. Aebi, C. Rogero, and J. A. Martín-Gago, Surf. Sci. **566**, 1047 (2004).

[372] C. Bonet, I. M. Scott, D. J. Spence, T. J. Wood, T. C. Q. Noakes, P. Bailey, and S. P. Tear, Phys. Rev. B **72**, 165407 (2005).

[373] I. Brihuega, E. Dupont-Ferrier, P. Mallet, L. Magaud, S. Pons, J. M. Gómez-Rodríguez, and J.-Y. Veuillen, Phys. Rev. B **72**, 205309 (2005).

[374] E. Dupont-Ferrier, P. Mallet, L. Magaud, and J.-Y. Veuillen, Phys. Rev. B **75**, 205315 (2007).

[375] E. P. Rugeramigabo, T. Nagao, and H. Pfnür, Phys. Rev. B **78**, 155402 (2008).

[376] M. Lohmeier, W. J. Huisman, G. ter Horst, P. M. Zagwijn, E. Vlieg, C. L. Nicklin, and T. S. Turner, Phys. Rev. B **54**, 2004 (1996).

[377] P. Wetzel, C. Pirri, G. Gewinner, S. Pelletier, P. Roge, F. Palmino, and J. C. Labrune, Phys. Rev. B **56**, 9819 (1997).

[378] I. Engelhardt, C. Preinesberger, S. K. Becker, H. Eisele, and M. Dähne, Surf. Sci. **600**, 755 (2006).

[379] T. P. Roge, F. Palmino, C. Savall, J. C. Labrune, and C. Pirri, Surf. Sci. **383**, 350 (1997).

[380] M. Franz, S. Appelfeller, M. Rychetsky, and M. Dähne, Surf. Sci. **609**, 215 (2013).

[381] A. Kirakosian, J. L. McChesney, R. Bennewitz, J. N. Crain, J.-L. Lin, and F. J. Himpsel, Surf. Sci. **498**, L109 (2002).

[382] A. A. Saranin, A. V. Zotov, I. V. Pisarenko, V. G. Lifshits, M. Katayama, and K. Oura, Jpn. J. Appl. Phys. **43**, 1110 (2004).

[383] C. Battaglia, H. Cercellier, C. Monney, M. G. Garnier, and P. Aebi, Europhys. Lett. **77**, 36003 (2007).

[384] M. Franz, *Atomic structure and electronic properties of self-assembled clusters on silicon surfaces*, phdthesis, TU Berlin, 2015.

[385] J. L. McChesney, A. Kirakosian, R. Bennewitz, J. N. Crain, J.-L. Lin, and F. J. Himpsel, Nanotechnology **13**, 545 (2002).

[386] C. Tegenkamp, J. Phys. Condens. Matter **21**, 013002 (2009).

[387] H. Lüth, *Surfaces and Interfaces of Solid Materials*, Springer Verlag, 3rd edition, Berlin 1997.

[388] F. Genz, *Atomar auflösende off-axis-Elektronenholographie mit zwei Biprismen*, Phd thesis, TU Berlin, 2014.

[389] A. Ishizaka and Y. Shiraki, J. Electrochem. Soc. **133**, 666 (1986).

[390] A. V. Latyshev, A. L. Aseev, A. B. Krasilnikov, and S. I. Stenin, Surf. Sci. **213**, 157 (1989).

[391] Y. Homma, R. J. Mcclelland, and H. Hibino, Jpn. J. Appl. Phys. **29**, L2254 (1990).

[392] Y.-N. Yang, E. S. Fu, and E. D. Williams, Surf. Sci. **356**, 101 (1996).

[393] N. M. Ravindra, B. Sopori, O. H. Gokce, S. X. Cheng, A. Shenoy, L. Jin, S. Abedrabbo, W. Chen, and Y. Zhang, Int. J. Thermophys. **22**, 1593 (2001).

[394] H. B. Elswijk, Anal. Chim. Acta **283**, 35 (1993).

[395] K. Hata, T. Kimura, S. Ozawa, and H. Shigekawa, J. Vac. Sci. Technol. A **18**, 1933 (2000).

[396] A. N. Chaika, D. A. Fokin, S. I. Bozhko, A. M. Ionov, F. Debontridder, V. Dubost, T. Cren, and D. Roditchev, J. Appl. Phys. **105**, 034304 (2009).

[397] *Technical Reference Manual: DCA Instruments High Temperature Effusion Cell 2000 °C Series (Model DCA EC 2000-6-35-21)*, DCA Instruments Oy, 2011.

[398] J. P. Ibe, P. P. Bey Jr., S. L. Brandow, R. A. Brizzolara, N. A. Burnham, D. P. DiLella, K. P. Lee, C. R. K. Marrian, and R. J. Colton, J. Vac. Sci. Technol. A **8**, 3570 (1990).

[399] A. J. Melmed, J. Vac. Sci. Technol. B **9**, 601 (1991).

[400] I. Horcas, R. Fernández, J. M. Gómez-Rodríguez, J. Colchero, J. Gómez-Herrero, and A. M. Baro, Rev. Sci. Instrum. **78**, 013705 (2007).

[401] J. Schwinger, Phys. Rev. **75**, 1912 (1949).

[402] M. Richter and G. Ulm, PTB-Mitteilungen **124**, 3 (2014).

[403] D. Attwood, *Soft X-Rays and Extreme Ultraviolet Radiation: Principles and Applications*, Cambridge University Press, Cambridge 1999.

[404] J. Falta and T. Möller, *Forschung mit Synchrotronstrahlung*, Vieweg+Teubner, Wiesbaden 2010.

[405] *http://www.helmholtz-berlin.de/*, retrieved 02 September 2017.

[406] S. Sasaki, K. Miyata, and T. Takada, Jpn. J. Appl. Phys. **31**, L1794 (1992).

[407] K. J. S. Sawhney, F. Senf, M. Scheer, F. Schäfers, J. Bahrdt, A. Gaupp, and W. Gudat, Nucl. Instrum. Meth. A **390**, 395 (1997).

[408] S. Böttcher, *Adsorption und Funktionalisierung von Graphen auf Metalloberflächen*, Phd thesis, Freie Universität Berlin, 2014.

[409] *PHOIBOS Hermispherical energy analyser - User manual*, Specs, 1999.

[410] *https://arpes.stanford.edu/research/beamline-facilities/ssrl-beamline-5-4*, retrieved 13 September 2017.

[411] Electron tube division, *MCP assembly – Technical information*, Hamamatsu Photonics K. K., 2006.

[412] D. A. Shirley, Phys. Rev. B **5**, 4709 (1972).

[413] S. Tougaard, Surf. Interface Anal. **11**, 453 (1988).

[414] S. Doniach and M. Šunjić, J. Phys. C Solid State **3**, 285 (1970).

[415] F. Timmer, J. Bahlmann, and J. Wollschläger, J. Phys. Condens. Matter **29**, 435304 (2017).

[416] I. Miccoli, F. Edler, H. Pfnür, S. Appelfeller, M. Dähne, K. Holtgrewe, S. Sanna, W. G. Schmidt, and C. Tegenkamp, Phys. Rev. B **93**, 125412 (2016).

[417] F. Edler, I. Miccoli, H. Pfnür, and C. Tegenkamp, private communication, 2014.

[418] H. J. W. Zandvliet, H. K. Louwsma, P. E. Hegeman, and B. Poelsema, Phys. Rev. Lett. **75**, 3890 (1995).

[419] S. Chandola, E. Speiser, N. Esser, S. Appelfeller, M. Franz, and M. Dähne, Appl. Surf. Sci. **399**, 648 (2017).

[420] Y. Borensztein, N. Witkowski, and S. Royer, Phys. Status Solidi C **0**, 2966 (2003).

[421] Y. Borensztein and N. Witkowski, J. Phys. Condens. Matter **16**, S4301 (2004).

[422] N. Witkowski, R. Coustel, O. Pluchery, and Y. Borensztein, Surf. Sci. **600**, 5142 (2006).

[423] L. Kipp, D. K. Biegelsen, J. E. Northrup, L.-E. Swartz, and R. D. Bringans, Phys. Rev. Lett. **76**, 2810 (1996).

[424] S. G. Jaloviar, J.-L. Lin, F. Liu, V. Zielasek, L. McCaughan, and M. G. Lagally, Phys. Rev. Lett. **82**, 791 (1999).

[425] W. G. Schmidt, F. Bechstedt, and J. Bernholc, Phys. Rev. B **63**, 045322 (2001).

[426] K. Hingerl, R. E. Balderas-Navarro, A. Bonanni, P. Tichopadek, and W. G. Schmidt, Appl. Surf. Sci. **175-176**, 769 (2001).

[427] R. Shioda and J. van der Weide, Phys. Rev. B **57**, R6823 (1998).

[428] K. Fleischer, S. Chandola, N. Esser, W. Richter, and J. F. McGilp, Phys. Status Solidi A **188**, 1411 (2001).

[429] A. Pratt, C. Woffinden, C. Bonet, and S. Tear, Phys. Rev. B **78**, 155430 (2008).

[430] T. A. Nguyen Tan, J.-Y. Veuillen, S. Kennou, and L. Magaud, Appl. Surf. Sci. **70**, 520 (1993).

[431] M. Kubicki, *Überwachsen von Silizidnanodrähten*, Bachelor thesis, TU Berlin, 2012.

[432] Z. He, D. J. Smith, and P. A. Bennett, Phys. Rev. B **70**, 241402 (2004).

[433] G. Ye, J. Nogami, and M. A. Crimp, Thin Solid Films **497**, 48 (2006).

[434] G. Ye, M. A. Crimp, and J. Nogami, J. Appl. Phys. **105**, 104304 (2009).

[435] T. Niermann and M. A. Schubert, private communication, 2015.

[436] Y. Tu, J. Tersoff, G. Grinstein, and D. Vanderbilt, Phys. Rev. Lett. **81**, 4899 (1998).

[437] H. Eisele, O. Flebbe, T. Kalka, and M. Dähne-Prietsch, Surf. Interface Anal. **27**, 537 (1999).

[438] J. Márquez, L. Geelhaar, and K. Jacobi, Appl. Phys. Lett. **78**, 2309 (2001).

[439] H. Eisele and K. Jacobi, Appl. Phys. Lett. **90**, 129902 (2007).

[440] R. M. Feenstra, Physica B **273**, 796 (1999).

[441] M. Kuzmin, M. P. J. Punkkinen, P. Laukkanen, R. E. Perälä, M. Ahola-Tuomi, T. Balasubramanian, and I. J. Väyrynen, Phys. Rev. B **78**, 045318 (2008).

[442] R. J. Hamers, J. Vac. Sci. Technol. B **6**, 1462 (1988).

[443] S. R. Schofield, P. Studer, C. F. Hirjibehedin, N. J. Curson, G. Aeppli, and D. R. Bowler, Nat. Commun. **4**, 1649 (2013).

[444] A. C. Thompson, editor, *X-Ray Data Booklet*, U.S. Governement Printing Office, Lawrence Berkeley National Laboratory, 3rd edition, Berkeley 2009.

[445] M. Cardona and L. Ley, editors, *Photoemission in Solids I: General Principles*, Springer, Berlin 1978.

[446] S. Kennou, J.-Y. Veuillen, and T. A. Nguyen Tan, Appl. Surf. Sci. **56**, 520 (1992).

[447] R. Losio, K. N. Altmann, and F. J. Himpsel, Phys. Rev. Lett. **85**, 808 (2000).

[448] Kris Holtgrewe and Simone Sanna, private communication, 2018.

[449] J.Q. Song, T. Ding, J. Li, and Q. Cai, Surf. Sci. **604**, 361 (2010).

[450] J. Q. Song, T. Ding, and Q. Cai, Appl. Phys. Lett. **96**, 203113 (2010).

[451] W. Heisenberg, Z. Phys. **43**, 172 (1927).

[452] S. D. Kevan, Phys. Rev. Lett. **50**, 526 (1983).

[453] S. D. Kevan and R. H. Gaylord, Phys. Rev. B **36**, 5809 (1987).

List of publications

Parts of this work have been published:

Tb silicide nanowire growth on planar and vicinal Si(001) surfaces
S. Appelfeller, S. Kuls, and M. Dähne, Surf. Sci. **641**, 180 (2015).

The electronic structure of Tb silicide nanowires on Si(001)
S. Appelfeller, M. Franz, H.-F. Jirschik, J. Große, and M. Dähne, New J. Phys. **18**, 113005 (2016).

Capping of rare earth silicide nanowires on Si(001)
S. Appelfeller, M. Franz, M. Kubicki, P. Reiß, T. Niermann, M. A. Schubert, M. Lehmann, and M. Dähne, Appl. Phys. Lett. **108**, 013109 (2016).

Atomic size effects studied by transport in single silicide nanowires
I. Miccoli, F. Edler, H. Pfnür, S. Appelfeller, M. Dähne, K. Holtgrewe, S. Sanna, W. G. Schmidt, and C. Tegenkamp, Phys. Rev. B **93**, 125412 (2016).

Optical anisotropy of quasi-1D rare-earth silicide nanostructures on Si(001)
S. Chandola, E. Speiser, N. Esser, S. Appelfeller, M. Franz, and M. Dähne, Appl Surf. Sci. **399**, 648 (2017).

Publications in preparation:

Structure and one-dimensional metallicity of rare earth silicide nanowires on Si(001)
J. Heggemann, S. Appelfeller, T. Niermann, M. Lehmann, and M. Dähne, submitted to New J. Phys.

Structure and one-dimensional metallicity of rare earth silicide nanowires on Si(001)
K. Holtgrewe, W. G. Schmidt, S. Appelfeller, M. Franz, M. Dähne, and S. Sanna, in preparation.

Electronic structure of non-polar GaN($10\bar{1}0$)
M. Franz, S. Appelfeller, H. Eisele, P. Ebert, and M. Dähne, in preparation.

Further publications:

Antimony induced cluster formation on the Si(111)7×7 surface
S. Appelfeller, M. Franz, and M. Dähne, Surf. Sci. **608**, 109 (2013).

Formation and atomic structure of self-assembled Dy silicide clusters on the Si(111)7×7 surface
M. Franz, S. Appelfeller, M. Rychetsky, and M. Dähne, Surf. Sci. **609**, 215 (2013).

Growth and electronic properties of Tb silicide layers on Si(111)
M. Franz, S. Appelfeller, C. Prohl, J. Große, H.-F. Jirschik, V. Füllert, C. Hassenstein, Z. Diemer, and M. Dähne, J. Vac. Sci. Technol. A **34**, 061503 (2016).

Rare-earth silicide thin films on the Si(111) surface
S. Sanna, C. Dues, W. G. Schmidt, F. Timmer, J. Wollschläger, M. Franz, S. Appelfeller, and M. Dähne, Phys. Rev. B **93**, 195407 (2016).

Strain-induced quasi-one-dimensional rare-earth silicide structures on Si(111)
F. Timmer, R. Oelke, C. Dues, S. Sanna, W. G. Schmidt, M. Franz, S. Appelfeller, M. Dähne, and J. Wollschläger, Phys. Rev. B **94**, 205431 (2016).

Instruction of students

Student theses, which were performed under my guidance:

Rastertunnelspektroskopie an $DySi_2$-Nanodrähten auf Si(001),
K. Irmer, Bachelor thesis, Technische Universität Berlin, 2012.
Guidance in cooperation with Dr. Martin Franz

Untersuchung von Terbiumsilizid-Nanodrähten auf der Si(001)-Oberfläche,
S. Kuls, Bachelor thesis, Technische Universität Berlin, 2013.

TEM-Querschnittsuntersuchungen an überwachsenen Seltenerd-Silizid-Nanodrähten,
P. Reiß, Bachelor thesis, Technische Universität Berlin, 2014.
Guidance in cooperation with Dr. Tore Niermann

Wachstum von Silizid-Nanodrähten auf vizinalen Si(111)-Oberflächen,
C. Hassenstein, Bachelor thesis, Technische Universität Berlin, 2015.

Terbiumsilizid-Nanostrukturen auf den Si(553)- und Si(775)-Oberflächen,
L. Freter, Bachelor thesis, Technische Universität Berlin, 2016.
Guidance in cooperation with Dr. Martin Franz

Untersuchung der elektronischen Eigenschaften von Seltenerdsilizid-Nanodrähten,
H.-F. Jirschik, Master thesis, Technische Universität Berlin, 2017.

HRTEM-Strukturuntersuchungen an überwachsenen Seltenerd-Silizid-Nanodrähten,
J. Heggemann, Master thesis, Technische Universität Berlin, 2017.
Guidance in cooperation with Dr. Tore Niermann

Wachstum von Übergangsmetall-Silizid-Nanostrukturen auf Siliziumoberflächen,
L. Freter, Master thesis, Technische Universität Berlin, 2018.
Guidance in cooperation with Dr. Martin Franz

Wachstum organischer Moleküle auf der Au/Su(553)-Oberfläche,
G. Hweidi, Bachelor thesis, in preparation.
Guidance in cooperation with Dr. Martin Franz

Acknowledgments

Finally, I would like to thank all the people, without who this thesis would not have been possible.

First of all, I want to thank Prof. Dr. Mario Dähne for providing me with the opportunity to work in his work group and for supervising my thesis. I am grateful for your support, the helpful discussions, and your infectious enthusiasm for physics. Of course, also thank you for proofreading this thesis.

I would like to thank Prof. Dr. Joachim Wollschläger for refereeing this thesis, the interest he showed in my work throughout the years, and the fruitful cooperation. I am especially grateful for the invitation to participate in a beamtime at the ESRF in Grenoble.

Prof. Dr. Thomas Möller is gratefully acknowledged for chairing the final defence of this thesis.

Long parts of my thesis, I was accompanied by students, with whom I tackled unknown territories. Their help with keeping the measurements going cannot be overestimated. Thus, I thank Kevin Irmer, Stefan Kuls, Paul Reiß, Christian Hassenstein, Lars Freter, Hans-Ferdinand Jirschik, Jonas Heggemann, and Gada Hweidi.

The students and me would have had a lot more trouble, if there would not have been the assistance of Dr. Martin Franz. His knowledge and help was vital for the successful measurements not only at the home laboratory at the TU Berlin, but also at BESSY II. In addition, I would also like to thank all other former and current members of the Dähne workgroup for the nice working atmosphere, the help during the measurments, e.g. at BESSY II, the sometimes helpful, sometimes interesting, and sometimes funny discussions, and the great experiences at the yearly Ostseeseminar symposia. Especially mentioning deserve Christopher Prohl, my fellow PhD student in the Diplomandenzimmer, Celina Schulze, and Wjatscheslav Martyanov. I had the pleasure to teach undergraduate students together with all three of them. Scientific help is nice, but also administrative support and technical help are necessary. For these, I thank Angela Berner and Jörg Döhring.

This thesis would only contain half of its information without extensive collaborations. In addition to Prof. Dr. Joachim Wollschläger already mentioned above, I thank: Dr. Frederic Timmer, Dr. Frederik Edler, Dr. Ilio Miccoli, Prof. Dr. Christoph Tegenkamp, Prof. Dr. Herbert Pfnür, Kris Holtgrewe, Prof. Dr. Simone Sanna, Prof. Dr. Wolf Gero Schmidt, Julian Plaickner, Dr. Sandhya Chandola, Dr. Eugen Speiser, Prof. Dr. Norbert Esser, Dr. Markus Andreas Schubert, Dr. Tore Niermann, and Prof. Dr. Michael Lehmann. Furthermore, I would like to thank all fellow PhD students of FOR 1700, of FOR 1282, and of the IMPRS Complex Surfaces in Material Science for the interesting and often eventful times at the PhD meetings and the symposia.

Photoemission experiments would have been impossible without the set-up of Prof. Dr. Karsten Horn and PD Dr. Christian Papp, thank you. My colleagues and I would not have been able to the operate this set-up successfully without the help of Dr. Hendrik Vita,

Dr. Stefan Böttcher, and Dr. Roland Koch. Furthermore, I would like to acknowledge BESSY II (Helmholtz-Zentrum Berlin) for granting beamtimes and the beamline scientists Dr. Willy Maler and Dr. Birgit Zada for their support.

I would like to thank my entire family for their support throughout the years, especially my mother for her help (and the always welcome chocolate bars) during beamtimes at BESSY II. I am very thankful for Diana to be at my side since nearly a decade. She carefully protected me from overworking and her diversion and support together with Rufus kept me continuing even when the experiments, data analysis, or writing did not go as planned.

This work was supported by the Elsa-Neumann-Stipendium des Landes Berlin and by the Deutsche Forschungsgemeinschaft through FOR1700 project E2 and through FOR1282 project D.